UAB
Universitat Autònoma de Barcelona

Advanced Catalytic Materials and Systems for Electroconversion of Carbon Dioxide to Ethylene

Tandava Venkata Siva Rama Krishna

ADVERTIMENT. L'accés als continguts d'aquesta tesi doctoral i la seva utilització ha de respectar els drets de la persona autora. Pot ser utilitzada per a consulta o estudi personal, així com en activitats o materials d'investigació i docència en els termes establerts a l'art. 32 del Text Refós de la Llei de Propietat Intel·lectual (RDL 1/1996). Per altres utilitzacions es requereix l'autorització prèvia i expressa de la persona autora. En qualsevol cas, en la utilització dels seus continguts caldrà indicar de forma clara el nom i cognoms de la persona autora i el títol de la tesi doctoral. No s'autoritza la seva reproducció o altres formes d'explotació efectuades amb finalitats de lucre ni la seva comunicació pública des d'un lloc aliè al servei TDX. Tampoc s'autoritza la presentació del seu contingut en una finestra o marc aliè a TDX (framing). Aquesta reserva de drets afecta tant als continguts de la tesi com als seus resums i índexs.

ADVERTENCIA. El acceso a los contenidos de esta tesis doctoral y su utilización debe respetar los derechos de la persona autora. Puede ser utilizada para consulta o estudio personal, así como en actividades o materiales de investigación y docencia en los términos establecidos en el art. 32 del Texto Refundido de la Ley de Propiedad Intelectual (RDL 1/1996). Para otros usos se requiere la autorización previa y expresa de la persona autora. En cualquier caso, en la utilización de sus contenidos se deberá indicar de forma clara el nombre y apellidos de la persona autora y el título de la tesis doctoral. No se autoriza su reproducción u otras formas de explotación efectuadas con fines lucrativos ni su comunicación pública desde un sitio ajeno al servicio TDR. Tampoco se autoriza la presentación de su contenido en una ventana o marco ajeno a TDR (framing). Esta reserva de derechos afecta tanto al contenido de la tesis como a sus resúmenes e índices.

WARNING. The access to the contents of this doctoral thesis and its use must respect the rights of the author. It can be used for reference or private study, as well as research and learning activities or materials in the terms established by the 32nd article of the Spanish Consolidated Copyright Act (RDL 1/1996). Express and previous authorization of the author is required for any other uses. In any case, when using its content, full name of the author and title of the thesis must be clearly indicated. Reproduction or other forms of for profit use or public communication from outside TDX service is not allowed. Presentation of its content in a window or frame external to TDX (framing) is not authorized either. These rights affect both the content of the thesis and its abstracts and indexes.

UAB
Universitat Autònoma de Barcelona

Doctorate program in Materials Science

Doctoral thesis

Advanced Catalytic Materials and Systems for Electroconversion of Carbon Dioxide to Ethylene

Tandava Venkata Siva Rama Krishna

Director: Prof. Dr. Joan Ramón Morante

Director: Dr. Sebastián Murcia López

Tutor: Prof. Dr. Jordi Arbiol

Institut de Recerca en Energia de Catalunya (IREC)

Department of Physics, Faculty of Sciences

Universitat Autònoma Barcelona (UAB)

2024

IREC
Shaping Energy for a Sustainable Future

DOC-FAM
DOCtoral training programme in Functional Advanced Materials
H2020-MSCA-COFUND-2016

MARIE CURIE ACTIONS

UAB
Universitat Autònoma
de Barcelona

Dissertation

presented for obtaining the Degree of Doctor from the

Universitat Autònoma Barcelona (UAB)

by

Tandava Venkata Siva Rama Krishna

Prof. Dr. Joan Ramón Morante	**Dr. Sebastián Murcia López**	**Prof. Dr. Jordi Arbiol**
(Director)	(Director)	(Tutor)

Barcelona, September 2024

Prof. Dr. Joan Ramon Morante Lleonart, Head of Energy Storage Harvesting and Catalysis; Director, Institut de Recerca en Energia de Catalunya (IREC), Professor, University of Barcelona.

Dr. Sebastián Murcia López, Scientific Researcher, Institut de Recerca en Energia de Catalunya (IREC).

Prof. Dr. Jordi Arbiol, ICREA Research Professor, Institut Català de Nanociència i Nanotecnologia (ICN2).

CERTIFY

that Mr. Tandava Venkata Siva Rama Krishna, M.Sc in Analytical Chemistry, has carried out the research work entitled **"Advanced Catalytic Materials and Systems for Electroconversion of Carbon Dioxide to Ethylene"** to opt for the Degree of Doctor from the Autonomous University of Barcelona (UAB) under their direction and qualify for the degree of Doctor under their supervision.

that the design, synthesis, characterization of the experimental work and analysis of the results, writing of the articles and this dissertation are the result of the work of research carried out by Tandava Venkata Siva Rama Krishna

And for this record, they sign this certificate,

Prof. Dr. Joan Ramón Morante	**Dr. Sebastián Murcia López**	**Prof. Dr. Jordi Arbiol**
(Director)	(Director)	(Tutor)

Barcelona, September 2024

“Be a Scientist; Save the World”

– Prof. Richard E. Smalley, Nobel Prize in Chemistry, 1996

“If it can’t be reduced, reused, repaired, rebuilt, refurbished, refinished, resold, recycled or composted, then it should be restricted, redesigned or removed from production”

– Pete Seeger

“Sustainability is not a concept; it is the way Nature is constructed”

– Sadhguru Jaggi Vasudev

Acknowledgements

I have not failed. I've just found 10,000 ways that won't work- **Thomas A. Edison**

One of the lines that kept resonating in my brain during these past few years of this PhD journey with almost every moment in the lab and I am one step away from the milestone. These years have been a great experience altogether both in the lab and being in Barcelona, my first international home. Although the experience in the lab and the whole IREC had been a great moment of joy forever, I cannot deny the fact that the personal challenges and hardships were extremely difficult, stressful and even painful at times. Having said this, I am extremely grateful to all the wonderful, kind people with whom I spent these years contributed and of course the whole journey that landed me at this moment of my life.

Having been a biology undergraduate, chemistry postgraduate and now on this path to attain doctorate in Material science, the path of landing into electrochemistry (the topic which I never thought I would pursue) was quite an interesting journey and the wholesome knowledge and experience during all these years is beyond words. With the learnings from the situations and of course the smart scientific and social souls around me, I feel I have had the major learnings of my life, and I would like to thank all these people.

Prof. Morante. Thank you for being the Director of my thesis. I am ever grateful to you trust in me and welcoming to the group and giving me a challenging task and a free hand to experiment in beginning a new line of research in the group that helped me in gaining a sound knowledge. I feel your deep scientific knowledge and the interest in highlighting some bold or difficult to pursue ideas were truly inspiring. I wish I would have got more one-on-one brainstorming sessions from you, but I shall utilize this experience in the times ahead.

Dr. Sebastián. The Boss. Thank you for being the Director and driving force of my thesis and you were the pillar of support. I am honestly falling short of words to acknowledge your guidance and support throughout this journey.

Prof. Jordi Arbiol. Thank you for being the Tutor of my Thesis and also the contribution of your group for initially offering the microscopy measurements and later accepting me as a Visiting PhD student to your group and I thank your group as well.

Dra. Teresa. Thank you for directing the group with the right motivation back then with your vast scientific knowledge. Your organizing works and effort during my initial days was extremely helpful particularly during the COVID times.

Dr. Ignacio. I had an amazing time in our loooong meetings back then. You have a strong passion for the real scientific outcomes, and I would like to learn more the fundamentals of electrochemistry from your perspective. I also thank you for your hospitality in Edinburgh.

M Dr. Nina. Nina, my cariño. Thank you for being my support system throughout my PhD journey. At the initial moment of my PhD, the knowledge you have shared was exceptional and definitely contributed to my work. Of course, we had a great time outside the lab.

Dr. Jordi Jacas. Jordi, thank you for the conversations and sharing your experiences and for your critical comments during the group meetings which helped me all the time.

Dr. Jordi Guilera. You are a wonderful and motivated researcher and the very little time and conversation with you had motivated me and I really thank you for supporting my stay extension through the CO2SAF project.

Dr. Paolo. Paolo, my third boss. It's been a while you left IREC, and I miss the good old times. At the beginning of my PhD, you were a ready to go person to find a solution for the difficulties in designing and executing some experiments.

Dr. Andrés. Sir Andrés, my fourth boss. Lately you are my ready to go person to discuss any topic both scientific and personal levels. I have enjoyed all the discussions including the heated debates we have had about different aspects of the work.

Dr. Marti. I often say, a week without my directors is manageable but a day without you in the lab can be very difficult. Thank you for the support in providing me all the logistics and even with nice cartoons for the articles and thesis. Anything is possible if Marti is there. You are just awesome and no less than the Superman of ESEH.

Dr. Maria. Thank you for your help particularly during my writing times. Your skills definitely helped me in organizing this thesis much more efficiently.

I am forever thankful to the whole group of ESEH with whom I have had the best times during these years by spending time at work, coffee and lunch breaks and most importantly the group's team building activities where I had fantastic experiences, and these memories stays forever. I am thankful to the current and past members of the group who were a pleasure to work with. **Dr. Elias, Dr. Marisa, Dra. Elena, Dr. Paolo, Dr. Hemesh, Dr. Carles, José Miguel, Dr. Prakasha, Dr. Viktoria, Dr. Monalisa, Marcelo, Dr. Andreina, Dr. Yonca, Maximiliano, Ivan, Ting, Xu, Dr. Alireza, Dr. Marc, Maximiliano, Rolando, Jesus, Karen, Sergio, Dr. Rossana Boccia** and so on. I am sorry if I miss someone here in the list.

I would also thank the cohort of DOCFAM team, including the first and second call fellows. I thank particularly Laura for so well coordinating the team and my co fellows, Dr. Viktoria and Dr. Monalisa, Dr. Jewela and the list continues. I had an amazing time with you guys.

Dra. Viktoria. Dear Vics. Thank you for being a fantastic friend and an amazing host and of course the long walks and talks we had. I miss you in IREC as of now, but I think you are doing great.

Dra. Monalisa. Mona ji. I thank you personally for being an amazing friend and host and our forever discussions during the coffee breaks. I miss you in IREC. I wish you all the best

Dra. Andreina. Andy. You are a great friend and whatever Spanish words; I have learnt was majorly because of your Spanish and my English conversation. I believe you are doing great.

Marcelo. Mars. The Doctor about to be. We started the journey together and we have had major ups and downs in our careers at IREC and even on a personal note as well. You are such an incredible friend and bear with me in pulling your leg forever. We had an amazing time travelling together and I want to go on many more trips with you.

I would like to thank **Dr. Dioudlé** for all the training activities at the beginning days and later followed by collaborating in the scientific outcomes. I also thank **Dr. Albert** for continuing help and support with IREC's instrumentation facilities. I also thank all the amazing friends and colleagues from other groups in IREC. I also thank all the administration people throughout these years particularly Francesc, Yolanda, Marcos, Ines, Cristian and Elba. **Francesc,** thank you for all the timely help with bureaucracy works which made my life a bit easier in Barcelona, Spain.

Dr. Kunal. Bhai. You are a gem of a person and your focus and passion for science have always motivated me. We have had a fantastic time during the scientific and personal discussions, and I believe this will continue forever I must say you are one of the most motivated scientists.

Prof. Nambiar. You are the epitome of passion for science, and you were the main person to tune my intuitions in pursuing a PhD. I am forever grateful, and I wish you a great health.

Dr. Prabhavathi. Ma'am thank you for your trust in me and the constant support I have received so far, and I just wish it continues forever.

Dr. Shiva. Shiva sir. You believed in me and kept the trust and supported me always and I had a great time with you and our conversations about Science in India and I know it just continues.

Dr. Chaitanya. Sir. You are an important person that I met in my career, and you always motivated me to raise the bar and I am truly thankful for your guidance and support.

I would like to **Dr. Vimal**. Bro. Thank you for being there whenever it was necessary. I would like to thank Dr. Sai Kumar, Dr. Vijender, Dr. Ganga Reddy and many other people. I would like to thank my friends here in Barcelona for being there whenever possible. Purandhar, Ram, Vinod, Prasanth and the list continues. Ram bro, my mother thanks you more than me and you know the reason. I will catch up with all of you soon. I would like to thank my friends in India with whom I have had an amazing journey so far. Prudhvi, Deep, Naresh, Praful, Ananya, Ramya, Sumithra, Aadarsh, Pavan, Rahul, Shashank, Vamshi and the list continues. I also thank some **ANGEL** people in my life with whom I have had a fantastic time.

I would love to thank all my brothers and sisters particularly my nephew Sai for some good vector images and all my family members for being there throughout my life and also for standing aside for my mother and helping her whenever and wherever necessary.

and the list of acknowledgements continues……..

With an immense gratitude, I acknowledge the European Union's Horizon 2020 research and innovation programme under the Marie Skłodowska-Curie grant agreement No 754397 through the COFUND DOCFAM program for the financial support of this thesis work. I also thank the financial support from SolDAC project, HEurope G.A. 101069359, ISF Number 10039331) and CERES projects (project PID2020-116093RB-C42), funded by MCIN/ AEI/10.13039/501100011033/ and by "ERDF A way of making Europe", by the "European Union" and also the CO2SAF project. Majority of this work has been carried out at IREC facilities and acknowledges the Generalitat de Catalunya for financial support through the CERCA Programme, M2E (2017 SGR 1246).

I would like to thank the Dr. Dr Ignacio Tudela-Montes and the team of Edinburgh Electrochemical Engineering Group (***e3***) particularly Mayra, for carrying advanced electron microscopy measurements and performing the electrochemical kinetic modelling studies.

I would like to acknowledge the Autonomous University of Barcelona for the academic support and tutoring in the framework of the doctorate programme in Materials Science.

Tandava. VSRK

Barcelona, September 2024.

Let us learn together.

– Dr. Sebastián, the Boss.

Boss, I am truly grateful for having you as the Director of my thesis. Let us learn together were the words mentioned by you at the beginning of my PhD when I expressed my concerns about being new to the field. Thank you for giving me the freedom to express every idea and further discuss about. Thank you for letting me do as much as I can and thank you for cutting down my wings at times which was necessary back then. Thank you for your patience in addressing my concerns and I have taken a long time among all your students from you amidst your workload. Thank you for your time at the coffee and at places like Garage where we further continued to have scientific discussions. You were very supportive and did more than you could during my stay here at IREC. This thesis would not have been a reality without your guidance. I owe you and am indebted. I am not falling short of words but **for being an amazing person and Director of my thesis**

You have a piece of my heart, Boss..!!

Though lost the heaven,

Everything is not lost.

The unconquerable Will and indomitable Spirit are not lost,

It can make the Heaven of hell or hell of a Heaven.

– lines by Prof. B. V. Appa Rao,

Professor of Physical Chemistry (Emeritus),

National Institute of Technology, Warangal, India.

I dedicate this thesis to my maternal uncles,

Balaiah Pittla (Rtd. Police Inspector)

Ch. Balaiah Pittla (Rtd. Police)

whose love, affection, support and guidance throughout my life so far made me stand here today and their untimely demise during this PhD journey is an irreparable loss forever.

Amma

I love you..!!

CONTENTS

Abstract ..... **i**

Resumen ..... **iii**

Resum ..... **v**

List of Abbreviations ..... **vii**

Chapter 1. General Introduction **1**

1.1 General Introduction Global warming and effective mitigation **2**

1.1.1 Global warming 2

1.1.2 CO_2 utilization technologies 8

1.1.3 References 11

1.2 Concept and practical aspects of Electrochemical CO_2 Reduction **13**

1.2.1 Product distribution 15

1.2.2 Major selectivity: Elemental classification from the periodic table 18

1.2.3 Techno-economic analysis: Reason for targeting the selectivity towards C_2H_4 20

1.2.4 Performance considerations to evaluate the ECO_2R 21

1.2.4.1. Onset potential 22

1.2.4.2. Overpotential (η) 22

1.2.4.3. Current density (j) 22

1.2.4.4 Faradaic efficiency (FE %) 22

1.2.4.5 Energy efficiency (EE %) 22

1.2.4.6 Overall stability 23

1.2.5 Reaction mechanism of ECO_2R 23

1.2.6 Electrocatalyst for tuning the selectivity of ECO_2R to C_2H_4 25

1.2.7 System design and configuration for ECO_2R 26

1.2.8 Gas diffusion electrodes (GDE) 28

1.2.9 Ionomers 29

1.2.10 Ion-exchange membranes 30

1.2.11 Role of electrolyte 31

1.2.12 State of art electrocatalysts for ECO_2R to C_2H_4 32
1.2.13 Thesis scope and outline 35
1.2.14 References 37

Chapter 2. Experimental Materials, Methods and Systems Involved in Electrochemical CO_2 Reduction 43

2.1 Introduction 45
2.2 Catalyst synthesis and electrode fabrication 46
2.2.1 Materials 46
2.2.2 Hydrothermal Synthesis:
Synthesis of CuO-Cu_2O/C-Black (Cu_xO-C) heterostructures 47
2.2.3 Synthesis of Ni-N-AC Single Atom Catalysts (SAC) 48
2.2.4. Fabrication of GDEs (PTFE/SGL-Cu) 49
2.2.5. Electrode Fabrication 50
2.3 Physicochemical characterization 54
2.3.1 X-ray Diffraction (XRD) 54
2.3.2 Attenuated Total Reflectance- Fourier-Transform Infrared Spectroscopy 55
2.3.3 Brunauer–Emmett–Teller (BET) method for surface area analysis 56
2.3.4 Scanning Electron Microscopy (FESEM) 57
2.3.5 Transmission Electron Microscopy (TEM) 58
2.3.6 X-ray Photoelectron Spectroscopy (XPS) 60
2.3.7 Temperature Programmed Desorption (TPD) 60
2.3.8 X-ray Fluorescence Spectroscopy (XRF) 61
2.3.9 Four-Probe Method 61
2.3.10 Contact Angle 62
2.4 Electrochemical characterization 64
2.4.1 Open Circuit Voltage (OCV) 65
2.4.2 Linear Sweep Voltammetry (LSV) 65
2.4.3 Cyclic Voltammetry (CV) 66
2.4.4 Chronoamperometry (CA) 67
2.4.5 Chronopotentiometry (CP) 68

2.4.6 Electrochemical Impedance Spectroscopy (EIS) 68
Modelling of Electrochemical CO_2 reduction kinetics 69
2.5 CO_2 Electrolyzer Setup and Product Quantification 72
2.5.1 CO_2 electrolyzer 72
Electrochemical flow electrolyzer and components 72
Flow-by and flow-through operation mode of CO_2 Electrolyzer 73
2.5.3 Optimizing the Flow rate of CO_2 gas and electrolyte 75
2.5.4 Electrochemical CO_2 reduction experiments 75
2.5.5 Product quantification 76
Gas product analysis and quantification 76
Liquid product quantification 77
2.6 References 79

Chapter 3. Carbon-Supported Oxide-Derived Copper Heterostructures for the Electroconversion of CO_2 81

3.1 Abstract 83
3.2 Introduction 83
3.3 Objectives 84
3.4 Highlights 85
3.5 Experimental Methods 85
3.5.1 Synthesis of the electrocatalyst materials 85
3.5.2 Electrode Fabrication 86
3.6 Results and Discussion 86
3.6.1 Structural characterization of the electrocatalyst materials 86
3.6.2 Linear Sweep Voltammetry and ECSA Analysis 98
3.6.3 Electrochemical Reduction of CO_2 in a Flow Electrolyzer 100
3.7 Conclusions 112
3.8 References 113

Chapter 4. Best-Fit Tandem Approach for the Upscaled Electroconversion of CO_2 to C_2H_4 115

4.1 Abstract 117

4.2 Introduction 118

4.3 Objectives 122

4.4 Highlights 123

4.5 Experimental Methods 124

4.5.1 Synthesis of the electrocatalyst materials 124

4.5.2 Electrode Fabrication 124

4.6 Results and Discussion 127

4.6.1 Individual Catalyst performance 127

4.6.2 Tandem Catalysts 131

4.6.3 Tandem Electrodes 135

4.6.4 Tandem Devices 139

4.7 Conclusions 152

4.8 References 153

Chapter 5. Modulating the Surface Interface of PTFE/Copper-based Gas Diffusion Electrodes 155

5.1 Abstract 157

5.2 Introduction 158

5.3 Objectives 160

5.4 Highlights 160

5.5 Experimental Methods 161

Fabrication of PTFE/Cu-based GDEs 161

5.6 Results and Discussion 163

5.6.1 Surface interface modulation of PTFE/Cu GDEs by thickness variation of Cu catalyst layer 164

5.6.2 Surface interface modulation of PTFE/Cu GDEs by additive layer 176

5.6.3 Performance of PTFE/Cu-based GDEs at high current densities 192

5.6.4 Stability of PTFE/Cu-based GDEs during continuous operation 193

5.6.5 Scaling up of the PTFE/Cu-based GDEs deployed electrolyzers 195
5.7 Conclusions 197
5.8 References 198

Chapter 6. Conclusions and Future Perspectives 201
6.1 Conclusions 203
6.2 Future Perspectives 207

Curriculum vitae 211

Abstract

Circular economy of CO_2 is a hot issue amid global warming. While the large dependency on conventional fossil fuels is directly proportional to the ever-increasing levels of CO_2 in the atmosphere, the urge to develop reliable systems for CO_2 conversion is quite important and is a strong requisite to meet the global energy demands. Anthropogenic carbon cycle closure is aimed at achieving a tangible reality with the successful implementation of electrochemical CO_2 reduction (ECO_2R) coupled with renewable electricity. ECO_2R is proven to be a promising strategy in directly converting CO_2 to value-added products and is still believed to be a vast area for further advancements with the challenges associated with real-time practical implementation.

Despite considerable progress in products like CO and formate, value-added products like ethylene (C_2H_4) have been a distant reality in reaching the potential industrial scale. Practical limitations, such as poor selectivity for multi-carbon products in compliance with sluggish kinetics often lead electrocatalysts to suffer from high overpotentials while converting CO_2 to C_2H_4 and other C_{2+} products. Of the whole periodic table, copper (Cu) alone holds the unique capability to selectively reduce CO_2 to value-added products that led Cu as the “star metal”. Therefore, developing Cu and Cu-based functional advanced robust electrocatalysts and successive integration into gas diffusion electrodes (GDEs) and electrolyzer systems for an efficient and highly selective ECO_2R to C_2H_4 is a necessity to accomplish.

Primarily, in order to have a highly robust electrocatalyst, the initial focus of the thesis work was levied on, synthesizing copper and copper oxide-based materials (Cu_xO) supported over carbon black (C) via a facile hydrothermal method. The in-situ growth of platelet-like Cu_xO-heterostructures over carbon black; Cu_xO-C, was believed to enhance the catalytic efficiency due to the excellent distribution of Cu active sites over C facilitating a rapid electron transfer. The as-synthesized Cu_xO-C were found to be highly selective towards C_2H_4 and it is understood that the in-situ modification of CuO to Cu_2O at the onset potentials during the electrolysis is the driving force for the highly selective conversion of CO_2 to C_2H_4 through the *CO intermediates followed by C−C coupling.

In the continuum, inspired by nature’s cascade processes, an alternative tandem approach to ECO_2R route is proposed to modulate product generation from CO_2 to CO and further reduce

CO to C_2H_4. In order to tune the major selectivity towards C_2H_4, additional active sites of Ni-N-AC were integrated with Cu_xO-C for systematic screening of the tandem approach ranging from tandem electrocatalysts and tandem electrodes, followed by tandem devices to elucidate the best-fit tandem approach. In the tandem devices, when the unreacted CO_2 is trapped using an intermediate absorption chamber between the two electrolyzers, a surge in the faradaic efficiency towards C_2H_4 over 70 ± 3 % with 87 ± 5 % towards multi-carbon products at an average current density of -150 $mA \cdot cm^{-2}$ was noticed. This tandem approach seemed to be highly efficient not only in faradaic efficiency but also energetically thus demonstrating the tandem device setup can potentially reach the industrial scale.

Furthermore, tailored GDEs were fabricated by sputtering copper layers on polytetrafluoroethylene porous membranes followed by modulating the surface of the GDE with an additive layer (i.e., C/ ionomer and Cu_xO-C/ ionomer) which proved to be very effective in boosting selectivity towards C_2H_4 and other C_{2+} products. A comparative study of the modulated surface of PTFE/Cu GDEs led to an understanding of the role of the optimized catalyst/catalyst-additive layer heterojunction interface in not only tuning the selectivity towards C_2H_4 as the prime product but also significantly lowering the cathodic overpotential required to achieve high current densities. The PTFE/Cu-GDE with an optimized additive layer loading of Cu_xO-C converted CO_2 to C_2H_4 with a faradaic efficiency of 70 ± 2% (combined faradaic efficiency of 90 ± 3 % for C_{2+} products) with an *iR*-corrected potential of - 0.55 V *vs* RHE and at an industrially relevant current density of -250 $mA \cdot cm^{-2}$ in a flow electrolyzer. Moreover, the PTFE/Cu/Cu_xO-C GDE demonstrated the scope for successful upscaling followed by exhibiting excellent stability with a consistently high yield of C_2H_4 over 25 hours and effectively suppressing the competitive hydrogen evolution reaction.

From the obtained results, it can be concluded that it is not only the advanced catalyst materials but also the optimization of the electrode and electrolyzer systems that play a substantial role in the overall enhancement of the electroconversion of CO_2 to C_2H_4.

Resumen

La economía circular del CO_2 es un tema central en el contexto del calentamiento global. Dados que los niveles cada vez mayores de CO_2 en la atmósfera son directamente proporcionales a la gran dependencia en los combustibles fósiles convencionales, urge desarrollar sistemas confiables para la conversión de CO_2 como requisito importante para satisfacer las demandas energéticas globales. El objetivo de cerrar el ciclo de carbono antropogénico como una realidad tangible se puede lograr con la implementación exitosa de la reducción electroquímica de CO_2 (ECO_2R) acoplada a electricidad renovable. Se ha demostrado que la ECO_2R es una estrategia prometedora para convertir directamente el CO_2 en productos de valor añadido y aún se cree que es un área amplia para futuros avances con los desafíos asociados con la implementación práctica en tiempo real.

A pesar del progreso considerable en productos como el CO y el formiato, los productos multicarbonados como el etileno (C_2H_4) han sido una realidad lejana para alcanzar la escala industrial potencial. Las limitaciones prácticas, como la baja selectividad hacia productos multicarbonados con una cinética lenta, a menudo llevan a que los electrocatalizadores sufran de altos sobrepotenciales para convertir CO_2 en C_2H_4 y otros productos C_{2+}. De toda la tabla periódica, solo el cobre (Cu) posee la habilidad única de reducir selectivamente el CO_2 a productos de valor añadido que lo hacen el metal "estrella". Por esta razón, el desarrollo de electrocatalizadores robustos avanzados de Cu y materiales basados en Cu, y la integración sucesiva en electrodos de difusión de gases (GDEs) y sistemas electrolizadores para una ECO_2R eficiente y altamente selectiva, es una necesidad por alcanzar.

Primero que todo, para conseguir un electrocatalizador altamente robusto, el enfoque inicial del trabajo de la tesis se basó en la síntesis de materiales de cobre y óxidos de cobre (Cu_xO) soportados en carbono (C) a partir de un método hidrotermal simple. El crecimiento in-situ de heteroestructuras tipo láminas de Cu_xO sobre carbono, parecen mejorar la eficiencia catalítica debido a la excelente distribución de sitios activos de Cu sobre el C, facilitando una rápida transferencia electrónica. Se encontró que el Cu_xO-C sintetizado de esta manera es altamente selectivo hacia C_2H_4, y se asocia la modificación in-situ del CuO a Cu_2O a los potenciales iniciales durante la electrólisis con la fuerza impulsora para la alta conversión selectiva de CO_2 a C_2H_4, a través de intermedios *CO seguidos de acoplamiento C-C.

A continuación, inspirados por los procesos en cascada de la naturaleza, una aproximación alternativa en tándem ha sido propuesta como ruta ECO_2R para modular la generación de productos desde CO_2 a CO, y reducción posterior de CO a C_2H_4. Con el objetivo de controlar la selectividad hacia C_2H_4, se integraron sitios activos adicionales de Ni-N-AC con Cu_xO-C, para el cribado de la aproximación tándem desde electrocatalizadores y electrodos, seguidos por dispositivos tándem, con el fin de encontrar el mejor ajuste de la aproximación tándem. En los dispositivos tándem, cuando el CO_2 sin reaccionar es atrapado usando una cámara intermedia de absorción entre los dos electrolizadores, se encontró un incremento en la eficiencia faradaica a C_2H_4 hasta cerca del 70 ± 3 %, con 87 ± 5 % a productos multicarbonados, a una densidad de corriente promedio de 150 $mA \cdot cm^{-2}$. Esta aproximación tándem demostró ser altamente eficiente no solo en eficiencia faradaica sino también energéticamente, demostrando así que el dispositivo tándem puede potencialmente alcanzar la escala industrial.

Adicionalmente, GDEs a medida fueron fabricados a través de "sputtering" de capas de cobre en membranas porosas de politetrafluoroetileno, seguido de una regulación de la superficie del GDE mediante una capa de aditivo (i.e., C/ionómero y Cu_xO-C/ionómero), lo que demostró ser muy efectivo en impulsar la selectividad hacia C_2H_4 y otros productos C_{2+}. Un estudio comparativo de la superficie regulada de los GDEs PTFE/Cu permitió entender el rol de la intercara entre la heterounión catalizador/catalizador-aditivo optimizada no solo para afinar la selectividad hacia C_2H_4 como principal producto, sino también para disminuir considerablemente el sobrepotencial catódico requerido para alcanzar altas densidades de corriente. El PTFE/Cu-GDE con carga óptima de capa aditiva of Cu_xO-C convirtió CO_2 a C_2H_4 con una eficiencia faradaica de 70 ± 2% (eficiencia faradaica combinada de 90 ± 3 % a productos C_{2+}) a un potencial con corrección *i*R de -0.55 V vs RHE y a una densidad de corriente con relevancia a nivel industrial de 250 $mA \cdot cm^{-2}$ en un electrolizador en flujo. Adicionalmente, el GDE PTFE/Cu/Cu_xO-C consiguió el objetivo de escalado exitoso, mostrando excelente estabilidad con un alto rendimiento de C_2H_4 durante 25 horas, limitando eficientemente la reacción competitiva de evolución de hidrógeno.

A partir de los resultados obtenidos, se puede concluir que no solo los materiales catalíticos avanzados, sino también la optimización del electrodo y de los sistemas electrolizadores desempeña un rol fuerte en la mejora global de la electroconversión de CO_2 a C_2H_4.

Resum

L'economia circular del CO_2 és un tema central en el context del calentament global. Atès que els nivells cada vegada més alts de CO_2 a l'atmosfera són directament proporcionals a la gran dependència als combustibles fòssils convencionals, és urgent desenvolupar sistemes fiables per a la conversió de CO_2 per satisfer les demandes energètiques globals. L'objectiu de tancar el cicle de carboni antropogènic com una realitat tangible es pot aconseguir amb una bona implementació de la reducció electroquímica de CO_2 (ECO_2R) acoblada a electricitat renovable. S'ha demostrat que l'ECO_2R és una estratègia prometedora per convertir directament el CO_2 en productes de valor afegit i es creu que és un àmbit ampli per a futurs avenços amb els desafiaments associats a la implementació pràctica en temps real.

Tot i el progrés considerable en productes com el CO i el formiat, els productes multicarbonats com l'etilè (C_2H_4) són una realitat llunyana a l'hora d'aconseguir una potencial escala industrial. Les limitacions pràctiques, com la baixa selectivitat cap a productes multicarbonats amb una cinètica lenta, sovint fan que els electrocatalitzadors pateixin alts sobrepotencials per convertir CO_2 en C_2H_4 i altres productes C_{2+}. De tota la taula periòdica, només el coure (Cu) posseeix l'habilitat única de reduir selectivament el CO_2 cap a productes de valor afegit, la qual cosa el converteix en el metall "estrella". Per aquesta raó, el desenvolupament d'electrocatalitzadors robusts avançats de Cu i materials basats en Cu, així com la integració successiva en elèctrodes de difusió de gasos (GDEs) i sistemes electrolitzadors per a una ECO_2R eficient i altament selectiva, és una necessitat a assolir.

Primer de tot, per aconseguir un electrocatalitzador altament robust, l'enfocament inicial del treball de la tesi es va basar en la síntesi de materials de coure i òxids de coure (Cu_xO) suportats en carboni (C) a partir d'un mètode hidrotermal senzill. El creixement in-situ d'heteroestructures de tipus làmina de Cu_xO sobre carboni sembla millorar l'eficiència catalítica gràcies a l'excel·lent distribució de llocs actius de Cu sobre el C, facilitant una ràpida transferència electrònica. Es va trobar que el Cu_xO-C sintetitzat d'aquesta manera és altament selectiu cap a C_2H_4, i s'associa la modificació in-situ del CuO a Cu_2O als potencials inicials durant l'electròlisi amb la força impulsora per a la alta conversió selectiva de CO_2 a C_2H_4, a través d'intermedis *CO seguits de l'acoblament C-C.

A continuació, inspirats pels processos en cascada de la natura, s'ha proposat un enfocament alternatiu en tàndem com a ruta ECO_2R per modular la generació de productes des de CO_2 a CO, i reducció posterior de CO a C_2H_4. Amb l'objectiu de controlar la selectivitat cap a C_2H_4, s'integraren llocs actius addicionals de Ni-N-AC amb Cu_xO-C per a l'avaluació de l'enfocament en tàndem, estudiant sistemes compostos per electrocatalitzadors, elèctrodes o dispositius en tàndem, amb la finalitat de trobar la millor adaptació de l'enfocament en tàndem. En els dispositius en tàndem, quan el CO_2 sense reaccionar és atrapat utilitzant una cambra intermèdia d'absorció entre els dos electrolitzadors, es va trobar un increment en l'eficiència faradaica a C_2H_4 fins a prop del 70 ± 3 %, amb un 87 ± 5 % d'eficiència faradaica cap a productes multicarbonats, a una densitat de corrent mitjana de 150 $mA \cdot cm^{-2}$. Aquest enfocament en tàndem va demostrar ser altament eficient no només en eficiència faradaica sinó també energèticament, demostrant així que el dispositiu en tàndem pot potencialment assolir l'escala industrial.

Addicionalment, GDEs a mida van ser fabricats a través del "sputtering" de capes de coure en membranes poroses de politetrafluoroetilè, seguit d'una regulació de la superfície del GDE mitjançant una capa d'additiu (i.e., C/ionòmer i Cu_xO-C/ionòmer), la qual va demostrar ser molt efectiva per impulsar la selectivitat cap a C_2H_4 i altres productes C_{2+}. Un estudi comparatiu de la superfície regulada dels GDEs PTFE/Cu va permetre entendre el rol de la interfície entre la heterounió catalitzador/catalitzador-additiu optimitzada no només per afinar la selectivitat cap a C_2H_4 com a principal producte, sinó també per reduir considerablement el sobrepotencial catòdica requerit per aconseguir altes densitats de corrent. El PTFE/Cu-GDE amb càrrega òptima de capa additiu de Cu_xO-C va convertir CO_2 en C_2H_4 amb una eficiència faradaica del 70 ± 2% (eficiència faradaica combinada del 90 ± 3 % cap a productes C_{2+}) a un potencial amb correcció *i*R de -0.55 V vs RHE i a una densitat de corrent amb rellevància a nivell industrial de 250 $mA \cdot cm^{-2}$ en un electrolitzador en flux. Addicionalment, el GDE PTFE/Cu/Cu_xO-C va aconseguir l'objectiu de l'escalat exitós, mostrant una excel·lent estabilitat amb un alt rendiment de C_2H_4 durant 25 hores, limitant eficientment la reacció competitiva d'evolució d'hidrogen.

A partir dels resultats obtinguts, es pot concloure que no només els materials catalítics avançats, sinó també l'optimització de l'elèctrode i dels sistemes electrolitzadors exerceixen un rol important en la millora global de l'electroconversió de CO_2 a C_2H_4.

List of abbreviations

AC	Alternating Current
Ag/ AgCl	Silver/ Silver chloride electrode
AL	Additive Layer
ATR	Attenuated Total Reflectance
BET	Brunauer–Emmett–Teller
BID	Barrier discharge Ionization Detector
CA	Chronoamperometry
CB	Carbon-Black
CDL	Double-Layer Capacitance
CE	Counter Electrode
CFC	Chlorofluorocarbons
CP	Chronopotentiometry
CSTR	Continuous stirred tank reactor
CV	Cyclic Voltammetry
DAD	Diode Array detector
DC	Direct-Current
ECO2R	Electrocatalytic Carbon-dioxide Reduction
ECOR	Electrocatalytic Carbon-monoxide Reduction
ECSA	Electrochemical Active Surface Area
EE	Energy Efficiency
EELS	Electron Energy Loss Spectroscopy
FE	Faradaic Efficiency
FE-SEM	Field Emission Scanning Electron Microscopy
FIB	Focused ion beam
FID	Flame Ionization Detector
FTIR	Fourier-Transform Infrared Spectroscopy
GC	Gas Chromatography
GDEs	Gas Diffusion Electrodes
GDL	Gas Diffusion Layer
GHG	Greenhouse Gas

Gt	Giga ton
HAADF-STEM	High Angle Annular Dark-Field Scanning Transmission Electron Microscopy
HER	Hydrogen Evolution Reaction
HPLC	High-Pressure Liquid Chromatography
HR- TEM	High-Resolution Transmission Electron Microscopy
HS-GC	Head Space Gas Chromatography
IC	Ion Chromatography
LbL	Layer-by-Layer
LC	Liquid Chromatography
LSV	Linear Sweep Voltammetry
MMO	Mixed Metal Oxide
MPL	Microporous Layer
Mt	Metric ton
OER	Oxygen Evolution Reaction
PCET	Proton-coupled electron transfer
PEIS	Potentiostatic Electrochemical Impedance Spectroscopy
PFR	Plug flow reactor
PTFE	Polytetrafluorethylene
RE	Reference electrode
RHE	Reversible Hydrogen Electrode
RID	Refractive Index Detector
SAC	Single Atom Catalyst
Seg	Segmented
TC	Tandem Catalysts
TCD	Thermal Conductivity Detector
TD	Tandem Devices
TE	Tandem Electrodes
TPD	Temperature-programmed desorption
vs/vs	versus
WE	Working Electrode

WMO	World Meteorological Organization
XPS	X-ray photoelectron spectroscopy
XRD	X-Ray Diffraction
XRF	X-Ray Fluorescence

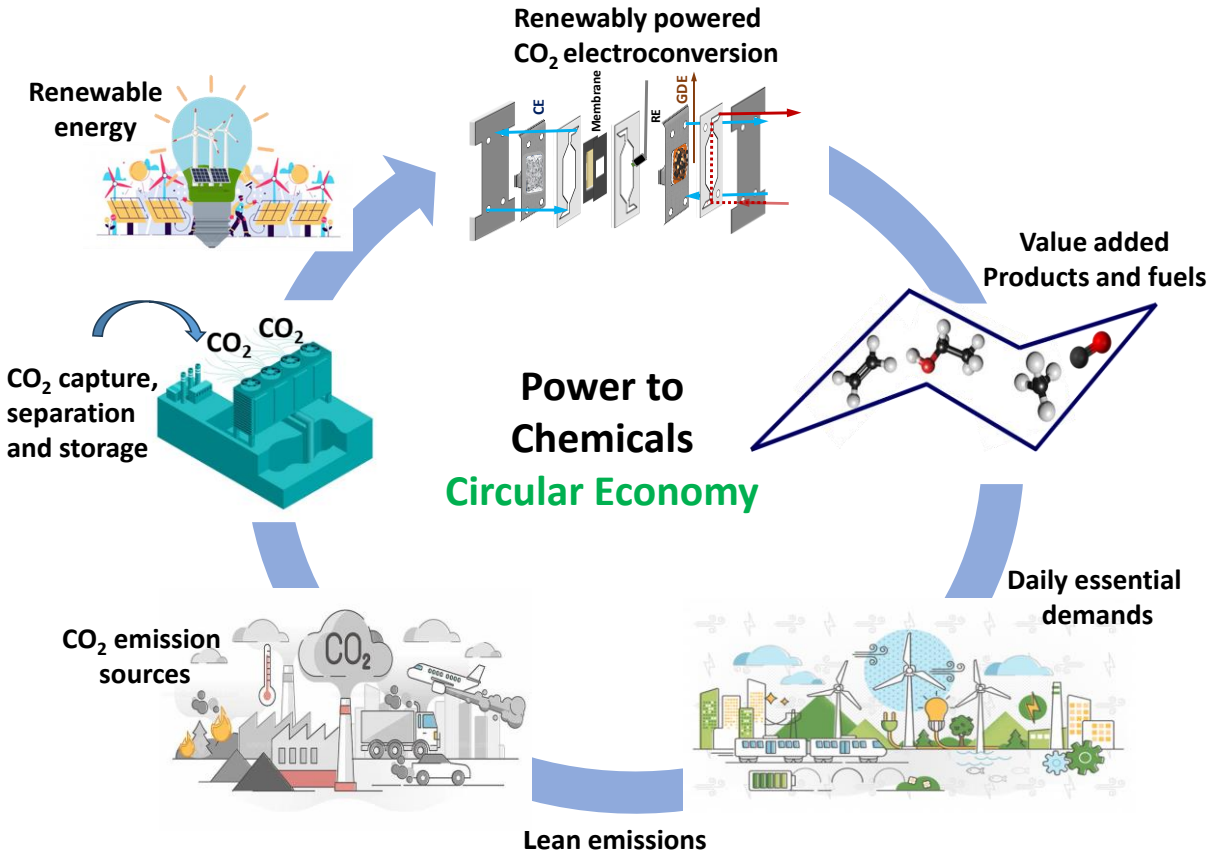
List of Chemical symbols

C_2H_4	Ethylene
C_2H_5OH	Ethanol
C_3H_7OH	Propanol
CH_3COO^-	Acetate
CH_3COOH	Acetic acid
CH_3OH	Methanol
CH_4	Methane
CO	Carbon monoxide
CO_2	Carbon-dioxide
Cu	Copper
Cu_xO	Oxide-derived Copper
Cu_xO-C	Oxide-derived Copper- Carbon
e^-	Electron
H^+	Proton
H_2	Hydrogen
$HCOO^-$	Formate
HCOOH	Formic acid
N_2O	Nitrous oxide
Ni	Nickel
O_2	Oxygen

Chapter 1

1.1. General Introduction:

Mitigating the Global Warming through Electrochemical Carbon-dioxide Reduction



This thesis begins with the Introduction by categorizing it into two sections. The first section deals with a General Introduction and background of the global warming and the effective ways of mitigation with a motivation towards the circular economy. Of the several concepts of mitigation, the latter introduces the concept and practical aspects of Electrochemical CO_2 Reduction (ECO_2R) followed by emphasizing the selectivity towards ethylene (C_2H_4).

1.1. General Introduction: Global warming and effective mitigation.

1.2. Concept and practical aspects of Electrochemical CO_2 Reduction to C_2H_4.

"If all the insects were to disappear from the Earth, within fifty years all life on Earth would end. If all human beings disappeared from the Earth, within fifty years all forms of life would flourish" - Jonas Salk

1.1 General Introduction

1.1.1 Global Warming

1.1° C was the human-induced global temperature rise, popularly termed as "global warming" ever since the beginning of the Industrial Revolution dating back to the 18th century. ~ 1.5° C (1.1- 1.9° C) is the predicted global mean near-surface temperature during 2024-2028 which clearly exceeds the previous rise in temperature according to the World Meteorological Organization (WMO) [1]. Yes, the numbers seem minute, but the threat level from the rising global warming to life's existence on the planet Earth is vast. Global Warming alone holds the responsibility for seasonal and regional climate change resulting in natural calamities of harsh weather conditions, rise in sea level by melting of glaciers, severe droughts and famines leading to the extinction of species that play a major role in maintaining the sovereignty of the ecosystem [2, 3]. Technically speaking, the planet Earth's temperature solely depends on balancing the energy entering and exiting the planet. It is well known that sunlight radiation is the major source of heat energy on the Earth and upon irradiation a part of it is absorbed by the Earth and the remaining is reflected back to space. The reflected solar energy does not primarily warm the Earth. However, a certain variety of gases like carbon dioxide (CO_2), methane (CH_4) and nitrous oxide (N_2O) including the chlorofluorocarbons (CFCs) in the Earth's atmosphere shall absorb the reflected heat energy hindering the return to space. These gases are prescribed to be the Greenhouse gases (GHGs) which are the major apprehension towards the alarming rise in Earth's temperatures annually. The abundance of atmospheric GHGs is primarily the outcome of excessive human exercise primarily in the post-industrial era according to the latest report submitted by the Intergovernmental Panel on Climate Change (IPCC) [4-6], a body of the United Nations. The entire human race of the modern era is solely responsible for the increased GHGs due to daily necessities including the increased energy demand in electricity generation, agriculture and chemical feedstock production. To meet the above-stated daily energy needs and demands, a large dependence on conventional fossil fuel sources was levied resulting in the excessive pileup of GHGs in the atmosphere. According to

the data obtained from the International Energy Agency (IEA), as depicted in Figure 1.1.1, it was shown that out of 100 % energy supply to the human population in order to meet all sorts of energy needs, 80 % of the Total Energy Supply (TES) is done through the fossil fuels like crude oil, coal and natural gas [7].

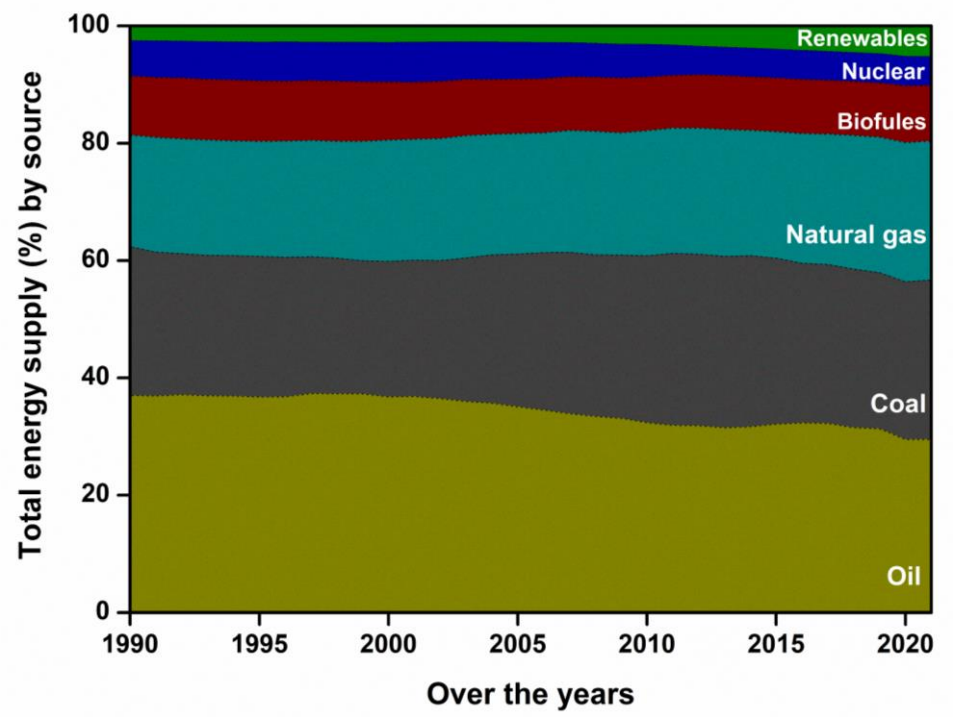


Figure 1.1.1 World's Total Energy Supply by source in percentage comparison during 1990-2001. The data is obtained from the International Energy Agency (IEA) [7].

To mitigate global warming, although the recent scientific efforts over the past 30 years have indicated a minor decline in the dependency on fossil fuels, the damage being caused has a substantial impact on the Earth with the excessive GHG emissions from fossil fuels. Of all the major GHGs, CO_2 holds the unprecedented major composition holding over 37 Gigatons (Gt) of emissions out of the overall 52 Gt GHG emissions accounted for worldwide [8]. As depicted in Figure 1.1.2, it is visualized that anthropogenic CO_2 emissions piled up from 278 parts per million (ppm) during the initial stages of the Industrial Revolution and over 320 ppm during the 1960s to an explosive level of 426 ppm in June 2024, demonstrating the global devastation caused by the exponential economic growth over the worldwide during the past 60 years [9, 10]. The aforementioned alarming situation reflects an overall increase in global CO_2 emissions during the post-industrial era.

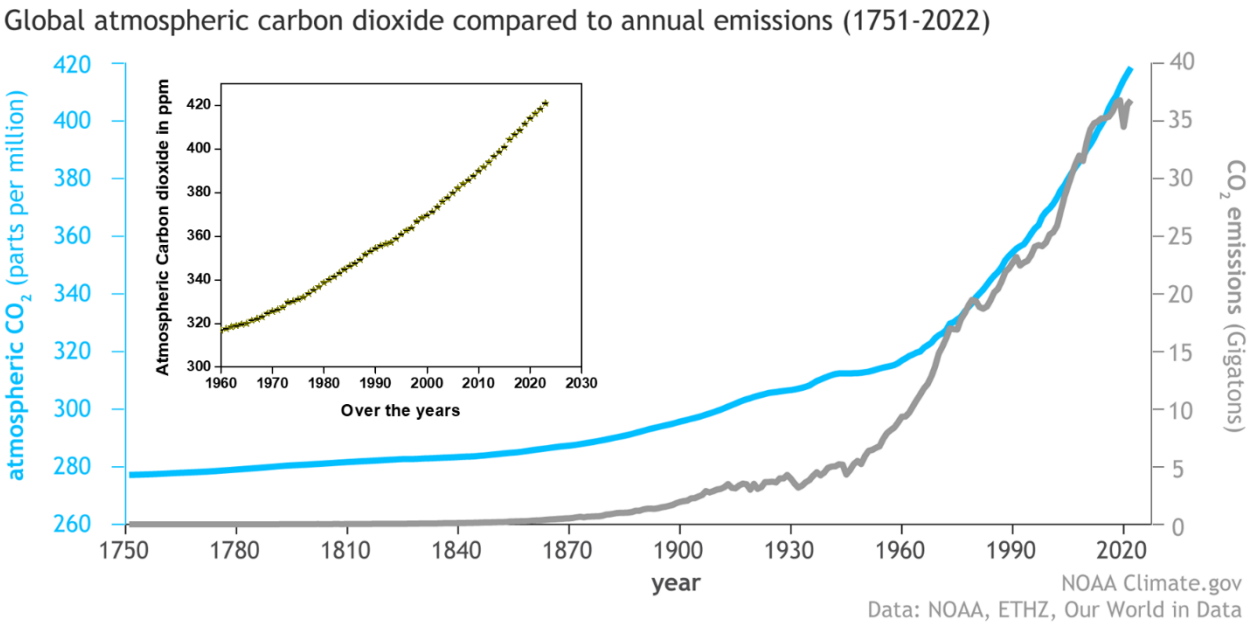


Figure 1.1.2 Amount of carbon dioxide in the atmosphere (blue) and human-induced annual emissions (grey) from 1750- 2022. The inset represents the exponential surge in the atmospheric CO_2 in ppm during the last 60 years. Data obtained from the official website of Scripps Institution of Oceanography (SIO) [9, 10]. Figure adapted and modified from Climate.gov.

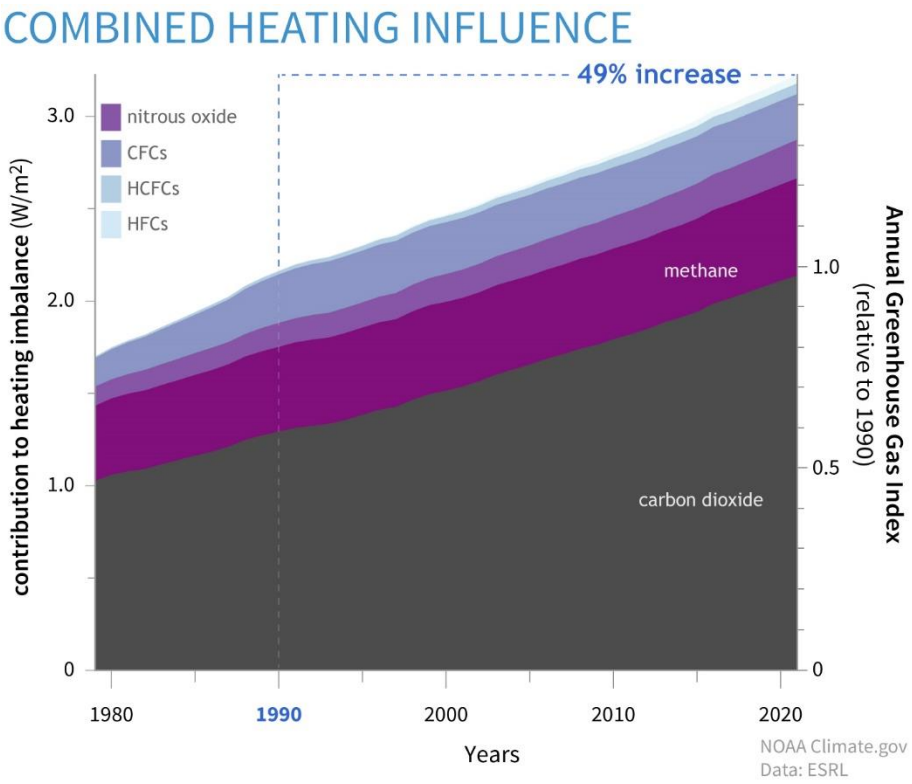


Figure 1.1.3 Human-induced heating influence by the Greenhouse gas emissions representing the major role of CO_2 towards global warming [11, 12]. Figure adapted from the Climate.gov.

As depicted in Figure 1.1.3, obtained from the Climate.gov wing of the National Oceanic and Atmospheric Administration (NOAA), the global heating influence is majorly by the dominant CO_2 followed by CH_4, N_2O and CFCs. When compared to the conditions of 1750, it is observed that the present-day's earth atmosphere absorbs more than 3 extra watts of energy per square meter of Earth's surface. An overall increase of 49 % in GHG emissions in the past 30 years, from 1990 to 2022 was noticed with CO_2 accounting for about 78 % making it the largest contributor to the much-concerned global warming possessing an indefinite threat [11, 12]. The increased CO_2 presence therefore needs the necessary steps and actions to delink the growing energy demands worldwide in effective decarbonization thus reaching the much-targeted net zero CO_2 emissions by 2050 [13].

Before delving into the net zero by 2050, it is wise to elucidate and assimilate the detailed role of anthropogenic CO_2 emissions and their redistribution over the Earth and Earth's atmosphere. An active natural carbon cycle represents the anthropogenic emissions that circulate the carbon between reservoirs ideally over the atmosphere, ocean, and terrestrial biosphere on a timeframe spanning daily to decades and centuries together or even longer durations [14]. Pierre Friedlingstein et. al., [15] presented the Global Carbon Budget (GCB, 2023) referring to trends and variations with the perturbation of CO_2 in the immediate environment describing the major components in the general carbon cycle and the impact of human-induced robust atmospheric CO_2 emissions post 1960s. Figure 1.1.4, depicts the overall global carbon cycle during the last decade, from 2013-2022 with the projections of 2023 representing the input of CO_2 into the atmosphere by human activity leading to the growth of atmospheric CO_2 concentrations thus directing the changes to the natural carbon cycle affecting the natural storage. GCB provides a detailed overview of the input the CO_2 to the Earth's atmosphere considering the human-induced fossil fuel emissions along with the land and ocean use CO_2 sinks. The experts of the GCB estimated that the amounts of human-induced CO_2 emissions are at least double the ability of natural sinks that are aiding in absorbing the emissions which in turn indicates the rising levels of atmospheric CO_2 each year. It was also believed that a sustainable decrease in CO_2 emissions of -1 % is possible only after a decade indicating the severity of the imbalances created. However, it is to be noted that there is a declining trend in overall emissions due to the vast scientific awareness of reaching net-zero emissions like moving to renewable energy sources like solar, wind and hydro-based

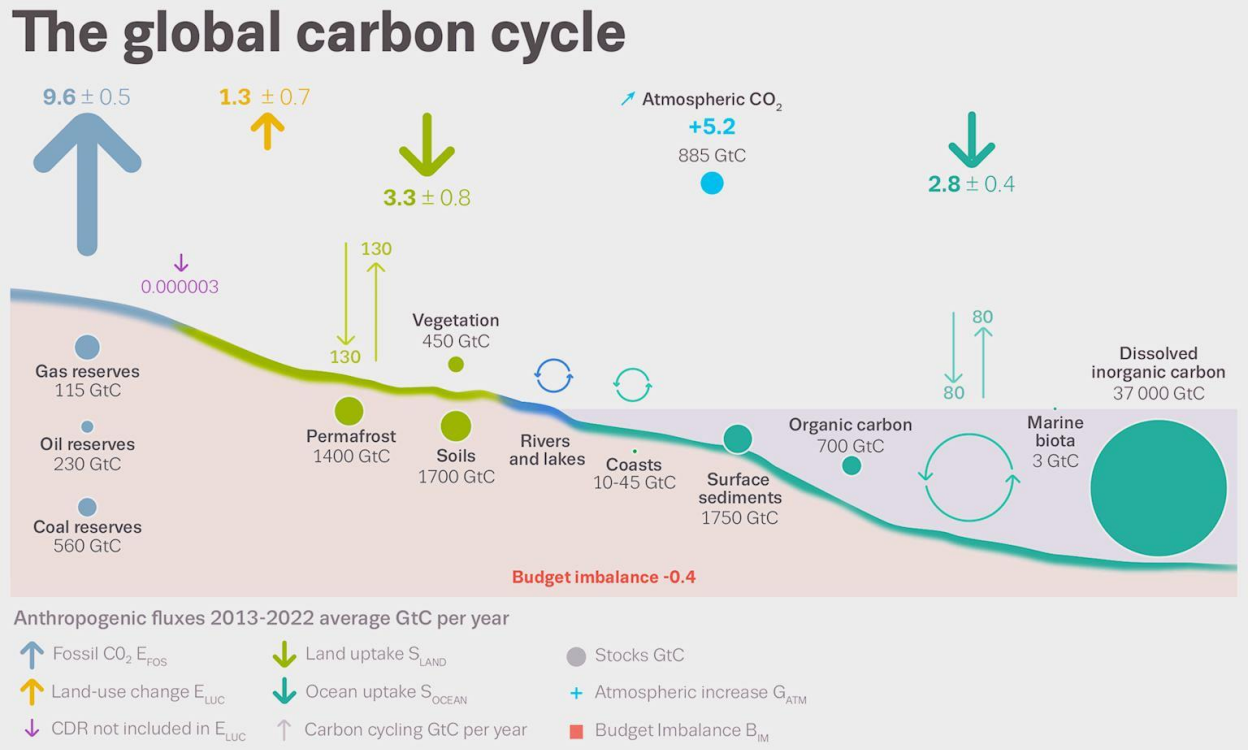


Figure 1.1.4 Schematic representation of the overall perturbation of the global carbon cycle caused by human-induced anthropogenic activities globally during the last decade 2013-2022. Figure adapted from the Global Carbon Budget 2023 [15].

technological advancements but the net contribution to the world's total energy demand is limited to only a small fraction. Therefore, the need for extensive efforts in the ongoing investigations to mitigate global warming through effective decarbonization and going forward to become CO_2 neutral is quite essential. In this regard, there are several technologies put forward by the scientific community for the utilization and conversion of CO_2 to value-added products (chemicals and fuels) as an alternative to the fundamental fossil fuel-based energy supply. In fact, if done effectively by demonstrating a benchmarking technology, the emitted CO_2 can turn into the feedstock or raw material in the place of conventional crude oil for the production of value-added products. The aforementioned strategy of capturing the CO_2 and further utilization can be referred to as Carbon Capture, Storage and Utilization (CCUS) [16,17]. In principle, CCUS aims at the mitigation of global warming caused by the enormous amounts of CO_2 emissions worldwide by capturing the CO_2 and storing it for later utilization by converting it into value-added products.

1.1.2 CO_2 utilization technologies

Once the CO_2 is captured, there are diversified ways to utilize and produce the value-added products. According to the first principles and recapitulation of CO_2 utilization, the technologies range from biological and chemical routes for the conversion of CO_2 [18] as depicted in Figure 1.1.5. Primarily divided into chemical and biological routes, the biological route comprises nature-driven photosynthesis and non-photosynthetic way of aerobic and anaerobic fixation [19, 20]. The chemical route comprises chemical reforming, thermal hydrogenation and plasma-assisted catalytic hydrogenation [21-23] mildly operating at extreme temperatures and pressure along with the ambient operating conditions of photocatalysis and the renewably powered photoelectrocatalysis and electrocatalysis [24-26].

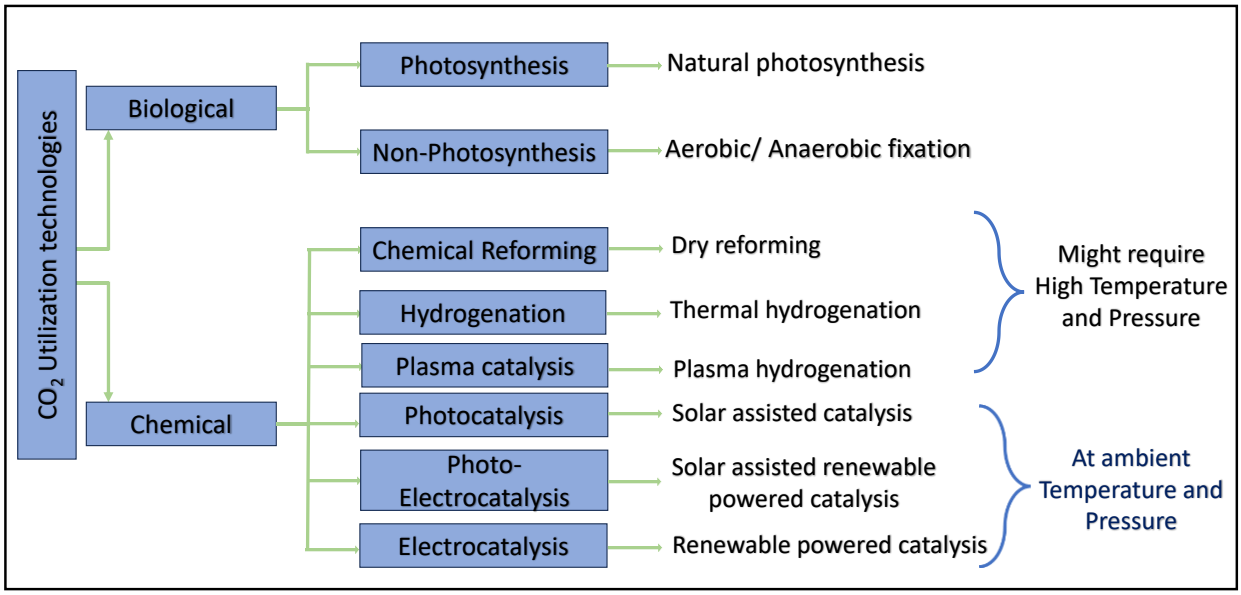


Figure 1.1.5 Schematic representation of the various CO_2 utilization technologies. Figure adapted and modified from Ariane D.N. Kamkeng et.al. [18].

Among the aforementioned catalytic routes, owing to operating at ambient conditions and being easy to implement at the industrial scale, electrocatalytic/ electrochemical CO_2 reduction (ECO_2R) has gained the upper hand in effective decarbonization technologies [27]. ECO_2R is the only proven technology which can directly convert CO_2 to C_2H_4 when coupled with renewable energy. Furthermore, ECO_2R has seemed to attract the scientific community as noticed in Web of Science (WoS) over the other routes which is evident by the significant growth since 2010. Figure 1.1.6 depicts the comparison between the CO_2 reduction and ECO_2R. It is also to be noted that there has been an increase in the attempts of ECO_2R to find

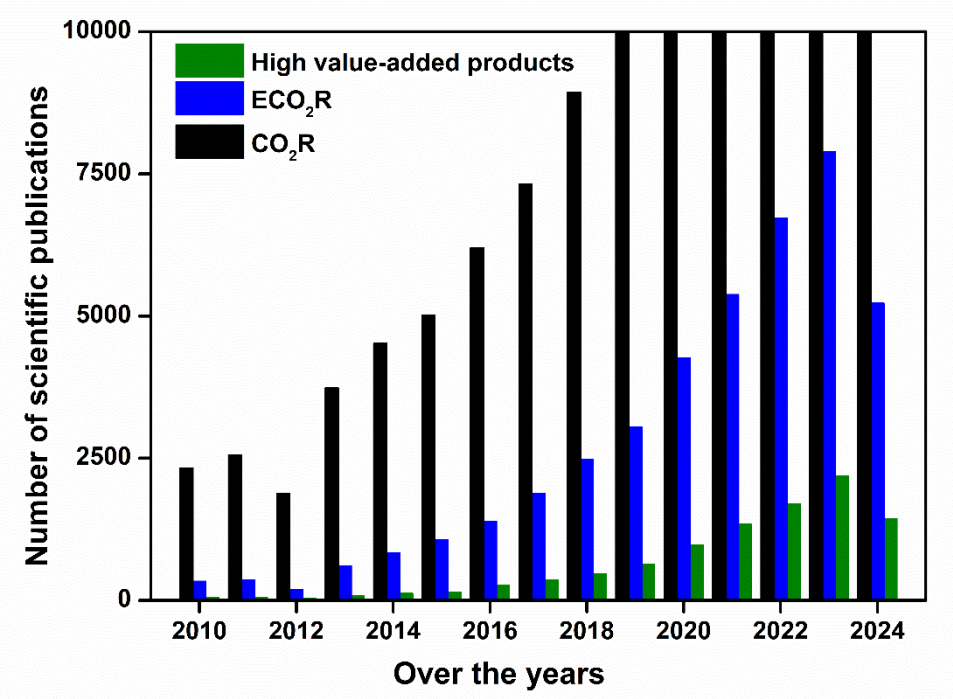


Figure 1.1.6 Number of scientific publications in various CO_2 utilization technologies from 2010 to the present. The Web of Science search was conducted on 21st June 2024.

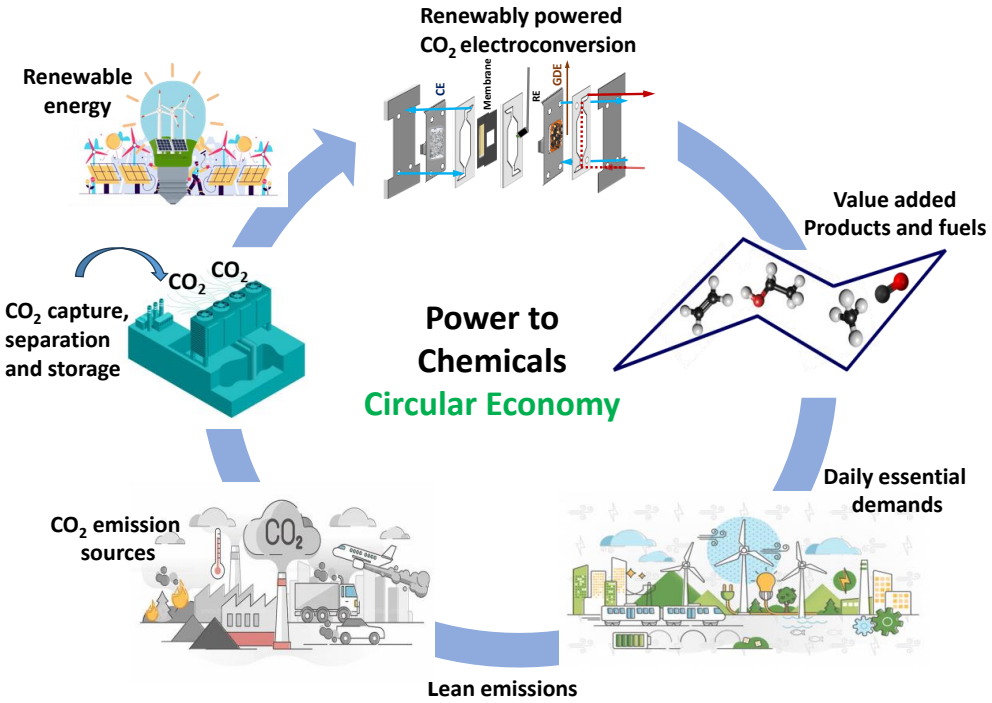


Figure 1.1.7 Schematic representation of simplified Power to Chemicals concept enabling the circular economy.

novel routes to generate high-value-added products like ethylene (C_2H_4) and ethanol as seen in Figure 1.1.6 which can potentially transform the plastic production industries by replacing the primarily used feedstock, crude oil with the atmospheric captured CO_2. which can potentially transform the plastic production industries by replacing the primarily used feedstock, crude oil with the atmospheric captured CO_2. The direct ECO_2R might possess numerous advantages [28-29] when compared to other counterparts like hydrogenation of CO_2.

- Operates at room temperature and pressure (ambient conditions).
- Direct generation of hydrocarbons like C_2H_4 which may not be easy to generate via thermal or plasma-assisted processes.
- Combines the competent water splitting and further hydrogenation in a single step.
- Direct use of the overly-produced renewable energy from intermittent sources.

When executed effectively by coupling with renewable energy sources and integrating CO_2 capture technologies, ECO_2R has the potential to significantly lower CO_2 emissions and eventually aid in decarbonization. As depicted in Figure 1.1.7, it is a high requisite to execute a carbon cycle at an industrial level where the atmospheric CO_2 from the sources is captured [30-32] and eventually converted into much-needed high-value-added products [32] when coupled with the existing renewable energy (electricity).

It is to be noted that, this thesis focuses on the advanced catalyst materials and systems for the electroconversion of CO_2 to C_2H_4, the concept of CO_2 capture and storage was not discussed here, and the direct focus was levied on the ECO_2R. In this regard, to understand the concept and practical approaches of ECO_2R and further, the techno-economic importance in targeting the selectivity towards C_2H_4 was discussed to give the reader thoughtful insights into the processes.

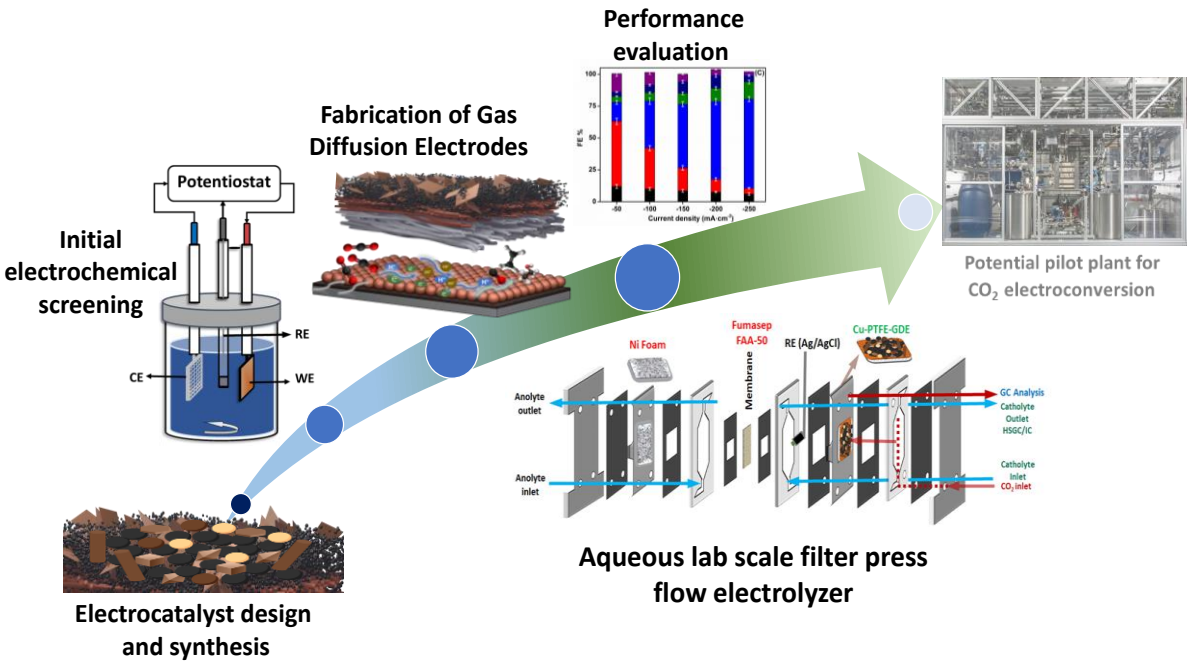
1.1.3. References

1. Press release by World Meteorological Organization, 05th June **2024**.
2. A. Bradford, S. Pappas, *Live Science*, Effects of global warming, **2017**. www.livescience.com/ 37057-global-warming-effects
3. B. Gates, **2021**. How to Avoid a Climate Disaster: The Solutions We Have and the Breakthroughs We Need.
4. IPCC - Intergovernmental Panel on Climate Change: Climate change 2014: *Synthesis report*; **2015**.
5. J. Rogelj, M. den Elzen, N. Höhne, *Nature*. **2016**, 534, 631–639.
6. Intergovernmental Panel on Climate Change (IPCC) **2023**, 287–422. 'Changing State of the Climate System', in Climate Change 2021.
7. International Energy Agency (IEA), World Energy Data from the source, World Energy Statistics and Balances, **2021**. https://www.iea.org/dataandstatistics/datatools/energystatisticsdatabrowser?country=WORLD&fuel=Energy%20supply&indicator=TESbySource
8. R. S. Dimitrov. "*The Paris Agreement on climate change: Behind closed doors*" **2016**, 1-11.
9. Climate, N. Atmospheric carbon dioxide amounts and annual emissions, **2023**. https://www.climate.gov/media/14596.
10. C. David Keeling, *Scripps Institution of Oceanography (SIO)*, scrippsco2.ucsd.edu
11. G. J. M. Velders, S. O. Andersen, J. S. Daniel, D. W. Fahey, M. McFarland, *PNAS*, **2007**, 104, 4814-4819.
12. Intergovernmental Panel on Climate Change (IPCC) **2023**, 923-1054. '*Changing State of the Climate System*', in Climate Change 2021.
13. S. Bouckaert, A. F. Pales, C. McGlade, U. Remme, B. Wanner, L. Varro, D. D'Ambrosio, T. Spencer. "*Net zero by 2050: A roadmap for the global energy sector*". 2021
14. A. David, E. Michael, B. Victor, R. Andy, C. Long, M. Uwe, C. Ken, M. Katsumi, M. Guy, M. Alvaro, T. Kathy. *Annual Review of Earth and Planetary Sciences*, **2009**, 37, 117-134.
15. Friedlingstein, Pierre et al. "*Global Carbon Budget 2023*." **2023,** ESSD, 15, 5301–5369.
16. *International Energy Agency*, Technology Roadmap: Carbon capture and storage in industrial applications, Encycl. Prod. Manuf. Manag, **2011**, 781–782.

17. C. F. Heuberger, and I. Staffell, N. Shah, N. M. Dowell, *Energy Environ*. Sci, **2016,** 9, 2497-2510.
18. A.D.N. Kamkeng, M. Wang, J. Hu, W. Du, F. Qian., *Chemical Eng. Journal*, **2021,** 409, 1385-8947.
19. J. D. J. Paul, , M. D. Lambreva, N. Plumeré, B. Cecilia, A. Antonacci, K. Buonasera, R. N. Frese, V. Scognamiglio, , G. Rea, *Frontiers in Chemistry,* **2014,** 2296-2646.
20. P. J. le B. Williams, L. M. L. Laurens, *Energy Environ. Sci.,* **2010**, 3, 554-590
21. B. Abdullah, N. A. Abd Ghani, D-V. N. Vo, *Journal of Cleaner Production*, **2017**, 162, 170-185.
22. M. B. Peiró, R. Mey, J. Guilera, T. Andreu, *Chemical Eng. Journal,* **2020,** 393, 1385-8947.
23. L. Wang, Y. Yi, H. Guo, and X. Tu, *ACS Catalysis*, **2018**, 8, 90-100.
24. S. Fang, M. Rahaman, J. Bharti, E. Reisner, M. Robert, G. A. Ozin, Y. H. Hu, *Nat Rev Methods Primers,* **2023** 3, 61.
25. P. Chen, Y. Zhang, Y. Zhou, F. Dong, *Nano Materials Science* **2021,** 3, 344-367.
26. X. Zhang, Si-X. Guo, K. A. Gandionco, A. M. Bond, J. Zhang, *Materials Today Advances*, **2020,** 7, 100074.
27. S. Verma, B. Kim, H.-R. Jhong, S. Ma, P. J. A. Kenis, ChemSusChem **2016**, 9, 1972.
28. M. Götz, J. Lefebvre, F. Mörs, A. Mc. D. Koch, F. Graf, S. Bajohr, R. Reimert, T. Kolb, *Renewable Energy*, **2016,** 85, 1371-1390
29. E. V. Kondratenko, G. Mul, J. Baltrusaitis, G. O. Larrazábalc, J. P. Ramírez, *Energy Environ. Sci*., **2013**,6, 3112-3135.
30. R. Sharifian, R. M. Wagterveld, I. A. Digdaya,C. Xiang, D.A. Vermaas, *Energy Environ. Sci.*, **2021**, 14, 781-814.
31. Christopher W. Jones, *JACS Au* **2023,** *3* (6), 1536-1538.
32. I. A. Digdaya, I. Sullivan, M. Lin, L. Han, W-H. Cheng, H. A. Atwater, C. Xiang. *Nat Commun,* **2020** 11, 4412.

Chapter 1.2

Concept and practical aspects of Electrochemical CO_2 Reduction to C_2H_4



This thesis further delves into the introduction of the concept and practical aspects of Electrochemical CO_2 Reduction followed by emphasizing the selectivity towards Ethylene (C_2H_4) from electrocatalysts to potential industrial scale operations. The latter part also introduces the advancements as the state-of-the-art attained by the scientific community in the present work during the past decade.

1.2 Concept and practical aspects of Electrochemical CO_2 Reduction

The present thesis is focused on electrochemical CO_2 reduction (ECO_2R) to value-added products and further emphasizes the selectivity towards C_2H_4. In principle, ECO_2R has the potential to utilize the captured CO_2 effectively and transform it into value-added products like hydrocarbons and oxygenates thereby lowering carbon emissions and steering the industry away from the dependence on fossil fuels. As of today, direct air capture for CO_2 is not economically viable operating at an industrial scale but there has been significant progress in recent days thus making it a near reality [1].

In the present section of the thesis, the overall background, concept and practical aspects of ECO_2R are discussed in detail to enable the reader a thorough understanding.

Electrochemical CO_2 Reduction (ECO_2R): An overview

Before diving into the ECO_2R, it is vital to have a background of carbon dioxide (CO_2). CO_2 is a chemical compound made of carbon (C) and oxygen (O) in a linear arrangement and exists as a colourless and odourless gas molecule at standard temperature and pressure conditions. Though in nature, it is atmospherically available accounting for less than 1 %, as stated in the previous section of this thesis, CO_2 turned out to be the major end product of the many processes involving the predominant use of carbonaceous materials [2]. It is both a kinetically and thermodynamically very stable molecule with strong doubly bonded O on either side. The standard heat of formation of CO_2 is around -393 $KJ{\cdot}mol^{-1}$, thus explaining the excellent stability [3]. Owing to its significant stability, a high amount of energy is usually required to transform CO_2 into value-added products.

Inherently, at the lab scale, ECO_2R is performed in an electrolytic compartment, often referred to as an electrocatalytic cell fundamentally comprised of two half-cell reactions at the positively and negatively charged electrodes immersed in the chosen electrolyte. With respect to ECO_2R, the positively charged electrode is often referred to as the anode or the counter electrode where usually the Oxygen Evolution Reaction (OER) occurs, and the negatively charged electrode is a cathode or working electrode where the reduction of CO_2 takes place along with the competitive Hydrogen Evolution Reactions (HER) [4-8]. The material used to fabricate the electrodes is referred to as an electrocatalyst and based on the characteristics of

the catalyst deployed, specific reactions take place at the respective electrodes and subsequently targeted products shall be generated over the surface of the electrocatalyst. The general representation of the cathodic half-reaction (the focus of the present thesis) during ECO_2R shall be written as

$$x\ CO_2 + n\ H^+ + n\ e^- \rightarrow product + n\ H_2O \qquad 1.2.1$$

The choice of electrocatalysts, electrolytes and operating procedures define the rate of reactions and the altered reaction kinetics modulate the product selectivity. The entire studies performed in this thesis are under aqueous conditions and the product generation technically relies on the proton-coupled electron transfer (PCET) mechanism. Based on the choice of the electrocatalyst, electrolyte and other operating parameters, several products of gaseous and liquid nature shall be generated like the notable single-carbon products, carbon monoxide (CO), formic acid (HCOOH), methane (CH_4), methanol (CH_3OH), and multicarbon products like ethylene (C_2H_4), ethanol (C_2H_5OH) and propanol (C_3H_7OH). While single carbon products like CO and formate only require 2 e^- for the direct electroreduction of CO_2, often the multicarbon products involves multiple proton-electron transfer reactions with possible longer reaction steps [9-10]. With this short description of the fundamental concept involved in ECO_2R, the present section further focuses on the overall aspects like product distribution and selectivity, electrocatalysts, fabrication of gas diffusion electrodes, the role of electrolyte and finally concludes with the aqueous flow-electrolyzer advancements in the recent past.

1.2.1 Product distribution

Based on the number of proton-electron transfer reactions during the ECO_2R, different types of carbon products can be generated using CO_2 as the feed material with varying selectivity [4]. Products like carbon monoxide (CO) and formic acid (HCOOH) are based on two-electron transfer reactions and six or more electrons are required for the high-value-added multi-carbon products like methane (CH_4), methanol (CH_3OH), ethylene (C_2H_4), ethanol (C_2H_5OH) and propanol (C_3H_7OH). Apart from these carbon-based products, the unwanted HER also competes for the electron transfer reactions. Based on the early works of Hori. Y [11] and other researchers [12, 13], the list of half-cell reactions to the majorly reported products at the cathode during ECO_2R are listed in Table 1.2.1. The standard potentials for each electrochemical reaction are also included.

Table 1.2.1 Electrochemical Reactions during ECO_2R and ECOR along with the respective equilibrium potentials (E°).

Electrochemical reaction	E° (V) vs RHE	Product/Name
$x\ CO_2 + n\ H^+ + n\ e^- \rightarrow product + y\ H_2O$	---	*ECO_2R*
$2\ H^+ + 2\ e^- \rightarrow H_2$	0	HER
$2\ H_2O \rightarrow O_2 + 4\ H^+ + 4\ e^-$	+1.23	OER
$CO_2 + 2\ H^+ + 2\ e^- \rightarrow CO_{(g)} + H_2O$	-0.10	Carbon monoxide
$CO_2 + 2\ H^+ + 2\ e^- \rightarrow HCOOH_{(aq)}$	-0.12	Formic acid
$CO_2 + 6\ H^+ + 6\ e^- \rightarrow CH_3OH_{(aq)} + H_2O$	0.03	Methanol
$CO_2 + 8\ H^+ + 8\ e^- \rightarrow CH_{4\ (g)} + 2\ H_2O$	0.17	Methane
$2CO_2 + 8\ H^+ + 8\ e^- \rightarrow CH_3COOH_{(aq)} + 2\ H_2O$	0.11	Acetic acid
$2CO_2 + 12\ H^+ + 12\ e^- \rightarrow C_2H_{4\ (g)} + 4\ H_2O$	0.08	Ethylene
$2CO_2 + 12\ H^+ + 12\ e^- \rightarrow C_2H_5OH_{(aq)} + 3\ H_2O$	0.09	Ethanol/EtOH
$2CO_2 + 14\ H^+ + 14\ e^- \rightarrow C_2H_{6\ (g)} + 4\ H_2O$	0.14	Ethane
$3CO_2 + 18\ H^+ + 18\ e^- \rightarrow C_3H_7OH_{(aq)} + 5\ H_2O$	0.10	Propanol/PrOH
$x\ CO + n\ H^+ + n\ e^- \rightarrow product + y\ H_2O$	---	*ECOR*
$2\ CO + 8\ H^+ + 8\ e^- \rightarrow C_2H_{4\ (g)} + 2\ H_2O$	0.17	Ethylene
$2\ CO + 8\ H^+ + 8\ e^- \rightarrow C_2H_5OH_{(aq)} + H_2O$	0.19	Ethanol/EtOH
$3\ CO + 12\ H^+ + 12\ e^- \rightarrow C_3H_7OH_{(aq)} + 3\ H_2O$	0.21	Propanol/PrOH

The respective equations were adapted from the previously published reports on the ECO_2R of Hori. Y and other researchers [11-13].

A note to the reader: Apart from the products listed above, other products like acetaldehyde, oxalic acid and propionaldehyde can also be generated with ECO_2R but are omitted as they do not fall into the direction of this thesis.

As already stated above, during ECO_2R the generation of value-added products like C_2H_4 and C_2H_5OH involving a higher number of proton-electron transfers, slightly positive equilibrium potentials (E°) are required than products like CO and HCOOH.

1.2.2 Major selectivity: Elemental classification from the periodic table

From Table 1.2.1, it is evident that several products shall be generated from the direct ECO_2R, and the selectivity is technically dependent on the designing of the catalysts and catalyst systems which are based on the elements of the periodic table. In theory, from the early reports of Hori. Y [11], ECO_2R selectivity has relied on the metal surfaces and largely classified as groups of materials that selectively catalyze and reduce CO_2 to various products as listed above. Three major groups can be classified along with the competing HER, along with a pictorial representation as depicted in Figure 1.2.1 as follows.

- Reduction of CO_2 to CO was largely studied on metal catalysts based on Ag [14], Au [15]. Many recent alternative catalyst systems based on metal-nitrogen-carbon (M-N-C) were proposed to enhance the selectivity of CO along with the idea of promoting the use of non-noble metal-based catalyst systems [16, 17].
- Reduction of CO_2 to HCOOH has been extensively studied on metal surfaces like Sn [18, 19], Bi [20], In [21] and Pb [22].
- Reduction of CO_2 to multicarbon products or value-added products like C_2H_4 and C_2H_5OH is severely constrained to a single metal, Cu, the star metal, with the unique property of optimal binding CO. Furthermore, the selectivity among the value-added products can be tuned by engineering the Cu and Cu-based materials [23- 28].
- Though the competent HER activity takes place with any metal surface, often the well-known metals like Pt and Ti generate H_2.

H_2	HCOOH	CO	"Beyond CO"
Pt, Ti	Sn [18, 19], Bi [20], In [21], Pb [22]	Ag [14], Au [15], M-N-C M= Ni/Fe [16, 17]	Copper [24-29]

Figure 1.2.1 Elemental classification of the periodic table based on the selectivity towards different products generated from ECO_2R.

The metal classification was adapted from the work of Bagger et.al [29] which explained that product selectivity largely depends on the binding energy for the key intermediates of ECO_2R and HER involving *H, *HOCO, *COOH and *CO. Cu as depicted in Figure 1.2.2, uniquely possesses the ability to reduce CO_2 to greater than 2 e^- products, possibly due to the negative adsorption energy for CO* and positive adsorption energy for H*, thus making Cu the star metal from the whole periodic table.

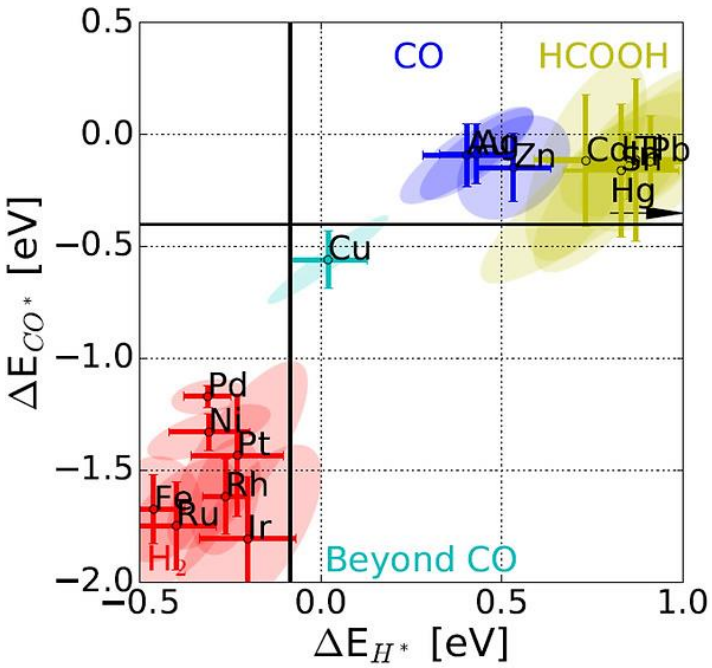


Figure 1.2.2 Metal classification of the periodic table based on the adsorption energy of key intermediate *CO. Reproduced from the work of Bagger et.al [29].

Therefore, it is now well-defined that Cu is the only metal capable of generating value-added products. However, of all the products obtained during ECO_2R, the present thesis focuses on targeting the selectivity majorly towards C_2H_4 along with monitoring the other by-products like CO and C_2H_5OH in addition to the competent HER-generating H_2.

1.2.3 Techno-economic analysis: Reason for targeting the selectivity towards C_2H_4

As mentioned above, C_2H_4 is the target product from ECO_2R in the present thesis; in order to evaluate the final economic and utilization potential of the ECO_2R at the commercial scale, it is vital to evaluate the market size and price of dominant ECO_2R products. Annually, over 150 Mt of C_2H_4 are produced globally. Traditionally, C_2H_4 majorly serves as the precursor in the plastic industries and is commercially produced on a large scale by steam-cracking of naphtha which is obtained from crude oil at very high temperatures in an unselective process [32]. The highly altering global prices of the crude oil can significantly affect the production of C_2H_4 thus affecting the market prices. When compared to the other products, C_2H_4 has the largest global market size estimated at over 230 billion USD ($B) with the largest record of current carbon emissions involving over 862 Mt CO_2e per year as depicted in Figure 1.2.3 B. In the USA and Canada, C_2H_4 is primarily produced from ethane cracking, making it available at a lower price when compared with Asia and Europe where C_2H_4 is primarily dependent on crude oil thus making it a highly expensive precursor.

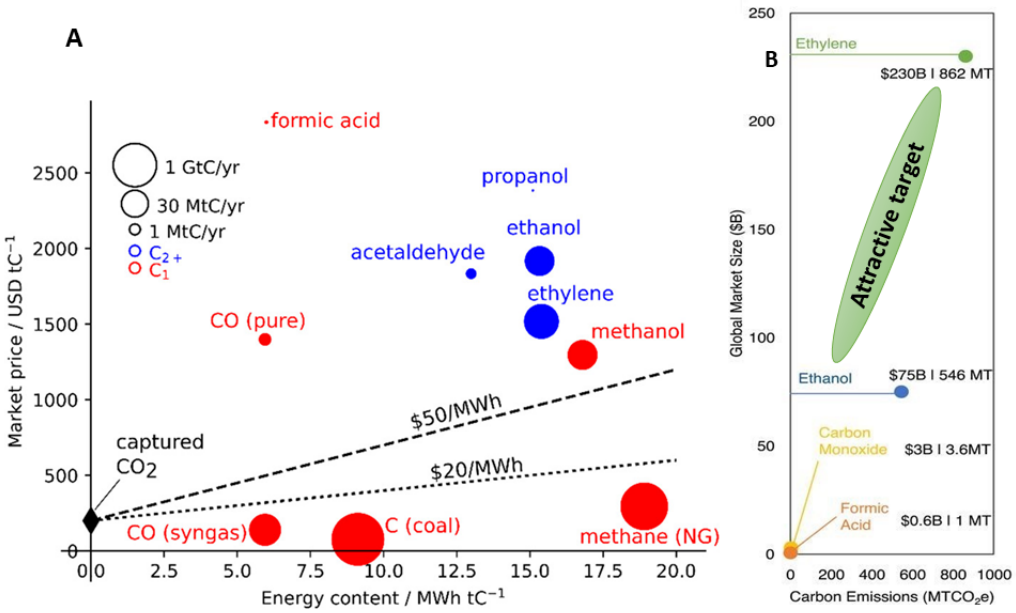


Figure 1.2.3 The market price of majorly produced ECO_2R products with respect to the energy content. Lines indicate the minimum energy input and CO_2 costs **(A)**. Global market size and the estimated carbon emissions of C_2H_4, C_2H_5OH, CO and HCOOH **(B)**. Reproduced from S. Nitopi et. al.[30] and Phil De Luna et al.[31].

The estimated global market size and the gap between the other products indicate that renewably coupled ECO_2R targeting the selectivity towards C_2H_4 shall significantly contribute to lowering the impact of global warming worldwide. Previous reports from S. Nitopi et. al. and Phil De Luna et al., revealed that products like CH_3OH, C_2H_4 and C_2H_5OH have a higher market size than other products obtained [30, 31]. As depicted in Figure 1.2.3 A, products like C_2H_4 and C_2H_5OH which are over and above the line marking the costs for capturing the CO_2 and the electricity cost involved represent the economic feasibility and the products below the line are economically unprofitable with the given capital costs. Additionally, C_2H_4 and C_2H_5OH balance the profitable market share and impactful market size with ECO_2R. The production of C_2H_4 and polyethylene from the renewably powered ECO_2R can be highly sustainable when the post-consumed plastic is recycled after combustion, as the generated heat energy is further coupled with the ECO_2R to further reduce emissions of combustion thereby closing the carbon cycle [33]. Therefore, it can be concluded that electrocatalysis has the great potential to mitigate the traditional dependence on the fossil fuel industry for a sustainable production of C_2H_4 thereby establishing an alternative circular economy towards closing the carbon cycle. It is also important to understand and leverage the expenses incurred with the products obtained from ECO_2R considering the capital and operational costs influencing the levelized cost of each product obtained. In this case, the capital costs are of the hardware and equipment involved in the ECO_2R electrolyzer and the product separation, feedstock availability and renewable power or electricity correspond to the operational costs. However, it is to be noted that the present thesis does not focus on the techno-economic analysis and the reader can obtain further information from the cited literature.

1.2.4 Performance considerations to evaluate the ECO_2R

Before delving into explaining the recent progress of ECO_2R with the mechanistic pathways involved, it is key to consider the figures of merit to evaluate and compare the performance of ECO_2R over different catalysts. There are several parameters like onset potential, current density (j), overpotential (η), Faradaic efficiency (*FE %*), Energy efficiency (*EE %*) and stability which contribute to evaluating the performance of the total electrolysis.

The role and importance of the above-mentioned parameters are discussed in detail in subsequent chapters and sections of this thesis.

1.2.4.1. Onset potential

Under the applied reduction parameters of ECO_2R, the minimum potential applied to the electrolyzer for the generation of the desired product in a measurable quantity with relevance to a reference electrode shall be referred to as onset potential.

1.2.4.2. Overpotential (η)

The difference between the actual applied potential and the theoretical thermodynamic equilibrium potential (onset potential) required for the generation of the desired product during the ECO_2R is referred to as the overpotential *(η)*. A perfect electrocatalyst is deemed to have a significantly minimal overpotential in order to drive an excellent ECO_2R. Cu and Cu-based catalysts often suffer from high overpotentials based on the conditions adopted.

1.2.4.3. Current density (*j*)

In the practical aspect of ECO_2R, current density (*j*) shall be defined as the ratio of the total current applied to the geometric area of the working electrode. It can be represented as

$$j = i/A \qquad 1.2.2$$

where *j* is the current density per unit area of the electrode; *i* is the total current applied, and *A* is the area of the working electrode. Current density (*j*) is an important parameter attributing to the performance and economic viability of the electrolyzer setup

1.2.4.4 Faradaic efficiency (*FE %*)

Faradaic efficiency (*FE %*) is the key performance indicator describing the selectivity of a desired product generated from ECO_2R. It is the proportion of the total electrons consumed in generating a certain amount (moles) of ECO_2R product and is expressed as a percentage. A high *FE %* towards the desired product/s usually signifies the overall efficiency of the ECO_2R process.

1.2.4.5 Energy efficiency (*EE %*)

Energy efficiency (*EE %*) is the amount of energy stored in the desired product to the applied energy input to the electrolyzer and is calculated using the FE of the product and the potentials involved considering the overpotential involved. *EE %* of the overall system can be

enhanced by working towards generating a high *FE %* of the desired product at a relatively lowered cell potential.

1.2.4.6 Overall stability

The deployed electrolyzer should meet the above key performance indicators of *j, FE %*, *EE %* and uphold over a prolonged period of time. The overall long-term stability of the ECO_2R electrolyzer significantly contributes to the overall efficiency of the electrolyzer thus making it reach the potential industrial scale.

1.2.5 Reaction mechanism of ECO_2R

ECO_2R holds a complex mechanistic pathway involving multiple electron transfer reactions coupled with protons leading to a variety of possible products [4]. A complete list of possible products of ECO_2R is already available in Table 1.2.1. The ECO_2R process starts with initial CO_2 adsorption over the catalyst's active sites followed by sequential transfer of electrons (e^-) and protons (H^+) simultaneously leading to several intermediates and final products. Figure 1.2.2 demonstrates the overall mechanism of the ECO_2R showing the key intermediate *CO [35], which is also the precursor in a tandem approach or the direct ECOR. As depicted in Figure 1.2.4, the feed CO_2 molecule adsorbed on the active sites and activated as $*CO_2^-$ and further to *COOH through a PCET. Both $*CO_2^-$ and *COOH serve as the key intermediates for generating *CO [36]. The reduction of *CO might further proceed with the multiple PCET *CO [36] or alternatively by the dimerization of *CO [13, 37]. The selectivity towards CO and HCOOH can be attributed to the initial binding mode of the intermediates during the initial electron transfer mechanism [37]. Nevertheless, the strong interaction between *CO intermediated and the electrocatalyst shall poison the active sites which might result in an exclusive competent HER activity which is unusual on the surface of Cu. It is believed that C–C coupling strongly involves the affinity of the electrocatalyst towards the *CO. The weak interaction favour the *CO desorption and therefore promotes the generation of CO and HCOOH as stated by the previously reported theoretical and experimental studies.

CO is considered to be the key intermediate for the generation of value-added products like C_2H_4 and C_2H_5OH indicating a similar pathway from the direct ECOR. Both ECO_2R and ECOR demands a similar potential dependency thus indicating that the rate determining step (RDS)

does occur after the CO generation [38, 39]. By omitting the activation energy barriers, CO accepts an H^+ to further form *CHO which is another RDS eventually leading to further dimerize of *CHO to generate C_2H_4 by deoxygenation [40- 42]. However, experimental results indicate that C–C coupling is promoted very early in the reaction pathway which can be significantly influenced by the low overpotentials for C_2H_4 under alkaline conditions. With respect to Cu as the electrocatalyst, on the surface of Cu (100), *CO dimerization is favoured at a lower overpotential and a higher overpotential, the protonation of *CO to *CHO takes place prior to *CO coupling to form a *COCHO intermediate [43]. On the surface of Cu (111), the selectivity of usually C_2H_4 is favoured at a higher overpotential. However, on polycrystalline surfaces, C_2H_4 selectivity is more favoured over C_2H_5OH [44]. Eventually, a higher rate of C_2H_5OH selectivity is noticed on possible oxide-derived species and often with bimetallic electrocatalysts [27, 45- 46].

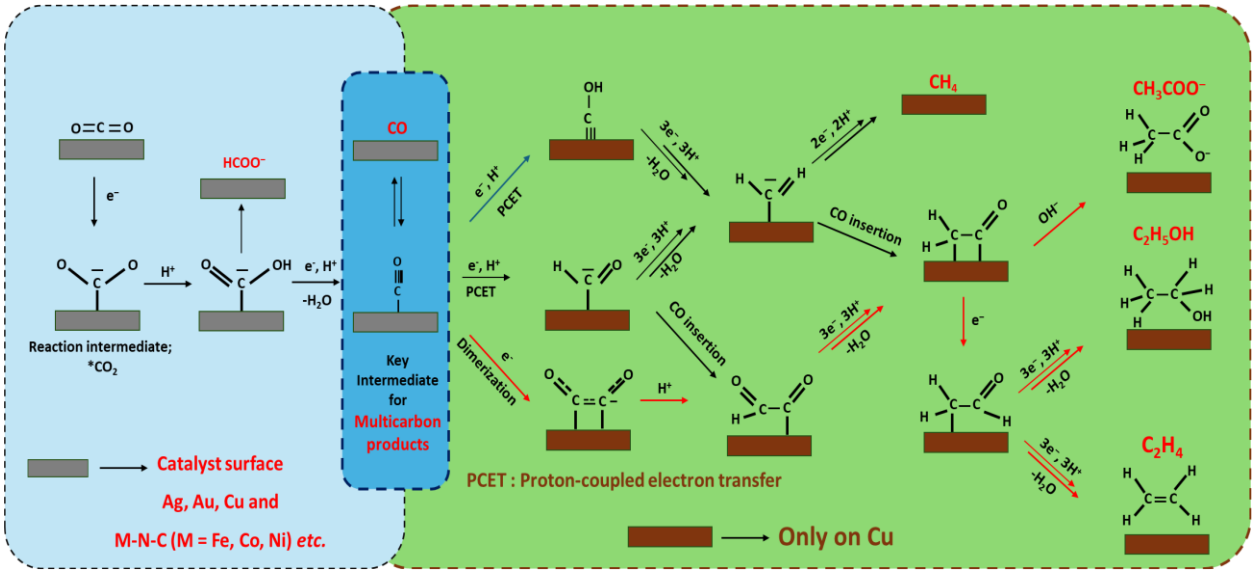


Figure 1.2.4 Plausible proposed mechanistic pathway of ECO_2R leading to various products. The blue section depicts the pathway for the generation of 2 e^- products like CO and HCOOH while the green represents the generation of value-added products. The intense blue in the centre represents the CO as the precursor for ECOR. The unified mechanism shall be identical to the tandem mechanistic pathway for the generation of value-added products. Mechanism adapted and slightly modified from Cao et.al. [34].

With this brief overview of the plausible ECO_2R (and ECOR) mechanism, the thesis further delves into describing the design and synthesis of electrocatalysts and electrolyzer setups.

1.2.6 Electrocatalyst for tuning the selectivity of ECO_2R to C_2H_4

During an electrochemical reaction, the driving force for the redox reaction is the potential-driven electron transfer from one source to another under thermodynamically equilibrium conditions. In order to meet this, the overall reaction requires a reducing agent to donate electrons at the cathode, performing a reduction reaction and an oxidizing agent which accepts the electrons with an oxidation reaction at the anode. As this thesis focuses on the reduction of CO_2, the section further discusses the electrocatalysts operating at the cathode. In this regard, the scientific community is on a quest to find the best-performing electrocatalyst towards ECO_2R. Therefore, the definition of the best catalyst can be attributed to three main parameters that play a crucial role in determining the overall performance.

Activity of the electrocatalyst describes the intrinsic relationship between the applied potential and the quantified current. Under constant potential conditions, the best catalyst shall be able to achieve high current densities with minimal overpotentials. Likewise, under constant current conditions, significantly a lower potential demonstrates the overall activity and efficiency of the chosen electrocatalyst.

Selectivity of the electrocatalyst effectively governs the effective transfer of electrons to generate the desired product and often selectivity of the chosen electrocatalyst can be assessed by quantifying the FE % of the targeted product.

Stability is the last yet important factor along with activity and selectivity which is crucial to determining the overall robustness of the chosen electrocatalyst. An ideal electrocatalyst shall be capable of withstanding elevated hours of operation under prescribed working conditions without severely affecting the activity and selectivity.

As discussed previously about the metal classification from the periodic table in 1.2.2, the ability of Cu to electrochemically reduce CO_2 to value-added products is of great interest to the scientific community and the field has seen significant contributions in the recent past. In order to improve the performance efficiency of Cu and Cu-based electrocatalysts, several strategies have been investigated and implemented including the primarily used Cu foil followed by various morphological and compositional alterations to the catalysts systems. A detailed progress depicting the state of the art shall be discussed in the subsequent sections.

1.2.7 System design and configuration for ECO_2R

H-cell reactor

Several studies have addressed the means to enhance the electrocatalyst development and optimization initially by testing them in a conventional three-electrode cell with anodic and cathodic compartments separated by an ion-exchange membrane. Both catholyte and anolyte are separated by a membrane in order to avoid the direct mixing of the electrolytes and the configuration represents a H-cell reactor. In a typical H-cell reactor, the feed CO_2 is subjected to dissolve in the liquid electrolyte, catholyte. In such an H-cell reactor, the cathode is majorly comprised of a regular glassy carbon electrode or a carbon paper thus favouring a simplified catalyst design and rapid screening of the optimized electrocatalysts. A typical configuration of the H-cell reactor is depicted in Figure 1.2.5.

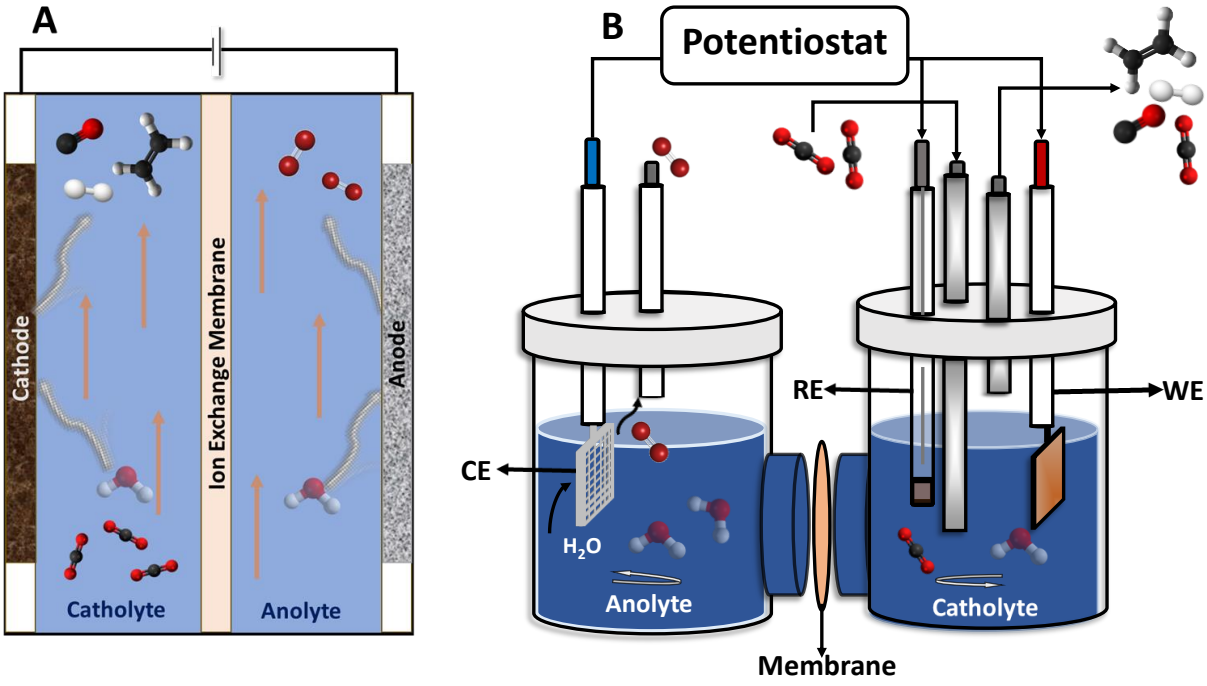


Figure 1.2.5 Conventional H-cell reactor. Scheme of a H-cell with dissolved CO_2 in the catholyte **(A)**, Graphical representation of the H-cell **(B).**

In a typical H-cell, the current density is often limited (usually < 100 $mA \cdot cm^{-2}$) due to the minimal availability of dissolved CO_2 in the catholyte. At the standard room temperature and pressure, the dissolved CO_2 is only about $34*10^{-3}$ M [47]. However, this thesis focused on the flow cell architecture to perform the ECO_2R experiments in order to operate at elevated

current densities and increased area of electrodes leading to higher productivities of the targeted products.

Aqueous flow electrolyzer

The scientific community adapted the concept of water electrolyzer architecture to fabricate a CO_2 flow electrolyzer which is relatively suitable for practical applications. A general flow cell architecture is the aqueous flow electrolyzer. Unlike the H-cell, both gas (CO_2) and (liquid) electrolytes are continuously circulated through the electrolyzer to enhance the CO_2 adsorption and minimize the mass transport limitations during the electrocatalytic reaction [48]. As depicted in Figure 1.2.6, the electrolyzer consists of three compartments, each for gas, catholyte and anolyte. A gas diffusion electrode (GDE) separates the gas and catholyte compartments and an ion exchange membrane separates the catholyte and anolyte to further prevent the direct crossover of reactants and products. The electrocatalyst layer is usually deposited on the catholyte facing front of the GDE thereby establishing contact with the electrolyte while the CO_2 gas is continuously supplied to the electrocatalyst through the backside of the GDE. The detailed demonstration of the architecture of the flow electrolyzer and its components shall further be discussed in section 2.5.1 of Chapter 2.

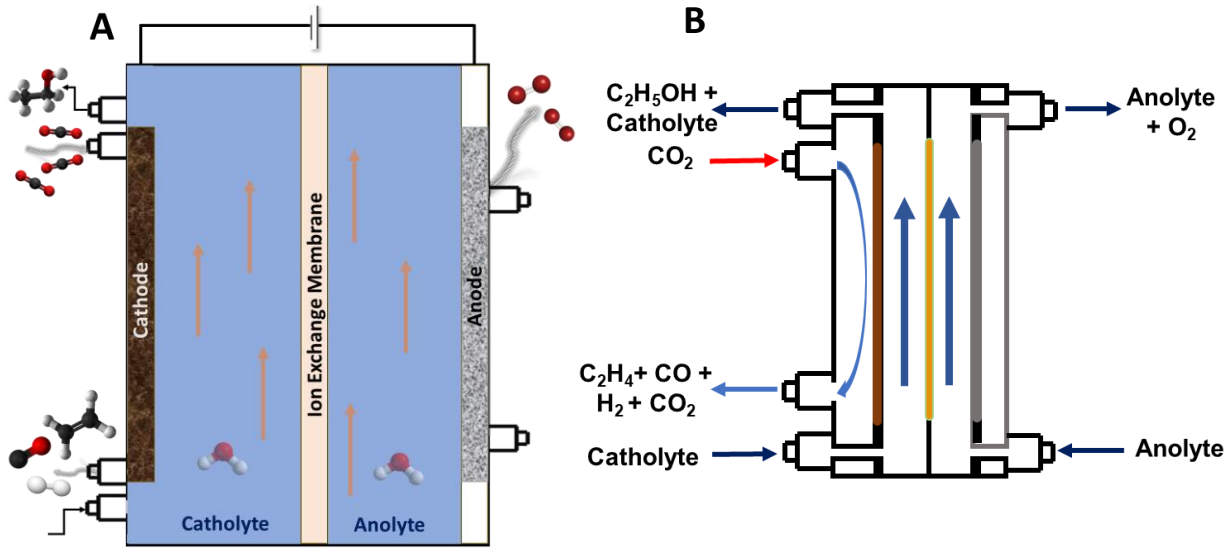


Figure 1.2.6 Conventional aqueous flow electrolyzer. Scheme of a flow electrolyzer **(A)**, Graphical representation of the electrolyzer with a continuous flow of CO_2 and electrolyte **(B).**

1.2.8 Gas diffusion electrodes (GDE)

GDE are the core and serves as an integral part of the flow electrolyzers holding the robust electrocatalyst promoting a higher rate of CO_2 conversion through enhanced mass transport of CO_2 to the catalyst surface. GDE is comprised of a gas diffusion layer (GDL) with the electrocatalyst deposited on one side. GDE shall direct the gas CO_2 from the inlet channel to the electrocatalyst surface by diffusing through the macroporous and microporous layers of the GDL. GDL is deemed to be a hydrophobic, highly porous and conductive structure. In conventional GDEs, which are typically made of carbon structures [49] (carbon paper, felt, cloth, etc.), the macroporous layer is usually thick and holds mechanical stability besides electrical conductivity. The microporous layer which is often made of carbon and hydrophobic polymer as depicted in Figure 1.2.7 A, lies between the macroporous layer and the catalyst layer with additional electrical contact and is often supposed to prevent the flooding of the GDE.

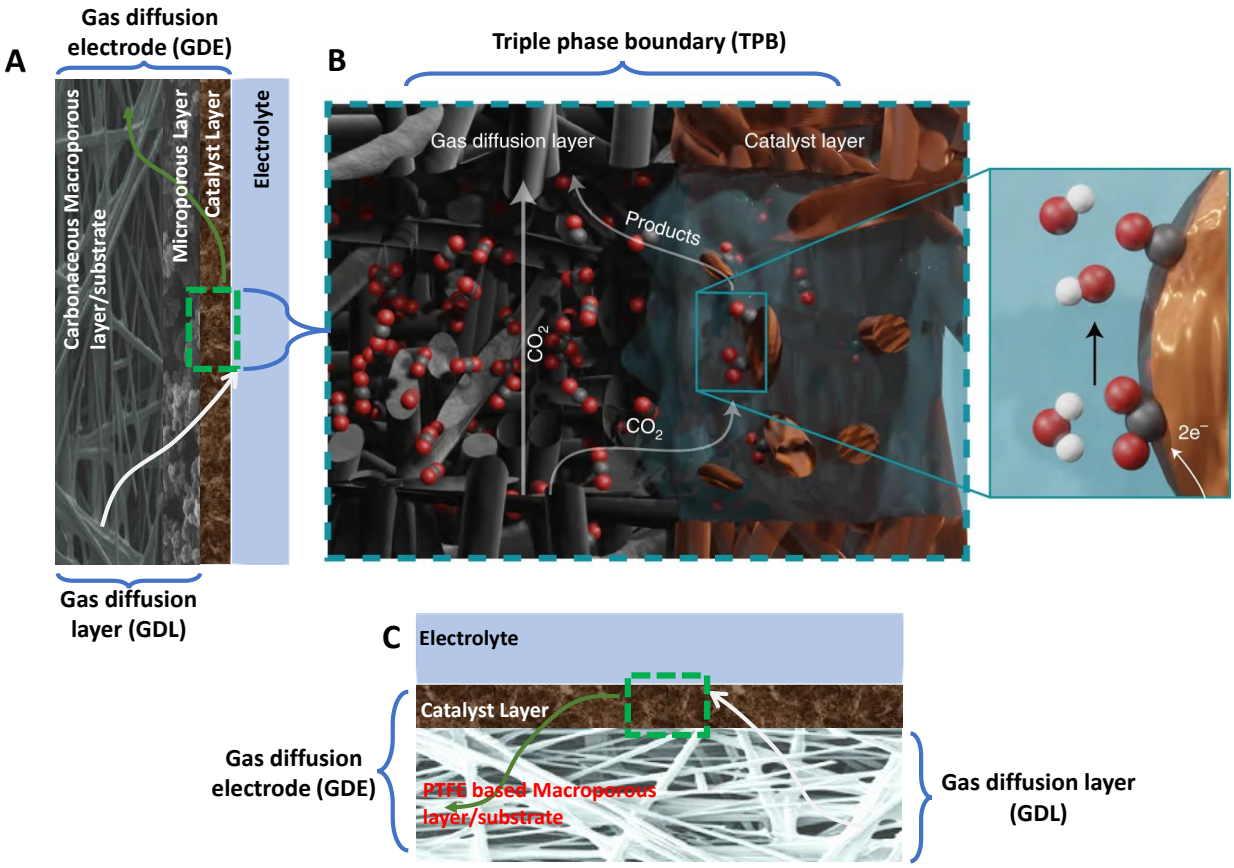


Figure 1.2.7 Structure of a conventional gas diffusion layer (GDL) holding the catalyst layer **(A)**, Schematic representation of a GDE during ECO_2R depicting the electrode-electrolyte interface **(B)** adapted from Wakerley. D. et al [50], PTFE-based gas diffusion electrode (GDE) **(C).**

Triple-phase boundary (TPB)

In a typical GDE, the essential factor for the enhanced mass transport of CO_2 is bound with the diffusion layer of the electrode representing a triple-phase boundary (TPB) replicating the interaction site for gaseous CO_2, liquid electrolyte and solid electrocatalyst surface. The concept of a TPB within the GDE eliminates the necessity to dissolve the CO_2 in the electrolyte as required in an H-cell. Wakerley. D. et al., demonstrated the mechanism of ECO_2R usually happening at the interface of the electrode (catalyst surface) and electrolyte [50] as depicted in Figure 1.2.7 B, the graphical representation of a TPB within the GDE where the incoming reactant gas is transported to the surface of the electrocatalyst which shall be in contact with the liquid electrolyte. Most recent studies demonstrate the successful alternative to the conventional carbon-based GDEs by using polytetrafluoroethylene (PTFE) based macroporous layer substrates as depicted in Figure 1.2.7 C. In such PTFE GDEs, electrical contact is often established by depositing a thin layer of metal on the PTFE substrate [51-53].

1.2.9 Ionomers

The catalyst layer of the GDE is typically made of a mixture of the electrocatalyst and an ionomer acting as the binder. An ionomer (technically a charged polymer) is added to the electrocatalyst to enhance the catalyst utilization by optimizing the ionic interaction by adhering the catalyst layer to the microporous layer surface. Nafion, a perfluorinated resin solution is the most reported cationic ionomer along with other anionic ionomers, Sustanion [54, 55]. Figure 1.2.8 depicts the backbone architecture of Nafion and Sustanion ionomers.

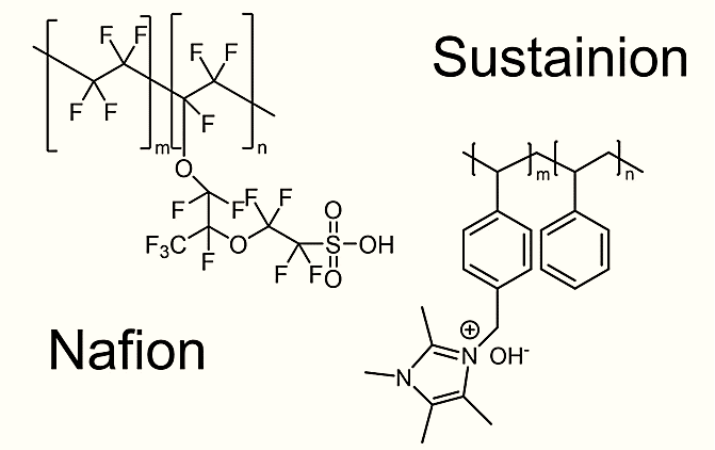


Figure 1.2.8 Structure of Nafion and Sustanion ionomers.

There are several other latest additions to the ionomers like Fumion, Aquivion, Piperion etc. which are very well described in the works of Fan Zeng et. al. [56].

1.2.10 Ion-exchange membranes

As already discussed in the system design for ECO_2R, the catholyte and anolyte are separated by an ion-exchange membrane. With the aid of a membrane, although the direct crossover of reactants and products is prohibited, it is still important to mobilize the ionic species across the compartments. Based on the ion exchange, the membranes are classified as cationic or proton exchange membranes (CEM/ PEM) anionic exchange membranes (AEM) and bipolar membranes (BPM). The membranes typically constitute a carbon backbone, providing mechanical strength along with the characteristic internal structure capable of transporting the intended ions. While CEM and AEMs have uniform functionality, BPM holds the stack of CEM and AEM in direct contact and regulates the dissociation of H_2O to H^+ and OH^- ions.

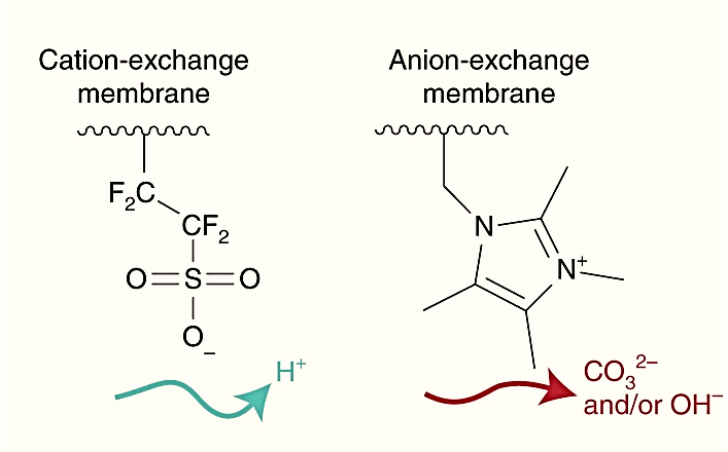


Figure 1.2.8 Structure of a cationic or proton exchange membrane (CEM/ PEM) and anionic exchange membrane (AEM).

1.2.11 Role of electrolyte

The reaction environment is majorly the result of the ionic transport which is majorly governed by the electrolyte and the nature of the electrolyte. Traditionally, the electrolytes used for ECO_2R are primarily aqueous in nature [12] and several reports have seen the implementation of organic electrolytes [57] and ionic liquids [58]. The aqueous electrolytes are composed of salty materials like $KHCO_3$, KOH etc. in water which further reduces the CO_2 solubility in the electrolyte thereby imbibing mass transport limitations [59] which is a non-negotiable problem with respect to H-cell reactors. The introduction of GDE in the aqueous

flow electrolyzers with separated gas and liquid chambers has significantly improved the mass transport of CO_2 at the electrode-electrolyte interface, often referred to as the TPB. Often the salts contain certain kinds of metal ion impurities which can poison the surface of the catalyst layer and further cause the deactivation of the GDE [60]. Therefore, it is often recommended to perform the cleaning of the electrolyte with a pre-electrolysis procedure or by using a chelating resin [61, 62].

However, high-purity analytical grade electrolyte solutions were used in the studies carried out towards this thesis.

One of the important parameters for product selectivity lies with the local pH of the electrolyte [63]. In theory, in aqueous electrolytes made of $KHCO_3$, KOH etc., CO_2 forms buffers from the electrolytes which significantly influences the local pH (highly alkaline with KOH) near the surface of the electrode which can be different to the pH of the bulk electrolyte. It has been revealed that the ECO_2R selectivity follows two different reaction pathways for the generation of value-added products with respect to the pH. In this case, the pH-dependent pathway can promote more CH_4 while C_2H_4 is independent of the local pH [64, 65]. With the rise in pH, i.e., under alkaline conditions, which are accessible only in flow electrolyzers, in the presence of a robust electrocatalyst, the targeted C_2H_4 selectivity is more favourable with reduced overpotentials [66]. In further attempts, studies revealed that cation effects greatly influence the ECO_2R selectivity. Larger cations like Cs^+ and K^+ shall enhance the total current density by lowering the charge transfer resistances while lowering the HER activity and improving the selectivity of C_2H_4 [67-69].

The introduction thus concludes here with the description of operating parameters employed in this thesis and further followed with the state-of-the-art electrocatalysts reported for ECO_2R with selectivity towards C_2H_4.

Although much advanced electrolyzers have been reported by the scientific community, the present thesis focused on aqueous flow electrolyzers and the use of gas-phase electrolyzers is a future outlook. The reader can refer to the previously reported literature to study the advanced electrolyzers [70-73].

Table 1.2.2 Overview of the system design and configuration for ECO_2R.

Reactor configuration	Operating parameters			Significance
	Electrolyte	Membrane	current density	
H-cell reactor	Aqueous electrolytes like $KHCO_3$	CEM, AEM or membrane-less	Typically < 100 $mA{\cdot}cm^{-2}$	Simple setup and rapid testing; Mass transport limitations and lack of scalability.
Flow electrolyzer	Aqueous electrolytes like $KHCO_3$, KOH with varying pH	CEM, AEM or membrane-less	Typically > 100 $mA{\cdot}cm^{-2}$ (ranging from ~ 0.1 – 1 $A{\cdot}cm^{-2}$)	Optimized management of the reaction environment. Able to perform at higher current densities leading to scalability. Often flooding and complicated system setup.

1.2.12 State of art electrocatalysts for ECO_2R to C_2H_4

Copper and copper-based materials have been extensively studied as the primary electrocatalysts for the ECO_2R with selectivity targeting towards C_2H_4. It is imperative that the total system for ECO_2R demands a high overpotential and often suffers from competing HER activity hindering the selectivity towards C_2H_4. In this regard, the scientific community has proposed several novel modifications to Cu and Cu-based materials by altering the catalyst size, composition and morphologies.

Morphology based design and fabrication of electrocatalysts is found to be one of the effective strategies in modulating the active sites. Several recent reports indicated the implementation of Cu electrocatalysts with varying morphologies for enhancing the selectivity of C_2H_4 like nanoparticles [74], nanocubes [25], nanowires [75], nanoneedles [76], nanotubes [77] etc.

Crystallinity of the electrocatalyst plays a critical role in tuning the selectivity towards C_2H_4. Along with the early works of Hori et. al., several recently reported literature demonstrated that the polycrystalline Cu(100) surfaces majorly generates C_2H_4 while the Cu(111) favours the CH_4 generation[78-80].

Oxide-derived electrocatalysts have greatly influenced the selectivity towards C_2H_4. Various oxide-derived electrocatalysts were designed and fabricated demonstrating the role of Cu^0 and Cu^+ as active sites in tuning the selectivity [24, 43, 81-82]. However, the true active site is still under debate, yet these have shown promising potential by lowering the potential required while enhancing the selectivity towards C_2H_4.

Bimetallic electrocatalysts involves the application of multiple metals to enhance the performance of the Cu-active sites due to the hypothesized metal-metal interactions. The additional metal active sites deliver a secondary active site thereby modulating the reaction pathway. Various combinations involving the use of CuAg [83-85], CuAu [86, 87], CuZn [27, 88] , CuPd [89] based electrocatalysts were developed to enhance the selectivity towards C_2H_4. Albeit a significantly enhanced overall C_{2+} products was delivered, these bimetallic electrocatalyst showed a lower selectivity towards a single targeted C_{2+} product**.**

Tandem electrocatalysts closely resembles the bimetallic electrocatalysts with reference to multiple active sites involving different catalytic sites. Unlike the bimetallic, tandem involves the sequential reaction steps in which each active site has a competent activity [90]. Tandem conceptualization breaks the linear scaling relationship and promotes the thermodynamic activity thereby enhancing the activity and selectivity. Tandem approach involves the use of variety of concepts ranging from tandem catalysts [91], tandem electrodes [92] and even tandem devices [93]. The recent studies over tandem s seen a significant progress and it still remains a great area with vast potential and operations.

Apart from the above stated various versions of electrocatalysts, there has been a novel finding to fabricate the gas diffusion electrodes by replacing the conventional carbon based GDLs with the improved PTFE based GDEs. The PTFE GDL is often supported by a conducting metal which can be further modified according to the desired study [51-52].

From the widely available source of reported literature, a brief summary of the recently reported state-of-art research in ECO_2R with selectivity targeting towards C_2H_4 majorly pertained to oxide-derived Cu electrocatalysts, tandem catalysts and modified GDEs is listed hereunder.

Table 1.2.3. Summarization of selected state-of-art research in ECO_2R to C_2H_4.

Electrocatalyst	Parameters					Ref.
	Reactor	Electrolyte	E_w (V) vs RHE	J mA·cm^{-2}	FE % C_2H_4	
Electrodeposited Cu_2O on Cu plate	H-cell	0.1 M $KHCO_3$	-1.0 V	12	33	94
Hydrothermally prepared Cu_2O	H-cell	0.1 M $KHCO_3$	-1.0 V	45	27	95
Oxide-derived Cu foil	H-cell	0.1 M $KHCO_3$	-1.37 V	36.5	28	96
Plasma-activated Cu	H-cell	0.1 M $KHCO_3$	-0.6 V	12	60	81
Plasma-treated Cl-induced Cu_2O–Cu	H-cell	0.1 M $KHCO_3$	-1.0 V	37	45	82
Branched copper oxide particles	H-cell	0.1 M $KHCO_3$	-1.05 V	17	68	97
Anodized Cu	H-cell	0.1 M $KHCO_3$	-1.05 V	21	38.1	98
Porous Cu	Flow cell	1M KOH	-0.67 V	660	38.6	99
Cu_2O/N–carbon shell	H-cell	0.1 M $KHCO_3$	-1.30 V	10	24.7	100
Cl induced CuO_x/C	H-cell	0.5 M $KHCO_3$	-1.12 V	16.65	33.3	101
Hydrothermally prepared CuO_x/C	Flow cell	1M K $KHCO_3$	-1.55 V	200	45	102*
B-doped Cu	H-cell	0.1 M KCl	-1.11 V	70	80	103
CuAg alloy films	Flow cell	1M KOH	-0.7 V	300	60	83
CuAg nanorods	Flow cell	1M KOH (CO_2 sat.)	-1.11 V	213	45	104
HKUST-1 derived Cu	Flow cell	1M KOH	-1.07 V	NA	45	105
Cu/N-doped carbon nanofibers	Flow cell	5M KOH	-0.57 V	373	62	106
CuO/Al_2CuO_4	Flow cell	0.5 M $KHCO_3$	-2.03 V	400	70	107
CuZn alloy	Flow cell	1M KOH	-0.76 V	93	40	108
CuAu	H-cell	0.1 M $KHCO_3$	-1.05 V	39	63.9	109

PTF(Ni)/Cu	H-cell	0.1 M KCl + 0.1 M $KHCO_3$	-1.10 V	15	57.8	[110]
Ni SA/Cu	H-cell	0.5 M $KHCO_3$	-1.4 V	20	50	[111]
$Cu_{1.0}/ZnO_{0.20}$ tandem electrode	Flow cell	1 M KOH	-0.73 V	213	49	[92]
Cu/Ni-N-C tandem electrode	Flow cell	1 M KOH	-0.73 V	415	62	[112]
Cu/Fe-N-C segmented electrode	MEA	0.5 M KOH	3.4 V (E_{cell})	700	65	[113]
Cu+ Ag Tandem device	Flow cell	1 M $KHCO_3$	-1.0 V	300	45	[114]
PTFE(varying thickness)/ Cu	Flow cell	1 M KOH	-0.75V	175	42.5	[53]
PTFE/ Cu and Cu nanoparticles	Flow cell	7 M KOH	-0.54 V	275	66	[54]
PTFE/ Cu/ CIPH and CIBH	MEA	10 M KOH	3.9 V (E_{cell})	1000	52	[55]

1.2.13 Thesis scope and outline

In summary, it is evident from the introduction of this thesis, that the main objective of the thesis is to aim for a carbon-neutral economy. Although several CO_2 utilization techniques are well advanced, the electrochemical route has an advantage as it can be powered by existing renewable energy sources. By coupling the ECO_2R with renewable energy to generate value-added products unprecedentedly seems to be a promising strategy to attain a sustainable economy. Of all the ECO_2R products, C_2H_4 uniquely possess high energy density and also holds the long-range global market size and demand. It is the main precursor to synthesize the plastic-based products. By successful integration of ECO_2R with renewable energy, it is inherent that the world can move away from the anthropogenic fossil fuel industry thereby lowering the levels of atmospheric CO_2 further leading to mitigating global warming.

Therefore, this thesis is focused on developing advanced catalyst materials and systems for the electroconversion of CO_2 to C_2H_4. The main objectives of the present thesis are as follows.

- Design and synthesis of a robust electrocatalyst which is capable of selectively generating C_2H_4 from ECO_2R. Investigation of the electrocatalyst by physicochemical and electrochemical characterization techniques thereby understanding its behaviour under reactive environment.
- Designing the additional active sites to the electrocatalyst by incorporating additional active sites resembling a tandem mechanism followed by systematic screening of the best-fit tandem approach to enhance the selectivity of C_2H_4 from ECO_2R.
- Design and fabrication of advanced gas diffusion electrodes using alternative GDLs like PTFE followed by modulating the electrode surface interface thereby elucidating the stir in selectivity towards C_2H_4.

Pertaining to the thesis objectives stated above, thorough investigations were carried out and the results are disseminated in the organized structure as follows.

- **Chapter 2** is focused on the experimental methodology constituting the synthetic protocols, brief overviews of the physicochemical and electrochemical characterization techniques involved, system design and configuration for ECO_2R and product quantification techniques.
- **Chapter 3** presents the design and synthesis of the hydrothermally fabricated carbon-supported oxide-derived copper heterostructures CuxO-C, a highly robust electrocatalyst for enhancing the electroreduction of CO_2 to C_2H_4.
- **Chapter 4** demonstrates the systematic investigation of the tandem approach where different tandem routes ranging from tandem catalysts, tandem electrodes and tandem devices were explored and concludes by depicting the best-fit approach to enhance the electroreduction of CO_2 to C_2H_4.
- **Chapter 5** delves into the fabrication of PTFE-based gas diffusion electrodes and successfully demonstrates the effective electrode surface interface modulation to stir the selectivity towards C_2H_4.
- **Chapter 6** depicts the conclusions by highlighting the contributions in reaching the aforementioned objectives followed by identifying the future research perspectives.

1.3 References

1. J. Hansen, P. Kharecha, *Joule* **2018,** 2, 1405-1407.
2. World Meteorological Organization, *Greenhouse Gas emissions*, **2019**.
3. R. L. Berg, C. E. Vanderzee, Thermodynamics of carbon dioxide and carbonic acid, *The Journal of Chemical Thermodynamics* **1978***,* 10, 1113-1136.
4. K. P. Kuhl, E. R. Cave, D. N. Abram, T. F. Jaramillo, *Energy Environ. Sci*., **2012**, 5, 7050-7059.
5. M. Goldman, E. Lees, P. Prieto, B. Mowbray, D. Weekes, A. Reyes, T. Li, D. Salvatore, W. Smith, C. Berlinguette, *RSC Energy and Environment Series,* **2021,** 28, 408-432.
6. Y. J. Sa, C. W. Lee, S. Y. Lee, J. Na, U. Lee, Y. J. Hwang, *Chem. Soc. Rev*., **2020**, 49, 6632-6665.
7. M. C. O. Monteiro, F. Dattila, N. López, and M. T. M. Koper*, Journal of the American Chemical Society*, **2022**, 144, 1589-1602.
8. K. D. Yang, C. W. Lee, K. Jin, S. W. Im, and K. T. Nam, *The Journal of Physical Chemistry Letters* **2017,** 8, 538-545.
9. X. Zhang, S-X Guo, K. A. Gandionco, A. M. Bond, J. Zhang, *Materials Today Advs.*, **2020**, 100074.
10. D. T. Whipple, P. J. A. Kenis, J. Phys. Chem. Lett. 2010, 1, 3451.
11. Hori. Y, *Electrochemical CO_2 Reduction on Metal Electrodes*, **2008,** 42, 89-189.
12. M. Gattrell, N. Gupta, A. Co, *J. Electroanal. Chem*. **2006**, 594, 1−19.
13. R. Kortlever, J. Shen, K. J. P. Schouten, F. Calle-Vallejo, and M. T. M. Koper, *The Journal of Physical Chemistry Letters* **2015** *6* (20), 4073-4082.
14. Q. Lu, J. Rosen, F. Jiao, *ChemCatChem* **2015**, 7, 38–47.
15. Y. Chen, C. W. Li, M. W. Kanan, *J. Am. Chem. Soc.* **2012,** 134, 19969–19972.
16. T. Zheng, K. Jiang, N. Ta, Y. Hu, J. Zeng, J. Liu, H. Wang, *Joule* **2019**, 3, 265.
17. T. Zhang, X. Han, H. Liu, M. Biset-Peiró, J. Li, X. Zhang, P. Y. Tang, B. Yang, L. R. Zheng, J. R. Morante, J. Arbiol, *Adv. Funct. Mater*. **2022**, 32, 2111446.
18. W. Leitner, *Angew. Chem.* **1995**, 107, 2391–2405.
19. S. Zhang, P. Kang, T. J. Meyer, *J. Am. Chem. Soc.* **2014**, 136, 1734-1737.
20. G. Jia, Y. Wang, M. Sun, H. Zhang, L. Li, Y. Shi, L. Zhang, X. Cui, T. W. Benedict Lo, B. Huang, J. C. Yu, *J. Am. Chem. Soc.* **2023,** *145* (25), 14133-14142.

21. S. Kapusta and N. Hackerman, *J. Electrochem. Soc.* **1983,** 130 607.
22. H. Wu, J. Song, C. Xie, Y. Hu, B. Han, *Green Chem*. **2018**, 20, 1765-1769.
23. C. Li, J. Ciston, M. Kanan, *Nature,* **2014**, 508, 504–507.
24. D. Kim, S. Lee, J. D. Ocon, B. Jeong, J. K. Lee and J. Lee, *Phys. Chem. Chem. Phys.*, **2015**, 17, 824-830.
25. Y. Kwon, Y. Lum, E. L. Clark, J. W. Ager, A. T. Bell, *ChemElectroChem* **2016**, *3*, 1012.
26. J. Kim, W. Choi, J. W. Park, C. Kim, M. Kim and H. Song*, J. Am. Chem. Soc.* **2019**, 141, 17, 6986–6994.
27. D. Ren, B. S.-H. Ang and B. S. Yeo, *ACS Catal*., **2016**, 6, 8239-8247.
28. S. Ma, M. Sadakiyo, M. Heima, R. Luo, R. T. Haasch, J. I. Gold, M. Yamauchi and P. J. Kenis, *J. Am. Chem. Soc.*, **2017**, 139, 47-50.
29. A. Bagger, W. Ju, A. S. Varela, P. Strasser, J. Rossmeisl, *Catalys. Tod*, **2017**, 288, 74-78.
30. S. Nitopi, E. Bertheussen, S. B. Scott, X. Liu, A. K. Engstfeld, S. Horch, B. Seger, I. E. Stephens, K. Chan, C. Hahn, J. K. Norskov, Chem. Rev. 2019, 119, 7610.
31. P. De Luna, C. Hahn, D. Higgins, S. A. Jaffer, T. F. Jaramillo, E. H. Sargent, Science 2019, 364, eaav3506.
32. L. Kniel, K. Stork, O. Winter, *Ethylene - A Keystone to the Petrochemical Industry*; *M. Dekker, New York,* **1980.**
33. A. Brems, R. Dewil, J. Baeyens, R. Zhang, *Nat. Sci*. **2013,** 05, 695–704.
34. B. Cao, F- Z. Li, and J. Gu, *ACS Catalysis* **2022,** 12 (15), 9735-9752.
35. X. Liu, J. Xiao, H. Peng, X. Hong, K. Chan, J. K. Nørskov, *Nat. Commun*. **2017**, 8 (1), 15438.
36. A. Wuttig, M. Yaguchi, K. Motobayashi, M. Osawa, and Y. Surendranath, *Proc. Natl. Acad. Sci. U. S. A.* **2016**, 113 (32), E4585−E4593.
37. T. Cheng, H. Xiao, W. A. Goddard, *Proc. Natl. Acad. Sci. U. S. A.* **2017**, 114 (8), 1795−1800
38. Y. Hori, A. Murata, R. Takahashi, *J. Chem. Soc., Faraday Trans. 1* **1989**, 85, 2309.
39. Y. Hori, A. Murata, R. Takahashi, S. Suzuki, *J. Am. Chem. Soc.* **1987**, 109, 5022.
40. J. H. Montoya, A. A. Peterson, J. K. Nørskov, *ChemCatChem* **2013**, 5, 737.
41. A. A. Peterson, F. Abild-Pedersen, F. Studt, J. Rossmeisl, J. K. Nørskov, *Energy Environ. Sci.* **2010**, 3, 1311.

42. W. J. Durand, A. A. Peterson, F. Studt, F. Abild-Pedersen, J. K. Nørskov, *Surf. Sci.* 2011, **605**, 1354.
43. A. J. Garza, A. T. Bell, and M. Head-Gordon, *ACS Catalysis* **2018,** 8 (2), 1490-1499.
44. Y. Huang, A. D. Handoko, P. Hirunsit, B. S. Yeo, *ACS Catalysis* **2017** *7* (3), 1749-1756.
45. X. Su, Y. Sun, L. Jin, L. Zhang, Y. Yang, P. Kerns, B. Liu, S. Li, J. He, *Applied Catalysis B: Environmental*, 2020, 269, 118800.
46. S. Lee, G. Park, J. Lee, *ACS Catalysis* **2017** *7* (12), 8594-8604
47. J. J. Carroll, J. D. Slupsky, A. E. Mather, *J. Phys. Chem. Ref. Data* 1991, **20**, 1201.
48. D. Weekes, D.A. Salvatore, A. Reyes, A. Huang, C. Berlinguette, *Acc. chem. research*, **2018**, 51, 4, 910-918.
49. K. Yang, R. Kas, W. A. Smith, and T. Burdyny, *ACS Energy Letters*, **2021**, 6 (1), 33-40.
50. Wakerley, D., Lamaison, S., Wicks, J. et al., *Nat Energy*, **2022**, 7, 130–143.
51. J. W. Blake, J. T. Padding, J. W. Haverkort, Electrochim. Acta 2021, 393, 138987.
52. C. T. Dinh, T. Burdyny, M. G. Kibria, A. Seifitokaldani, C. M. Gabardo, F. P. García de Arquer, A. Kiani, J. P. Edwards, P. De Luna, O. S. Bushuyev, C. Zou, Science 2018, 360, 783.
53. F. Huq, I. Sanjuán, S. Baha, M. Braun, A. Kostka, V. Chanda, J. R. C. Junqueira, N. Sikdar, A. Ludwig, C. Andronescu, ChemElectroChem 2022, 9, e202101279.
54. C. Yu, T. Lei, L. Xu, C. Jin et al., *J. Mater. Chem. A*, **2024**, 12, 17181-17192.
55. F. P. García de Arquer, C. T. Dinh, A. Ozden, J. Wicks, C. McCallum, A. R. Kirmani, D. H. Nam, C. Gabardo, A. Seifitokaldani, X. Wang, Y. C. Li, *Science* **2020**, 367, 661.
56. F. Zeng, H. Deng, M. Zhuansun, W. Tengab, Y. Wang, *J. Mater. Chem. A*, **2024**,12, 20990-20998.
57. L. Sun, G. K. Ramesha, P. V. Kamat, J. F. Brennecke, *Langmuir* **2014**, **30**, 6302.
58. S. Kaneco, K. Iiba, H. Katsumata, T. Suzuki, K. Ohta, *Electrochim. Acta* **2006**, 51, 4880.
59. Z. Duan, R. Sun, C. Zhu, I. M. Chou, *Mar. Chem.* **2006**, 98, 131–139.
60. C. W. Lee, K. D. Yang, D.-H. Nam, J. H. Jang, N. H. Cho, S. W. Im, K. T. Nam, *Adv. Mater*. **2018**, 30, 1704717.
61. A. Wuttig, Y. Surendranath, *ACS Catal.* **2015**, 5, 4479–4484.
62. P. Kedzierzawski, J. Augustynski, *J. Electrochem. Soc*. **1994**, 141 L58.
63. M. T. M. Koper, Chem. Sci. 2013, 4, 2710–2723.

64. A. S. Varela, M. Kroschel, T. Reier, P. Strasser, *Catal. Today* **2016**, 260, 8.

65. F. Calle-Vallejo, M. T. Koper, *Angew. Chem. Int. Ed. Engl*. **2013**, 52, 7282–7285.

66. S. Ma, M. Sadakiyo, R. Luo, M. Heima, M. Yamauchi, P. J. A. Kenis, *J. Power Sources* **2016**, 301, 219.

67. M. R. Thorson, K. I. Siil, P. J. A. Kenis, *J. Electrochem. Soc.* **2013**, 160, F69.

68. J. Resasco, L. D. Chen, E. Clark, C. Tsai, C. Hahn, T. F. Jaramillo, K. Chan, A. T. Bell, *J. Am. Chem. Soc.* **2017**, 139, 11277.

69. S. Kaneco, H. Katsumata, T. Suzuki, K. Ohta, *Energy Fuels* **2006**, 20, 409.

70. M. G. Kibria, J. P. Edwards, C. M. Gabardo, C.-T. Dinh, A. Seifitokaldani, D. Sinton, E. H. Sargent, *Adv. Mater.* **2019**, 31, 1807166.

71. Xing, Z., Hu, L., Ripatti, D.S. et al., *Nat Commun.* **2021**, 12, 136

72. Y. Cheng, P. Hou, X. Wang, P. Kang, *Accounts of Chemical Research* **2022,** 55, 3, 231-240.

73. A. Ozden, F. Li, F. P. Garci?a de Arquer, A. Rosas-Hernández, A. Thevenon, Y. Wang, S.-F. Hung, X. Wang, B. Chen, J. Li, J. Wicks, M. Luo, Z. Wang, T. Agapie, J. C. Peters, E. H. Sargent, D. Sinton, *ACS Energy Lett* **2020**, 5, 2811.

74. W. Tang, A. A. Peterson, A. S. Varela, Z. P. Jovanov, L. Bech, W. J. Durand, S. Dahl, J. K. Norskov, I. Chorkendorff, *Phys. Chem. Chem. Phys*. **2012**, 14, 76–81.

75. M. Ma, K. Djanashvili, W. A. Smith, *Angew. Chem., Int. Ed.* **2016,** 55, 6680.

76. C. Liu, J. Gong, J. Li, J. Yin, W. Li, Z. Gao, Li Xiao, G. Wang, J. Lu, L. Zhuang, *ACS Appl. Mater. Interfaces* **2022**, 14, 20953.

77. R. Wang, X. Wang, W. Weng, Y. Yao, P. Kidkhunthod, C. Wang, Y. Hou, J. Guo, *Angew. Chem., Int. Ed.* **2022**, 61, 202115503.

78. I. Takahashi, O. Koga, N. Hoshi, Y. Hori, *J. Electroanal. Chem*. **2002**, 533, 135−143.

79. Y. Huang, A. D. Handoko, P. Hirunsit, B. S. Yeo*, ACS Catal*. **2017**, 7, 1749−1756.

80. K. J. Schouten, Z. Qin, E. Perez Gallent and M. T. Koper, J. *Am. Chem. Soc*., **2012**, 134, 9864–9867.

81. H. Mistry, A. S. Varela, C. S. Bonifacio, I. Zegkinoglou, I. Sinev, Y. W. Choi, K. Kisslinger, E. A. Stach, J. C. Yang, P. Strasser and B. R. Cuenya, *Nat. Commun*., **2016**, 7, 12123.

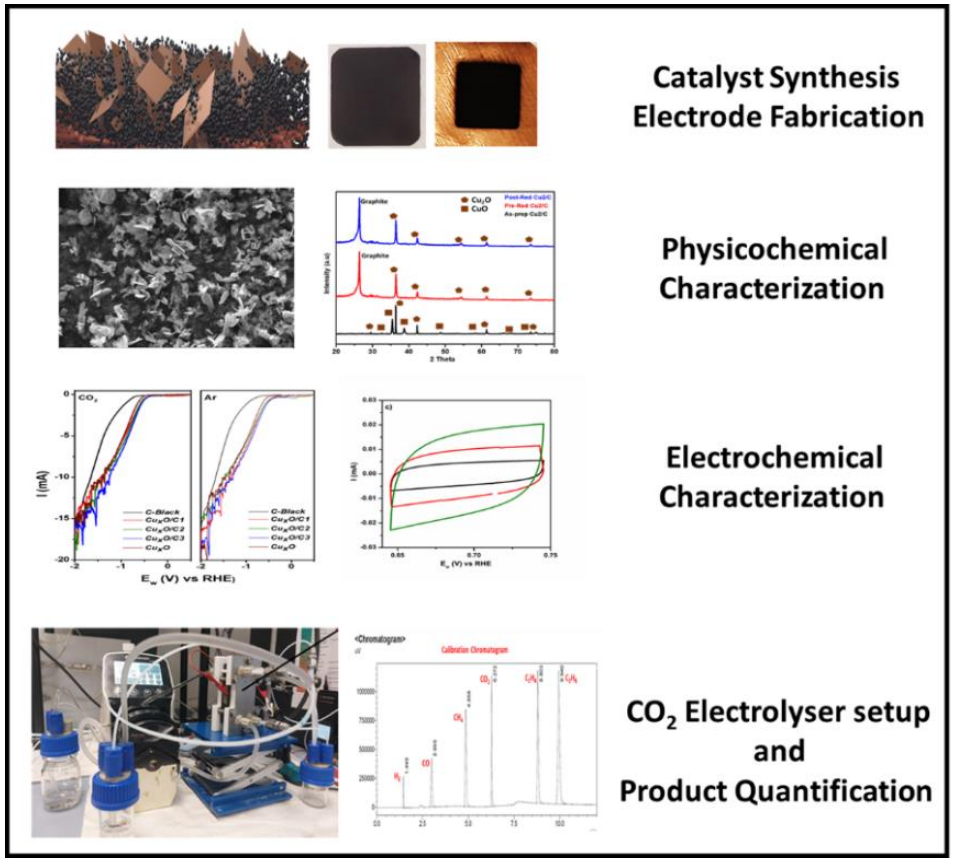
82. D. Gao, I. Zegkinoglou, N. J. Divins, F. Scholten, I. Sinev, P. Grosse and B. R. Cuenya, *ACS Nano,* **2017**, 11, 4825–4831.

83. T. T. H. Hoang, S. Verma, S. Ma, T. T. Fister, J. Timoshenko, A. I. Frenkel, P. J. A. Kenis, A. A. Gewirth, *J. Am. Chem. Soc*. **2018**, 140, 5791.
84. J. Q Wang, Z. Li, C. K. Dong, Y. Feng, J. Yang, H. Liu, X. W. Du, *ACS Appl. Mater. Interfaces* **2019,** 11, 2763–2767.
85. J. F. Huang, M. Mensi, E. Oveisi, V. Mantella, R. Buonsanti, *J. Am. Chem. Soc.* **2019**, 141, 2490–2499.
86. S. B. Shen, X. Y. Peng, L. D. Song, Y. Qiu, C. Li, L. C. Zhuo, J. He, J. Q. Ren, X. J. Liu, J. Luo, *Small* **2019**, 15, 1902229.
87. H. Feng, C. Chunyuan, S. Wang, M. Zhang, H. Ding, Y. Liang, and X. Zhang, J. *Phys. Chem. Lett*. **2022**, 13 (34), 8002-8009
88. Y. Baek, H. Song, D. Hong, S. Wang, S. Lee, Y.-C. Joo, G.-D. Lee, J. Oh, *J. Mater. Chem. A **2022***, 10, 9393.
89. S. Ma, M. Sadakiyo, M. Heima, R. Luo, R. T. Haasch, J. I. Gold, M. Yamauchi, Paul J. A. Kenis, *J. Am. Chem. Soc.* **2017**, 139 (1), 47-50.
90. X. X. Wang, Y. H. Duan, J. F. Zhang, Y. S. Tan, *J. Fuel Chem. Technol*. **2022**, 50, 538–563.
91. S. Louisia, D. Kim, Y. Li, M. Gao, S. Yu, I. Roh, P. Yang, *Proc. Natl. Acad. Sci.* **2022**, 119, e2201922119.
92. T. Zhang, Z. Li, J. Zhang, J. Wu, *J. Catal.* **2020**, 387, 163.
93. N. Theaker, J. M. Strain, B. Kumar, J. P. Brian, S. Kumari, J. M. Spurgeon, *Electrochim. Acta* **2018**, 274, 1.
94. R. Kas, R. Kortlever, A. Milbrat, M. T. Koper, G. Mul, J. Baltrusaitis, *Phys. Chem. Chem. Phys*, **2014**, 16, 12194–12201.
95. A. D. Handoko , K. W. Chan and B. S. Yeo , *ACS Energy Lett.*, **2017**, **2** , 2103 —2109.
96. Y. Pang, T. Burdyny, C-T Dinh, M. G. Kibria, J. Z. Fan, M. Liu, E. H. Sargent, D. Sinton, *Chem.*, **2017**,19, 4023-4030
97. J. Kim, W. Choi, J. W. Park, C. Kim, M. Kim, H. Song, *J. Am. Chem. Soc*, **2019** 141 (17), 6986-6994.
98. S.Y. Lee, H. Jung, N.-K. Kim, H.-S. Oh, B.K. Min, Y.J. Hwang, *J. Am. Chem. Soc.* **2019,** 141, 17, 6986–6994.
99. J.-J. Lv, M. Jouny, W. Luc, W. L. Zhu, J.-J. Zhu, F. Jiao, *Adv. Mater.* **2018**, 30, 1803111.

100. H. Ning , X. Wang , W. Wang , Q. Mao , Z. Yang , Q. Zhao , Y. Song and M. Wu , *Carbon*, **2019**, 146 , 218 —223
101. X. Wang, M. Miao, B. Tang, H. Duan, F. Zhu, H. Zhang, X. Zhang, W. J. Yin, Y. Fu, *Nano Res.* **2023**, 16, 8827–8835
102. V. S. R. K. Tandava, M. C. Spadaro, J. Arbiol, S. Murcia-López, J. R. Morante, *ChemSusChem* **2023**, 16, e202300344.
103. Zhou, Y., Che, F., Liu, M. *et al. Nature Chem,* **2018**, **10**, 974–980.
104. Y. H. Yu, D. Wang, Hong, Y. M. T. Zhang, C. W. Liu, J. Chen, G. W. Qin, S. Li, *Chem. Commun*. **2022**, 58, 11163–11166.
105. D. H. Nam, O. S. Bushuyev, J. Li, P. De Luna, A. Seifitokaldani,; C. T. Dinh, F. P. García de Arquer, Y. H. Wang, Z. Q. Liang, A. H. Proppe et al*. J. Am. Chem. Soc*. **2018**, 140, 11378–11386.
106. J. C. Lee, J. Y. Kim, W. H. Joo, et. al., *J. Mater. Chem. A* **2020**, 8, 11632–11641.
107. S. Sultan, H. Lee, S. Park, M. M. Kim, A. Yoon, H. Choi, T.-H. Kong, Y.-J. Koe, H.-S. Oh, Z. Lee, H. Kim, W. Kim, Y. Kwon, *Energy Environ. Sci*. **2022**, 15, 2397.
108. Y. Baek, H. Song, D. Hong, S. Wang, S. Lee, Y.-C. Joo, G.-D. Lee, J. Oh, *J. Mater. Chem. A* **2022**, 10, 9393.
109. J. Gao, H. Zhang, X. Guo, J. Luo, S. M. Zakeeruddin, D. Ren, M. Grätzel, *J. Am. Chem. Soc*. **2019**, 141, 18704-18714
110. D.-L. Meng, M.-D. Zhang, D.-H. Si, M.-J. Mao, Y. Hou, Y.-B. Huang, R. Cao, Angew. Chem. Int. Ed. 2021, 60, 25485.
111. Z.Y. Yin, J.Q. Yu, Z.H. Xie, S.W. Yu, L.Y. Zhang, T. Akauola, J.G. Chen, W.Y. Huang, L. Qi, S. Zhang, *J. Am. Chem. Soc.* **2022**, 144, 45, 20931–20938.
112. X. She, T. Zhang, Z. Li, H. Li, H. Xu, J. Wu, *Cell Rep. Phys. Sci.* **2020**, 1, 100051.
113. T. Zhang, J. C. Bui, Z. Li, A. T. Bell, A. Z. Weber, J. Wu, *Nat. Catal.* **2022**, 5, 202.
114. N.S. Romero Cuellar, C. Scherer, B. Kaçkar, W. Eisenreich, C. Huber, K. Wiesner-Fleischer, M. Fleischer, O. Hinrichsen, *J. CO_2 Util*. **2020**, 36, 263.

Chapter 2

Experimental Materials, Methods and Systems Involved in Electrochemical CO_2 Reduction.



This chapter emphasizes the experimental materials and methods and is precisely categorized into four major parts.

i. Catalyst synthesis and electrode fabrication
ii. Physicochemical characterization
iii. Electrochemical characterization
iv. CO_2 electrolyzer setup and product quantification

2.1 Introduction

The chapter is dedicated to presenting the experimental materials and methods of the relevant synthetic protocols, both physicochemical and electrochemical characterization techniques along with the CO_2 electrolyzer setup and the factors associated with electrochemical CO_2 reduction reactions. Thorough details of the product quantification with analytical instruments are also described. Brief introductions to the fundamentals of each technique are reported in relevance to the performed analysis and measurements in correlation within this thesis framework. The introductory part **(2.2)** describes the catalyst synthetic routes and protocols along with the various methods of electrode fabrication and CO_2 reduction at the cathode and the anodic oxidation reactions. The latter **(2.3)** is followed by physicochemical ex-situ characterization techniques detailing the structural, morphological and compositional properties of the prepared electrocatalysts. The third part **(2.4)** is oriented towards the description of the electrochemical techniques to perform the electrolysis along with the electrochemical characterization of the synthesised electrocatalysts. This chapter concludes with the final part **(2.5)** which outlines the details of the CO_2 electrolyzer setup and describes the Electrocatalytic CO_2 Reduction (ECO_2R) and the factors associated factors influencing the reduction reaction. Furthermore, the description of the analytical instrumentation like GC, HSGC and IC that are crucial in detecting and quantifying CO_2 reduction products while determining the faradaic and energy efficiencies of the process is discussed.

2.2 Catalyst synthesis and electrode fabrication

This section of the chapter begins with a description of the materials used throughout the thesis framework and the employed methodology for the synthesis of electrocatalysts along with the fabrication of various electrodes.

2.2.1 Materials

The complete list of chemical raw materials and various other components used are listed hereunder.

Vulcan XC-72 (Carbon-Black) from Cabot Corp, copper (II) acetate monohydrate, nickel nitrate, sodium hydroxide, nitric acid from Alfa Aesar, urea, cetyltrimethylammonium bromide (CTAB), sodium borohydride, potassium hydroxide, potassium bicarbonate, Nafion, methanol, ethanol, *n*-propanol, 2-propanol were obtained from Sigma-Aldrich. All the chemicals were of analytical grade and used directly without any further purification. Toray Carbon Paper with and without MPL, Sigracet 39BB was obtained from The Fuel Cell Store. Superhydrophobic polytetrafluoroethylene (PTFE) membranes with a 450 nm mean pore size were obtained from Sartorius Stedim Biotech. Both the PTFE membrane and Sigracet 39BB were used directly to prepare cathode materials without any further treatment.

2.2.2 Hydrothermal Synthesis

The hydrothermal method was the major synthetic protocol used for the synthesis of electrocatalysts. Hydrothermal synthesis in general illustrates the heterogenous reactions under aqueous conditions happening over 100° C and 1 bar. This, in contrast to the most conventional method, delivers numerous advantages in the controlled synthesis of compounds or materials with defined oxidation states [1] under controlled tight containers called autoclaves withholding the temperature and pressure. The co-existence of water (liquid) and gas above their boiling point temperature shall determine the compelling changes within the reactant species. These changes direct the mechanism of nucleation and growth of the desired heterostructures that are often said to be metastable and derive the desired morphology. Along with the precursors, additives are often added to tune the morphological and structural composition of the final heterostructures. In this PhD work, thoroughly tightened Teflon-lined stainless-steel autoclaves were used and heating was performed in

programmable hot air ovens. The hydrothermal method is often named solvothermal when any other solvent is used instead of water.

Synthesis of CuO-Cu_2O/C-Black (Cu_xO-C) heterostructures

Oxide-derived copper heterostructures supported over carbon were chosen to be the primary catalysts for the ECO_2R in tuning the selectivity towards ethylene. Inspired by a previous report of Z. Zhang et al., [2] a modified approach was applied to synthesize the oxide-derived Cu/C-Black heterostructures. The schematic illustration of the synthesis protocol is shown in Figure 2.1. As depicted, 40 mg of commercial Vulcan XC-72 (C-Black) were dispersed in 30 mL of Milli-Q water by strong ultrasonication for 2 h resulting in a uniformly well-dispersed homogenous mixture 1. In another beaker, solution 2 was prepared by adding 200 mg of copper (II) acetate monohydrate, [$Cu(CH_3COO)_2$] into 5 mL of Milli-Q water and stirring vigorously for over 30 min. 20 mg of NaOH and 20 mg of CTAB were added to solution 2. The solutions (1 and 2) were further mixed under constant stirring for 5 min. To this mixture, 20 mg of $NaBH_4$ was added under stirring. The final suspension was further stirred for 30 min in a hot water bath maintained at 60 ˚C. The contents were finally transferred to a Teflon-lined stainless-steel autoclave. The oven was programmed to operate at 160 ˚C for 12 h and allowed to cool naturally to room temperature.

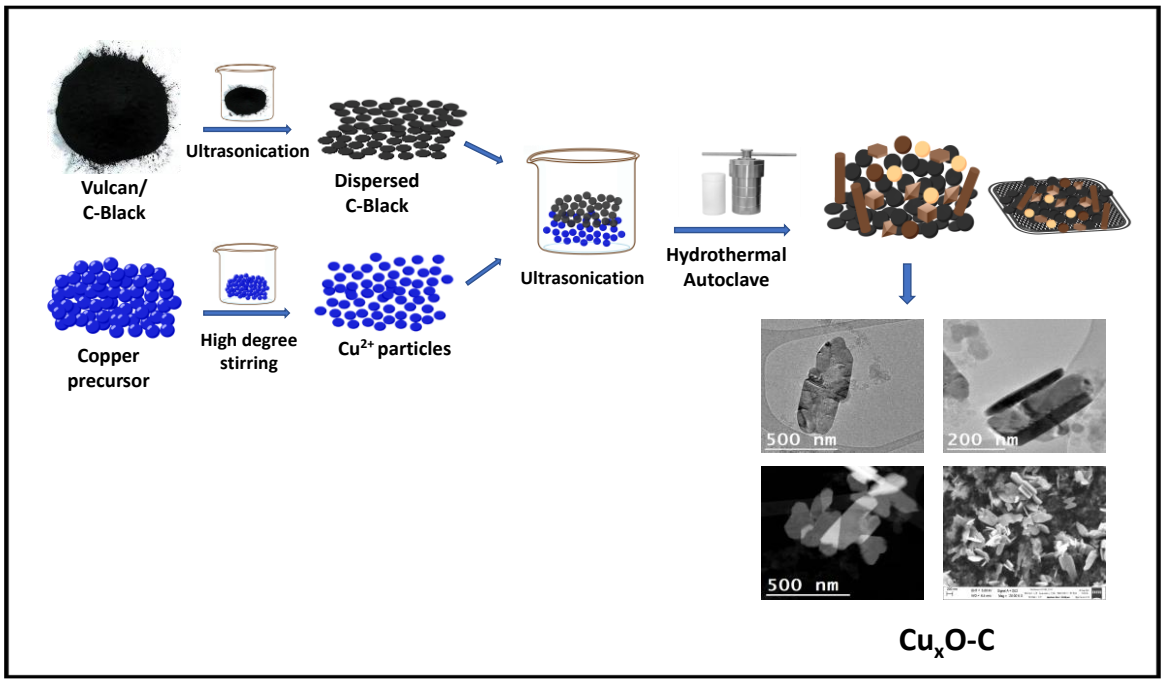


Figure 2.1 Schematic representation of the synthesis of CuO-Cu_2O/C-Black heterostructures.

The final product suspension named Cu_xO-C was cleaned by centrifugation with water followed by ethanol and vacuum dried at 60 °C for 24 h. The prepared samples are ground to a fine powder and stored in a vacuum desiccator until further use. The obtained catalyst is the mainly developed electrocatalyst, Cu_XO-C directed towards ECO_2R to C_2H_4 which is the prime target in this thesis work. The catalyst is modified and used in accordance with the target studies mentioned in the chapters ahead and the details are mentioned effectively in each chapter aimed to give the reader a clear understanding of the study carried out. The extensive characterization involving both structural and morphological properties of the Cu_XO-C is discussed in Chapter 3 of this thesis.

2.2.3 Synthesis of Ni-N-AC Single Atom Catalysts (SAC)

Nickel-based SAC were synthesized as a part of tandem catalysts in the final chapter discussing the tandem approach. The synthesis was adapted from a previously reported protocol from Zheng et al., [3] and was modified to adapt to our requirements. In brief, typical synthesis was divided into three steps where initially commercial carbon black (Vulcan XC-72) was activated and later Ni was incorporated by impregnation followed by thermal pyrolysis of urea under Ar atmosphere. Typically, 1 g of Vulcan XC-72 (C-Black) was dispersed in 50 mL of 9 M nitric acid solution and subjected to reflux for 3 hours at 90 °C. The solution mix is allowed to cool down to room temperature naturally. The contents were thoroughly washed with Milli-Q water by ultra-centrifugation until the pH was adjusted to near neutral (pH ~5-5.5) and later with ethanol. The obtained precipitate is dried under a vacuum in an Ar atmosphere. The obtained activated carbon (AC) is ground to a fine powder and 500 mg is dissolved in 200 mL of Milli-Q water and sonicated for 90 mins until a homogenous suspension is achieved. In another flask, 3 mg/mL of nickel nitrate (Ni^{2+}) precursor was prepared with Milli-Q water. 20 mL of Ni^{2+} solution was added dropwise to the AC suspension and kept under high-degree stirring overnight, after which it was centrifuged, vacuum dried and collected as Ni^{2+}-AC powder. The as-prepared powder was mixed with urea in a 1:10 ratio and heated to 800 °C in a tubular furnace for 1 h with a constant supply of Ar gas at 80 sccm. The final black powder was collected and stored under an inert atmosphere until further use and labelled as Ni-N-AC. The detailed schematic illustration of the synthesis protocol is shown in Figure 2.2.

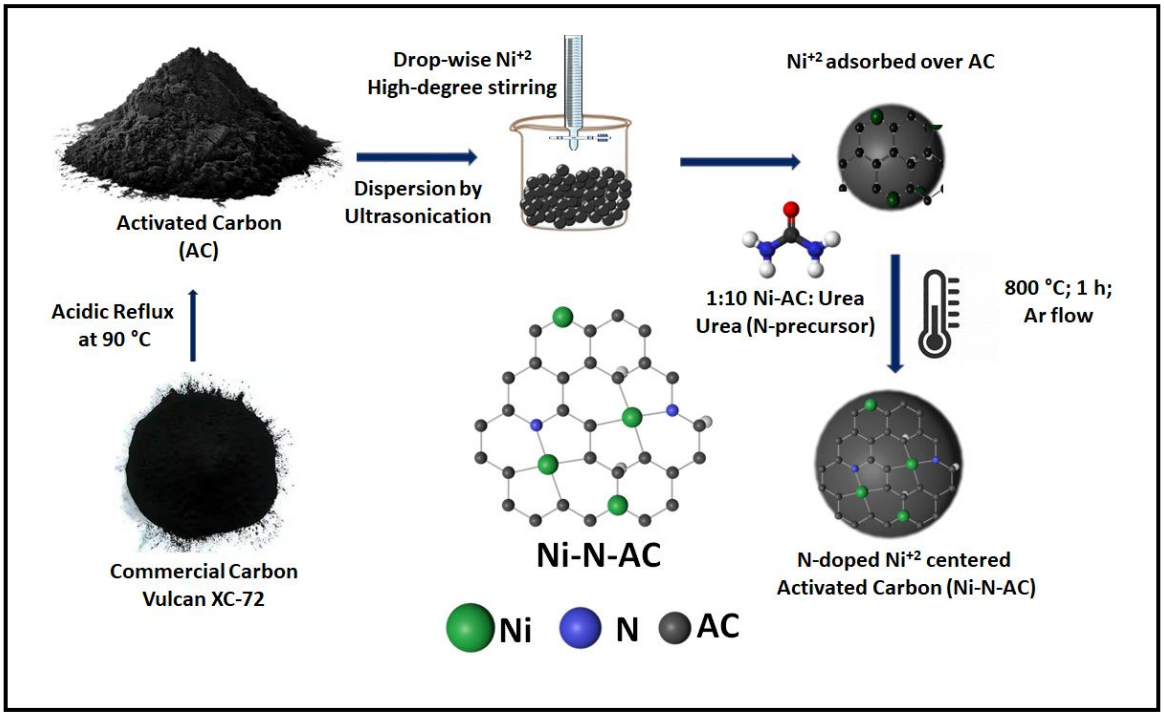


Figure 2.2 Schematic representation of the synthesis of Ni-N-AC Single Atom Catalysts.

2.2.4 Fabrication of GDEs (PTFE/SGL-Cu)

GDEs were obtained by depositing copper catalyst layers on hydrophobic PTFE membranes. Copper thin films were deposited with a direct-current (DC) -magnetron sputtering system (AC450, Alliance Concept). DC sputtering is a thin film deposition technique that employs ionized gas molecules to vaporize (sputter) molecules from the target material into plasma in a vacuum chamber. These vaporized atoms are then deposited and condensed into a thin layer onto the targetted substrate. DC sputtering is the most used method to obtain electrically conductive target materials due to the low cost and high degree of control. The schematic illustration of the DC Magnetron sputtering mechanism protocol is shown in Figure 2.3.

In Chapter 4 of this thesis, tailored-made GDEs were fabricated using hydrophobic PTFE membranes and commercial carbon-based GDLs. Initially, a 3 mm soda-lime glass substrate was used for thickness calibration and characterization studies. The deposition was carried out with a 99.99% purity target of Cu (diameter: 100 mm, thickness: 6 mm, Neyco, Vacuum & Materials). For comparison studies, SGL/Sigracet 39BB was also used as the substrate to deposit the copper. Both the substrates, PTFE and Sigracet 39BB were flattened on soda lime glass substrates with Kapton® tape to ease their vacuum processing deposition. Substrates were first loaded into the sputtering system where the chamber was evacuated to a base

pressure close to $4x10^{-6}$ mbar. Then, before the deposition process, the target was "pre-sputtered" for 5 min with the shutter closed to remove any contamination to the target surface. Finally, the deposition process was carried out with a power applied to the Cu target kept constant at 100 W and with an Ar (99.9999 +%) gas flow rate adjusted to 30 sccm for reaching a working pressure maintained at about 2.8×10^{-3} mbar approximately. The films were deposited at room temperature conditions and the substrate was rotated at 10 rpm for better surface homogeneity. The required thicknesses of the Cu films onto the glass substrate were varied in the range of 100 nm to 500 nm by adjusting the sputtering time and controlled by X-ray fluorescence spectroscopy (XRF, Fisherscope XVD) previously calibrated.

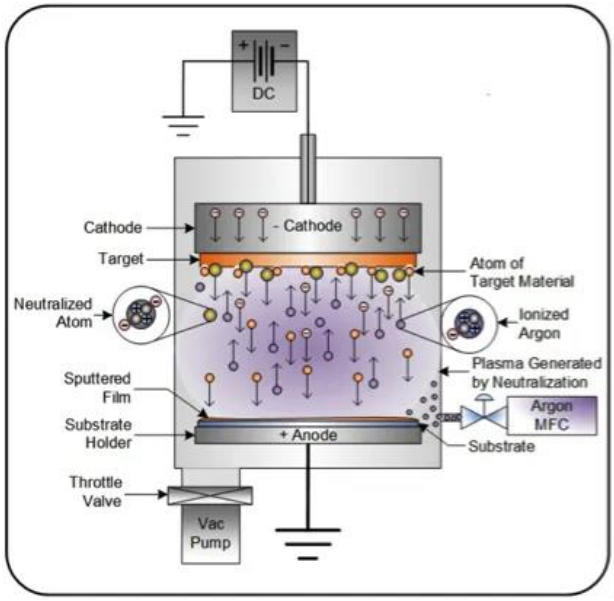


Figure 2.3 Schematic representation of DC-Magnetron sputtering

2.2.5 Electrode Fabrication

Cathode Fabrication

In the framework of this thesis, cathodes were fabricated using two basic methods, the drop-casting technique and the airbrush technique.

i. Drop casting technique.

Initially drop casting technique was followed to deposit the electrocatalysts on the GDE. Drop casting is a simple and reliable method as it does not involve any particular equipment. Certain amounts of catalyst inks are eventually deposited on the substrate followed by evaporation of

the solvent used as depicted in Figure 2.4. Catalyst ink was prepared by mixing the appropriate amounts of catalyst, a Nafion binder and isopropanol. In Chapter 3, electrodes are prepared using a drop-casting technique. To prepare the catalyst ink, 20 mg of catalyst powder was dispersed in 2 mL of isopropanol and 100 µL of Nafion 5%, (a cationic ionomer) by ultrasonication for 1 h. The dispersed catalyst ink is taken and deposited on the GDL covering the whole surface with uniform loading of the catalyst ink. All the electrodes prepared have a geometric area ranging from 1*1 to 2*2.5 cm^2 for different analysis. The final loading of the electrocatalyst on the electrode, GDE is measured by weighing the electrode before and after the drop-casting of the catalyst ink.

The drop-casting technique was mainly used in the initial stages of this thesis to deposit Cu_xO-C. A brief description of electrode fabrication is described in Chapter 3 of this thesis.

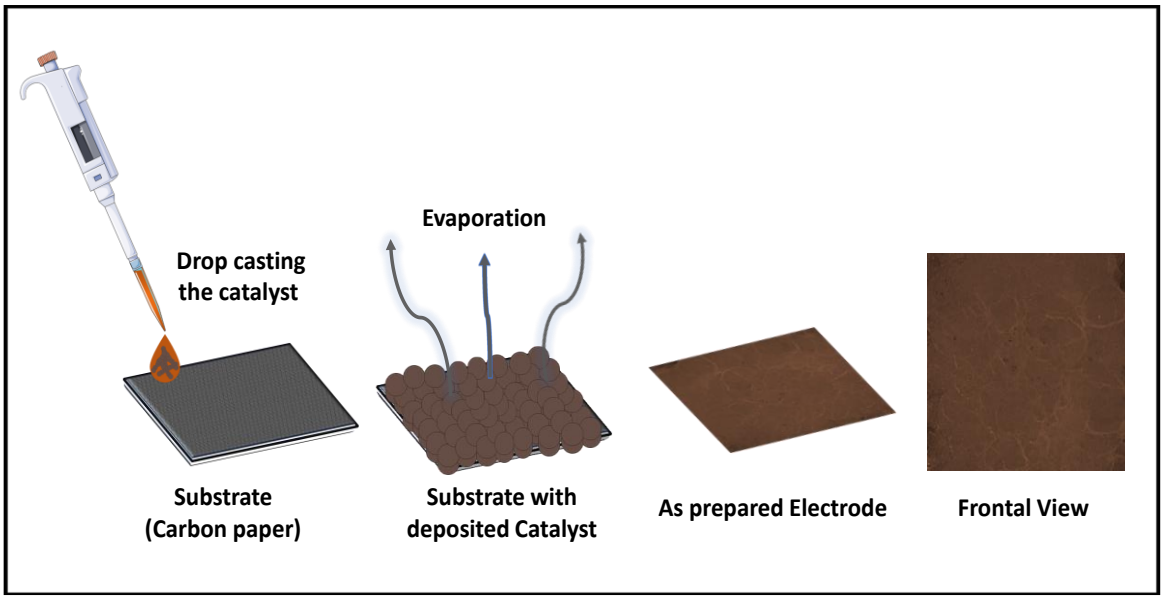


Figure 2.4 Schematic representation of the Drop Casting technique for the electrocatalyst deposition on the gas diffusion layers.

ii. Airbrush technique.

The airbrush method of deposition is further used to fabricate the electrodes. An airbrush is a small and hand-held instrument connected to an external compressed air that sprays the catalyst inks in a more controlled manner yielding a more homogeneous and controlled surface as depicted in Figure 2.5. Airbrush technique is most commonly used to prepare the electrodes in electrocatalytic applications. Catalyst ink was prepared similarly to the drop

casting method and the ink was loaded into the reservoir tank. By controlling the valve after adjusting the needle, the dispersion was evenly sprayed onto the substrate to have uniform mass loadings as desired. In Chapters 4 and 5, the airbrush technique is mainly used to fabricate the GDEs and a more descriptive way of preparing the electrodes will be discussed in the respective chapters.

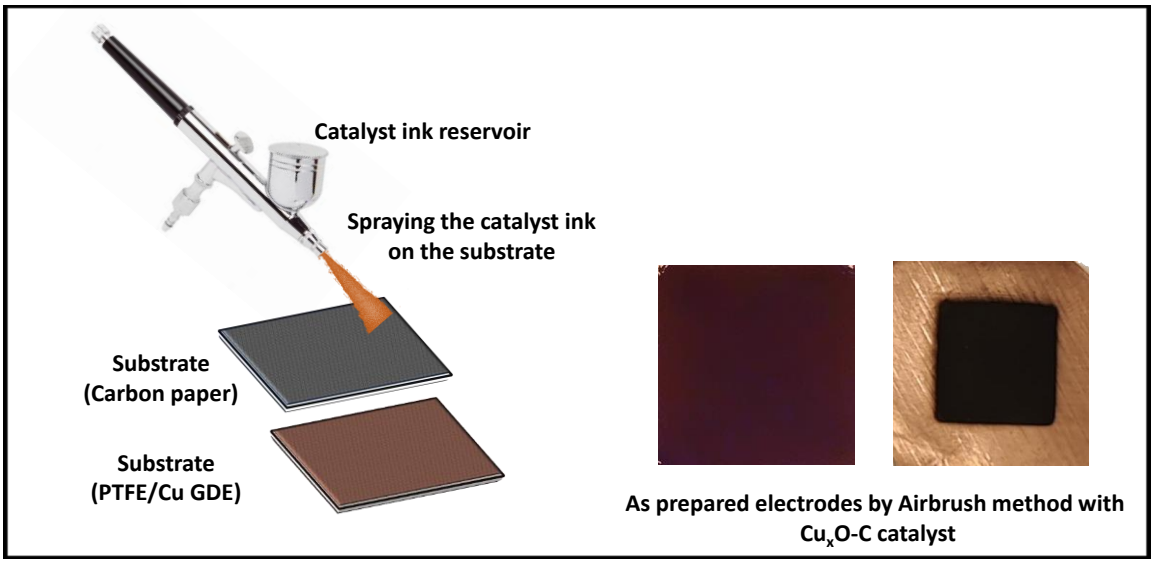


Figure 2.5 Schematic representation of the Airbrush technique for the electrocatalyst deposition on the gas diffusion layers.

Anode Fabrication

Although anodes are highly important in electrochemical reactions, the focus of this thesis was mainly on the cathode catalyst materials and electrode fabrications.

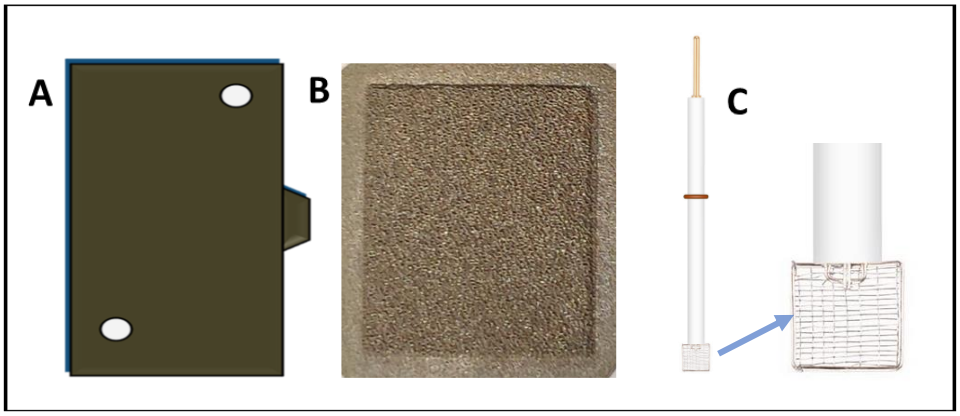


Figure 2.6 A) DSA (Dimensionally Stable Anode), **B)** Nickel foam **C)** Platinum mesh

For all practical purposes, concerning the experiments for ECO_2R, commercially obtained mixed metal oxide (MMO) (Ruthenium-Iridium oxides) based DSA (in Chapters 3) and Nickel (Ni) foam (in Chapters 4 and 5) were directly used as the anode materials without any further modifications. For electrochemical characterization techniques like CV, ECSA and PEIS, Pt mesh was used as the anode.

Reference Electrodes

Reference electrodes (RE) are prescribed to be stable and well-defined electrochemical potentials at STP and are non-polarizable. These are crucial in estimating the half-cell potentials concerned with either the cathode or anode in an electrochemical cell. In this thesis, a Silver/Silver chloride electrode was used in general. Typically, a conventional aqueous electrode is used for electrochemical characterization and a 1 mm leakless electrode was used in the flow electrolyzers.

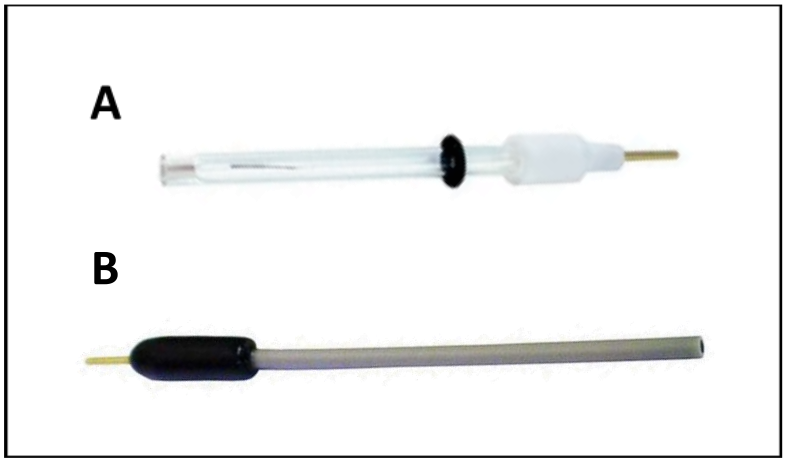


Figure 2.7 A) Aqueous Ag/AgCl reference electrode, **B)** Leakless Ag/AgCl Miniature Reference electrode.

The cathode potential is recorded with reference to Ag/AgCl (Silver Chloride electrode) RE during the experiments, which is converted into an electrode potential referred to as RHE by the following expression 2.1 as

$$E_{W_{RHE}} = E_{W_{Ag/AgCl}} + 0.209 + 0.059\,pH \qquad 2.1$$

where $E_{W_{RHE}}$ is the working potential of the electrode *vs* RHE and $E_{W_{Ag/AgCl}}$ is the applied potential referred to as the Ag/AgCl reference electrode used in the experiments.

2.3 Physicochemical characterization

This section aims to briefly describe the characterization techniques and their working principles used throughout the thesis framework and the employed methodology for each method in respective chapters.

2.3.1 X-ray Diffraction (XRD)

XRD is the most commonly used and powerful non-destructive technique to characterize crystalline materials providing wholesome information on the qualitative analysis, phase and structure identification including the lattice parameters or the Miller indices (h, k, l). It also provides valid information on grain size and crystal defects. In a typical X-ray diffractometer, electrons are generated by heating a filament in a cathode ray tube. When incoming electrons have enough energy to remove inner-core electrons from the target material, electrons from the outer shells decay to partially empty inner shells, emitting X-ray radiation.

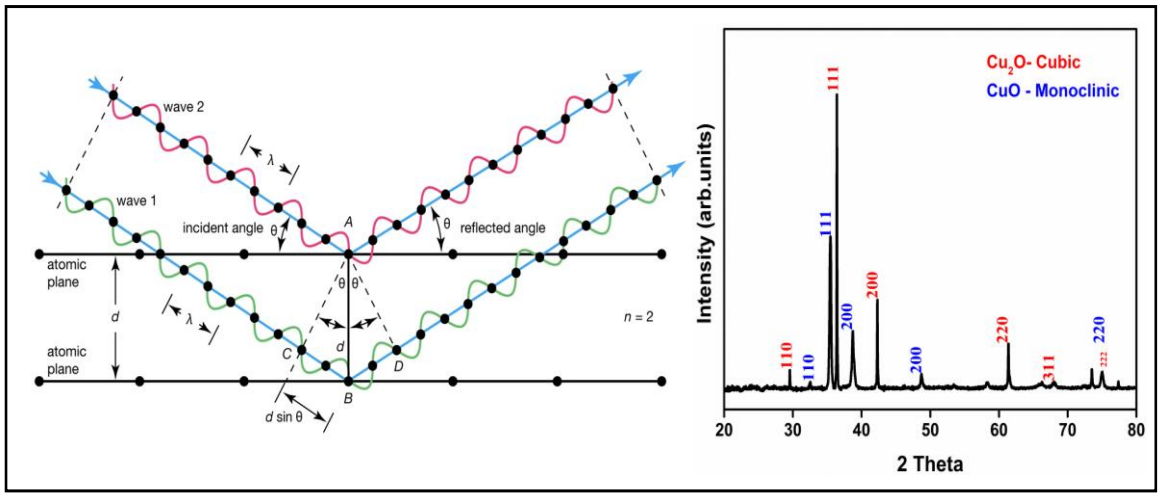


Figure 2.8 Schematic representation of the principle of XRD with Bragg´s equation and the XRD data of the majorly used catalyst in this thesis work, Cu_xO-C.

These emitted beams of monochromatic X-rays undergo constructive interference that is characteristic of a crystalline sample and the respective angles are established by using Bragg's law:

$$n\lambda = 2dsin\theta \qquad 2.2$$

where n is an integer, λ is the wavelength of the X-rays, d is the interplanar spacing producing the diffraction and θ is the diffraction angle.

Figure 2.8 represents the working principle of XRD with Bragg´s equation and the XRD data of the major used catalyst in this thesis work, Cu_xO-C.

In Chapters 3 and 4 of this thesis work, the results of the XRD analysis are discussed in a detailed manner. A Bruker type X-Ray D8 diffractometer (CuKα radiation, λ = 1.5418 Å, 40 kV, 40 mA) in a scanning range of 2θ from 10° to 80° with a step size of 0.025° and a measuring time of 2 s per step was initially used for as-synthesized catalyst powders and further modified with scanning in 2θ range from 35° to 95° at a scanning speed of 0.6 s per step and a step size of 0.017 degrees.

In Chapter 4, FWHM was calculated to estimate the crystalline size of the deposited Cu catalyst layers with different thicknesses. FWHM is the width at the half height of a given peak. Smaller FWHM indicates a higher crystalline order. Using the FWHM, the crystalline of each sputtered thickness was measured based on the Scherrer equation.

$$D = \frac{k\lambda}{\beta \cos\theta} \qquad 2.3$$

where D is the crystalline size, k is the Scherrer's constant, λ is the X-ray wavelength used (λ = 1.5418 Å), β is the measured FWHM and θ is the Bragg's angle.

2.3.2 Attenuated Total Reflectance- Fourier-Transform Infrared Spectroscopy (ATR-FTIR)

Infrared (IR) spectroscopy is a traditional chemical analytical technique that works on the principle of interaction between the IR light and the sample of interest. The introduction of the Fourier-Transform, a mathematical operation has improved and advanced the data analysis with higher speed, accuracy and an enhanced signal-to-noise ratio than the traditional IR spectroscopy. To further enhance the analytics, ATR has been introduced which directly involves IR light passing through a crystal to the sample to be analysed. Upon interaction with the sample, the light passes through the crystal again before it is detected [5]. ATR has the advantage over transmission FTIR and there is no extensive sample preparation required and a high-quality IR spectrum can be obtained from almost any type of sample. The working principle of ATR-FTIR is demonstrated in Figure 2.9.

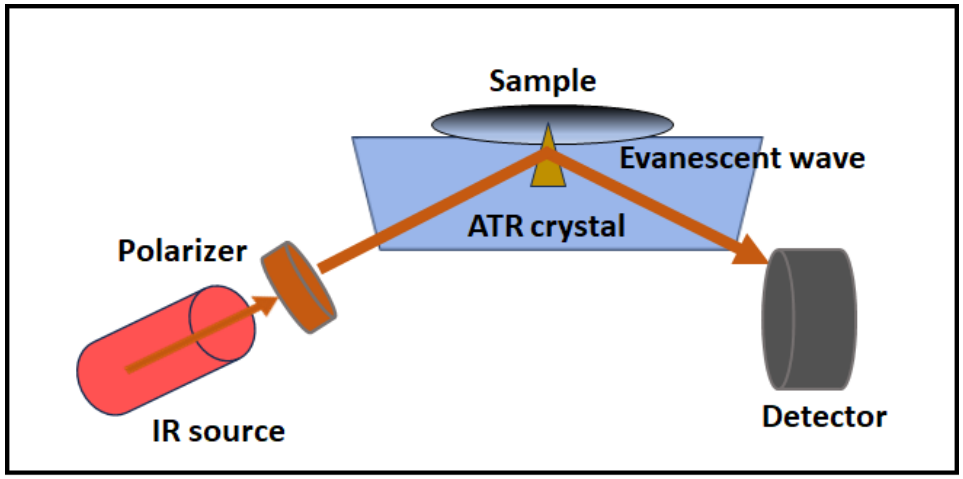


Figure 2.9 General schematic representation of the principle in ATR-FTIR Spectroscopy (Figure adapted and modified from Bruker products).

In the present thesis work, an ALPHA type from Bruker was used to identify the CuO-Cu_2O phases of the synthesized electrocatalyst, Cu_xO-C along with the identification of hydroxyl and carboxyl functional groups and a detailed study is mentioned in Chapter 3. In Chapter 4, ATR-FTIR was used to analyse the presence of functional groups in some GDE samples.

2.3.3 Brunauer–Emmett–Teller (BET) method for surface area analysis

The specific surface area of solids/powder is estimated from the amount of nitrogen adsorbed in relationship with its pressure, at the boiling point temperature of liquid nitrogen under normal atmospheric pressure conditions. The amount of gas adsorbed depends on the exposed surface area but also the temperature, gas pressure and strength of interaction between the gas and solid. The observations are interpreted following the model of Brunauer, Emmett and Teller (BET Method) and plotted as isotherm, which is the relation between the amount of gas adsorbed as the function of the relative pressure [6].

The BET surface area analysis was performed using a TriStar II 3020- Micromeritics equipment at liquid nitrogen temperature and the measurement set-up is reflected in Figure 2.10. Initially, the samples were degassed at 90° C for 1 h and then at 250° C overnight in a FlowPrep 060- Micromeritics. As described, the BET method was used to calculate the active surface area for a relative pressure (P/P_0) range of 0.05-0.025. There are typically 5 types of adsorption isotherms possible and the analysis of the electrocatalyst, Cu_xO-C followed a type III isotherm which is further discussed in Chapter 3.

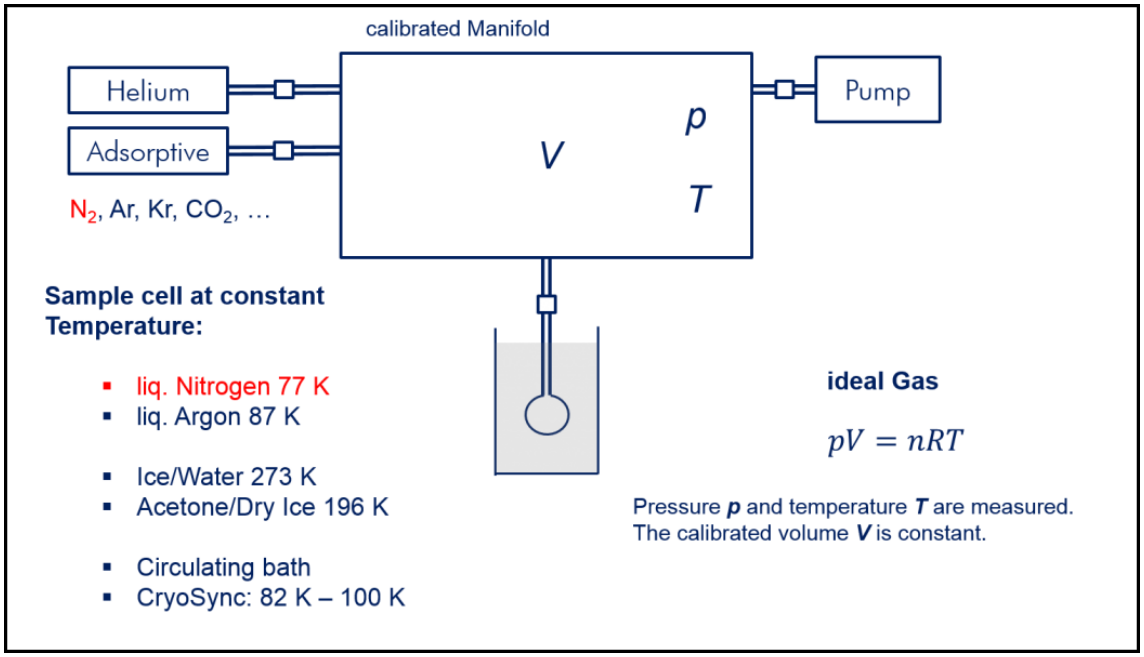


Figure 2.10 Schematic representation of measurement set up for BET analysis. (Figure adapted from 3P instruments).

2.3.4 Scanning Electron Microscopy (FESEM)

Scanning electron microscopy is a technique aiming to produce images of a sample by scanning the surface with a focused beam of electrons. The ejected electrons usually interact with the atoms in the sample generating signals unveiling the morphology and composition of the sample. Unlike the conventional SEM, FESEM is equipped with a field emission gun that generates extremely focused and high and low-energy electron beams. FESEM is equipped with additional In-Lens detectors that are optimized to operate at high resolution along with secondary electron (SE) and electron-backscattered detectors (ESB). While the SE detector unveils the topography and morphology of the sample, ESB plays its role in identifying the compositional variations of the sample analyzed [7]. In addition, elemental composition can be obtained using energy-dispersive X-ray spectroscopy (EDX). Additionally, the cross-sectional imaging can be done using the focussed ion beam (FIB) module operating at a certain angle to the specimen stage. Figure 2.11 shows the ZEISS Crossbeam 550 FESEM facility with a FIB column accessory used for cross-sectional analysis in Chapter 5.

In Chapter 3, morphological studies along with elemental composition were conducted using the in-house FESEM, Zeiss Auriga 60 equipped with EDX accessory to investigate the Cu_xO-C

with varying compositions. In Chapter 5, the surface morphology, cross-sectional structure and composition of fabricated GDEs were evaluated with a Zeiss, Gemini II crossbeam 550 (FIB-SEM) aided with a Ga beam allowing for localised milling of the surface of the sample coupled with an EDX as well. Surface, cross-sectional and EDX analysis was conducted at different voltages ranging from 1.2 to 5 kV. Before milling, a thin layer of platinum was applied to protect the cross-sectional area.

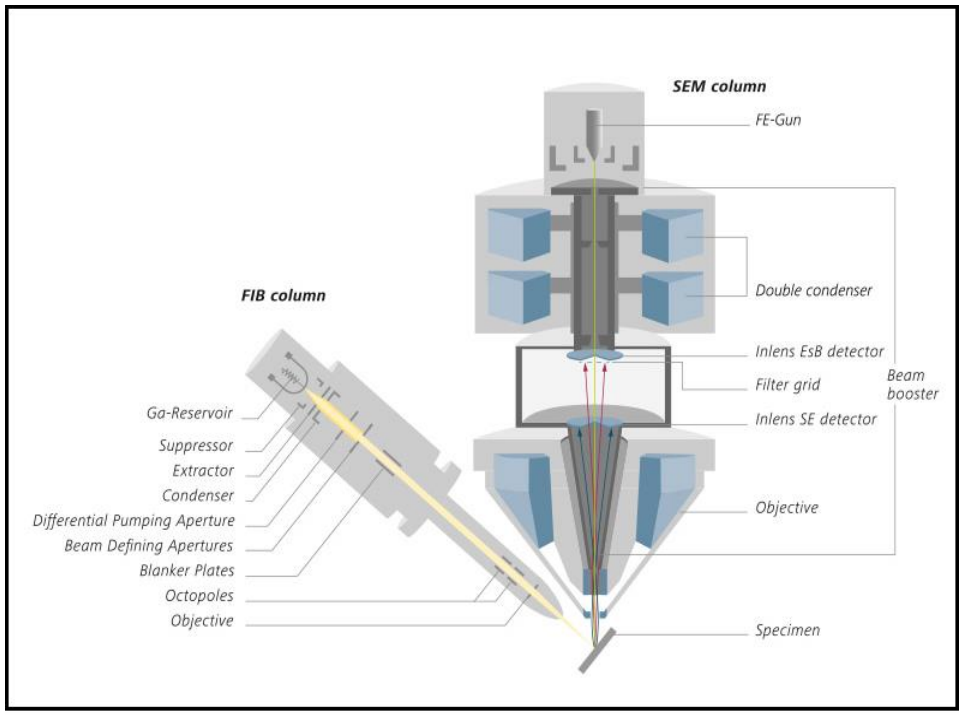


Figure 2.11 ZEISS Crossbeam 550 with a Gemini II column and a FIB column (Figure adapted from Zeiss FESEM facility)

2.3.5 Transmission Electron Microscopy (TEM)

Transmission Electron Microscopy is an advanced electron microscopic technique used to obtain images of the specimens where the electrons are transmitted through the sample/specimen before they are collected. High-resolution TEM (HR-TEM) follows a slightly different principle aiding in high-resolution imaging patterns at the atomic level. HR-TEM aids in offering valuable information on the inner structure of the sample such as morphology and crystal structure. Transmitted electrons interact with atoms within the sample via elastic and inelastic scattering. Electrons that undergo inelastic scattering have a change in energy after they are transmitted through the sample, whereas elastically scattered electrons maintain

their initial transmitted energy giving rise to Bright and Dark field images. Bright-field images are a result of scattered electrons and are responsible for the formation of the images unveiling the morphologies. In contrast, the Dark field which resulted from the scattered electrons assists in identifying the crystal structure to study defects based on the diffraction principle [8]. Figure 2.12 shows the schematic view of imaging and diffraction modes in TEM indicating the major components and operating patterns of the TEM.

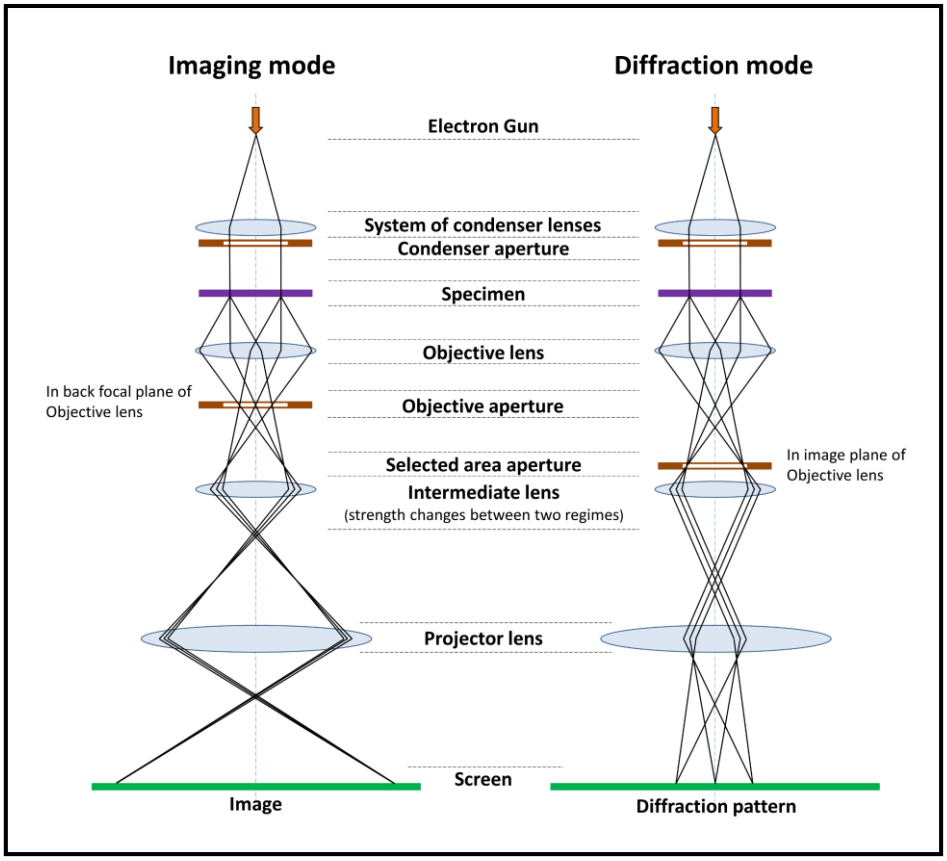


Figure 2.12 Schematic representation of imaging and diffraction modes in TEM.

Appropriately equipped TEM holds an advanced technique called Electron Energy Loss Spectroscopy (EELS) which works on the inelastic scattered electrons thereby separating them based on the kinetic energy and the energy loss from the incident beam energy. These differences are particular to elements which are crucial in providing information on the elemental composition of the analysed samples [9]. In Chapter 3, HR-TEM is performed using a field emission gun FEI Tecnai F20 microscope. High-angle annular darkfield (HAADF) scanning TEM (STEM) and EELS were performed in the Tecnai microscope using a GATAN QUANTUM

filter for in-depth morphological and compositional analysis of Cu_xO-C and the observations are clearly described.

2.3.6 X-ray Photoelectron Spectroscopy (XPS)

X-ray photoelectron spectroscopy is an excellent tool for the investigation of the elemental composition from the surface of a material as well as the chemical state and overall electronic structure of the material. XPS is proven to be an advantageous technique as it can identify not only the elemental composition but also their oxidation state. The XPS spectra are obtained by irradiating a solid surface (sample) with a focused beam of X-rays while simultaneously measuring the kinetic energy and electrons that are emitted from the top surface 1-10 nm of the sample being analyzed. The working principle of XPS is depicted in Figure 2.13.

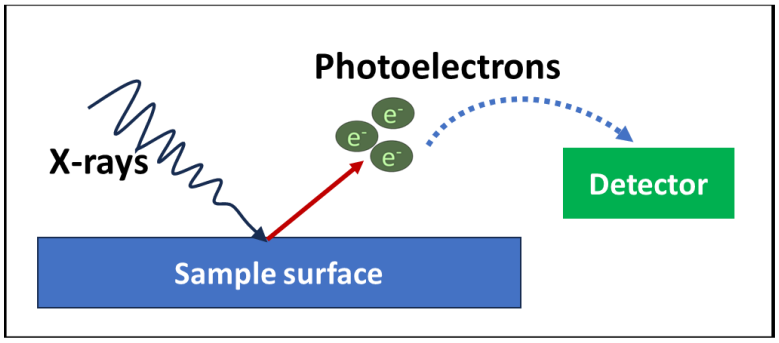


Figure 2.13 Schematic representation of basic working principle in XPS.

A photoelectron spectrum is recorded by counting ejected electrons over a range of electron kinetic energies. Peaks appear in the spectrum from atoms emitting electrons of a particular characteristic energy. The energies and intensities of the photoelectron peaks enable the identification and quantification of all surface elements except hydrogen [10].

In Chapter 3 of this thesis, XPS studies were performed to examine the surface structural composition of the as-prepared catalysts, Cu_xO-C heterostructures using a PHI instrument model 5773 Multitechnique with A1 Kα radiation (1486.6 eV).

2.3.7 Temperature Programmed Desorption (TPD)

The Temperature Programmed Desorption is used to study the desorption of physical and chemically bound species on the surface of a material. The temperature of the sample is increased until the thermal energy is sufficient to break the chemisorption or the

physisorption bonds. By monitoring the temperatures at which molecules are liberated and determining the volume of gas desorbed at each temperature, the strength and number of adsorption sites can be determined. TPD is a powerful and effective technique to obtain information about surface chemistry as the catalytic reactions only occur on a catalyst's surface, observing surface/adsorbate interactions is vital to understanding the origin of catalytic products [11].

In Chapter 3, TPD experiments were performed with CO for the Cu_xO-C2 sample and pristine C-black as a reference. The conditions followed were as follows: initial degasification at 200 °C under He atmosphere, followed by a CO adsorption step at 40 °C (with 10% CO in He flows), and finally a TPD measurement under He flow with a 5 °C $\cdot min^{-1}$ ramp.

2.3.8 X-ray Fluorescence Spectroscopy (XRF)

X-ray fluorescence analysis is suitable for the non-destructive thickness measurement of thin layers as well as for determining their chemical composition. The X-ray source and detector are located on the same side of the sample. When the layer on the substrate is subjected to X-rays, the radiation will penetrate the layer to a certain extent depending on the thickness, and in turn cause characteristic fluorescence radiation in the material of the underlying substrate. On its way to the detector, this fluorescence radiation will be attenuated by absorption at the layer. The thickness of the layer can be determined based on the intensity attenuation of the fluorescence radiation of the substrate material. In Chapter 4, the thickness of the sputtered PTFE/Cu GDEs was measured with an XRF Fisherscope XVD system from Helmut Fisher that aids in routinary thickness control measurements.

2.3.9 Four-Probe Method

Sheet resistance or surface resistivity is a common electrical property used to characterise thin films of conducting and semiconducting materials. It is the measure of the lateral resistance through a thin square of material, i.e. the resistance between opposite sides of a square. The schematic representation of a four-probe method is shown in Figure 2.14.

In Chapter 4, the sheet resistance, R_s (Ω/square) was measured with a four-point probe system (Everbeing) to determine the resistivity, ρ (μΩ.cm) of the layers on the glass substrate with

$$\rho = R_s . t \qquad 2.4$$

where ρ is the resistivity, and t is the thickness of the layer.

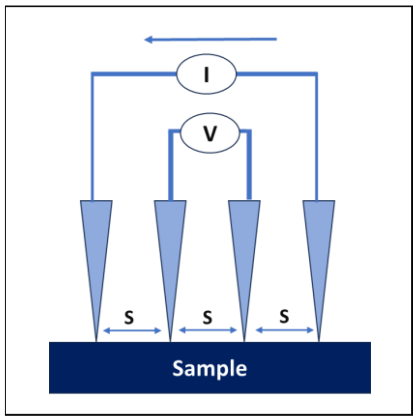


Figure 2.14 Schematic representation of a four-point probe. The four probes have equal spacing (s) and are shown in contact with a surface. A current (I) is injected through probe 1 and collected through probe 4, whilst the voltage is measured between probes 2 and 3.

2.3.10 Contact Angle

Wettability is the surface property of a material which is important to be studied to understand the affinity of that substrate/material towards any liquid medium. Contact angle measurement is an appropriate technique to understand the surface wettability of any material. The contact angle is the degree of angle formed by the liquid drop at the surface of the solid [12]. In theory, the sessile drop is the most commonly used method to measure surface wettability of a substrate which is often expressed as a contact angle. A drop of liquid (usually water) is placed on the surface of a substrate, the droplet stays static on the surface or the droplet recedes over the substrate. The surface wettability by the sessile drop method with the angle reflecting the hydrophobic or hydrophilic nature concerning the analysis carried out in Chapter 5 is depicted in Figure 2.15 A. The low degree of surface wettability is explained in terms of hydrophobicity showing a contact angle greater than 90° as seen in Figure 2.15 B which is advantageous for GDEs for ECO_2R holding a high stability in terms of operation. The lower hydrophobic one, as seen in Figure 2.15 C explains the high surface wettability and is less hydrophobic with a contact angle lower than 90° is deemed to be less significant in terms of stability of the GDEs.

In Chapter 4, the hydrophobicity of the modulated PTFE/Cu GDEs was analysed by measuring the contact angle with an OCA 20 system from DataPhysics. In each CA measurement, the sessile drop method was used to drop 10 µL of sample approximately over the surface of the GDE; the contact angle was measured within 30 s after the water drop. The reported values were derived from the average value from a minimum of three measurements at different spots on the same surface.

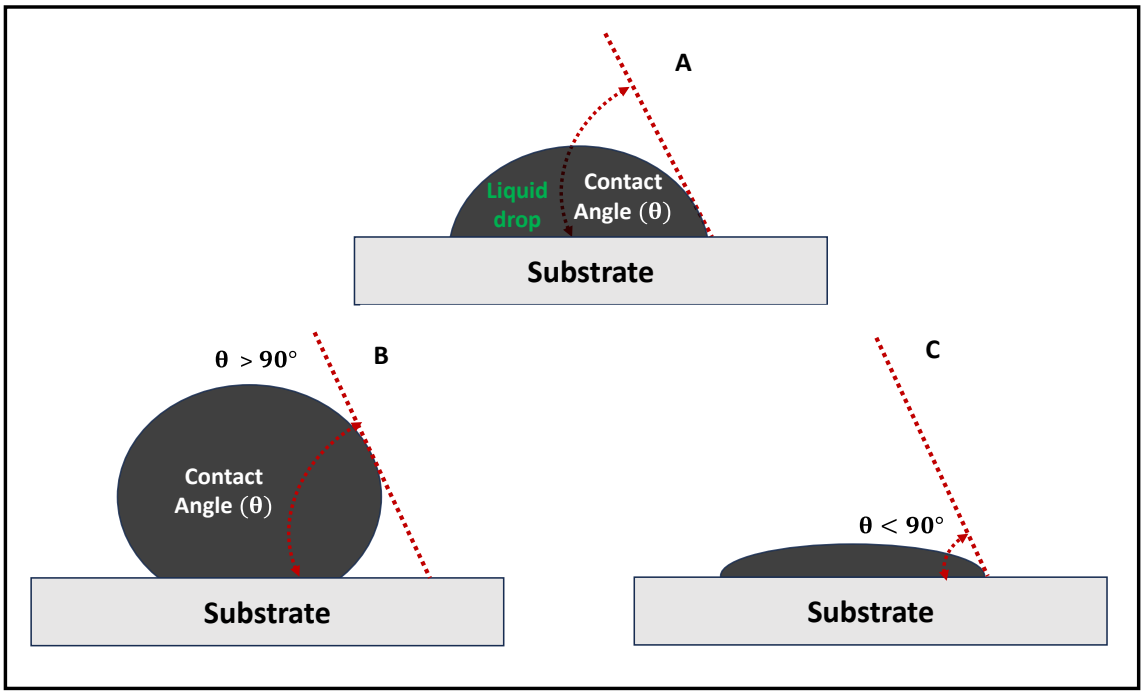


Figure 2.15 Schematic representation of the contact angle by sessile-drop method **(A)**. Liquid droplets show the high hydrophobicity **(B)** and low hydrophobicity **(C)** of the substrate surface.

2.4 Electrochemical characterization

This section is oriented towards describing the electrochemical techniques used initially to characterize the cathode catalyst materials and to perform the ECO_2R as well as the modelling of the kinetic studies.

A three-electrode setup as shown in Figure 2.16 was used for the prescribed analysis. The setup incorporates a cathode acting as a working electrode (WE) holding the catalyst undergoing reduction, a Platinum (Pt) mesh at the anode acting as a counter electrode and a reference electrode (RE), silver-silver chloride electrode [Ag/AgCl (KCl sat)], respectively. The applied potential or current is generally monitored using a potentiostat that adjusts the current passing through the WE and CE where the potential bias is set between the WE and RE respectively. The three-electrode cell as seen in Figure 2.16 is usually mounted in a beaker with the concerned electrolyte and a cap holder containing the respective electrodes.

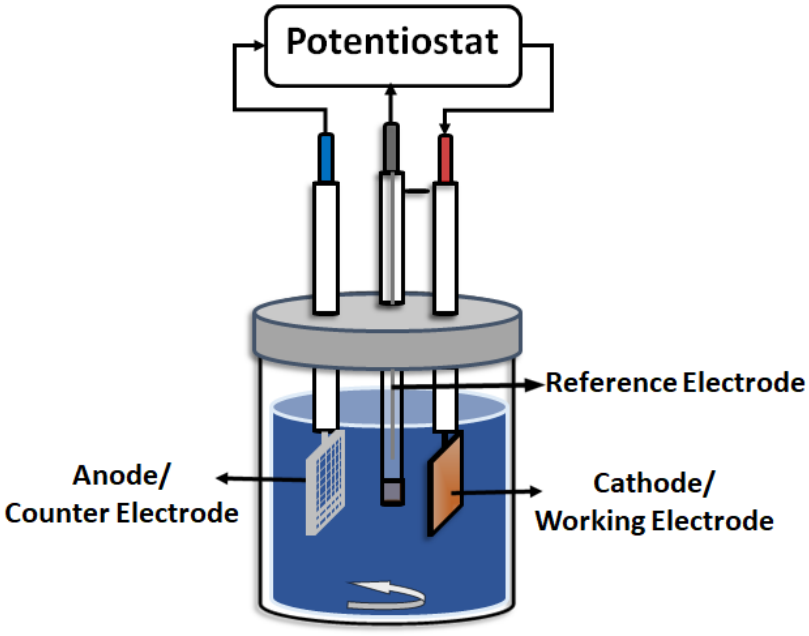


Figure 2.16 Schematic representation of a basic three-electrode setup

The fundamental electrochemical studies were carried out using this setup before the electrolysis in the ECO_2R electrolyzer.

2.4.1 Open Circuit Voltage (OCV)

The Open Circuit Voltage is the equilibrium electrode potential of the WE concerning the RE where no current is passing through the electrochemical cell and the resting potential is monitored. OCV is generally performed as a period of conditioning time and also to reach the system to thermodynamic equilibrium [13] while the resting potential is being measured between the WE and RE. A steady OCV (often ±5 mV or less) across time suggests thermodynamic stability leading to greater analytical certainty in measurement. In experiments like Electrochemical Impedance Spectroscopy (EIS), the potential is often set *vs.* OCV instead of the reference.

In all the measurements of this thesis, OCV was generally performed before the onset of any electrochemical measurement. Often this is also referred to as Open Circuit Potential (OCP).

2.4.2 Linear Sweep Voltammetry (LSV)

Linear Sweep Voltammetry is the standard potentiostatic electrochemical technique where the current of the WE is measured with the potential between the WE and RE swept linearly at a scan rate *v,* resulting in the output current vs. potential, called a voltammogram. LSV sweep is usually unidirectional across the electroactive species. LSV gives useful information on the kinetics of electrode reactions, including information about the existing redox active species, diffusion coefficients, and reaction processes. As the potential is swept, current fluctuations are noticed as a result of the electrode reaction. Upon performing an LSV, a few parameters that can be determined are:

- Peak potentials: The potentials at which oxidation or reduction peaks occur indicating the presence of redox-active species.
- Peak currents: The magnitude of the current at the peaks, which is proportional to the concentration of electroactive species at the interface.
- Scan rate effects: How the sweep rate affects the shape and location of peaks in a voltammogram.
- Diffusion coefficients: Voltammetric data can be used to determine the diffusion of species to and from an electrode surface.

In Chapter 3, LSV of the Cu_xO-C is performed in the presence of CO_2 and Ar-saturated electrolytes to study the behaviour of the electrocatalysts at different potentials and is further explained.

2.4.3 Cyclic Voltammetry (CV)

Cyclic Voltammetry is the commonly used potentiodynamic technique to obtain quantitative information about the electrochemical reactions. CV is generally used to investigate the oxidation and reduction processes in electron transfer reactions like catalysis and also offers information on the redox potentials of the electrocatalytic species [15]. In this method, a WE is immersed in an electrolyte solution containing the analyte of interest, along with a RE and a CE. A voltage is applied to the working electrode, causing a current to flow. The current is then measured as a function of the applied voltage, typically by sweeping the voltage linearly with time. CV is usually the measure of electrode currents with the potential ramp versus time in cyclic phases in forward and reverse scans thereby evaluating the reversibility of a redox reaction. Key information about the electrochemical behaviour of the analyte shall be obtained by analyzing the resulting cyclic voltammogram—which is a plot of current vs applied voltage including the identification of redox processes, determination of redox potentials, estimation of electron transfer kinetics, and assessment of chemical reaction mechanisms. The general representation of a CV is shown in Figure 2.17.

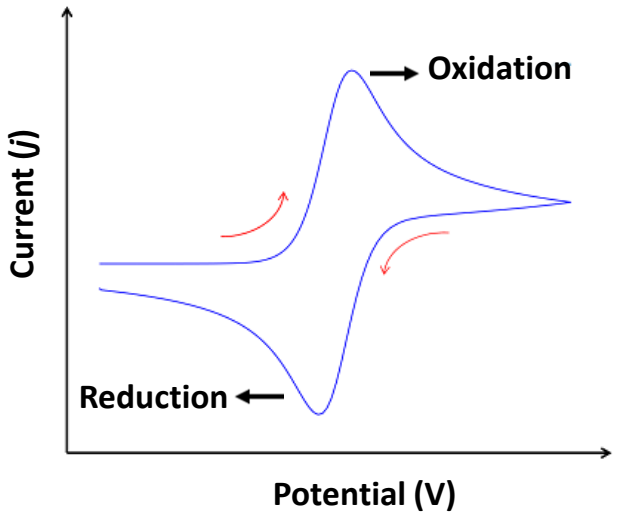


Figure 2.17 Basic CV profile (Cyclic Voltammogram) showing redox curves.

Electrochemical Active Surface Area (ECSA)

The Electrochemical Active Surface Area denotes the area on the electrode surface where electrochemical reactions occur. ECSA plays a crucial role in determining the performance of electrochemical processes and factors like surface roughness, porosity, and the presence of active sites can influence it. In electrocatalytic reactions, the accurate determination of the ECSA is very critical in estimating the surface area normalized intrinsic catalytic activity of the electrocatalysts. ECSA, in general, is estimated by measuring the double-layer capacitance (C_{DL}) of the electrode-electrolyte interface at the non-faradaic potential window by conducting CV measurements. In this thesis work, CVs were recorded at different scan rates (10, 25, 50 and 100 mV/s) with a minimum of nine cycles in the non-Faradaic region in a standard three-electrode voltammetric cell. The electrodes were usually 1 cm^2 (1 cm × 1 cm) of exposed geometrical area and directly used as WE placed over a titanium foil acting as a current collector; a platinum mesh was used as the CE, while a 3.5 M KCl Ag/AgCl RE was placed between both WE and CE. From the obtained current vs potential plot, the difference in currents between the forward and reverse scans, representing the redox reactions in each CV was calculated with respect to the applied non-faradaic potential window. The plotted difference between the anodic and cathodic peak currents in the middle of the potential window *vs* the scan rate defined for each specific CV enables the estimation of the C_{DL} from the slope obtained from the linear regression for each electrode evaluated [16]. From the obtained double-layer charging currents, ECSA can be derived by comparing it to that of a copper metal [17]. In Chapters 3 and 4, C_{DL} was calculated for the Cu_xO-C and the modulated PTFE/Cu GDEs and further discussed showing the differences in each analyzed sample.

2.4.4 Chronoamperometry (CA)

Chronoamperometry is the electrochemical technique where the potential applied between WE and RE is fixed and the current flowing between the WE and CE is measured *vs* time obtaining information about the electrochemical reaction kinetics. The potentials can be altered step-wise to monitor the current trends with an immediate change in the applied potential. Upon a potential step, the electrochemically active species will diffuse towards the working electrode leading to fluctuations in the currents observed. The current-time response reflects the changes in the concentration gradient in the electrode vicinity.

CA is one of the most commonly used techniques in ECO_2R to study the electrode process mechanism during CO_2 electrolysis due to its relative ease of implementation and analysis. Ideally, a constant potential is set between the WE and RE and the current is recorded indicating the potentiostatic approach. In Chapter 3, the potentiostatic approach is followed for the ECO_2R and the trends in currents with each sample were monitored at each applied potential over the prescribed time.

2.4.4 Chronopotentiometry (CP)

Chronopotentiometry is the galvanostatic electrochemical technique in which the current at the electrode is set constant for the prescribed time and the potential is monitored over time at the WE relative to the RE. This method enables to read the OCP/OCV when there is no current passing the electrochemical cell. CP is a very similar method to CA where potential steps are replaced by current steps and is used to study electrode kinetics, reaction mechanisms and electrochemical processes at a solid-liquid interface with time. Typically, the redox-active species diffuse to the surface of the working electrode thereby balancing the applied current, until the diffusion-limited concentration of redox species reaches zero at the electrode surface.

CP is also the most commonly used technique in ECO_2R to study the electrochemical reactions happening at the electrode vicinity. CP also aids in studying the reaction kinetics and understanding the reaction mechanisms. In Chapters 4 and 5, CP is used to perform the ECO_2R and to monitor the potential trends with each electrode measured.

2.4.4 Electrochemical Impedance Spectroscopy (EIS)

Electrochemical Impedance Spectroscopy is an effective and non-destructive electrochemical technique that offers information on the kinetic and mechanistic data of the electrochemical processes involving electrode-electrolyte interfaces. EIS is used to measure the impedance response of the system to the applied AC potential at different frequencies indicating the frequency-dependent impedance. By applying the AC potential to the system, ions tend to move back and forth leading to impedance fluctuations. In general, charge transfer mechanisms are noticeable at the lower frequencies while the ohmic resistance is at a high frequency.

Although EIS is one of the most complicated yet important electroanalytical techniques giving valuable information on parameters like double-layer capacitance, diffusion coefficients and charge-transfer resistance during electrochemical processes, in this thesis work EIS was mainly used to measure the serial resistance of the WE at a high frequency. . During an electrochemical process, the applied potential is often affected by the internal resistance offered by the electrode and electrolyte interfaces. This resistance-driven potential loss can be compensated from the actual potential thereby performing the *iR* compensation. The *iR* compensation aids in identifying the loss from the resistance within the cell thereby finding out the actual potentials of the desired electrochemical processes from the applied potentials. In Chapter 4 of this thesis, EIS is performed to estimate the serial resistance of the PTFE/Cu GDEs followed by quantifying the *iR* compensation enhancing the accuracy of the measured potentials using equation 2.5.

$$V_{actual} = V_{applied} - iR \qquad 2.5$$

Based on the *iR* compensation and obtained FEs, ECO_2R kinetic modelling for the reactions happening at the cathode was carried out for comparison.

A brief note to the reader: The kinetic modelling for the ECO_2R and HER reactions was carried out in collaboration with Dr. Ignacio Tudela from the University of Edinburgh.

Modelling of Electrochemical CO_2 reduction kinetics

In Chapter 4 of this thesis, a simplified kinetic model is formulated for both ECO_2R and HER reactions at the cathode to qualitatively compare the selectivity and performance of PTFE/Cu GDEs.

Based on the products generated during the experiments, the following reactions were assumed and written with the specified standard reduction potential *vs* RHE ($E°_{i_{RHE}}$) [18] without any further mechanistic considerations to simplify the approach:

1. $CO_2 + 2\ H^+ + 2\ e^- \rightarrow HCOOH_{(aq)}$ $E°_{HCOOH\ RHE} = -0.12$ V
2. $CO_2 + 2\ H^+ + 2\ e^- \rightarrow CO_{(g)} + H_2O$ $E°_{CO\ RHE} = -0.10$ V
3. $CO_2 + 8\ H^+ + 8\ e^- \rightarrow CH_{4(g)} + 2\ H_2O$ $E°_{CH_4\ RHE} = 0.17$ V
4. $2\ CO_2 + 8\ H^+ + 8\ e^- \rightarrow CH_3COOH_{(aq)}$ $E°_{CH_3COOH\ RHE} = 0.11$ V
5. $2\ CO_2 + 12\ H^+ + 12\ e^- \rightarrow C_2H_5OH_{(aq)} + 3\ H_2O$ $E°_{C_2H_5OH\ RHE} = 0.09$ V
6. $2\ CO_2 + 12\ H^+ + 12\ e^- \rightarrow C_2H_{4(g)} + 4\ H_2O$ $E°_{C_2H_4\ RHE} = 0.08$ V
7. $3\ CO_2 + 18\ H^+ + 18\ e^- \rightarrow C_3H_7OH_{(aq)} + 4\ H_2O$ $E°_{C_3H_7OH\ RHE} = 0.10$ V
8. $2\ H^+ + 2\ e^- \rightarrow H_2$ $E°_{H_2\ RHE} = 0$ V

In electrochemistry, the relation between the electrode overpotential η_i and the current density i_i for any reaction occurring under full kinetic control can be defined by the Butler-Volmer equation [19] :

$$j_i = j_i^e \left[e^{\frac{\alpha_{A_i} n_i F}{R T} \eta_i} - e^{-\frac{\alpha_{C_i} n_i F}{R T} \eta_i} \right] \quad 2.6$$

where j_i is the partial current density for a given reaction, j_i^e is its exchange current density, α_{A_i} is its anodic charge transfer coefficient, α_{C_i} is its cathodic charge transfer coefficient, n_i is the number of electrons involved in said reaction, F is the Faraday constant, R is the ideal gas constant and T is the temperature. The overpotential is defined as $\eta_i = (E_W - iR_\Omega)_{RHE} - E^e_{i\ RHE}$, where $(E_W - iR_\Omega)_{RHE}$ is the *iR*-corrected working electrode potential and $E^e_{i\ RHE}$ is the equilibrium potential of the specific reaction; both potentials would be referred to as the RHE reference electrode. In addition, due to the challenges associated with the correct estimation of the equilibrium potential of each reaction during the experiments (i.e. application of the Nernst equation incorporating the activity coefficients of reactants and products involved), it was assumed that the value of the equilibrium potential $E^e_{i\ RHE}$ may be close enough to the standard potential $E°_{i_{RHE}}$.

For practical reasons, it was assumed that the sum of symmetry coefficients α_{A_i} and α_{C_i} was equal to n_i for all of the reactions, enabling the definition of α_{A_i} as $n_i - \alpha_{C_i}$. This is only strictly true if the reaction mechanisms of both ECO_2R to different products and HER were literally as defined in reactions 1-8 above, which is not the case (as discussed by Guidelli et al. in the most recent IUPAC Technical Report [20] and Recommendations [21] on the definition of

charge transfer coefficients in electrochemistry, the "simultaneous transfer of more than one electron is highly improbable" in a single step. However, this approach was convenient enough to estimate the values of both α_{C_i} and i_i^e that not only enabled the qualitative comparison of the different GDEs prepared in this study but also facilitated design and engineering calculations for future upscaling of the process. Values of α_{C_i} and i_i^e for reactions 3-8 above were estimated by applying the least squares method to find the best fitting of eq. (2.6) to the experimental data. This was achieved with the Solver tool embedded in MS Excel, where the generalised reduced gradient (GRG) solving method was used. Special attention was paid to the objective function in each calculation, where residuals were manually weighed in line with recent suggestions made on topic [22] to minimise perpendicular offsets as well as the vertical offsets accounted for in the least squares method [23].

2.5 CO_2 Electrolyzer Setup and Product Quantification

In the last section of this chapter, the electrolyzer setup used in this thesis is discussed in detail with all the components and factors associated with or influenced by the electrochemical cell and ECO_2R. The analytical techniques used in this thesis work for product identification are mentioned in detail along with the quantification of ECO_2R products at a glance.

2.5.1 CO_2 electrolyzer

Any CO_2 electrolyzer has to be properly treated before the actual operation to remove the deposited salts before each experiment. Various electrochemical cells with several modifications and improvements have been reported in the literature already. The most commonly reported one is the H-type cell. A typical H-type cell usually consists of only two compartments, cathodic and anodic which are separated by an ion exchange membrane like Nafion. The WE and RE are in the cathode compartment with the reactant gas directly bubbled into the electrolyte through the inlet and outlet for ECO_2R products while the CE is in the anodic compartment with or without any gas being monitored. In this thesis work, an H-type cell was only used in the initial stages to understand the mechanism of the ECO_2R.

A flow-type electrolyzer is used throughout the thesis work. A commercial flow-type electrolyzer (filter-press electrochemical flow cell), a Micro Flow Cell from Electrocell A/S is used which was adapted from previous works [24] of the group and modified according to the requirements.

Electrochemical flow electrolyzer and components

The electrochemical flow electrolyzer consists of three compartments, namely gas, catholyte and anolyte as shown in Figure 2.18. The anolyte compartment holds the anode whereas the catholyte compartment includes a leak-free 3.5 M KCl Ag/AgCl reference electrode. Both anolyte and catholyte compartments were separated by an ion exchange membrane (anion exchange membrane). The gas compartment holds the cathode (the electrode for the ECO_2R) which is embedded in a titanium current collector. The exposed geometrical area of the cathode was limited to 5-10 cm^2 depending on the target experiment and all the components were separated by EPDM (Ethylene Propylene Diene Monomer) gaskets to prevent any leakage of both electrolytes and reactant/product gas. In the present thesis, three types of

anion exchange membranes were used. In Chapter 3, Fumasep FAB-PK-130 was used while in Chapter 4 Fumasep FAA-PK-130 with lesser thickness was used. In Chapter 5, FAA-PE-50 with a further lower thickness was mounted as the ion exchange membranes.

In Chapter 3, a titanium current collector holding the WE based on Cu_xO-C GDE acts as the cathode and is coupled with a commercial DSA as the anode. In Chapters 4 and 5, a titanium current collector holding the Ni foam acts as the anode in the anodic compartment and a similar titanium current collector holds the respective modified GDEs as per the prescribed studies.

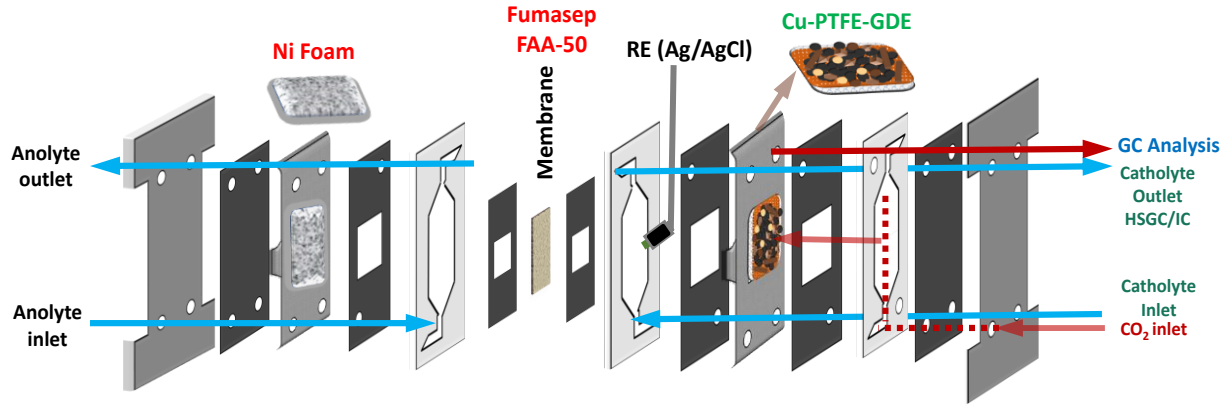


Figure 2.18 Experimental setup of Flow electrolyzer for ECO_2R showing Ni foam as anode and PTFE/Cu-GDE as the cathode. The setup is the actual representation used in Chapter 4.

Flow-by and flow-through operation mode of CO_2 Electrolyzer

In the early assessment, the CO_2 electrolyzer was operated in two different modes: flow-through and flow-by. Initially, a flow-through mode was employed where the CO_2 gas is forced to pass through the GDE matrix and the outlet gas is mixed with the catholyte as shown in Figure 2.19B.

Additionally, the flow-by configuration was also evaluated with CO_2 entering the cell from the top inlet to the gas compartment and flowing by the GDE as seen in Figure 2.19A. In this mode, the diffused CO_2 passes through the MPL of GDE interacting at the liquid-solid (electrolyte-catalyst) interface and thus leaves the system together with the gas products at the bottom of the cell without mixing with the catholyte.

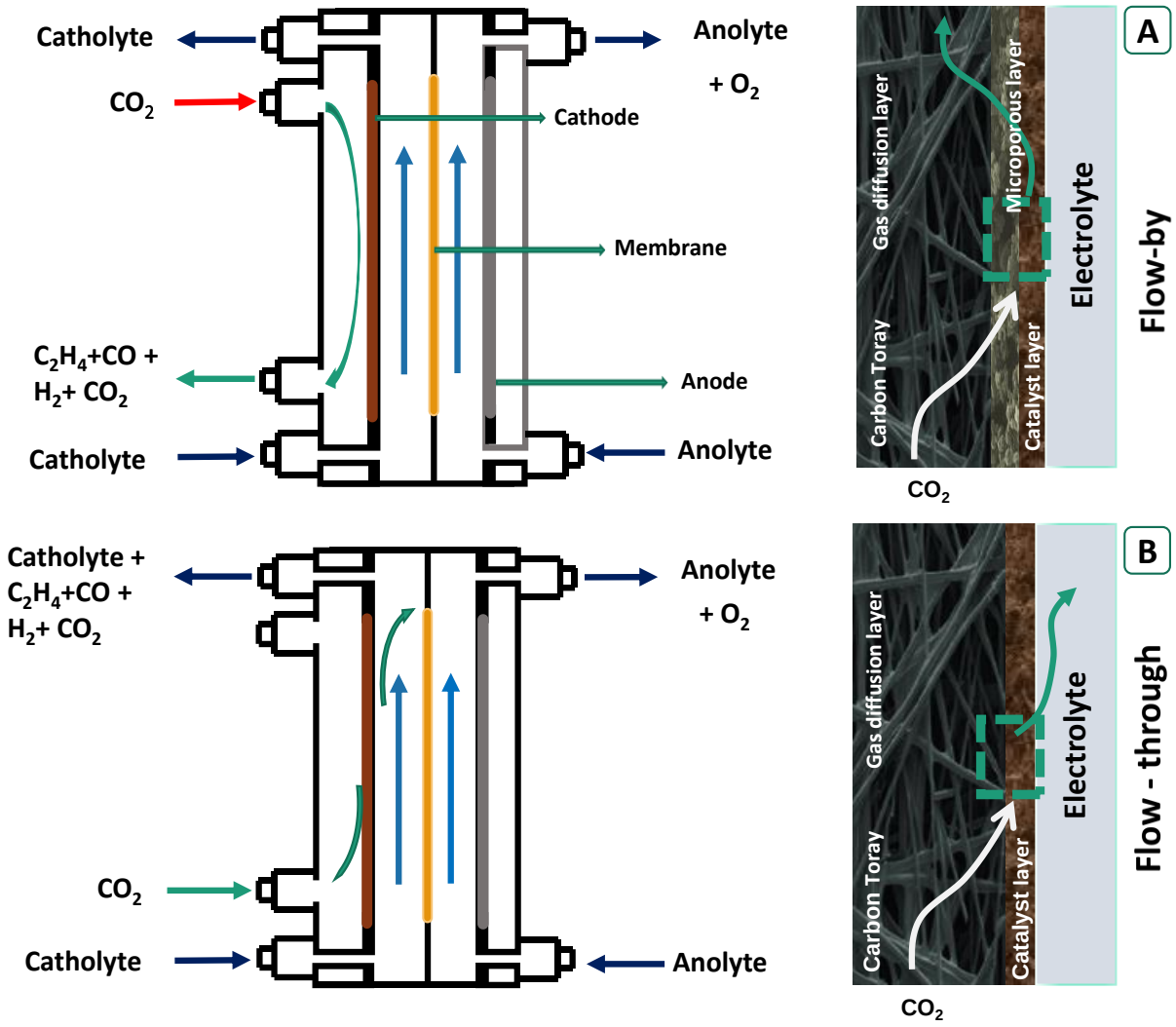


Figure 2.19 Flow-by **(A)** and Flow-through **(B)** operation mode of CO_2 electrolyzer

In general, flow-by mode has been considered to be more suitable for industrial applications than flow-through configuration, based on certain advantages such as lower ohmic drops and higher stability attained by controlled perspiration (provided flooding is avoided) and decreased salt formation which was also discussed in previous works [25]. Chapter 3 discusses the results from both modes of operation for a more detailed understanding of the benefits of flow-by mode of operating the electrolyzer. Nevertheless, in Chapters 4 and 5, ECO_2R is performed only in the flow-by mode of operation where the gaseous and liquid products are separated.

2.5.3 Optimizing the Flow rate of CO_2 gas and electrolyte

Flow rate of CO_2

Certain flow rates of CO_2 gas were chosen such as 5, 10, 20 and 30 sccm. The cell architecture and the GDE play a crucial role in selecting the appropriate flow rate. The feed flow of CO_2 should ensure sufficient availability at the electrode surface. To optimize the CO_2 flow initially a constant flow rate was supplied to the electrolyzer. Three different flow rates, 10, 20 and 30 $mL{\cdot}min^{-1}$ of feed CO_2 were supplied and investigated to understand the optimum feed flow over 90 min. In Chapter 3, the influence of the flow rate of CO_2 in altering product selectivity is discussed with FE for each product.

Flow rate of Electrolyte

The optimization of the flow rate of electrolytes can improve the efficiency of ECO_2R as too-high and too-low flow rates can hinder the proposed reaction. Also, the local pH plays a crucial role in tuning the selectivity of ECO_2R product distribution. Efforts were put into optimizing the required flow rate by investigating three different electrolyte flow rates of 10, 20 and $30mL.min^{-1}$ and the obtained results indicated no major differences in product selectivity.

In all the experiments of this thesis, 50 mL of catholyte and anolyte were taken and the electrolytes were continuously recirculated using a peristaltic pump with an optimised flow rate of 15-20 $mL{\cdot}min^{-1}$ for the prescribed experiments. Fresh catholyte and anolyte were used for every experiment conducted at each applied current density.

2.5.4 Electrochemical CO_2 reduction experiments

ECO_2R experiments are conducted with a Bio-Logic SP-50 potentiostat and a standard bench power supply device whenever necessary. ECO_2R experiments were performed by adopting both potentiostatic (Chapter 3) and galvanostatic approaches (Chapters 4 and 5) respectively. At each applied potential or current, the electrolysis is performed for at least one hour. To minimize the errors in data quantification, the electrolysis shall start once the product gas stream measured in the outlet of the gas compartment reaches a steady state. The potentiostat operating records the cathode potential referred to Ag/AgCl reference electrode during the experiments, which was then converted into an electrode potential as mentioned

in equation 2.1. In Chapter 3, a potentiostatic approach is employed to perform the ECO_2R while in Chapters 4 and 5, the galvanostatic approach is used.

2.5.5 Product quantification

ECO_2R generates several products based on the electrocatalysts primarily and several other reaction parameters along with the competitive HER. In this sub-section, a brief description of the analytical instruments that were used to measure the ECO_2R products is given along with their quantification.

Gas product analysis and quantification

During the electrolysis, the product stream is directly connected to the inlet of the Gas Chromatograph (GC) and automatically injected to quantify the products. As part of this thesis, initially, a Shimadzu GC 2010 system was used which is equipped with both the flame ionization detector (FID) and thermal conductivity detectors (TCD) with the HP-PLOT column and He as the carrier gas. Later, the GC equipment used was upgraded with a Shimadzu GC-2030 equipped with a Carboxen®-1010 PLOT column and a barrier discharge ionization detector (BID) to detect and quantify all the gas products generated during the experiments. In all the experiments of ECO_2R, at each applied potential or current, electrolysis was performed for at least 60 min and the gas products were analysed and quantified at 30-minute intervals. The respective gas chromatograms and the calibration are shown in the Appendix at the end of the thesis.

The Faradaic efficiency for each specific gas product was determined using Faraday's Laws of electrolysis under the operating conditions as a function of the applied current, the gas product ratios measured and quantified by the GC system and the outlet gas flow from the gas compartment using the following equation:

$$FE_i\ \% = 100\left(\frac{n_i\, v\, M_i\, F}{J_{total}}\right) \qquad 2.7$$

where n_i is the number of electrons required to form each product (e.g. 12 e^- to produce a single molecule of C_2H_4 from two molecules of CO_2), v is the outlet flow of the gas, M_i is the

number of moles of the specific gas product formed, F is the Faraday's constant and J_{total} is the total applied current.

In addition, the half-cell energy efficiency (EE) for ethylene was calculated by the following equation:

$$EE\ \% = \frac{\left(E^{e}_{C_2H_4\,RHE} - 1.23\right) FE_{C_2H_4}}{\left(E_{W\,RHE} - 1.23\right)} \cdot 100 \qquad 2.8$$

where $E^{e}_{C_2H_4\,RHE}$ is the equilibrium potential for ECO_2R to ethylene referred to RHE reference electrode, $E_{W\,RHE}$ is again the working electrode potential vs RHE and $FE_{C_2H_4}$ is the faradaic efficiency for ECO_2R to ethylene.

Liquid product quantification

Although, the liquid products generated during the ECO_2R studies in this thesis work are not the major products, still quantifying the liquid products is critical in understanding the patterns in product selectivity and distribution.

In this thesis, initially, the in-house available GC used to detect the gaseous products was later used to analyse and quantify the liquid products. The GC was equipped with a Head Space (HS-GC) accessory with an autosampler and was used to detect and quantify the alcohol-based ECO_2R products.

Additionally, high-performance liquid chromatography (HPLC), Agilent 1200 series running with a Rezex™ ROA-Organic Acid H^+ (8%) column (LC column 300 x 7.8 mm), equipped with both Refractive Index (RID) and Diode Array (DAD) detectors operating at 210 nm was also used to detect the liquid products. The mobile phase consists of a 0.005 N sulfuric acid solution with a flow rate of 0.45 mL·min^{-1} and a temperature of 40 °C.

Based on the ionic nature of some products, ion chromatography (IC) is used to detect and quantify both the acetate and formates. A Thermo-Fisher Dionex 1100 ICS, equipped with a Dionex Ion Pac AS-22 anion exchange column and a chemical suppressor (ASR-ultra 4mm) was used. In general, the mobile phase (eluent) was comprised of 4.5 mM sodium carbonate (Na_2CO_3) and 1.4 mM sodium hydrogen carbonate ($NaHCO_3$), with a flow rate of 1.5 mL·min^{-1} was run through the column.

In all experiments, catholyte samples were collected every 60 min and kept refrigerated until samples were prepared for the analysis. For HS-GC analysis, 1mL aliquots were taken and placed in auto-sampler vials and the products were quantified using the calibration factor. For IC, 0.5 mL aliquots were diluted 10 times (up to 5mL) with DI water and injected using the auto-sampler. The eluent for the IC consisted of an aqueous solution containing 4.5 mM Na_2CO_3 and 1.4 mM $NaHCO_3$ with a flow rate of 1.5 mL min^{-1}. For HPLC, 1mL aliquots were taken and placed in auto-sampler vials and the products were quantified using the calibration.

FE values for each liquid product were again estimated using Faraday's laws of Electrolysis. In this case, the charge passed between catholyte sampling was estimated based on the quantified product ratios obtained from HS-GC and IC analysis accounting for the total volume of catholyte at each time:

$$FE_i\ \% = \left(\frac{n_i\ V\ M_i\ F}{Q_{total}}\right) \cdot 100 \qquad 2.9$$

where n_i is again the number of electrons required to form each product (*e.g.* 12 e^- to produce a single molecule of ethanol from two molecules of CO_2), V is the total volume of electrolyte, M_i is again the number of moles of the specific liquid product formed; F is again Faraday's constant, and Q_{total} is the total charge applied for each applied current over 60 mins time intervals.

Though sophisticated analytical instruments are used to detect liquid products, the quantification remains similar.

2.6 References.

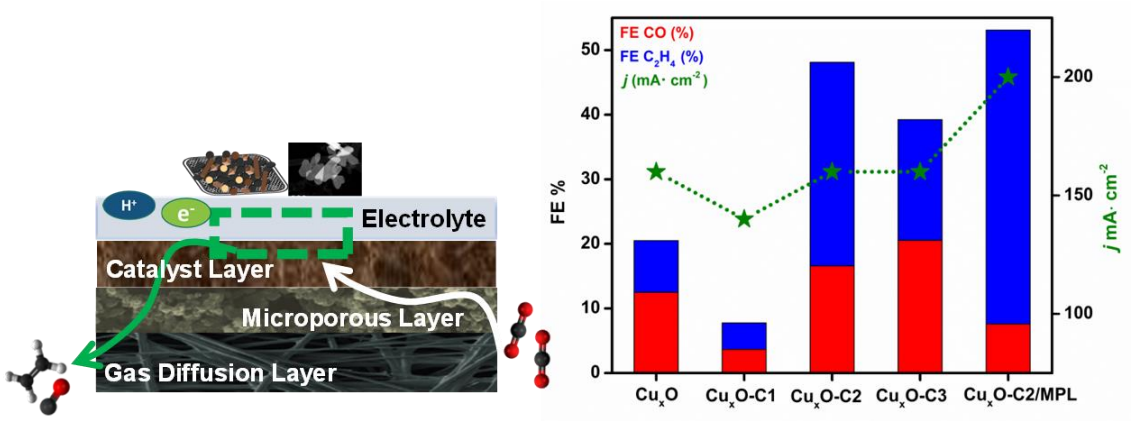
1. A. Rabenau, *Angew. Chem. Int. Ed. Engl.* **1985**, 24, 1026.
2. Z. Zhang, L. Sun, Z. Wu, Y. Liu, S. Li, *New J. Chem.* **2020**, 44, 6420.
3. T. Zheng, K. Jiang, N. Ta, Y. Hu, J. Zeng, J. Liu, H. Wang, *Joule* **2019**, 3, 265.
4. A. A. Bunaciu, E. G. Udriştioiu, H. Y. Aboul-Enein, *Crit. Rev. Anal. Chem.* **2015**, 45, 289.
5. W. M. Doyle, Principles and Applications of Fourier Transform Infra-red (FTIR) Process Analysis **2017**.
6. K. S. W. Sing, *Pure Appl. Chem*. **1985**, 57, 603.
7. W. Zhou, R. Apkarian, Z. L. Wang, D. Joy, *Springer* **2007**, 1.
8. J. M. Thomas, P. A. Midgley, *Chem. Commun.* **2004**, 11, 1253.
9. R. F. Egerton, *Springer Science & Business Media*, **2011**.
10. D. Briggs, M. Seah, Wiley, **1996**, 1, 607.
11. D. A. King, *Surf. Sci.* **1975**, *47*, 384.
12. T. Huhtamäki, X. Tian, J. T. Korhonen, R. H. Ras, *Nat. Protoc.* **2018**, 13, 1521.
13. C. G. Zoski, J. Leddy, A. J. Bard, Student Solutions Manual (2nd ed.) John Wiley: New York, **2002**.
14. T. M. Nahir, R. A. Clark, E.F. Bowden, *Anal. Chem.* **1994**, 66, 2595.
15. N. Elgrishi, K. J. Rountree, B. D. McCarthy, E. S. Rountree, T. T. Eisenhart, J. L. Dempsey, *J. Chem. Educ.* **2018**, 95, 197.
16. O. Gharbi, M. T. T. Tran, B. Tribollet, M. Turmine, V. Vivier, *Electrochim. Acta* **2020**, 343, 136109.
17. S. Trasatti, O. A. Petrii, *J. Electrochem. Chem.* **1992**, 327, 353.
18. Z. Di, Y. Qi, X. Yu, F. Hu, *Catalysts* **2022**, 12, 1582.
19. D. Pletcher, F. C. Walsh, Industrial Electrochemistry (2nd ed.), Springer Dordrecht, **1993**.
20. R. Guidelli, R. G. Compton, J. M. Feliu, E. Gileadi, J. Lipkowski, W. Schmickler, S. Trasatti, *Pure Appl. Chem.* **2014**, 86, 245.
21. R. Guidelli, R. G. Compton, J. M. Feliu, E. Gileadi, J. Lipkowski, W. Schmickler, S. Trasatti, *Pure Appl. Chem.* **2014**, 86, 259.
22. K. R. M. Corpus, J. C. Bui, A. M. Limaye, L. M. Pant, K. Manthiram, A. Z. Weber, A. T. Bell, *Joule* **2023**, 7, 1289.

23. J. H. Sampaio Jr, *Appl. Math. Comput.* **2006**, 176, 91.

24. F. Urbain, P. Tang, N.M. Carretero, T. Andreu, J. Arbiol, J.R. Morante, *ACS Appl. Mater. Interfaces* **2018**, 10, 43650.

Chapter 3

Carbon-Supported Oxide-Derived Copper Heterostructures for the Electroconversion of CO_2



The contents of this chapter have been published in ChemSusChem as

Hydrothermal Fabrication of Carbon-Supported Oxide-Derived Copper Heterostructures: A Robust Catalyst System for Enhanced Electro-Reduction of CO_2 to C_2H_4

V. S. R. K. Tandava, M. C. Spadaro, J. Arbiol, S. Murcia-López, J. R. Morante, ChemSusChem 2023, 16, e202300344.

The contents of the published article were modified according to the Thesis structure by moving certain aspects of the general introduction and experimental section to the respective Chapter 1 and Chapter 2. Additional figures from the Supporting information were used in this text.

3.1 Abstract

Anthropogenic CO_2 can be converted to alternative fuels and value-added products by electrocatalytic routes. Copper-based catalysts are found to be the star materials for obtaining longer-chain carbon compounds beyond $2e^-$ products. Herein, we report a facile hydrothermal fabrication of a highly robust electrocatalyst: in-situ grown heterostructures of plate-like CuO−Cu_2O on carbon black. Simultaneous synthesis of copper-carbon catalysts with varied amounts of copper was conducted to determine the optimum blend. It is observed that the optimum ratio and structure have aided in achieving the state-of-the-art faradaic efficiency for ethylene > 45 % at −1.6 V vs. RHE at industrially relevant high current densities over 160 to 200 mA · cm^{-2}. It is understood that the in-situ modification of CuO to Cu_2O at the onset potentials during the electrolysis is the driving force for the highly selective conversion of CO_2 to ethylene through the *CO intermediates followed by C−C coupling. The excellent distribution of Cu-based platelets on the carbon structure enables rapid electron transfer and enhanced catalytic efficiency. It is inferred that choosing the right composition of the catalyst by tuning the catalyst layer over the gas diffusion electrode can substantially affect the product selectivity and promote reaching the potential industrial scale.

3.2 Introduction

The background and general introduction including the literature review of this work have been mentioned and discussed in Chapter 1.

As discussed in the introductory chapter, copper and copper-based materials are found to be exceptionally active and effective in the selective conversion of CO_2 to greater than 2 e^- products by possessing adequate adsorption energy towards *CO intermediate [1, 2] and have shown a unique ability in aiding C−C coupling to C_2 and C_{2+} products. Notably, oxide-derived Cu heterostructures have significantly affected the CO dimerization through the C−C coupling mechanism leading to C_2H_4 selectivity [3]. Also, the addition of oxides on Cu sites has been reported to alter the adsorption behaviour of the reaction intermediates, thus tuning the reduction mechanism[4]. However, oxide-derived Cu catalysts are prone to be reduced to metallic copper (Cu^0) when working under reduction potentials or currents as the ones required to drive the ECO_2R. Once they are reduced to metallic copper, it is highly likely that

the catalysts become inactive or decrease their ability towards C–C coupling, thereby hampering the C_2 product formation in a short span[5], and even favouring the competitive HER. Therefore, the rational design of highly stable oxide-derived copper-based catalysts is required to achieve higher CO_2 conversions operating at industrially relevant current densities and with greater stability.

In the present chapter, the study on Cu/C-based electrocatalysts (Cu_xO-C) for the efficient electro-reduction of CO_2 to ethylene operating at high current densities is reported. A facile hydrothermal route to design a robust electrocatalyst having C-Black supported oxide-derived copper heterostructures is discussed. Initial chemical reduction of a copper precursor followed by in-situ growth of CuO and Cu_2O heterostructures over C-Black was obtained. Different nominal Cu/C ratios were synthesized to determine the optimum blend and to attain the state-of-the-art conversion to ethylene at industrially relevant high current densities. The as-synthesized electrocatalysts were deposited on GDEs and evaluated in flow electrolyzers. We elucidate the high selectivity towards ethylene as a factor of in-situ reduction of the derived Cu_xO heterostructures to Cu_2O, along with the blending with C-Black that helps to increase the conductivity and enhance the CO_2 distribution. It is also understood that choosing the right composition of the catalyst layer over the GDE can fetch the overall CO_2 reduction operating at high current densities for long hours and can make an industrially viable alternative.

3.3 Objectives

Pertaining to the concerns mentioned earlier in the introduction, the major objectives of the present study are

- To design and synthesize a robust electrocatalyst which has high catalytic activity, selectivity and overall stability. Therefore, as an alternative to the conventional protocols where the catalyst ink is fabricated by the physical addition of Cu/Cu_xO particles to carbon, this study aims to in-situ synthesis of the carbon-supported oxide-derived copper heterostructures, a highly robust electrocatalyst system.
- To target a significant influence on the enhanced catalytic efficiency as a result of the increased number of Cu active sites in contact with the C-Black facilitating the rapid electron transfer mechanism of the as-synthesized Cu_xO-C heterostructures.

3.4 Highlights

To meet the stated objectives of having an in-situ grown robust electrocatalyst, thorough investigations were conducted, and successful observations were highlighted.

- An easy and scalable in-situ synthesis of Cu_xO-C heterostructures was synthesized and effectively tested for CO_2 conversion to ethylene.
- In-situ evolution of the active sites from CuO to Cu_2O at lower polarization conditions are found to be the active catalytic sites.
- Evaluation of flow-by and flow-through modes of operation to evaluate the best fit.
- The robust electrocatalyst material is proven to have achieved state-of-the-art faradaic efficiency for ethylene i.e., > 45 % at a maximum current density of 200 $mA \cdot cm^{-2}$.

3.5 Experimental Methods

A note to the reader

The experimental methods and materials from this chapter have been discussed in detail in Chapter 2, *Experimental Materials, Methods, and Systems involved in Electrochemical CO_2 Reduction.* A detailed explanation concerning the synthesis of the electrocatalysts, technique for GDE fabrication, general characterization techniques and experimental setup involving the CO_2 flow electrolyzer was also included in Chapter 2. A brief description of the synthesis and fabrication of the GDE is mentioned to enable the reader to follow this chapter thoroughly.

3.5.1 Synthesis of the electrocatalyst materials

In a typical synthesis, C-Black was sonicated to widely disperse following the addition of copper acetate precursor. The mixture solution was heated to 60 ^{0}C before transferring to the hydrothermal autoclave which was maintained at 160 ^{0}C for 12 h. A similar method is followed for bare Cu_xO without having the C-Black. For a comparative study, we also synthesized different combinations of Cu/C ratios by altering the copper content to understand the best blend for the in-situ growth of Cu heterostructures. By keeping the amount of C-Black (40 mg) constant, the quantity of Cu precursor was varied in order to obtain samples with different Cu_xO-C ratios: Cu_xO-C1 (100 mg of Cu precursor), Cu_xO-C2 (200 mg of Cu precursor) and Cu_xO-C3 (300 mg of Cu precursor). The conventional physical addition of C-Black to the as-

synthesized bare Cu_xO catalyst heterostructures was also prepared during the catalyst ink formulations to understand the advantage of the direct in-situ growth of oxide-derived copper heterostructures over the C-Black and their role in facilitating the rapid electron transfer mechanism.

3.5.2 Electrode Fabrication

Catalyst inks were prepared by adding 20 mg of catalyst to 2 mL of 2-propanol and 100 µL of 5 wt. % Nafion. The mixtures were sonicated over an hour and directly deposited via drop-casting on the GDEs (Toray Carbon Paper 060 with and without MPL) covering the whole surface with uniform loading of the catalyst ink. All the electrodes prepared have a geometric area of 2*2.5 cm^2 exposed to the electrolyte and CO_2 interaction. The final loading of the electrocatalyst on the electrode, Toray Carbon paper is measured by weighing the electrode before and after the drop-casting of the catalyst ink. The final loading of the catalyst (Cu_xO-C) on the GDE is found to be around 2.5 ± 0.2 $mg \cdot cm^{-2}$. A commercial DSA (dimensionally stable anode) was directly used as the anode.

3.6 Results and Discussion

3.6.1 Structural characterization of the electrocatalyst materials

Initial compositional and structural properties were examined using XRD analysis of the as-prepared samples: Bare Cu_xO, Cu_xO-C1, Cu_xO-C2 and Cu_xO-C3 heterostructures, along with the C-Black. As shown in Figure 3.1, the standard Cu_xO-C2 is deemed to have the CuO tenorite monoclinic phase *(JCPDS 048-1548)* at 35.5°, 38.7°, 38.9°, 48.7°, 53.3° and 66.2°corresponding to (-111), (111), (200), (-202), (020), (-311) planes. The peaks located at 36.4°, 42.3°, 61.4° and 73.5° correspond to (111), (200), (220) and (311) planes of Cu_2O cuprite cubic phases respectively *(JCPDS 005-0667)*. On the other hand, samples of Bare Cu_xO, Cu_xO-C1, and Cu_xO-C3 were analyzed under the same conditions. The presence of metallic copper *(JCPDS 004-0836)* in the bare Cu_xO sample (prepared without any addition of C-Black) along with dominant CuO and Cu_2O phases are seen. The sample Cu_xO-C1 revealed the sole presence of CuO having low copper content, and the Cu_xO-C3 seemed to be very coherent with Cu_xO-C2 but with a higher content of Cu_2O along with CuO. Table 3.1 shows the quantitative comparison of CuO, Cu_2O and metallic Cu, estimated from the XRD of all the blends. As seen, CuO content in the Cu_xO-C samples decreases inversely with the initial ratio of Cu precursor

to C-Black, while the opposite occurs with the Cu_2O phase. The presence of metallic Cu is only observed in the bare Cu_xO sample, in agreement with having more reduced species (Cu, Cu_2O) in the materials with lower C-black content. This suggests that copper precursor is more easily reduced in the absence (or in the synthesis with lower content) of carbon.

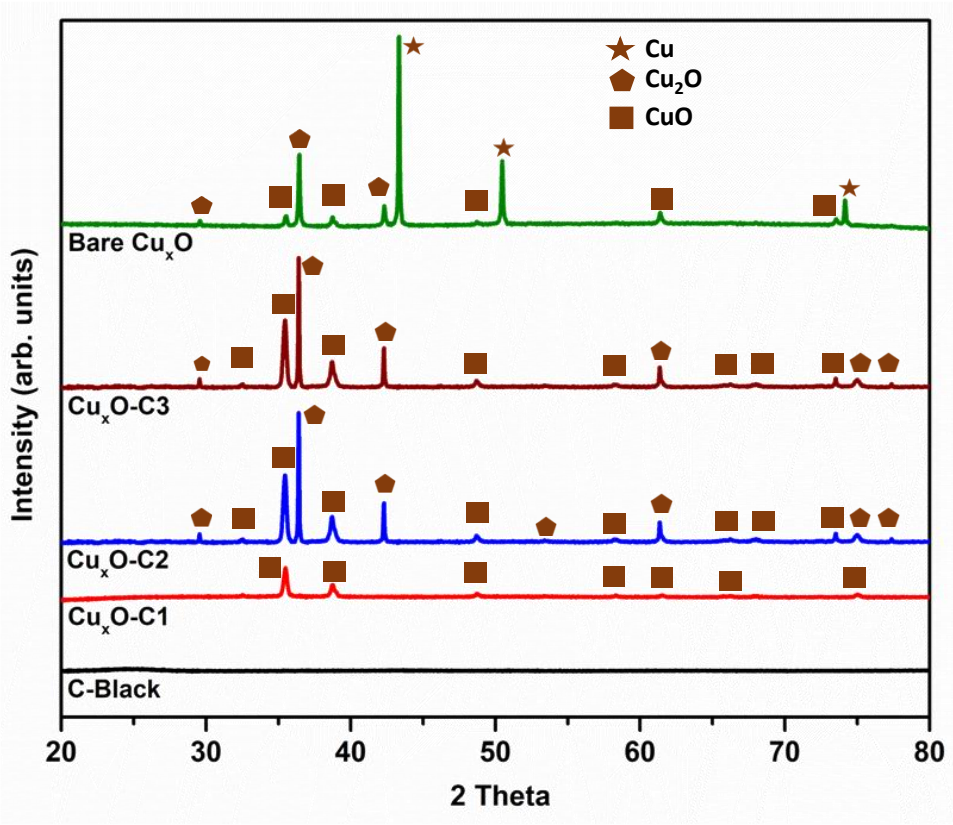


Figure 3.1 XRD of the as-prepared Cu_xO-C heterostructures.

Table 3.1 Quantification of CuO, Cu_2O and Cu from the XRD of all the compared blends.

Sample	Cu_xO-C1			Cu_xO-C2			Cu_xO-C3			Bare Cu_xO		
Cu phase (%)	Cu	Cu_2O	CuO	Cu	Cu_2O	CuO	Cu	Cu_2O	CuO	Cu	Cu_2O	CuO
As Prepared	0	0	100	0	25	75	0	64	36	11	44	45
Post-Electrolysis	0	100	0	0	100	0	0	100	0	13	87	0

The nitrogen adsorption-desorption measurements were performed to assess any changes in the surface area of copper heterostructures as a result of the incorporated C-Black. The surface area was calculated using BET analysis and the resultant pore size distributions were analyzed. The BET adsorption plots and linear isotherms with the corresponding pore size distributions shown in Figure 3.2 (a, b) clearly depict a type III isotherm. The relative surface area of Cu_xO-C2 is around 57.3 $m^2 \cdot g^{-1}$ whereas the one of the bare Cu_xO is only around 6.3 $m^2 \cdot g^{-1}$ showing a 9-fold increase in the relative surface area. Thus, this analysis in turn proves that the direct growth of supported copper on carbon black leads to heterostructures with higher surface area and pore volumes with respect to Cu_xO particles. This increased area and porosity might facilitate the diffusion of active species (i.e., CO_2 and ions).

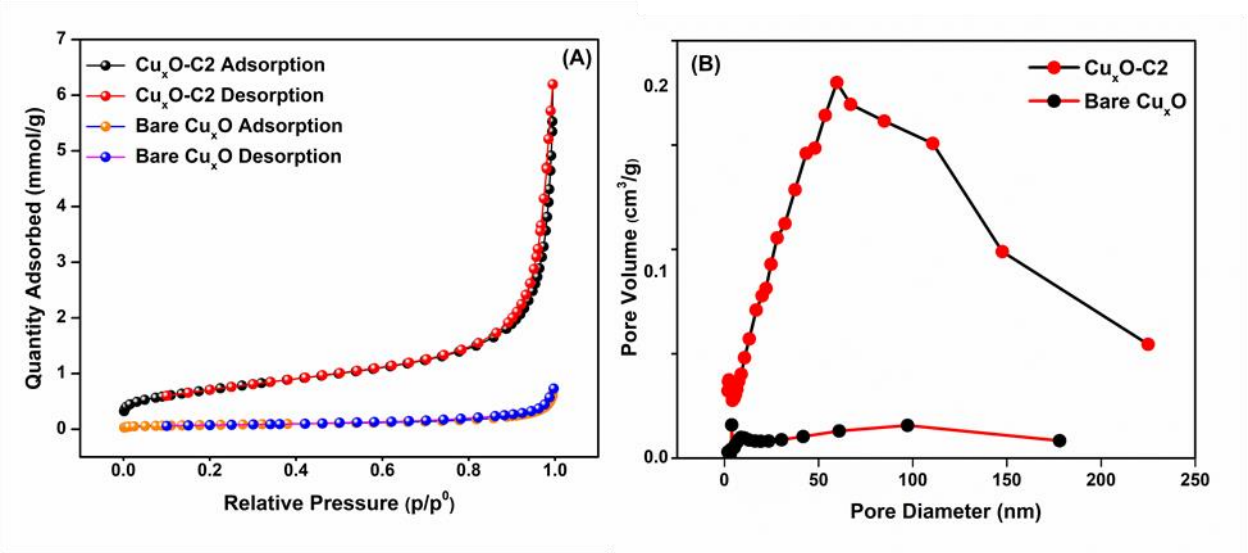


Figure 3.2 (a) N_2 adsorption and desorption isotherm of Bare Cu_xO and Cu_xO-C2 and **(b)** pore volume analysis of Bare Cu_xO and Cu_xO-C2.

FTIR-ATR analysis confirmed the presence of CuO and Cu_2O in the Cu_xO-C2 heterostructures as shown in Figure 3.3. Strong adsorption bands appearing at 520 cm^{-1} are attributed to the vibrations of Cu-O from CuO structures[6] and the sharp peak at 612 cm^{-1} corresponds to the vibration of Cu-O-Cu originating from Cu_2O [7]. Strong brands at 3200-3500 cm^{-1} correspond to hydroxyl groups and are observed in correlation with the C-Black band spectrum. Also, at 1560 cm^{-1}, carboxyl functional groups were identified with higher intensity compared to the pure C-Black.

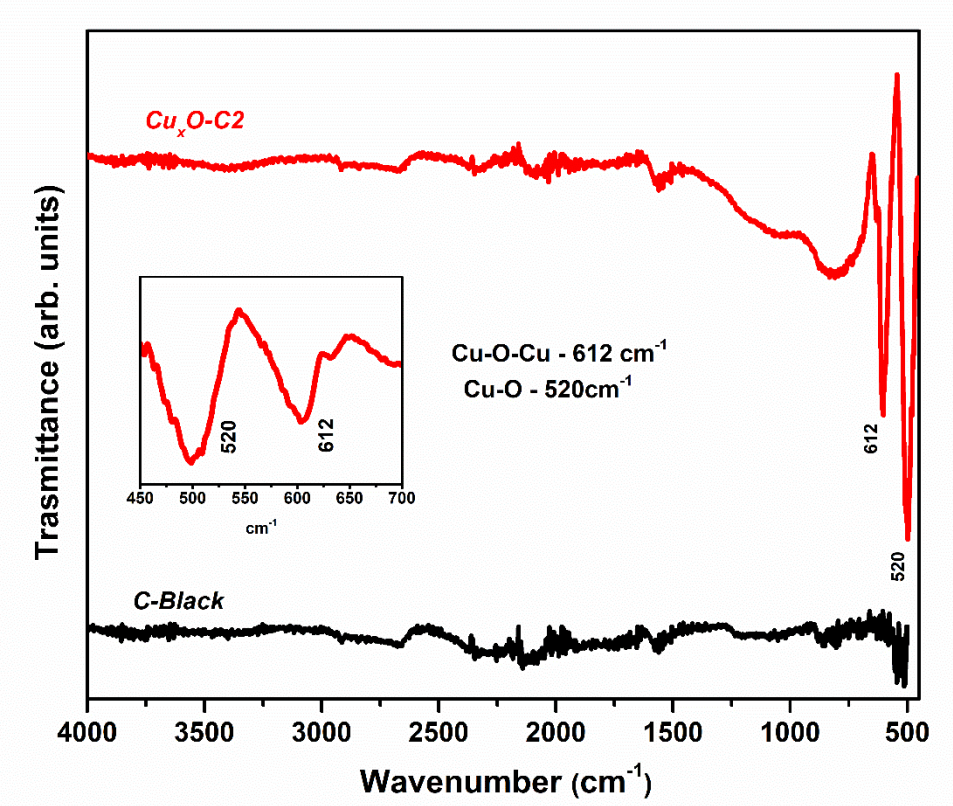


Figure 3.3 ATR-FTIR spectrum of Cu_xO-C2 and comparison with C-Black (Inset of Cu_xO-C2 representing Cu_2O and CuO).

XPS was used to investigate the surface and compositions of the synthesized catalysts. A comparative study has been done on the carbon-supported Cu_xO-C2 catalyst and as prepared bare Cu_xO. The obtained XPS spectrum confirmed the presence of the elements Cu, O and C in correlation with the corresponding binding energies of Cu 2p, O 1s and C 1s orbitals. Figure 3.4a shows the high-resolution spectrum of the core 2p level revealing the main characteristic peaks. Upon further deconvolution of the set of two peaks representing the main Cu 2p3/2 and 2p1/2 spin orbits, the presence of Cu^+ in the Cu_2O structures was confirmed by two peaks at 933.13 and 953.01 eV. Similarly, peaks with the binding energies 934.8 and 955.2 eV and corresponding to Cu^{2+} in CuO heterostructures were found. On the other hand, the deconvolution of O 1s, Figure 3.4b shows the typical peaks of lattice O_2^- in CuO and Cu_2O at 530.18 and 531.30 eV, along with a prominent peak at 532.65 eV corresponding to the C-O-C species on the Cu/C interface. Also, the high-resolution C 1s spectrum (Figure 3.4c) shows the C-C bonding at 284.76 eV from C-Black. The presence of C-O and C=O species are attributed to 285.71 and 287.08 eV peaks, respectively. Similarly, we have analyzed the bare Cu_xO

without any C-Black added. The deconvoluted high-resolution spectrum of Cu 2p level in Figure 3.4d shows the presence of metallic copper in correlation with XRD. Metallic copper (Cu^0) is identified, unlike the Cu2/C, along with Cu^+ and Cu^{2+} at 933.74 and 935.02 eV respectively, indicating Cu-Cu_2O-CuO heterostructures in the absence of C-Black. Also, considering the high-resolution deconvolution of O 1s, Figure 3.4e depicts the presence of O_2^- in CuO and Cu_2O at 530.11 and 531.45 eV, with much lower content of C-O-C species as expected, given the absence of C-Black in this sample. Considering the C 1s spectrum as depicted in Figure 3.4f, adventitious carbon derived from partial exposure to atmospheric conditions during the synthesis is noticed as C-C and C=O species at 284.85 and 285.74 eV, respectively.

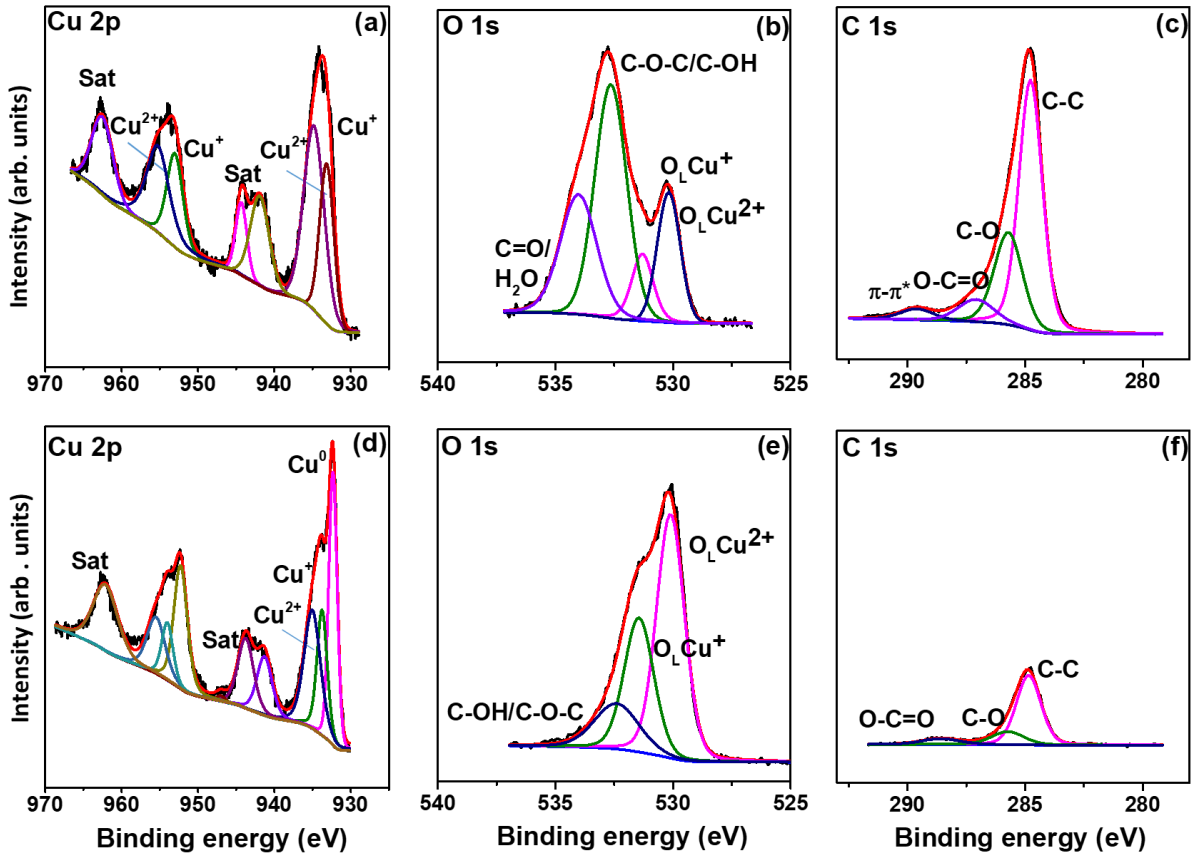


Figure 3.4 High-resolution deconvoluted XPS spectra of Cu_xO-C2 and bare Cu_xO **(a)** Cu 2p; **(b)** O 1s; **(c)** C 1s spectra of Cu_xO-C2; **(d)** Cu 2p; **(e)** O 1s; **(f)** C 1s spectra of bare Cu_xO.

Additional XPS analyses of Cu_xO-C1 and Cu_xO-C3 samples as shown in Figure 3.5 show similar trends to the XRD results in terms of Cu oxidation states, as depicted in the Cu 2p spectra. In the Cu_xO-C1 sample, Cu is mostly in fully oxidized form (Cu^{2+}), while in Cu_xO-C3, an important

contribution of Cu^+ is also observed. Further comparison of the spectra in the Cu LMM Auger region is included below in Figure 3.6. In general terms, the chemical composition (Cu-related phases) follows a similar trend to what we observed by XRD analysis: a predominant presence of Cu^{2+} in the samples with lower nominal Cu/C ratio (Cu_xO-C1), and a higher tendency to have Cu^+ in the sample with higher nominal Cu/C (Cu_xO-C2). The only difference we have observed with respect to the XRD-based analysis is a minor presence of Cu^+ in Cu_xO-C1 observed by XPS, implying its initial presence cannot be fully disregarded.

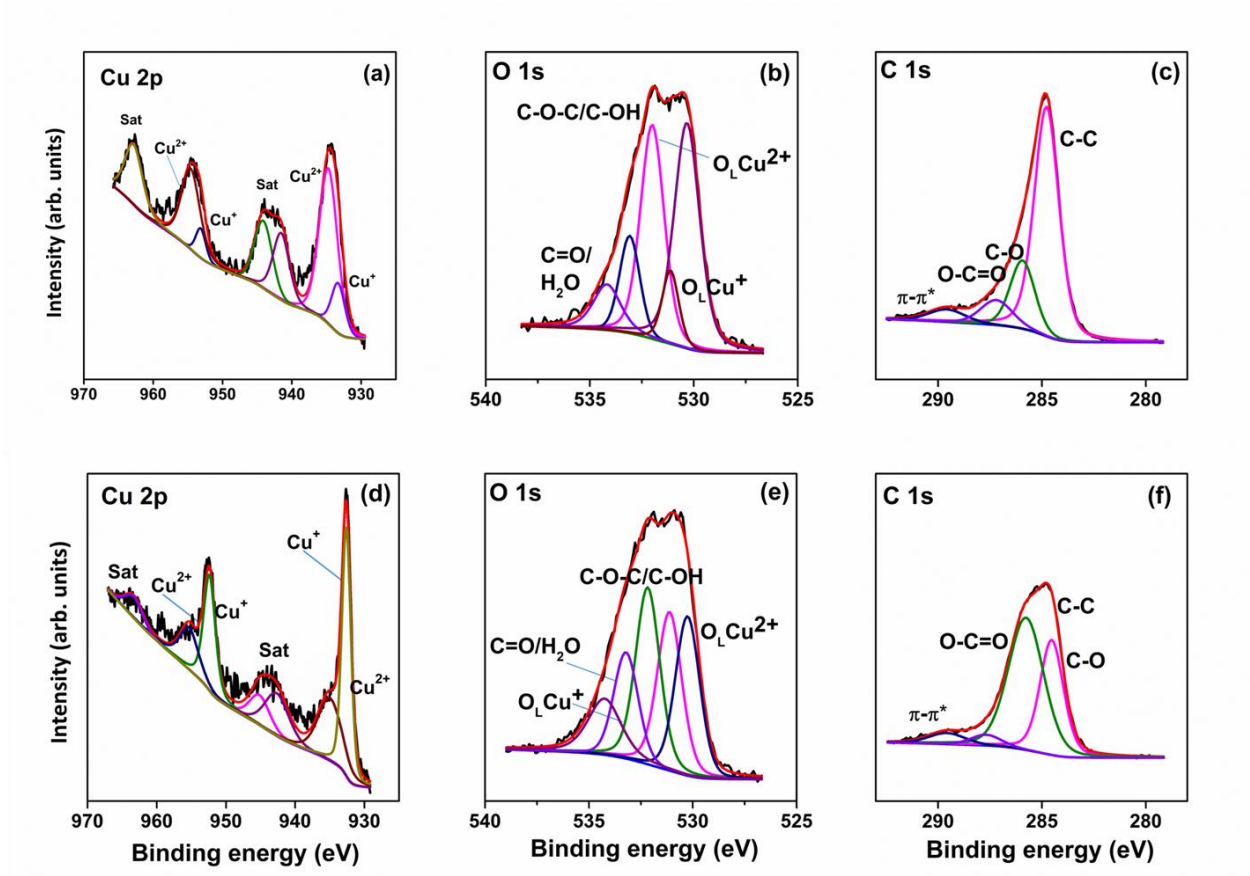


Figure 3.5 High-resolution deconvoluted XPS spectra of Cu_xO-C1 and Cu_xO-C3 **(a)** Cu 2p; **(b)** O 1s; **(c)** C 1s spectra of Cu_xO-C1; **(d)** Cu 2p; **(e)** O 1s; **(f)** C 1s spectra of Cu_xO-C3.

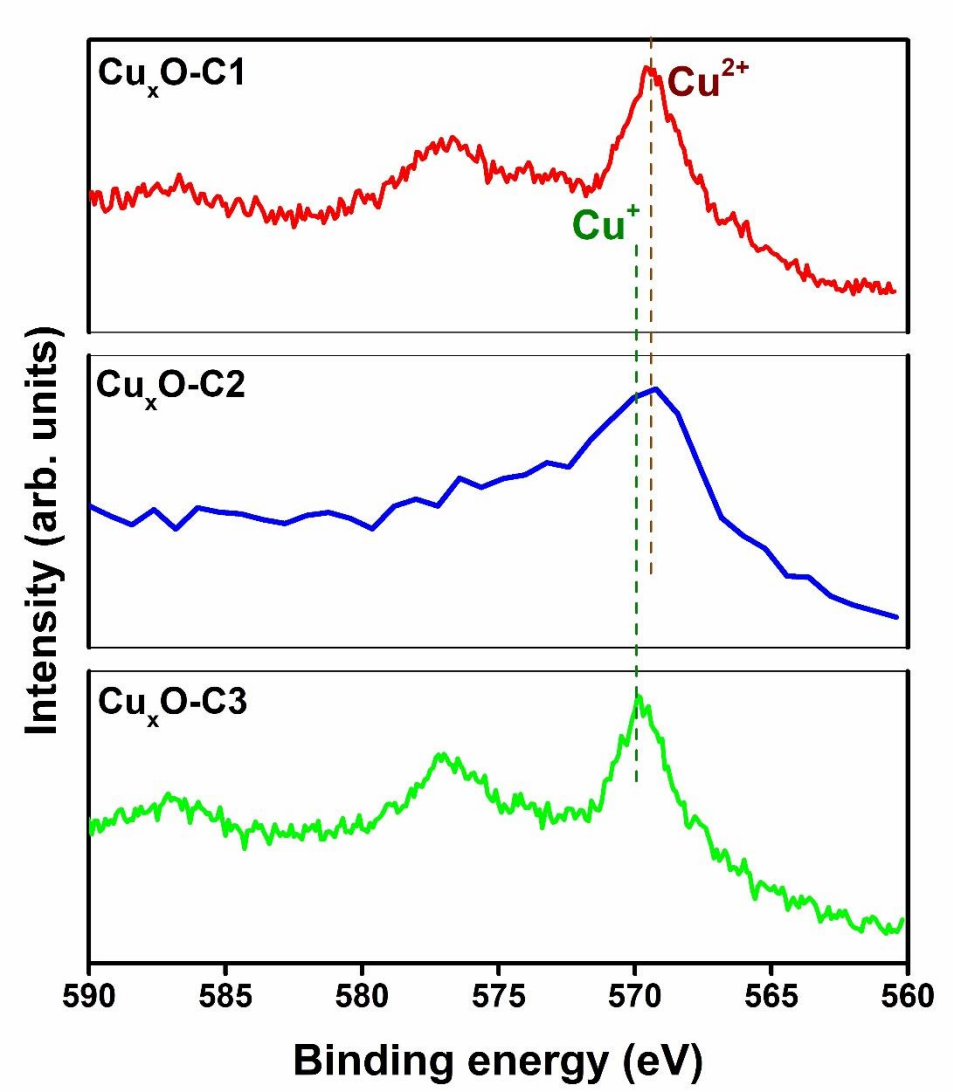


Figure 3.6 Cu LMM XPS spectra of the Cu_xO-C1, Cu_xO-C2 and Cu_xO-C3 samples.

The bare Cu_xO particles obtained in the absence of C-Black, Figure 3.7 (a, b, c) show mixed morphologies like rods, cubes, and rectangular structures with varied particle sizes. The Cu_xO-C2 sample Figure 3.7 (g, h, i) is found to have a more uniform morphology consisting mainly of platelet-like structures along with a minor presence of rod-like particles and a homogenous distribution of Cu_xO-C heterostructures. The Cu_xO-C1 sample with lower copper content has exhibited similar morphology to Cu_xO-C2 but with lesser coverage of Cu, in Figure 3.7 (d, e, f). The Cu_xO-C3 blend, with higher nominal copper content as seen in Figure 3.7 (j, k, l) has a drastic change in terms of morphology showing cubic and large octahedral crystals with heterogeneous particle size. The EDX analysis of the different compositions in Figure 3.8 (a, b, c) revealed the presence of Cu, C and O with Cu averaging around 25-40%, O around 10% and the rest by carbon. A comparison of the elemental composition along with the EDX analysis is

given in Table 3.2 along with the nominal Cu/C ratios. Interestingly, despite the higher nominal amount of Cu precursor on the Cu_xO-C3 sample, the Cu content on Cu_xO-C2 and Cu_xO-C3 is similar and lower than the theoretical one as per the amount of Cu precursor. In fact, both the samples depict similar Cu/C atomic ratios of 0.1, which ultimately implies that the differences in the performance between both materials are not associated with different Cu content.

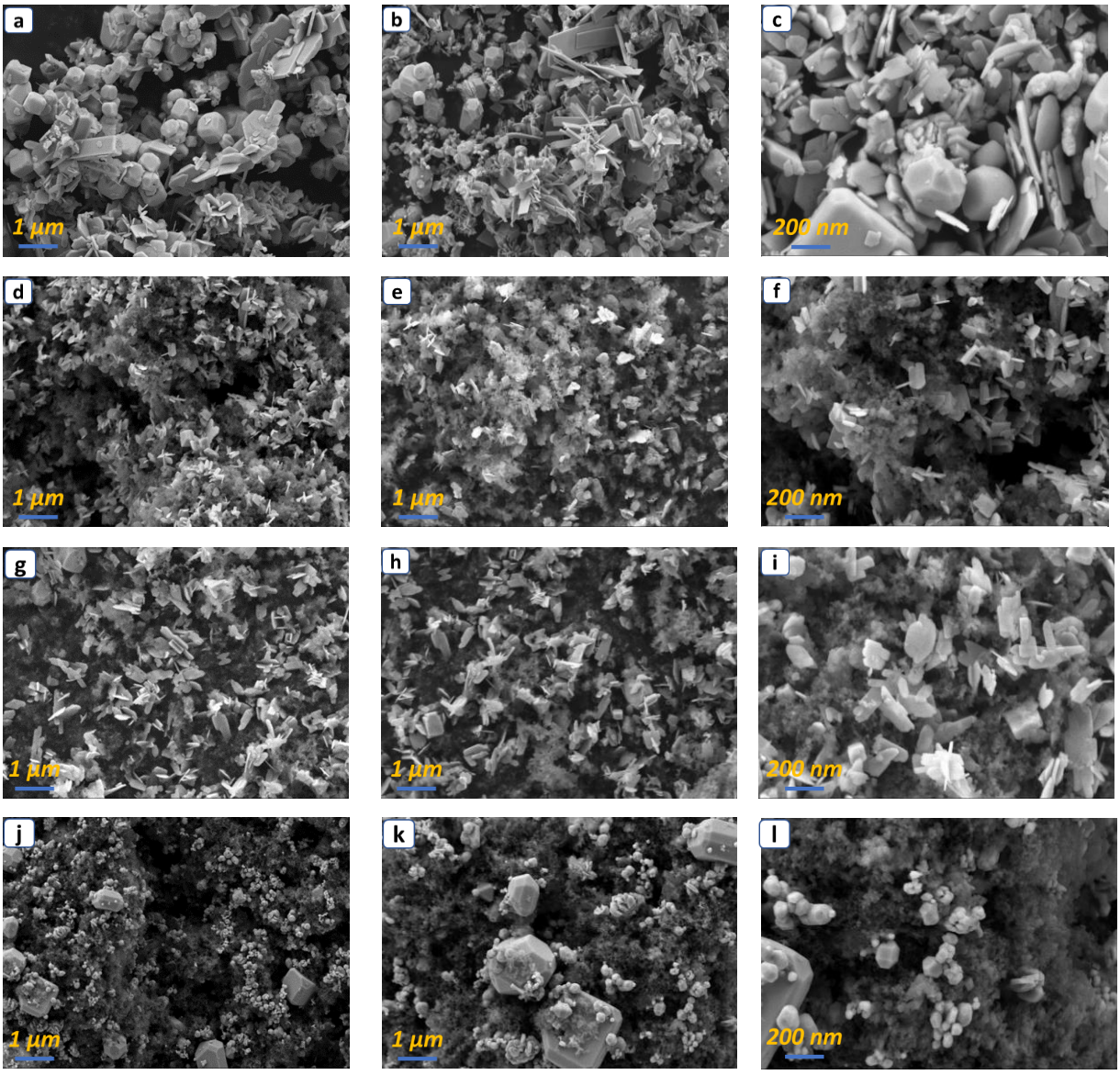


Figure 3.7 FE-SEM images of as-prepared samples **(a, b, c)** bare Cu_xO **(d, e, f)** Cu_xO/C1 **(g, h, i)** Cu_xO/C2 **(j, k, l)** Cu_xO/C3.

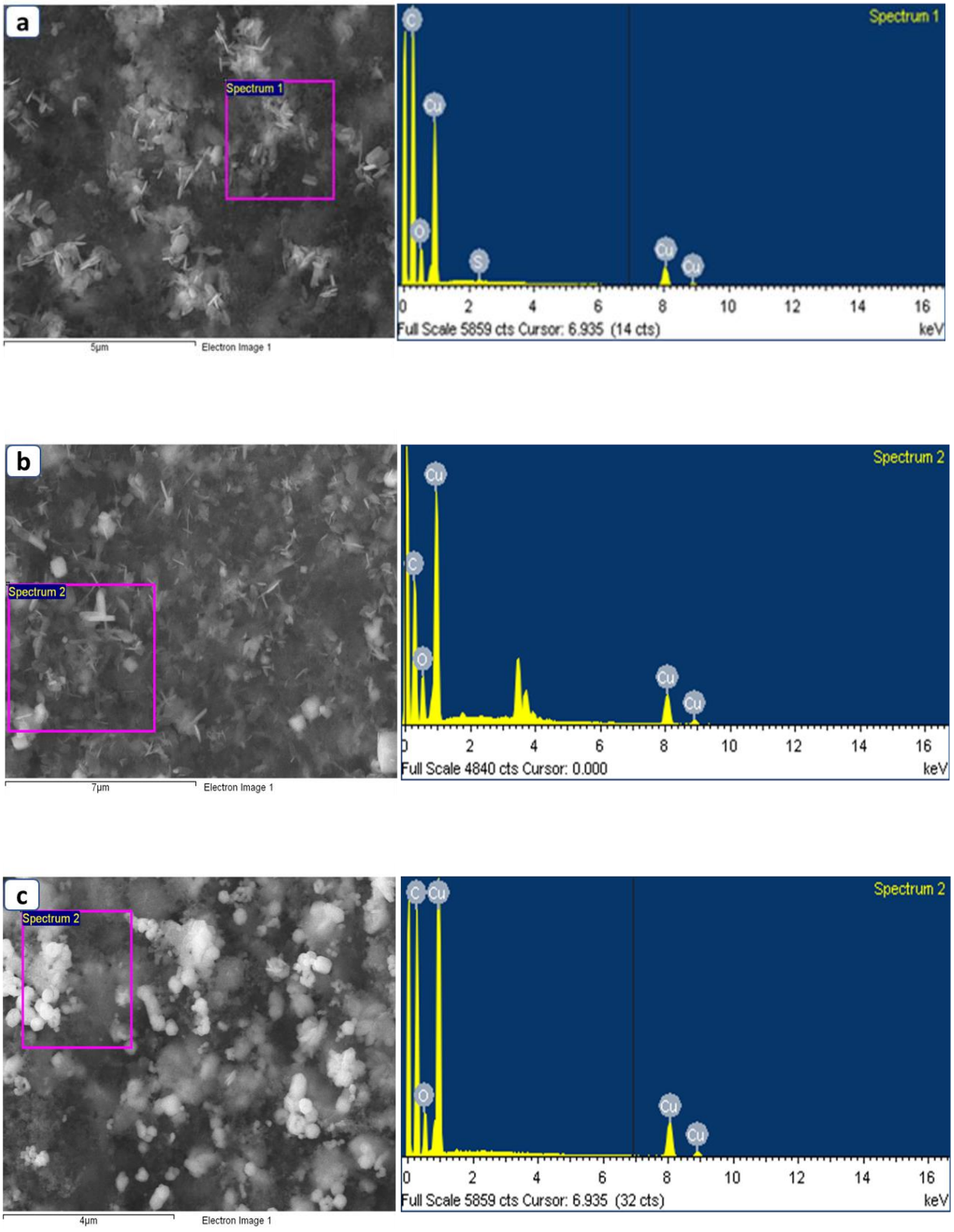


Figure 3.8 EDX spectrum of as-prepared samples **(a)** Cu_xO-C1, (b) Cu_xO-C2, (c) Cu_xO-C3.

Table 3.2. Comparison of Elemental composition from EDX analysis of as-prepared samples.

Sample/ Element	Cu_xO-C1		Cu_xO-C2		Cu_xO-C3	
	Weight %	Atomic %	Weight %	Atomic %	Weight %	Atomic %
Cu K	24.81	6.08	37.59	10.73	37.63	10.58
O K	10.98	10.68	13.12	14.87	9.04	10.10
C K	64.21	83.24	49.29	74.41	53.33	79.32
Cu/C	0.39	0.07	0.76	0.14	0.71	0.13
Nominal Cu/C	0.79	0.15	1.59	0.3	2.38	0.45

The presence of partially oxidized copper species surrounded by cloud-like carbon structures is evident from TEM as shown in Figure 3.9 (a, b) images. Low magnification TEM confirmed the presence of Cu-based heterostructures surrounded by C-based clouds. HAADF-STEM images in Figure 3.9 (c, d) clearly show Cu heterostructures with dominating platelet-like morphologies, which present various faceting. The power spectra (fast Fourier transforms) calculated on the HR-TEM images obtained on the C-based "cloud-like" structures Figure 3.9 (e, f) show that they present a periodicity corresponding to an interplanar distance of about 0.34 nm, in perfect agreement with a graphitic-like crystal structure. The C-based structures are evidenced in red in the frequency-filtered map reported in 3.9 (f). These carbon nanostructures resemble graphitic onion-like rings. The HR-TEM analyses performed on the Cu-based nanoplatelets suggest that their structure corresponds to the monoclinic tenorite CuO crystal phase, in complete agreement with our initial XRD studies. The observed CuO structures imaged in Figure 3.10 (a, b) are oriented along the [011] and [101] zone axes parallel to the electron beam. Electron Energy Loss Spectroscopy (STEM-EELS) as seen in Figure 3.10 (c, d) was used to obtain the elemental composition of the sample, focusing the attention on C K-edge at 284 eV (Green), O K-edge at 532 eV (blue) and Cu L-edge at 931 eV (red). The analysis performed over the platelet-like structures revealed the homogenous distribution of Cu and O surrounded by carbon structures. The low magnification TEM of the bare Cu_xO also confirms the presence of Cu-based structures with sizes in the range of a few microns with varied morphologies like platelets, rods, or cubes as shown in Figure 3.11 (a, b). These large-

sized particles are highlighted using the image contrast of HAADF-STEM as shown in Figure 3.11 (c, d). Detailed investigation using the power spectrum analysis of HR-TEM (Figure 3.11 (e, f)) confirmed the presence of both CuO tenorite monoclinic crystal phase as on the left side, imaged along [011] and Cu_2O cuprite cubic structure as on the right side, imaged along [11-1] zone axis. STEM-EELS maps (Figure 3.9 g) on the C K-edge at 284 eV (Green), O K-edge at 532 eV (blue) and Cu L-edge at 931 eV (red) indicate that the Cu and O are homogeneously distributed within the nanostructures, in good agreement with the structural analysis.

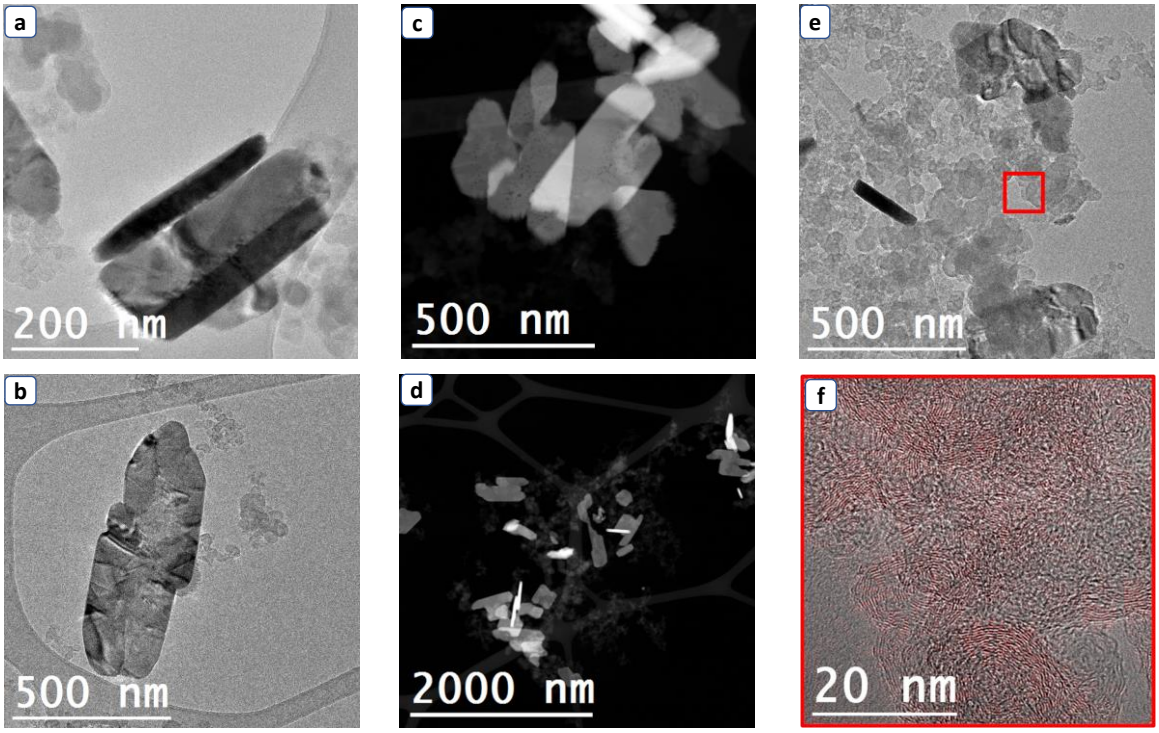


Figure 3.9 TEM and STEM-HAADF images of Cu_xO-C2: **(a, b, e)** Low Magnification TEM; **(c, d)** Low magnification STEM-HAADF images; **(f)** High-Resolution TEM combined with the frequency filtered map to evidence the graphitic structure (in red).

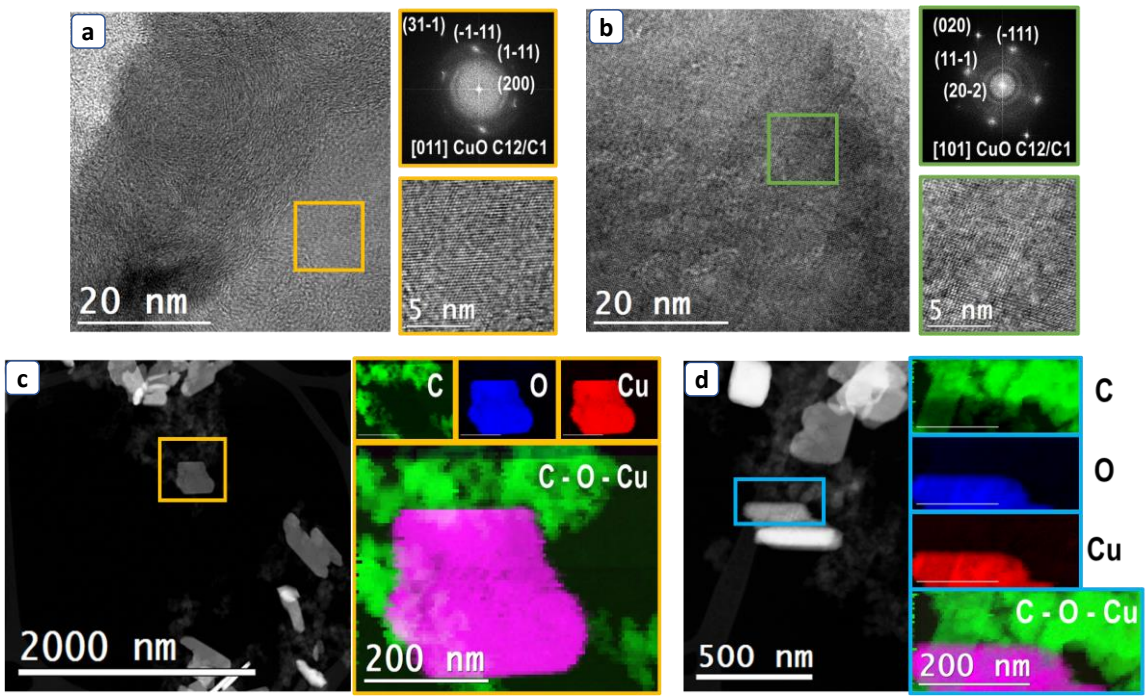


Figure 3.10 HR-TEM and STEM-EELS images of Cu_xO-C2: **(a, b)** HR-TEM together with image and power spectra; **(c, d)** STEM-HAADF and corresponding STEM-EELS compositional analysis.

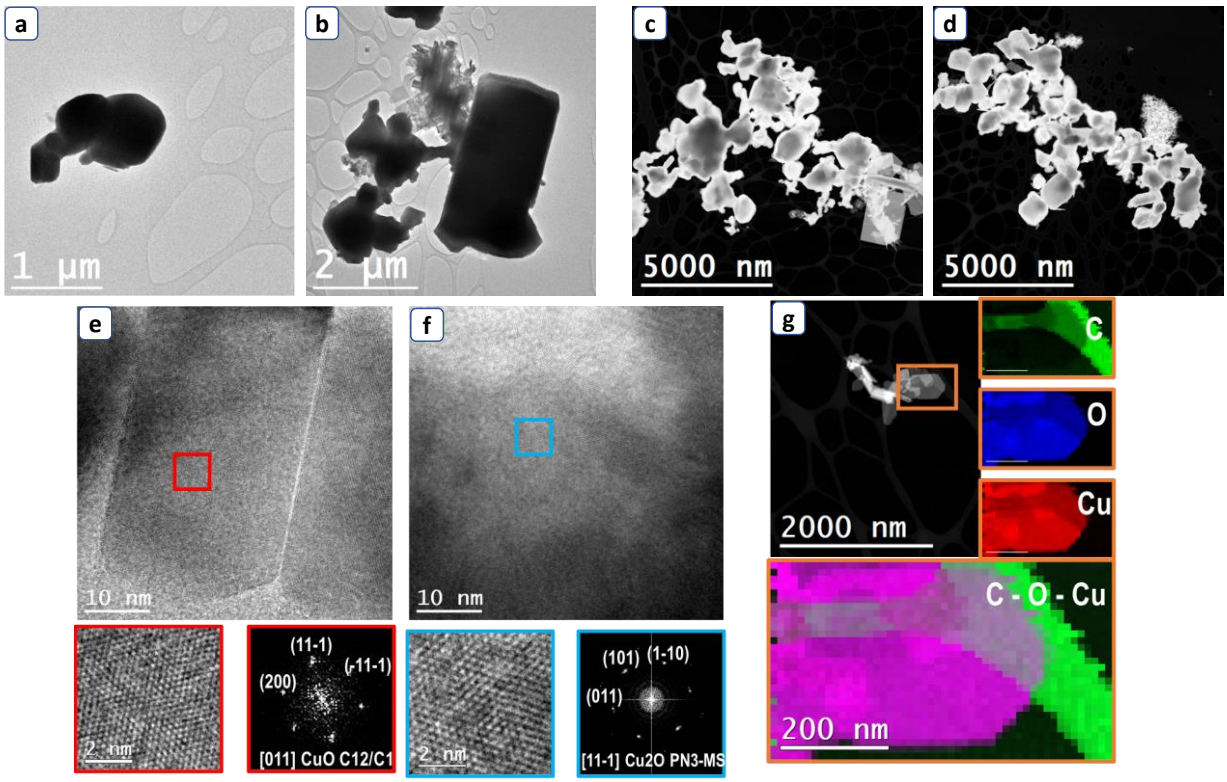


Figure 3.11 HR-TEM and STEM-EELS images of Bare Cu_xO: **(a, b)** Low Magnification TEM; **(c, d)** Low mag STEM-HAADF images; **(e, f)** HR-TEM together with image and power spectra; **(g)** STEM-HAADF and corresponding STEM-EELS compositional analysis.

3.6.2 Linear Sweep Voltammetry and ECSA Analysis

Electrochemical double-layer capacitance measurements were performed to analyze the active surface area of the synthesized electrocatalysts. Figure 3.12 depicts the ECSA analysis along with double-layer capacitance C_{DL} plots. ECSA analysis was performed in a standard three-electrode cell configuration. A glassy carbon electrode with the catalyst ink deposited was used as the working electrode, a platinum mesh as the counter electrode and a Hg/ Hg_2SO_4 electrode as the reference. A non-faradaic region with the applied potential range of -0.4 to -0.5 V vs RHE was chosen, and cyclic voltammetry was performed at various scan rates in Ar-saturated 1M $KHCO_3$ aqueous solution. The plots of scan rates ($mV \cdot s^{-1}$) vs current (I) are shown, and the slope represents the specific double-layer capacitance C_{DL}.

Cu_xO-C1 and Cu_xO-C2 are found to have C_{DL} values of 0.3 and 0.27 mF, respectively, higher than bare Cu_xO (0.11 mF), suggesting the presence of a higher number of active sites. Though the sample with higher copper nominal content, Cu_xO-C3 presents the highest capacitance (0.83 mF), the morphology and the ratio of CuO to Cu_2O seem to be the limiting factors in its selectivity towards ethylene via ECO_2R. From the obtained double-layer charging currents, the ECSA can be derived by comparing it to that of a copper metal. Linear sweep voltammetry studies as shown in Figure 3.13 were performed under CO_2 and Ar-saturated electrolytes to study the behaviour of the electrocatalysts at different potentials. In general, all the Cu-based samples exhibit lower onset potentials than C-Black.

Although minor differences were observed in the LSV curves under CO_2 and Ar flows, Cu_xO-C2 displays slightly higher cathodic currents in the presence of CO_2, thus confirming its intrinsic higher activity towards ECO_2R. On the contrary, both Cu_xO-C3 and bare Cu_xO show high currents with Ar at more cathodic potentials. More intense reduction peaks are observed in all the samples at less negative potentials (0 to -0.2 V vs RHE) in the measurements under Ar flow, suggesting a lower tendency of Cu_xO species to be reduced in the presence of CO_2.

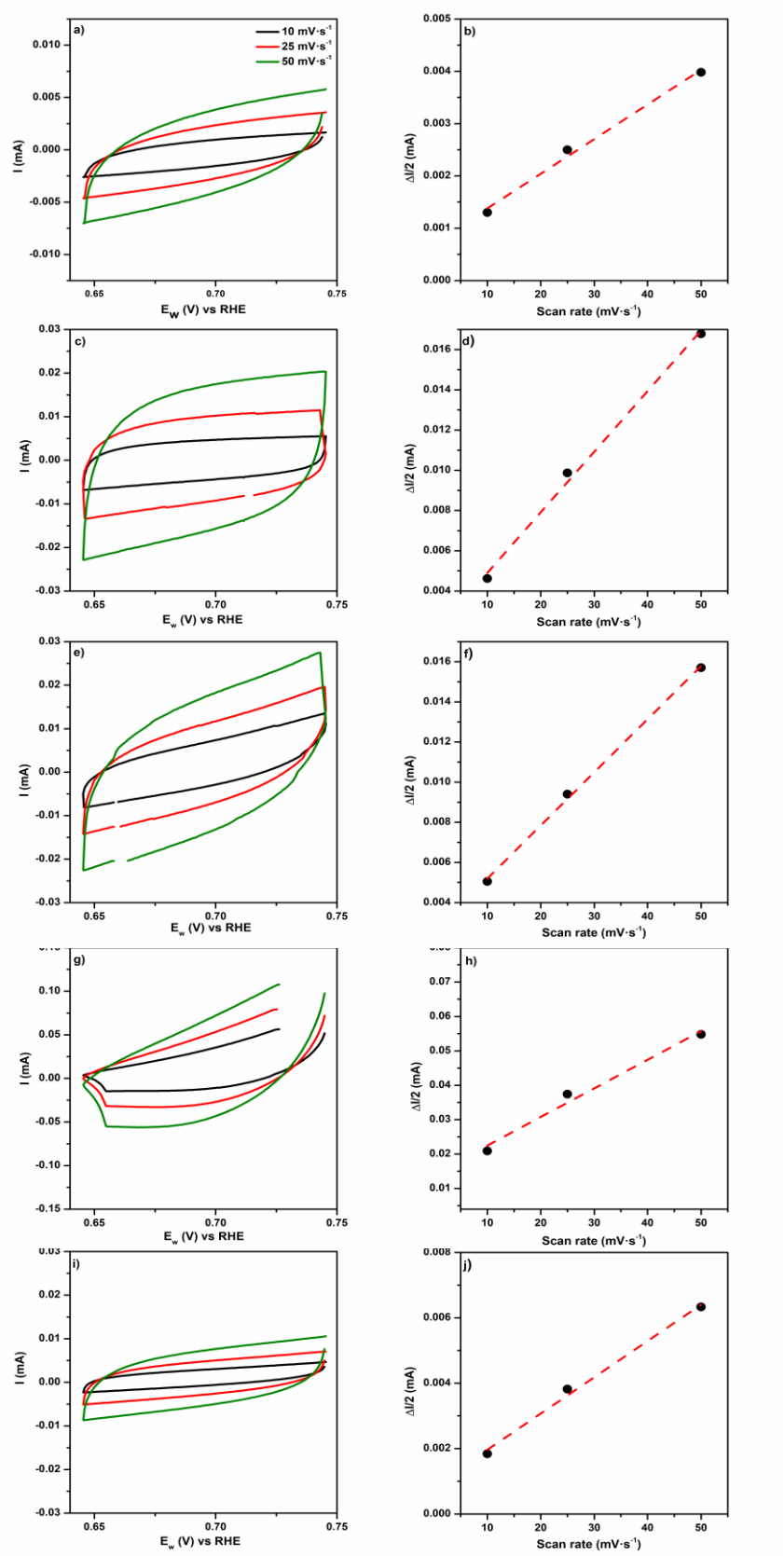


Figure 3.12 C_{DL} of (**a, b)** Vulcan/C-Black **(c, d)** Cu_xO-C1 **(e, f)** Cu_xO-C2 **(g, h)** Cu_xO-C3 **(i, j)** bare Cu_xO.

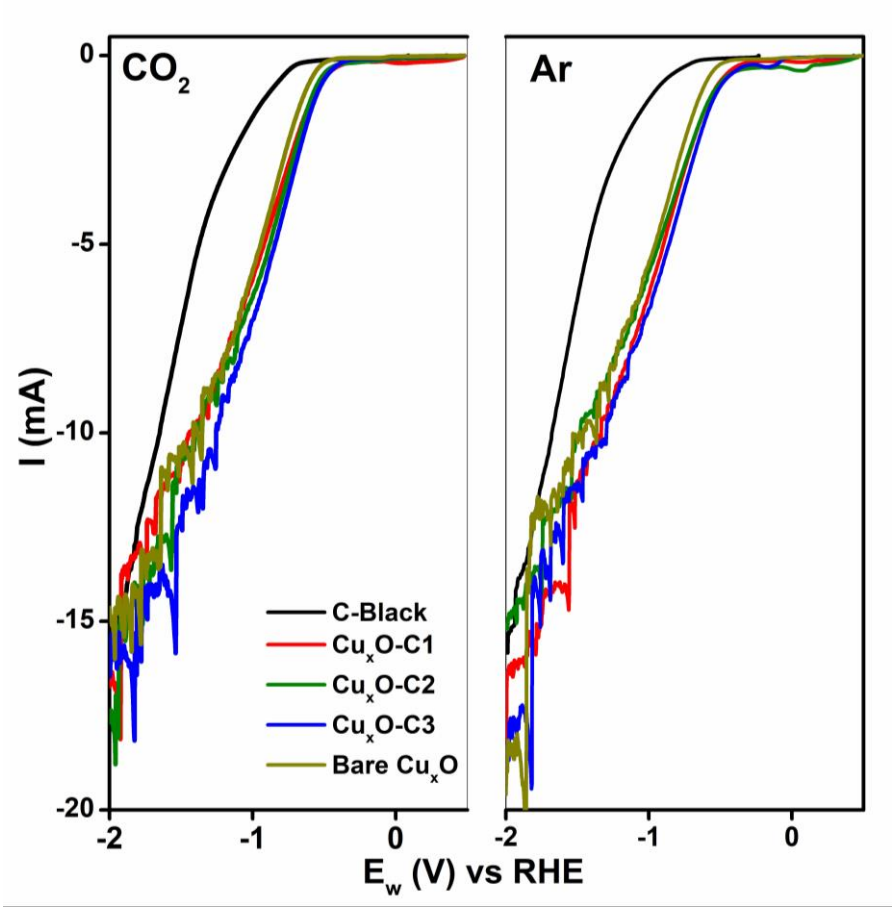


Figure 3.13 LSV curves with the different materials in CO_2 and Ar atmospheres.

3.6.3 Electrochemical Reduction of CO_2 in a Flow Electrolyzer

We have performed the electrochemical reduction of CO_2 by deploying the synthesized Cu/C heterostructures in an electrochemical flow cell in a three-electrode configuration as shown in Figure 2.16. in chapter 2. We have assessed all the synthesized catalysts and made a comparative study to find the best blend and morphology. Two approaches to the gas-electrolyte configuration have been carried out: flow-by and flow-through operational modes. Initially, the optimization of the CO_2 flow rate was carried out. We have explored the effect of feed CO_2 at different flow rates on the ECO_2R. Three different flow rates of CO_2 (10, 20 and 30 $mL{\cdot}min^{-1}$) were investigated to study the optimum feed flow over a period of 90 min. When operated at a constant potential at -1.5 V vs RHE as seen in Figure 3.14, the selectivity towards C_2H_4 is favoured more with an initial flow rate of 10 $mL{\cdot}min^{-1}$, a faradaic efficiency close to 40% was noticed and is found to be stable with time. We further increased the flow rate of CO_2 to 20 $mL{\cdot}min^{-1}$ and the faradaic efficiency is limited to an average of 25-26%. Upon further increase in the flow rate of CO_2 to 30 $mL{\cdot}min^{-1}$, the faradaic efficiency is well limited to less

than 20% leaving a large amount of unreacted CO_2. Upon careful consideration of the current densities at different flow rates, initially at the flow rate of 10 mL·min^{-1}, the current density ranged over 140-150 mA·cm^{-2}. While the production of CO remained at an FE of 10-12%, H_2 seemed to escalate over time. At a flow rate of 20 mL·min^{-1}, the current density enhanced over 160-170 mA·cm^{-2} along with the surge in H_2 while maintaining the selectivity of CO. A further increase to 30 mL·min^{-1} seemed to have further degradation as a result of higher current densities of 180-190 mA·cm^{-2} and enhanced FE of H_2 over 70% along with the decline in the selectivity towards CO.

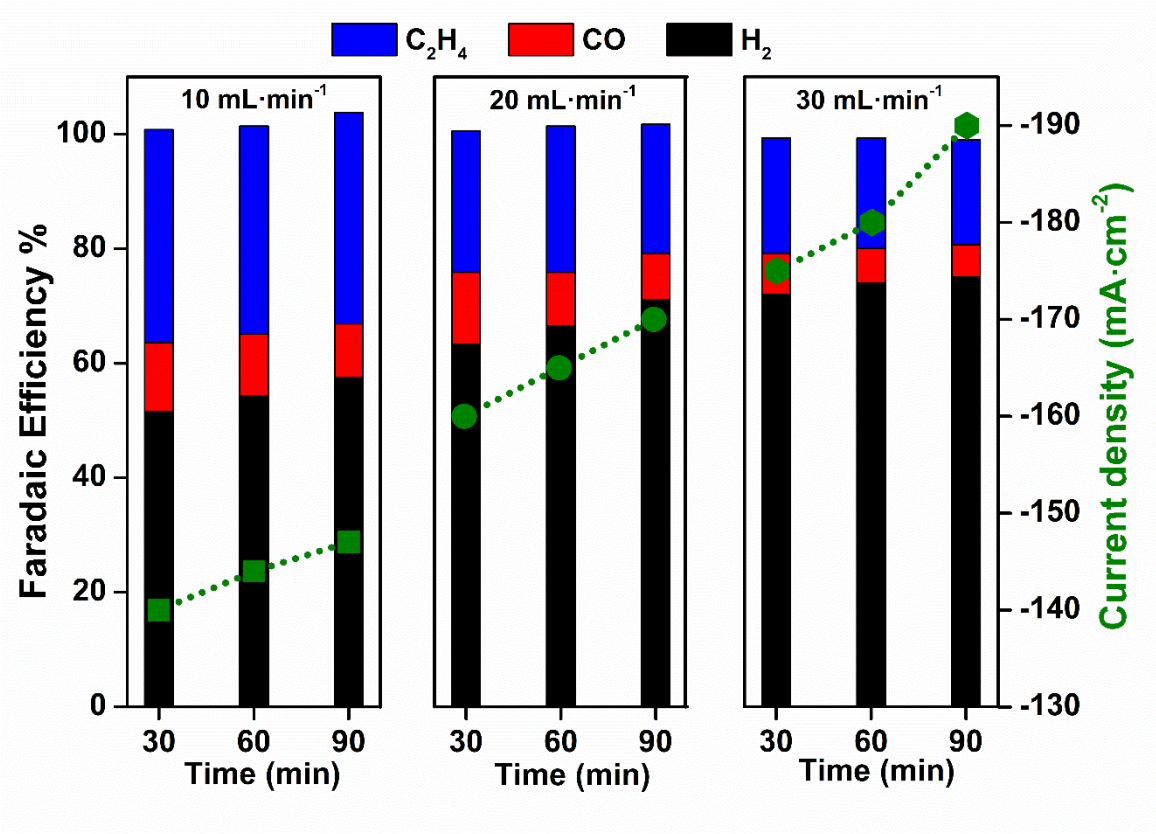


Figure 3.14 Comparison of ECO_2R performance at various CO_2 flow rates.

As these studies were performed under flow-through conditions, at a high flow rate of CO_2, it shall be inferred that a high amount of inlet CO_2 escalates the current densities favouring the selectivity of H_2 instead of C products. A closer look at the CO production revealed that the selectivity declines with increased flow of CO_2 which in turn limits the residence time of the intermediate CO* at the triple-phase boundary resulting in overall poor performance of the ECO_2R. Therefore, it can be concluded that by modulating the availability of the local CO_2 coverage with the optimized flow rate over the gas diffusion electrode, we can achieve higher

CO_2 conversion rates thus enabling high single-pass CO_2 conversion efficiency. Owing to the above inference, we further carried the ECO_2R at the constant flow of 10 $mL \cdot min^{-1}$ in all the following experiments.

The general electrolysis to evaluate the ECO_2R performance of Cu/C heterostructures was performed via chronoamperometric measurements for at least 60 min at each applied potential ranging between -1.1 and -1.5 V vs RHE. The electrolysis was performed for 60 min with periodic injections to quantify the gas products by online GC. The performed ECO_2R fetched the potential-dependent selectivity of the main products as ethylene, carbon monoxide, hydrogen and trace amounts of methane and ethane.

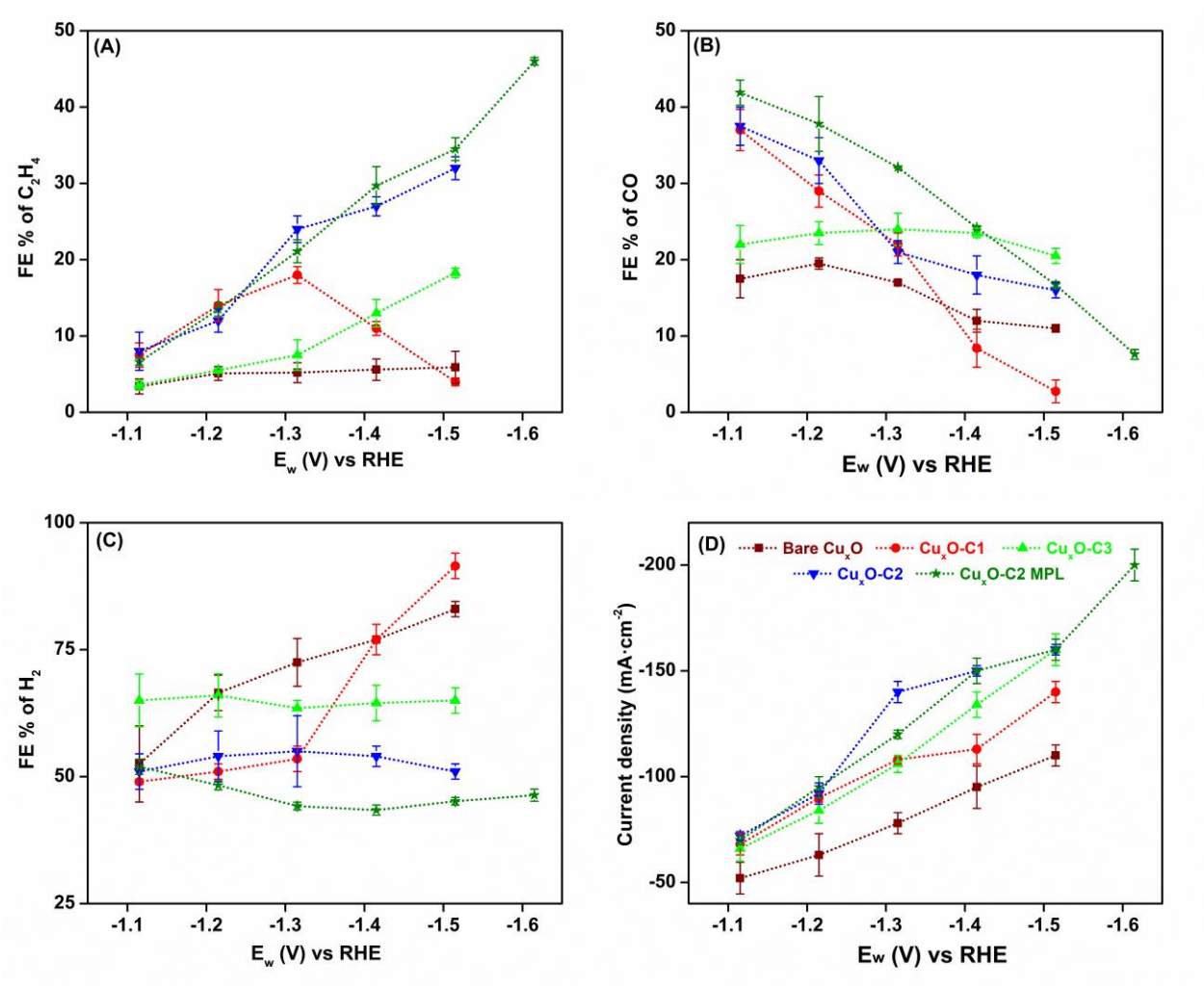


Figure 3.15 ECO_2R performance of different samples. Faradaic efficiencies (FE %) of **(A)** C_2H_4, **(B)** CO, and **(C)** H_2 **(D)** current densities at different potentials.

The oxide-derived copper heterostructures are highly selective towards ethylene as observed during the gradual sweep towards increasing cathodic potentials. All different compositions were evaluated and compared, and the faradaic efficiencies of various catalysts for major gas products at different applied potentials are plotted in Figure 3.15 where all the samples measured are by flow-through and only the GDE with MPL by flow-by modes respectively. The analyzed samples detected C_2H_4, CO and H_2 as the major products while negligible amounts of CH_4 and C_2H_6 were also noticed (<0.5% FE).

The observed current densities were also represented in Figure 3.15 (D) for all the samples measured. Comparatively, enhanced selectivity towards C_2H_4 is seen with the Cu_xO-C2 sample, while the other samples led to much lower FE C_2H_4 values. At low potential values (-1.1 to -1.3 V vs RHE), Cu_xO-C1 exhibited only slightly lower efficiencies than Cu_xO-C2, although the values rapidly dropped after further increasing the polarisation values, with a concomitant increase in the H_2 generation. This composition (Cu_xO-C1) resulted in an initial faradaic efficiency of 41% towards CO, but the lower number of available active sites (low Cu/C ratio) turned the catalyst layer inactive towards carbon products within a short time. Similarly, the material with higher nominal copper content, Cu_xO-C3, which is seen to have a completely different morphology and higher initial Cu_2O compared to Cu_xO-C2, shows higher overpotential towards C_2H_4 formation, with the FE C_2H_4 linearly increasing with working potential, while efficiency to CO is kept relatively constant between 20-25%. Therefore, despite the higher nominal Cu-content and the higher ECSA value in Cu_xO-C3, it is inferred that the morphology and crystalline structure are not favouring the higher selectivity towards C_2H_4 over H_2.

It is understood that, even at higher applied potentials and currents, the morphology, and the ratio of initial oxide states of copper of the synthesized heterostructures play a crucial role in tuning the selectivity towards the desired ethylene. We have also analyzed bare Cu_xO along with the addition of C-Black in the physical mixture to understand the efficiency of the synthesis and to see if the in-situ growth of CuO over C-Black is advantageous over the addition of physical mixture during the catalyst ink formulations. It is noted that these catalysts are poorly selective towards C_2H_4, and only competitive HER is favoured, with faradaic efficiencies to H_2 higher than 75%. An additional test was performed with the Cu_xO-C2 material by preparing an electrode on commercial carbon Toray with MPL and using flow-by

conditions. The productivity differences between all the analyzed blends have been given in Table 3.3.

Table 3.3 Productivity comparison of the synthesized blends with respect to weight % of Cu

Sample	Weight % of Cu (in mg)	Productivity of specific product ($\mu mol \cdot min^{-1}$)			Productivity of specific product ($\mu mol \cdot min^{-1} \cdot mg_{Cu}^{-1}$)		
		H_2	CO	C_2H_4	H_2	CO	C_2H_4
Cu_xO-C1 Flow-through	**4.96**	**143**	**7.53**	**1.4**	**28.8**	**1.5**	**0.3**
Cu_xO-C3 Flow-through	**7.53**	**157**	**37.8**	**7.9**	**14.7**	**5.5**	**1.1**
Cu_xO-C2 Flow-through	**7.52**	**138**	**41.5**	**11.4**	**16.4**	**6.9**	**1.5**
Cu_xO-C2 Flow-by	**7.52**	**111**	**42.5**	**13.4**	**19.2**	**5.7**	**1.8**
Cu_xO-C2 Flow-by at 200 $mA \cdot cm^{-2}$	**7.52**	**146**	**23.7**	**23.7**	**20.7**	**3.2**	**3.2**
Bare Cu_xO Flow-through	**12**	**210**	**27.9**	**2.4**	**17.5**	**2.3**	**0.2**

In Figure 3.16, we show the performance of the prepared Cu_xO-C2 blend with flow-through and flow-by analysis. It is observed that initially, CO is more favoured and the gradual increase in the cathodic sweep tuned the selectivity towards ethylene. At the potential -1.5 V, a high faradaic efficiency towards ethylene (FE C_2H_4) was achieved (36%) at a current density of 160 $mA \cdot cm^{-2}$. When a current density of 200 $mA \cdot cm^{-2}$ was continuously applied in flow-by mode, an enhancement in FE of C_2H_4 to 46% was achieved, while limiting the one of H_2 to around 40%. At the end of the electrolysis, the liquid products were analyzed by taking a fraction of the catholyte and using GC with a Head Space accessory coupled with an auto-sampler. It was found that trace amounts of methanol (96 ppm), ethanol (1350 ppm) and n-propanol (390 ppm) were formed and accumulated in the catholyte, which accounts for insignificant FE values of FE %.

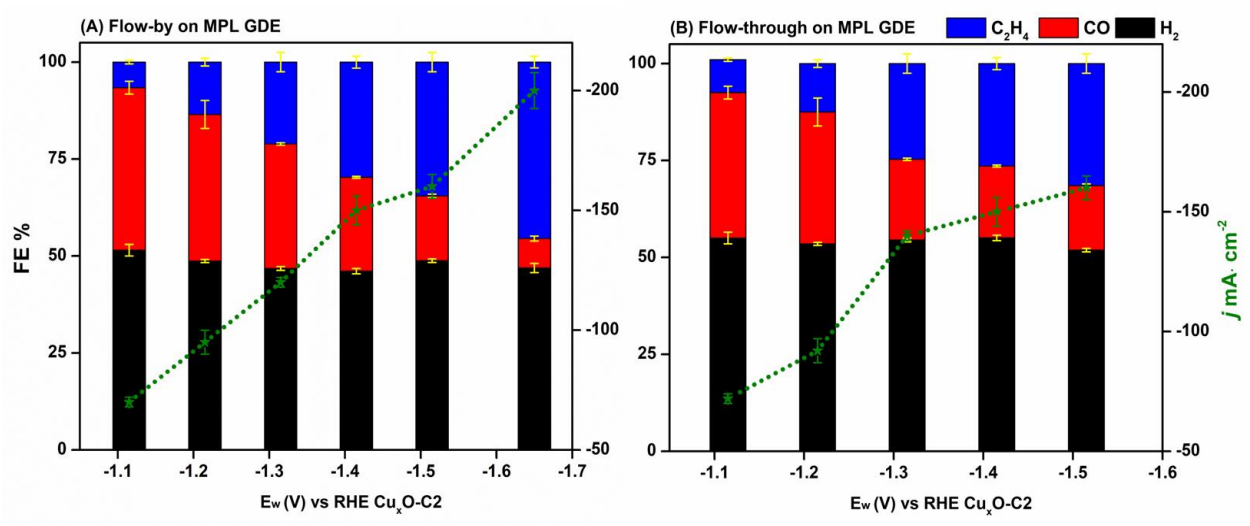


Figure 3.16 ECO_2R performance via Flow-by **(A)** and Flow-through **(B)** operation modes.

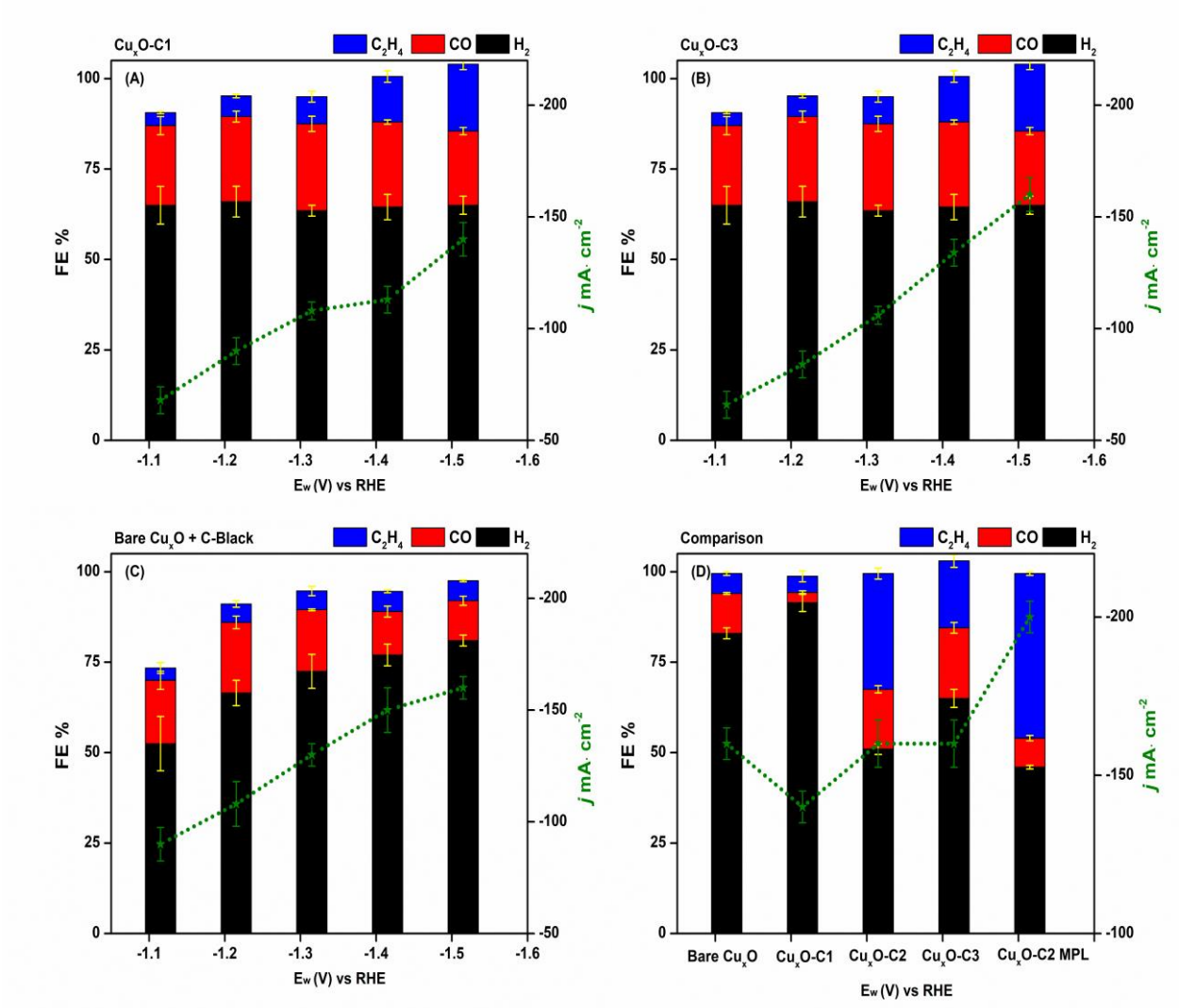


Figure 3.17 Electrocatalytic performance of CO_2 reduction **(A)** Cu_xO-C1 **(B)** Cu_xO-C3 **(C)** Bare Cu_xO **(D)** Comparison of different compositions.

A detailed representation of corresponding faradaic efficiencies and current densities for each analyzed sample is shown in Figure 3.17. In addition, Figure 3.17 (d) includes a comparative analysis of the efficiencies with the different materials at the best operation conditions for ethylene generation along with the obtained current densities. Figure 3.18 demonstrates a comparative analysis of FE % of CO and C_2H_4 from ECO_2R of different compositions prepared and analyzed concerning the applied potentials. Although at the lower onset potentials, CO is the initial favoured product noticed, the gradual cathodic sweep has shown the selectivity towards C_2H_4 indicating the unique ability of the synthesized electrocatalysts by promoting the dimerization of C products.

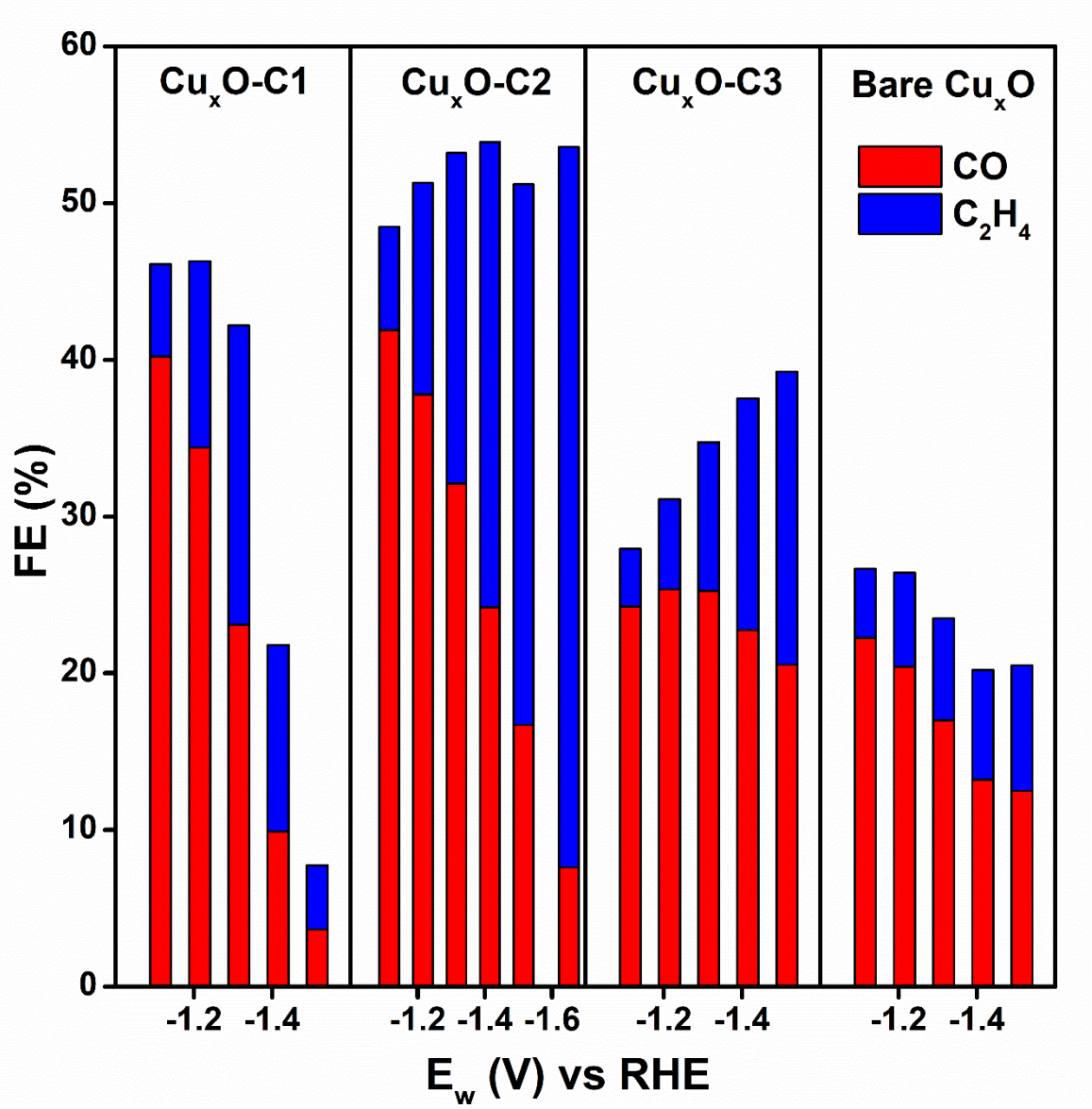


Figure 3.18 Comparison of FE% of CO and C_2H_4 of the different compositions evaluated

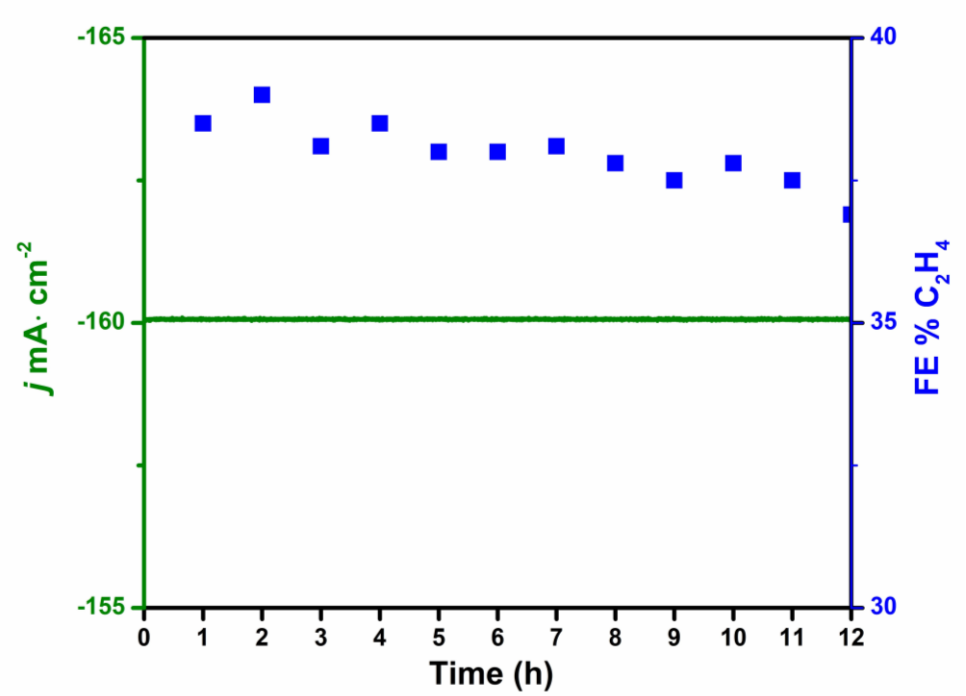


Figure 3.19 Stability performance over 12 hours at a constant current of 160 mA·cm^{-2}

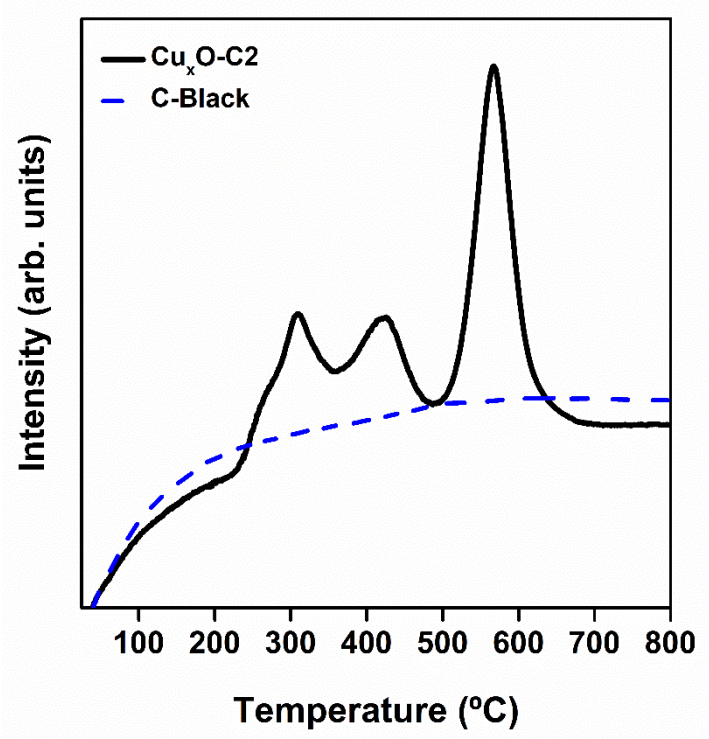


Figure 3.20 TPD results under CO atmosphere obtained with Cu_xO-C2 and C-Black samples.

An additional stability test was performed at the standard operating galvanostatic conditions with a constant applied current of 160 mA·cm^{-2} yielding a faradaic efficiency of over 38% holding excellent stability of more than 12 hours. This test has been done in the flow-by mode

using the Cu_xO-C2 blend drop-casted on the Micro-Porous Layer Carbon Toray and Figure 3.18 shows the stability performance in the aforementioned conditions.

We have performed TPD with CO for the Cu_xO-C2 sample and pristine C-Black as a reference as shown in Figure 3.20. As observed in the figure below, three prominent desorption peaks are found at around 310, 425 and 570 °C. The comparison with pristine C-black, where no desorption peaks were observed, clearly indicates Cu_xO species in Cu_xO-C2 have CO capacity adsorption, which in turn has the potential to favour the generation of hydrocarbons such as C_{2+} products during ECO_2R.

XRD post-electrolysis measurements in Figure 3.21 (A) confirm that CuO is reduced to Cu_2O in all the compared samples. Figure 3.21 (B) depicts the change in the Cu phases of Cu_xO-C2 during the stages of electrolysis showing that the complete in-situ modification of CuO to Cu_2O phase takes place rapidly even after preliminary polarisation at low voltages. It can be further understood that the as-seen reduction to Cu_2O is the driving factor for the selectivity along with the optimum Cu/C ratio of active sites. Figure 3.22 shows the FE-SEM morphological comparison of the Cu_xO-C2 deposited on carbon paper: (a) as deposited on the GDE, (b) after an initial pre-reduction step and (c) post-electrolysis. The morphology depicts platelet-like structures on the as-deposited electrodes changing to small cube-like particles after the pre-reduction and in whole after the CO_2 electrolysis.

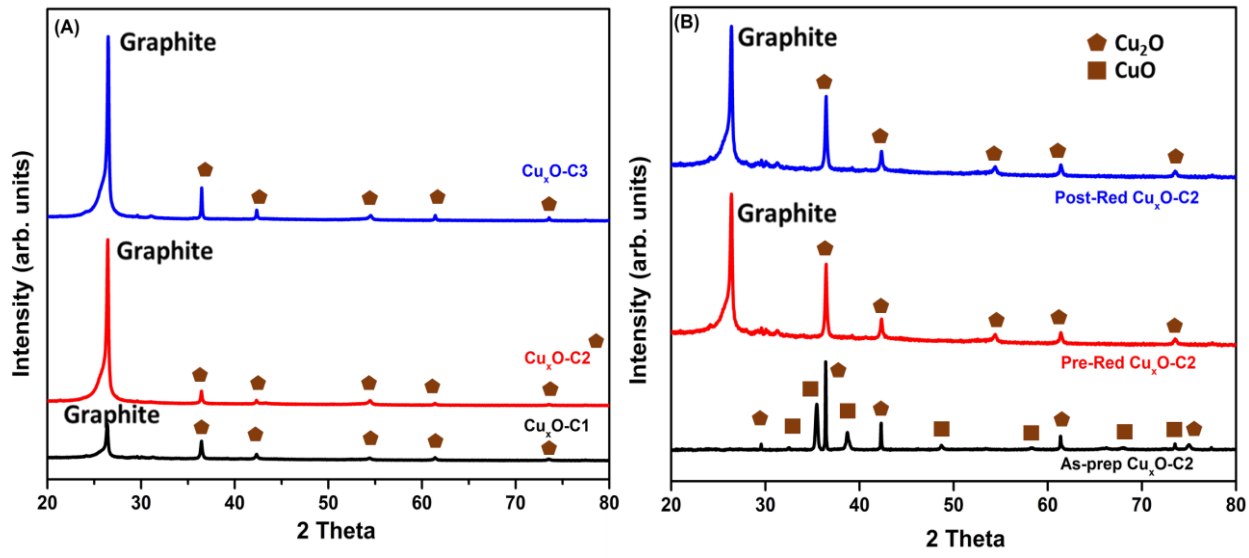


Figure 3.21 Post-electrolysis XRD measurements **(a)** Comparison of different compositions **(b)** Comparison of Cu_xO-C2 at various steps.

The post-electrolysis TEM and HR-TEM analysis of the electrocatalysts in Figure 3.23 (obtained from carefully scratching the GDE surface) revealed the morphological changes to cubic and rectangular-shaped particles as agglomerates as a result of the applied cathodic potentials. Modifications were seen in both structural and morphologies as mentioned above.

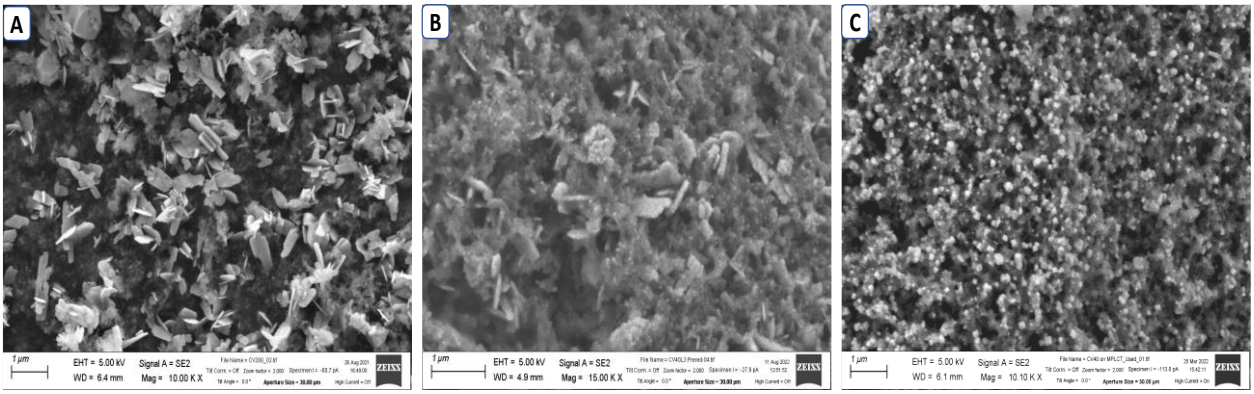


Figure 3.22 Post-electrolysis FE-SEM measurements of CuxO-C2 on the GDE **(A)** As-prepared, **(B)** pre-reduction for 10 min, **(C**) post-reduction.

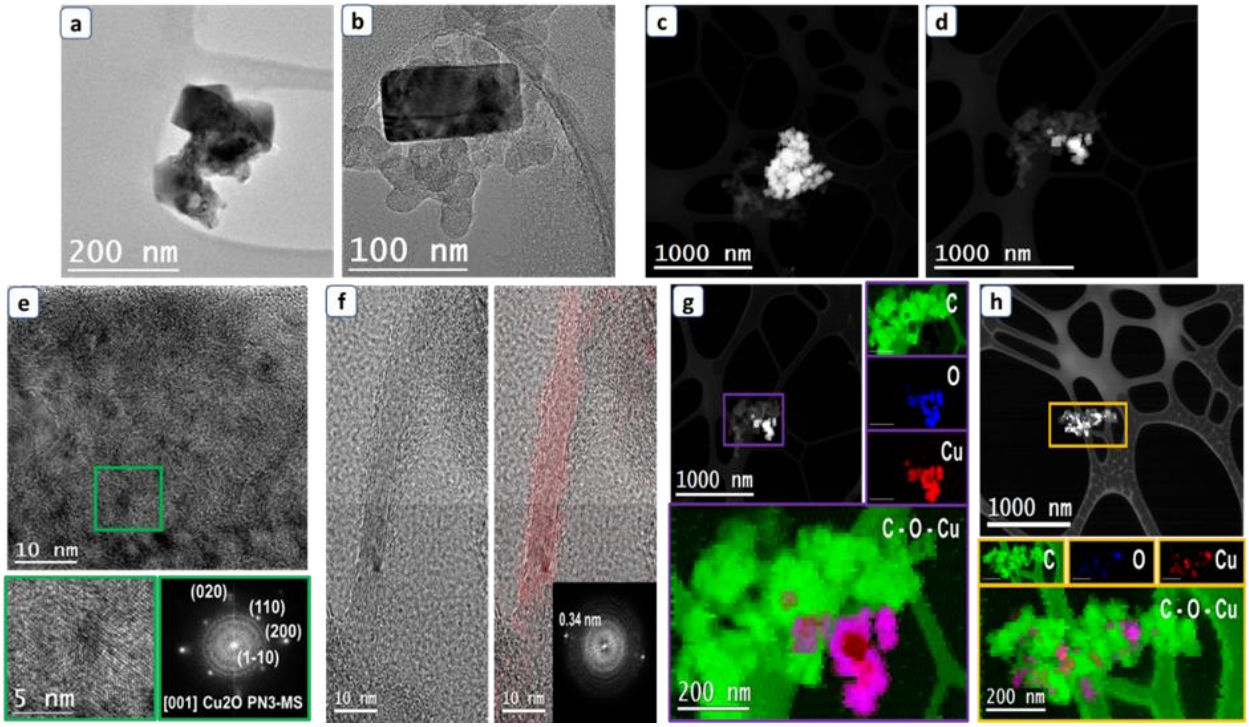


Figure3.23. HR-TEM, STEM-HAADF and STEM-EELS images of Cu_xO-C2 post electrolysis: **(a, b)** Low Magnification TEM **(c, d)** Low mag STEM-HAADF images **(e, f)** High-Resolution TEM combined with the frequency filtered map to evidence the graphitic structure **(g, h)** STEM-EELS compositional analysis.

Figure 3.23 depicts the low magnification TEM images of Cu-based nanostructures possessing an average size in the range of 100 mm and the HAADF-STEM studies; Figure 3.23 (c, d) clearly distinguishes the C-based graphitic onion rings from the agglomerated Cu-based nanostructures. Further detailed investigation with the HR-TEM in Figure 3.23 (e, f) led to the identification of corresponding structural analysis of the Cu-based nanostructures. Power spectrum analysis evaluated that all the Cu-based nanostructures possessing Cu_2O Cuprite-based cubic structures are imaged with the [001] zone axis that is parallel to the electron beam. To gain further insights into the elemental distribution, STEM-EELS mapping was carried out (Figure 3.23 (g, h)) focusing the attention on C K-edge at 284 eV (Green), O K-edge at 532 eV (blue) and Cu L-edge at 931 eV (red). A good agreement with the structural analysis is observed as the Cu and O are homogeneously distributed within the nanostructures. It is understood that the C-based nanostructures are in good contact with the Cu_2O nanoparticles. This summarizes the whole mechanism involving the reduction of the CuO heterostructures to Cu_2O nanoparticles, thereby acting as the catalytic active sites for the reduction of CO_2. The post-electrolysis characterization of the catalysts indicates the presence of Cu_2O [Cu(I)] as the final state of copper. However, in-situ minor formation of Cu(0) during the electrolysis is not completely excluded, with the possibility of further reoxidation prior to ex-situ analysis.

From the obtained results and the characterization studies, the derived Cu_2O is found to be the main active catalytic site for the highly selective conversion of CO_2 to C_2H_4 at high current densities. Cu_2O is partially formed during the synthesis of the materials but is also derived from the electrochemical but is also derived from the electrochemical pre-reduction of CuO occurring under the initial steps. In fact, LSV studies show slightly unfavourable $Cu^{2+}/Cu^{+}/Cu^{0}$ reduction steps in the presence of CO_2, in comparison to the Ar atmosphere, suggesting a certain stabilization of oxidised forms. Besides the crystallographic-related aspects, mechanistic considerations already described in the literature regarding C_2H_4 formation and its correlation with the initial generation of CO* intermediate, indicate that CO* needs to be formed and adsorbed on the electrocatalyst surface in order to dimerise through a C-C coupling mechanism.[2] As seen at low polarization values, mostly CO is formed with Cu_xO-C1 and Cu_xO-C2, which seem to have adequate adsorption energies to promote CO* formation (and further desorption as CO product). This agrees with the fact of initially observing mostly plate-like morphology on both the samples. At higher polarization, C_2H_4 generation is

promoted with Cu_xO-C2 at the expense of a concomitant decrease in CO formation, thus suggesting a correlation between the two products. In the case of Cu_xO-C1, the lower Cu content seems to be the reason for the poor selectivity towards C_2H_4 at high polarization values, although the comparison between Cu_xO-C2 and Cu_xO-C3, with similar Cu/C ratios (as seen by EDX analysis), demonstrates that the differences are not only related to the Cu content. Moreover, even while having higher ECSA (and achieving slightly higher current densities), Cu_xO-C3 depicts a different behaviour with FE to CO being constant along all the polarisation conditions, and the one of C_2H_4 increasing linearly with the applied potential (although much lower than those of Cu_xO-C2). These results clearly suggest that the polymorphic nature of Cu_xO-C3 has a detrimental effect on the ECO_2R. The effect of C-Black is not only in enhancing CO_2 diffusion but also in attaining higher current densities. In fact, the evaluation of bare Cu_xO (in physical mixture with C-Black), reaching significantly lower currents than the Cu_xO-C materials, shreds of evidence that Cu_xO-C interaction obtained by the in-situ synthetic method is necessary to achieve higher operating current.

Related synthetic approaches have been followed in other studies for the in-situ preparation of Cu_xO-C structures including carbon black and other carbonaceous materials. For instance, Yang et. al prepared CuO-supported catalysts, demonstrating improved FE to C_2H_4 in correlation with CO_2 uptake capacity attained with N-doped carbon materials [8]. Although evaluated under different conditions, comparatively, the CuO material supported on XC-72 Vulcan, reached FE to C_2H_4 of 20% at current densities of 140 mA· mg-Cu^{-1}, while in the present work, we achieve 46% with the estimated current of 133 mA· mg-Cu^{-1}. In a different approach, Wang et. al has developed CuO_x/C materials with mixed oxidation states based on a chlorine-induced transformation, achieving FE to C_2H_4 of 22% at 60 mA·cm^{-2}, and demonstrating stabilisation of mixed Cu^0/Cu^+ valence states for long operation times in H-cell.[9] In general, this strategy has been demonstrated to be an effective alternative to obtain electrocatalysts with state-of-the-art activities for C_{2+} products, with scalable and relatively simple synthesis methods, while also deploying catalysts with low metal content with respect to other approaches with pure Cu-derived materials. Differently from those studies, we have developed in the present work systems with larger area electrodes, implemented in flow-cell devices with optimized flow configuration, thus attaining higher efficiencies and productivities.

3.7 Conclusions

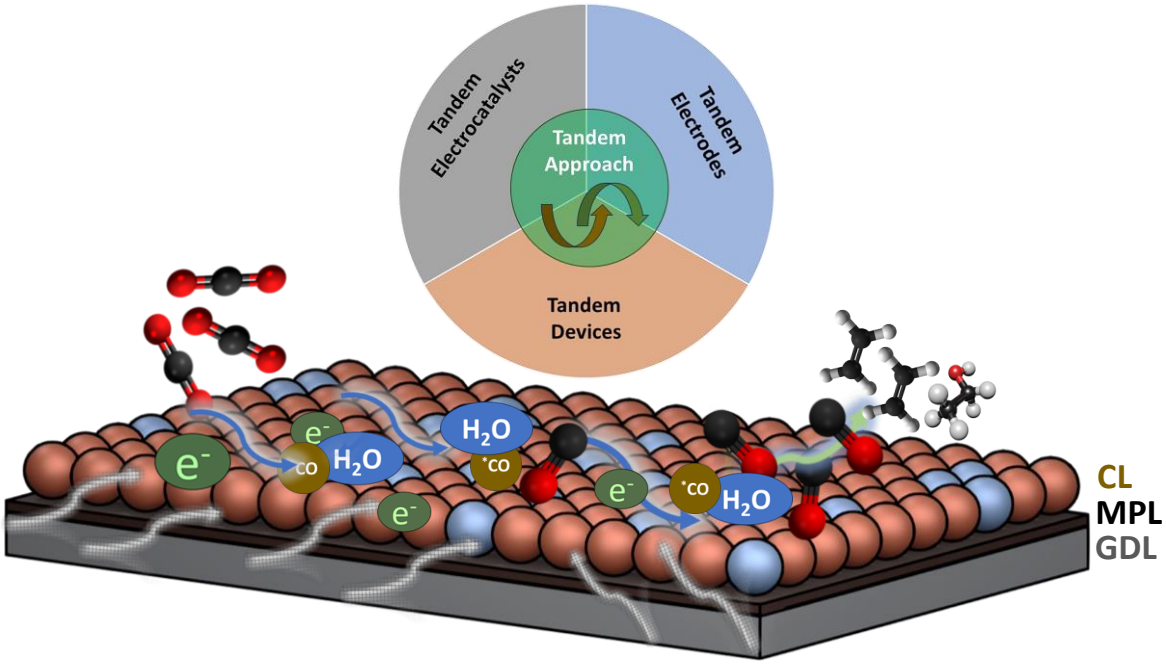
Here, we demonstrated an easy and scalable method to produce in-situ growth of oxide-derived copper-based heterostructures over C-Black as a highly robust electrocatalyst for the effective conversion of CO_2 to ethylene. At the interface of Cu_xO-C deposited over the GDE, we attained a faradaic efficiency of 46% at a current density of 200 $mA \cdot cm^{-2}$ in an aqueous flow electrolyzer in neutral media and room temperature electrolysis. GDE-based cathodes exhibited a stable performance for a minimum of 12 hours when sweeping through increasing cathodic potentials after an initial pre-reduction at -0.5V vs RHE. Structural and compositional characterization revealed that nominal Cu/C ratios were determinant in the final structural and morphological properties of the heterostructures. In the blending with optimum performance, we have confirmed the presence of initial dominating CuO phases with platelet-like morphologies having homogenous distribution over the C-Black. The effective reduction of CuO to Cu_2O indicates the initial self-evolution of the catalysts at low polarization conditions. The presence of C-Black had a cumulative effect in not only enabling the high local CO_2 diffusion but also high current densities while having an impact on the formation of more oxidized Cu phases with more homogeneous morphologies during the synthetic procedure. This work from the thesis helps in understanding the concept of carbon-supported metal oxide heterostructures synthesized by a facile hydrothermal route as robust and highly efficient electrocatalysts achieving high conversion and selectivity towards ethylene operating at high current densities thus paving the way for developing industrially viable alternatives to produce high value-added products.

3.8 References

1. Y. Hori, Electrochemical CO_2 Reduction on Metal Electrodes. In: Modern Aspects of Electrochemistry, 42, Springer, New York, NY 2008, p. 89–189.
2. S. Nitopi, E. Bertheussen, S. B. Scott, X. Liu, A. K. Engstfeld, S. Horch, B. Seger, I. E. L. Stephens, K. Chan, C. Hahn, J. K. Nørskov, T. F. Jaramillo, I. Chorkendorff, Chem. Rev. 2019, 119, 7610–7672.
3. S. Y. Lee, H. Jung, N.-K. Kim, H.-S. Oh, B. K. Min, Y. J. Hwang, J. Am. Chem. Soc. 2018, 140, 8681–8689.
4. X. Wei, Z. Yin, K. Lyu, Z. Li, J. Gong, G. Wang, L. Xiao, J. Lu, L. Zhuang, ACS Catal. 2020, 10, 4103–4111.
5. J. Kim, W. Choi, J. W. Park, C. Kim, M. Kim, H. Song, J. Am. Chem. Soc. 2019, 141, 6986–6994.
6. L. Zheng, X. Liu, *Mater. Lett.* 2007, 61, 2222-2226.
7. S. Deng, V. Tjoa, H.M. Fan, H.R. Tan, D.C. Sayle, M. Olivo, S. Mhaisalkar, J. Wei, C.H. Sow, *J. Am. Chem. Soc.* 2012, 134, 4905–4917.
8. H.J. Yang, H. Yang, Y.H. Hong, P.Y. Zhang, T. Wang, L.N. Chen, F.Y. Zhang, Q.H. Wu, N. Tian, Z.Y. Zhou, S.G. Sun, ChemSusChem 2018, 11, 881 – 887.
9. X. Wang, M. Miao, B. Tang, H. Duan, F. Zhu, H. Zhang, X. Zhang, W.J. Yin, Y. Fu, Nano Res. 2023.

Chapter 4

Best-Fit Tandem Approach for the Upscaled Electroconversion of CO_2 to C_2H_4



The contents of this chapter are due for a scientific communication and the manuscript preparation is in progress and will be communicated in a peer-reviewed journal with the title,

Elucidating the Best-Fit Tandem Approach for the Upscaled Electroconversion of CO_2 to C_2H_4

V. S. R. K. Tandava, Andrés Alberto García, Martí Biset-Peiró, Joan Ramón Morante, Sebastián Murcia-López*

4.1 Abstract

Anthropogenic carbon cycle closure is aimed at achieving a tangible reality with the successful implementation of electrochemical CO_2 reduction coupled with renewable electricity. Despite tremendous progress in obtaining carbon products, such as CO and formate, multi-carbon products have been a distant reality in reaching the potential industrial scale. Practical limitations, such as poor selectivity for multi-carbon products in compliance with sluggish kinetics, lead to electrocatalysts suffering from high overpotentials while directly converting CO_2 to C_{2+} products. Several attempts have been made to mimic nature's cascade processes in electrochemical CO_2 reduction as an alternative route to modulate product generation from CO_2 to CO and further reduce CO to C_{2+} products resembling a tandem approach. Multiple tandem approaches have been extensively investigated for multiple reaction steps involving tandem electrocatalysts to tandem devices. While most of these yield a noteworthy multi-carbon product formation, the product distribution varies in the range of products such as ethylene, ethanol, and propanol, including acetates. Therefore, it is important to investigate the most suitable approach for steering the major selectivity towards a single multi-carbon product. Herein, we have carried out a systematic approach to elucidate the best-fit tandem approach starting from tandem electrocatalysts and tandem electrodes, followed by tandem devices. To understand the product selectivity, we chose to operate with a Ni-N-AC single-atom catalyst and Cu_xO-C-based cathodic materials. Initial investigations began with tandem electrocatalysts with Ni-N-AC and Cu_xO-C with varying compositions in the ink formulations and deposited on the gas diffusion layers. A wide range of product distributions were observed, with C_2H_4 being the dominant product. We further executed the tandem electrode design with layer-by-layer deposition of the catalysts followed by a segmented electrode which further enhanced the selectivity towards C_2H_4. Finally, we incorporated a tandem device in which CO_2 is converted to CO in the first cell and CO is sequentially converted to multi-carbon products in the second. When the unreacted CO_2 is trapped using an absorption chamber between these two electrolyzers, a surge in the faradaic efficiency towards C_2H_4 (> 70 ± 3 %) thus accounting for more than 87 ± 5 % towards multi-carbon product faradaic efficiency at an average current density of -150 $mA \cdot cm^{-2}$. This approach was found to be highly efficient not only in terms of faradaic efficiency but also energetically thus aiding the cascade approach with a tandem device setup reaching the potential industrial scale.

4.2 Introduction

As discussed in the previous chapters, recent years have noticed a substantial rise in exploring the ECO_2R with attention to the selectivity towards greater than $2e^-$ products, most multicarbon products. From the previous chapters, it was evident that copper and copper-based materials are the most sought catalytic support for the electroconversion of CO_2 to multicarbon products. Although, copper-based materials are proven to be the right catalysts in the selectivity towards multicarbon products like ethylene, ethanol and propanol, often practical limitations such as deprived selectivity, stability together with sluggish kinetics for C-C coupling hindered the technological advancement. Practically, in ECO_2R, the electron transfer reactions involve a multi-step pathway with several intermediates precisely towards the generation of the multicarbon products. With CO being the stable and key intermediate, ECOR has gained attention as well in the recent past as a result of more favourable kinetics and the formation of oxygenated products at lowered overpotentials. ECOR is further advantageous in avoiding the carbonate/bicarbonate formation, unlike anticipated in ECO_2R which usually suffers from poor CO_2 balance [1-5]. In this regard, inspired by nature, the scientific community invested in mimicking the cascade catalytic processes with multiple reaction intermediates in a tandem approach. Over the years, several studies reflecting the cascading reaction pathways towards the ECO_2R upholding concurrent or sequential steps have been reported to enhance the multicarbon product selectivity and efficiency [6]. In a typical tandem approach, one catalytically active site over the electrode surface selectively reduces the CO_2 to CO. The generated local CO facilitates the surface adsorption as CO* while the other catalytic site performs the necessary C-C coupling to boost the multicarbon product generation [7]. While catalysts like Ag, Ag, Zn and M-N-C (M: Fe/Ni/Co) selectively promote the generation of CO, Cu-based materials promote the generation of multicarbon products like C_2H_4 and ethanol reaching a remarkable surge in FEs over 80-90% for C_{2+} products [8-11].

Several tandem strategies [12] ranging from tandem electrocatalysts/tandem electrodes to tandem devices were explored and are still extensively ongoing with the idea of mimicking nature's multistep reaction pathway enhancing the ECO_2R product selectivity as an alternative to the commonly performed single-step reduction. Although, the tandem studies yielded a substantial enhancement in reaching the targeted selectivity, often the product distribution ranges over several products from C_2-C_3 products [8, 13-16]. Nevertheless, the aforementioned

tandem studies often used noble metal-based catalysts like Ag and Au to generate the CO intermediate which can be a potential drawback at the industrial scale operation with the raw material costs and limited availability. Owing to this, recent works reported the use of M-N-C (Fe/Ni/Co) based single-atom catalysts, metal-organic frameworks, and covalent-organic framework-based catalysts [17-20] representing the usage of non-noble metal-based catalytic systems integrated with the Cu-based catalysts.

Although high FE is usually reported, the practical challenges like separation of the ECO_2R products are complicated procedures making the process energetically below par. Therefore, it is crucial to identify a tandem approach to tune the selectivity majorly towards a single carbon product. As this thesis was focused on the catalyst materials and systems for the electro-conversion of CO_2 to C_2H_4, this chapter presents an emphasis on elucidating the best-fit tandem approach for an upscaled electro-conversion of CO_2 to C_2H_4 including the other majorly detected products. Out of several strategies explored, a few majorly reported approaches were identified at the reactor level to understand product distribution which are

- Tandem catalysts (TC)
- Tandem electrodes (TE)
- Tandem devices (TD)

Tandem catalysts (TC)

As discussed previously, in a standard tandem catalyst system, two different catalytic centres exist, where the CO selective catalytic sites promote the generation of CO which further sheds on to the adjacent Cu-active sites to reduce to C_{2+} products. On the other hand, in most cases, the generated CO rate might outperform the C-C coupling yielding a lowered C_{2+} product formation [21] indicating a high FE for CO which might not be the ideal requirement in a tandem approach. Not only do the CO selective active sites convert CO_2 to CO, but also significantly influence the catalytic properties of the adjacent Cu-active sites, which strongly impact the further reduction of CO to C_{2+} products. Therefore, it is imperative to fabricate the right combination of tandem catalysts particularly focusing on a single majorly dominant ECO_2R product. Though the TCs in this work were a simple concept of the physical addition of catalyst materials during the ink formulations, often the previous works cited above were proof that the fabrication of TC requires a stringent and complex chemical synthesis.

Tandem electrodes (TE)

It is understood that the major determining factor in the tandem approach is to attain a superior C-C coupling by elevating the optimum local surface concentration of the CO at the Cu active sites [13]. To maximize the in-situ generated CO absorption and enhance C-C coupling, the separation of the catalyst layers was proposed so that the catalysts were deposited sequentially in different layers [22, 23] giving the scope for tandem electrodes (TE) in a layer-by-layer manner (LbL). As discussed previously by T. Zhang et.al., [22] the spatial arrangement of the catalyst layers shall govern the spatial and temporal profile of the local CO availability at the electrode level thus aiding in enhancing the generation of C_{2+} products. In the TEs, the temporal and spatial profiles of CO concentration can be analogous to a Plug-Flow (PF) reactor, while the TC approach resembles a Continuously-Stirred Tank Reactor (CSTR). As the additional CO is generated from the CO-active catalytic sites which further results in poor utilization of the local CO available, often a noticeable increase in the FE of CO shall be noticed in TCs. This highlights the importance of spatial management of the catalyst layers. Practically, in a TE, a CO-selective catalyst layer is deposited over/below the C_{2+} selective catalyst layer to maximize the gas transport in the GDE and the concentration of CO at the electrode-electrolyte interface and further dimerization along the layer of the C_{2+} catalyst layer. Also, the fabrication of TEs is simple as it requires a simple yet orderly deposition of catalyst materials on the GDEs, unlike the traditional TCs. Additionally, the TEs benefit from lower onset potentials and higher partial currents with the intrinsic effects aided by the electrode architecture as the reaction pathways are broken down into multiple steps across the catalyst layers instead of a direct ECO_2R. It is also to be noted that LbL electrodes modulate the in-situ generated CO in a planar direction which can be further improved along the electrode as suggested by Zhang, T *et al*. [18] employing segmented electrodes. Unlike the LbL, the segmented electrodes usually incorporate a CO-selective catalyst layer segment nearing the inlet of feed CO_2 followed by the C_{2+} catalyst layer over the remaining end of the electrode. Thus, the CO segment of the electrode initially maximizes the CO generation, and the effective spatial management of the locally concentrated CO tends to further dimerize to C_{2+} products across the length of the electrode.

Tandem devices (TD)

Both TCs and TEs previously reported demonstrated a substantial enhancement in C_{2+} selectivity at lowered overpotentials. From the concept of TEs, it is anticipated that the spatial management of catalyst layers intrinsically benefits from lowered overpotentials which in turn favour the concept of having separated catalyst deposited electrodes mounted electrolyzers over individual electrolyzers. Eventually, in another approach towards the cascade mechanistic catalysis, previous studies have reported the breakdown of complex electron transfer reactions in a multistep pattern where the products from one reaction become the reactants for the next. Instead of utilizing the in-situ generated CO as stated in TC and TE, CO is generated at the maximum rate using the CO-selective GDE deployed electrolyzer and is directly supplied to the electrolyzer fitted with Cu-GDE to further reduce the CO to C_{2+} products implying a tandem mechanistic approach [24]. It is evident that the supplied CO_2 to the initial electrolyzer is not fully converted into CO, indicating the supply of a mixture of gases (CO_2 and CO) to the second electrolyzer. The mixture of CO_2 and CO supplied to the second electrolyzer is expected to have a lower selectivity for C_{2+} products when compared to the pure CO feed. Therefore, in order to absorb the unreacted CO_2, an alkaline solution to trap the unreacted CO_2 [25] further escalates the FE towards the C_{2+} products and more precisely towards C_2H_4. The trapped CO_2 generates the undesired carbonate reservoir that can further be used for direct carbonate/bicarbonate electroreduction to C-products [26].

Owing to the aforementioned tandem strategies, the study presented in this chapter demonstrates a systematic investigation that was carried out to elucidate the best-fit tandem approach to enhance the C_2H_4 selectivity. Therefore, two different catalyst systems were chosen to fabricate the catalysts and electrodes and further set up the individual electrodes for tandem devices. For these studies, the ideal catalysts were chosen based on the previous report by Zheng et al., [27] an earth-abundant/ non-noble metal, Ni-based single-atom catalysts over activated carbon (Ni-N-AC) and the previously discussed (in Chapter 3) Cu_xO-C heterostructures [28]. Ni-N-AC and Cu_xO-C are henceforth represented as Ni and Cu for easy understanding and representation. The initial screening began with the TC where Ni and Cu were chosen for the catalyst ink formulations in different ratios of Ni:Cu namely 1:1; 1:3; 1:5 and 1:10. The as-prepared inks were deposited onto the Sigracet 39 BB gas diffusion layers (SGL/GDEs) and directly evaluated to understand the product distribution over different ratios

of the catalysts chosen. In continuation to TC, the best-performing combination of Ni:Cu was chosen to fabricate the TE in a layer-by-layer and segmented manner to monitor the variations in product selectivity and overpotentials. To understand the effect of CO reduction, ECOR was carried out over Cu catalysts with CO feed along with a combination of CO and CO_2 mixtures to understand the variations in selectivity towards C_2H_4. The further extension was carried out with TD, where individual electrodes of Ni and Cu were fabricated and mounted over different electrolyzers. As described above, the products from the first electrolyzer act as the reactants for the second electrolyzer facilitating a higher degree of ECO_2R product combination. Subsequently, to further extend the TD set-up, a KOH absorption chamber was introduced in between the electrolyzers to trap the unreacted/excess CO_2 from the first electrolyzer. We report an exponential surge in the faradaic efficiency towards C_2H_4 (> 70 ± 3 %) thus nearly reaching the desired outcome of maximizing the C_2H_4 at a relatively lower overpotential when compared to the other tandem approaches mentioned above. The stated approach also accounts for more than 87 ± 5 % towards multi-carbon (C_{2+}) product faradaic efficiency at an average current density of -150 $mA \cdot cm^{-2}$. Additionally, with periodical replacement of the catholyte, the TD set-up is quite stable by maintaining the C_2H_4 selectivity and low HER activity for more than 18 hours of continuous operation. This approach was found to be highly efficient not only in terms of faradaic efficiency but also energetically thus aiding the cascade approach with a tandem device setup reaching the potential industrial scale. However, the excessively generated carbonated reservoir seems to be challenging, direct carbonate electroreduction must be a viable alternative at the industrial scale.

4.3 Objectives

The main objectives of the studies presented in this chapter are

- To identify a catalyst system with maximizing the CO selectivity to use along with the previously reported Cu_xO-C in a tandem approach.
- To initially fabricate the tandem electrocatalysts and understand the product distribution over different ratios of the catalysts chosen.
- To fabricate the tandem electrodes by tailoring the deposited catalyst layers to understand the variations in the product selectivity.

- To investigate the CO reduction (ECOR) with Cu_xO-C heterostructures thereby identifying the improvements in the selectivity towards C_2H_4 along with the combination of CO_2 and H_2 to understand the stir in product selectivity.
- To evaluate the tandem devices following the cascade mechanistic approach where the products of electrocatalytic cell-1 shall be the reactants of cell-2.
- To investigate the advantages of separating/trapping the unreacted feed CO_2 from cell-1 in upscaling the electroconversion of CO_2 to C_2H_4.

4.4 Highlights

To understand the tandem approach and to find the best strategy, a thorough investigation was carried out to meet all the mentioned objectives and the following observations are highlighted.

- An efficient, highly selective and stable electrocatalyst, Ni-N-AC was synthesized with a modified synthetic protocol for ECO_2R to CO generation.
- The previously discussed Cu_xO-C heterostructures were evaluated under alkaline conditions for superior performance towards C_2H_4 selectivity while lowering the HER activity at relatively higher partial current densities.
- Out of the different combinations of Ni:Cu TCs, fabricated and evaluated, 1:5 (Ni1:Cu5) was found to have superior performance with lowered HER and overpotential.
- The fabricated TE with a layer-by-layer approach with Cu5/Ni1) was found to enhance the CO selectivity at the initial currents and further C_2H_4 at higher current densities.
- The proposed TD was found to generate C_2H_4 at a relatively lower onset potential when compared to the TC and TE.
- After trapping the unreacted/excess CO_2 from the initial electrolyzer, a surge in FE towards C_2H_4 i.e., > 70 ± 3 %) is noticed at a cathodic potential of just -0.81 V *vs* RHE.
- The TD set-up with the trap chamber is exceptionally stable for more than 18 hours of continuous operations.

4.5 Experimental Methods

A note to the reader

The detailed experimental protocols for the synthesis of catalyst materials and chemical materials used in this chapter have been discussed in Chapter 2, *Experimental Materials, Methods, and Systems involved in Electrochemical CO_2 Reduction*. A detailed explanation concerning the technique for GDE fabrication, general characterization techniques and experimental setup involving the CO_2 flow electrolyzer was also included in Chapter 2. However, a brief description of the fabrication of the GDEs is mentioned hereunder to enable the reader to follow this chapter.

4.5.1 Synthesis of the electrocatalyst materials

Synthesis of Ni-N-AC

Ni-N-AC synthesis was adopted and slightly modified from the previous work by Zheng et al., [23]. The reader can find the detailed explanation in section 2.2.4 of Chapter 2 of this thesis.

Synthesis of Cu_xO-C

The detailed synthetic protocol for Cu_xO-C has been described in section 2.2.2 of Chapter 2 of this thesis. Additionally, the physicochemical and electrochemical characterization along with the evaluation of Cu_xO-C for ECO_2R under neutral conditions has been already discussed in Chapter 3. However, the studies reported in the present chapter are under alkaline conditions and also the GDE substrate was changed to Sigracet 39BB (SGL) instead of Toray carbon paper.

4.5.2 Electrode Fabrication

Fabrication of Ni-N-AC GDE

Catalyst ink was prepared by dispersing 20 mg of catalyst powder of Ni-N-AC to 2 mL of 2-propanol and 100 µL of 5 wt % Nafion. The dispersion was sonicated for an hour and the catalyst ink was spray-coated on the GDE uniformly with an effective mass loading of ≈ 1.5 ± 0.1 $mg \cdot cm^{-2}$. The as-prepared electrodes were dried in a vacuum oven at 60 °C for at least 12 h before use.

Fabrication of Cu_xO-C GDE

Catalyst ink was prepared by dispersing 20 mg of catalyst powder of Cu_xO-C to 2 mL of 2-propanol and 100 µL of 5 wt % Nafion. The dispersion was sonicated for an hour and the catalyst ink was spray-coated on the GDE uniformly with an effective mass loading of ≈ 1 ± 0.25 mg·cm^{-2}. The as-prepared electrodes were dried in a vacuum at 60 °C for at least 12 h before use. Additionally, similar electrodes were fabricated to evaluate under CO/ CO+CO_2/ CO+H_2 environments.

Fabrication of Tandem Catalysts

GDEs based on TC were fabricated by the physical addition of Ni-N-AC (Ni) and Cu_xO-C (Cu) in varying combinations. TC Ni1:Cu5 catalyst ink was formulated by the physical dispersion of both the catalyst materials in equal amounts (5 mg of each) in 2 mL of 2-propanol and 100 µL of 5 wt % Nafion. The mixture was sonicated for an hour and the catalyst ink was spray-coated on the GDE uniformly with an effective mass loading of ≈ 1 ± 0.2 mg·cm^{-2}. Similarly, TC Ni1:Cu3 (5 mg Ni and 15 mg Cu), TC Ni1:Cu5 (5 mg Ni and 25 mg Cu) and TC Ni1:Cu10 (5 mg Ni and 50 mg Cu) catalyst inks were formulated and carefully spray-coated on the GDE uniformly. The effective mass loading of each electrode is estimated to be around ≈ 1 ± 0.25 mg·cm^{-2}.

Fabrication of Tandem Electrodes

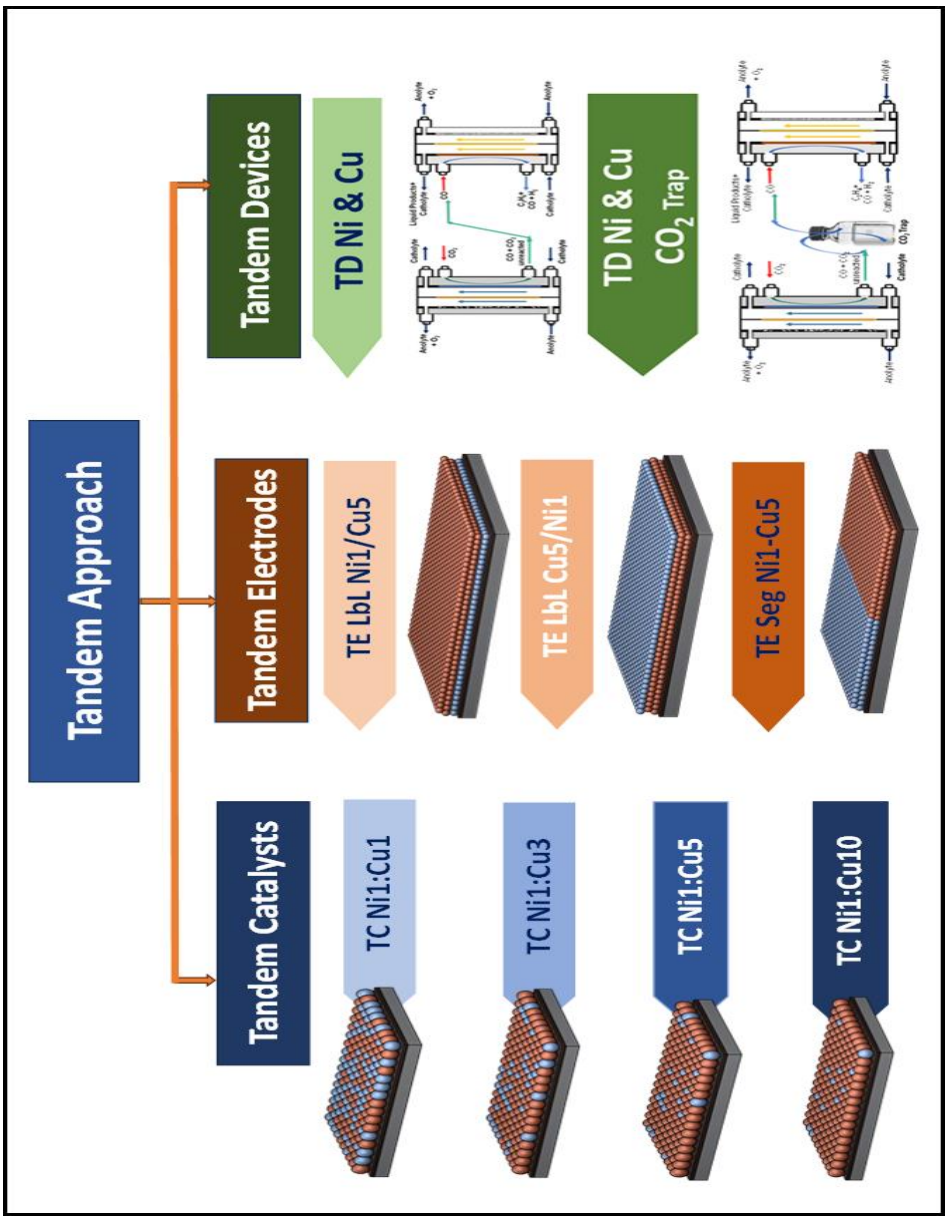
The best-performed combination of TC, *i.e.,* Ni1:Cu5 was chosen to fabricate the LbL oriented TEs. In the first instance, Ni-based catalyst ink was formulated as mentioned above and spray-coated over the GDE followed by Cu-based ink, represented as TE Ni1/Cu5. It was later followed by exchanging the layers by spray-coating the Cu first followed by Ni and represented as TE Cu5/Ni1. The segmented electrode TE Ni1-Cu5 is also prepared by first depositing Ni (1 mg of Ni) at the first half of the GDE where CO_2 initially passes and Cu (5 mg of Cu) at the other half of the GDE representing the varying segments of catalyst layers over the GDE.

Fabrication of Tandem Devices.

The as-prepared individual electrodes, Ni-N-AC and Cu_xO-C GDEs, as described above, were mounted in each electrolyzer and the electrolyzers were connected in tandem. All the electrodes prepared have a relative geometric area of 5 cm^2 (2*2.5 cm^2). However, for the TDs, to enhance the productivity of CO, a 10 cm^2 (3*3.4 cm^2) area electrode was used in the cell-1.

A chart containing all the approaches investigated using the fabricated electrodes with device set-up is depicted in Chart 4.1.

Chart 4.1 Chart representing the electrodes developed for elucidating the best-fit tandem approach.



4.6 Results and Discussion

To maximize the C_2H_4 selectivity, as discussed in previous sections, it was assumed to evaluate three varying tandem approaches. To begin with, individual catalyst evaluations were carried out to understand the ECO_2R product distribution in an individual electrolyzer set-up.

4.6.1 Individual Catalyst performance

This study first establishes the individual performance of an electrolyzer mounted with GDE with Ni-N-AC to maximize the selectivity of CO from CO_2. The electrode structure and the schematic activity of ECO_2R can be seen in Figure 4.1. Under neutral conditions, a constant circulation of 20 $mL \cdot min^{-1}$ of 1M $KHCO_3$ as the electrolyte and with DSA being the anode separated by an AEM, Fumasep FAB-PK-130, chronopotentiostatic measurements were carried out with a constant inlet CO_2 supply of 20 $mL \cdot min^{-1}$ at varying current densities ranging from -10 to -100 $mA \cdot cm^{-2}$.

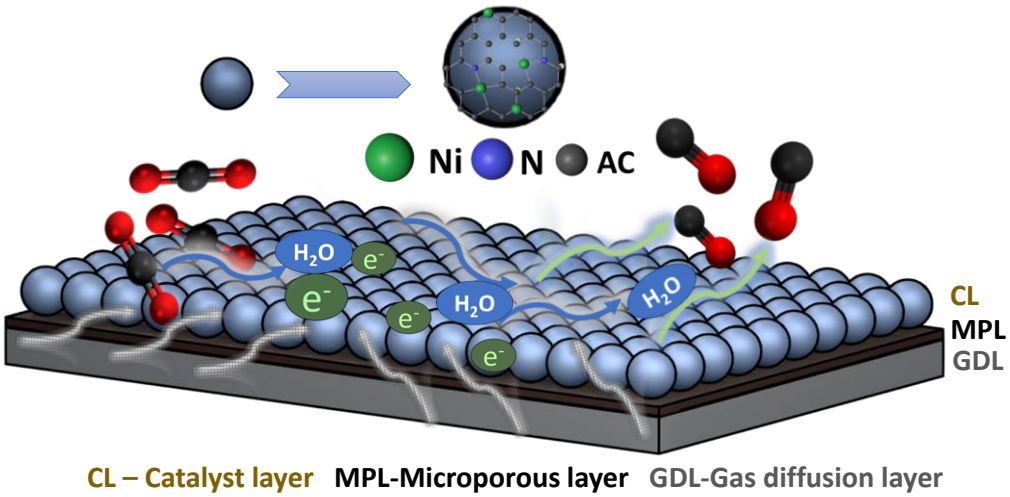


Figure 4.1 Schematic representation of GDE with Ni-N-AC for ECO_2R activity towards CO.

Each current density was applied for 1 h at least and the products were analyzed using the online GC at every 30-minute interval and the average FE % was reported. As depicted in Figure 4.2, the product distribution of CO and H_2 varied with increasing current densities. At an initial current density of -10 $mA \cdot cm^{-2}$, (Figure 4.2 A) the CO FE is noticed to be around 98.5 ± 1 %, corresponding to the cathodic potential of -0.63 V vs RHE with only 1.5 ± 1 % of H_2. When the current density further increased, a slightly higher FE% of H_2 was noticed. At -50 $mA \cdot cm^{-2}$, the CO FE was still maintained over 95 % with 4-5% of H_2. At a maximum of -100

mA·cm^{-2}, H_2 was found to surge to 16 % while CO still maintained over 85% of FE. The corresponding cathodic potentials along with partial current densities are shown in Figure 4.1 B. To further continue with Ni-N-AC, the electrolyzer was chosen to operate at -50 mA·cm^{-2} to maximize the CO productivity with minimal HER activity.

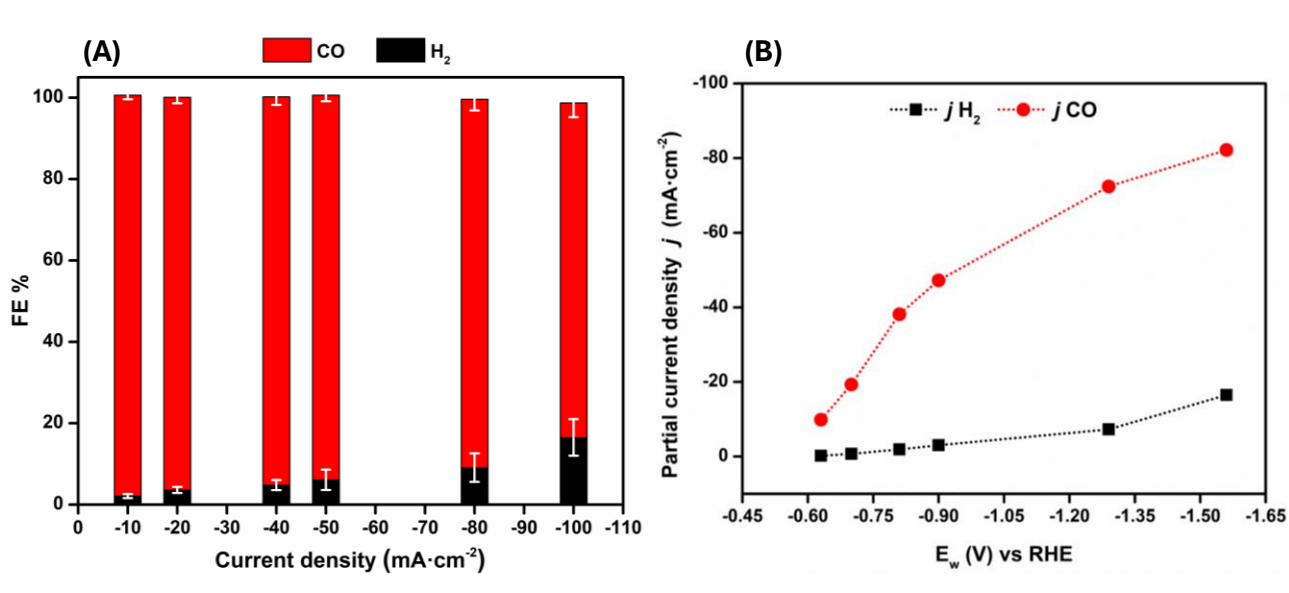


Figure 4.2 ECO_2R of Ni-N-AC **(A)** and respective cathodic potentials with observed partial current densities **(B)**.

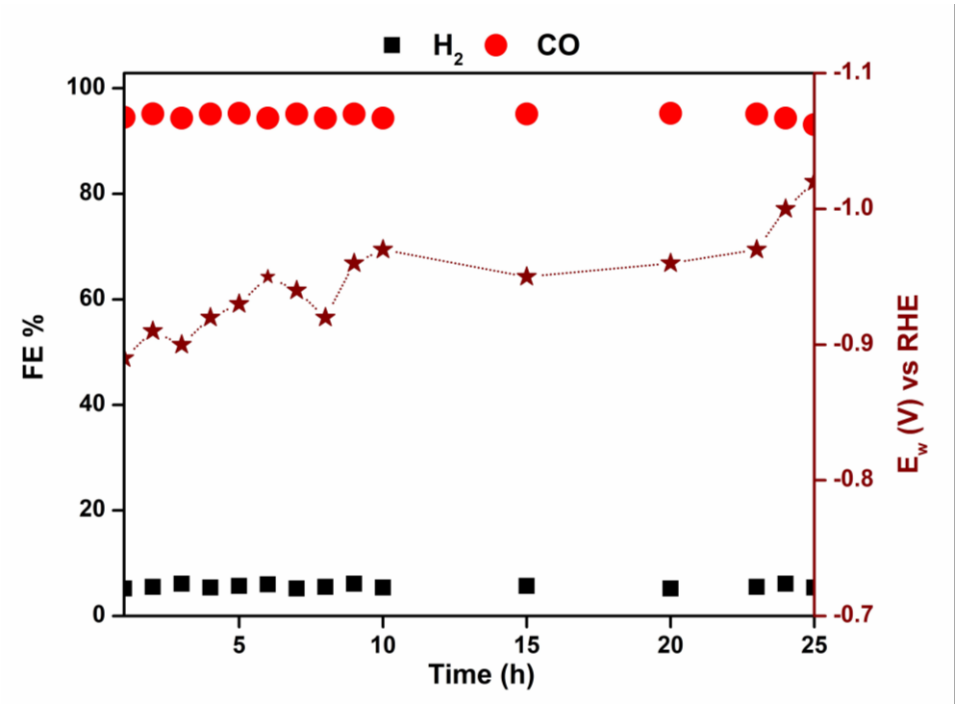


Figure 4.3 Long-term stability test of GDE with Ni-N-AC for ECO_2R.

In continuation, a stability test was conducted to evaluate the long-term sustainability of the electrolyzer at -50 $mA \cdot cm^{-2}$. The exceptional stability of the Ni-N-AC-based electrolyzer was observed as seen in Figure 4.3, over 25 h of continuous operation. While a constant FE towards CO (≈ 95%) with minimal HER activity, (FE of H_2 ≈ 5%) was noticed, and a spike in cathodic potentials with increasing hours of operation can be assigned to the slower degradation of the GDE along with the catalyst. It is important to note the electrolyte was replenished every 6-7 hours during the electrolysis to minimize the pH variations that could affect the overall performance of the electrolyzer.

In continuation to Ni-N-AC, further evaluation of Cu_xO-C was also carried out. Cu_xO-C was previously evaluated for ECO_2R under neutral conditions by chronoamperometric measurements. In parallel to this study, the catalyst was evaluated under alkaline conditions by chronopotentiostatic measurements. The previously used electrolyte, $KHCO_3$ was replaced by KOH to improve the ionic conductivity and operate at high local surface pH at the triple-phase boundary. It was evident that alkaline electrolytes favour the enhancement of C_{2+} products at relatively higher current densities while lowering the overpotentials and minimizing the selectivity towards H_2 and CH_4 [29-30]. Furthermore, over the pre-oxidized surfaces like Cu_xO-C, it was also demonstrated that the local pH shall partially lower the HER activity thereby promoting the selectivity of C_{2+} products [31-32]. A commercial nickel foam was used as the anode without any treatment and an AEM, Fumasep FAA-PE-50 membrane was used to separate the catholyte and anolyte compartments. The schematic representation of the electrode architecture is depicted in Figure 4.4 during ECO_2R with intermediates CO* and the final major product C_2H_4.

Under a constant supply of 12 $mL \cdot min^{-1}$ of both CO_2 and electrolyte, ECO_2R was performed at varying currents from -60 to -180 $mA \cdot cm^{-2}$ and the product selectivity was depicted in Figure 4.5 A. The corresponding cathodic potentials along with partial current densities of H2, CO, C_2H_4 and C_{2+} products are depicted in Figure 4.5 B. Under alkaline conditions, the initial onset potentials were lowered, and the FE was enhanced when compared to the previous results in neutral media [24]. At a maximum current density of -180 $mA \cdot cm^{-2}$, an average C_2H_4 FE of 43% was noticed with more than 60 % of FE for C_{2+} products. The decrease in the cathodic potentials shall be attributed to the localized pH because of the electrolyte along with a higher stability of Cu_2O, the critical active site playing a role in enhancing the selectivity towards C_2H_4

while limiting the FE of H_2 to < 22 % which is nearly half of the FE previously noticed under neutral conditions indicating a superior performance under alkaline conditions.

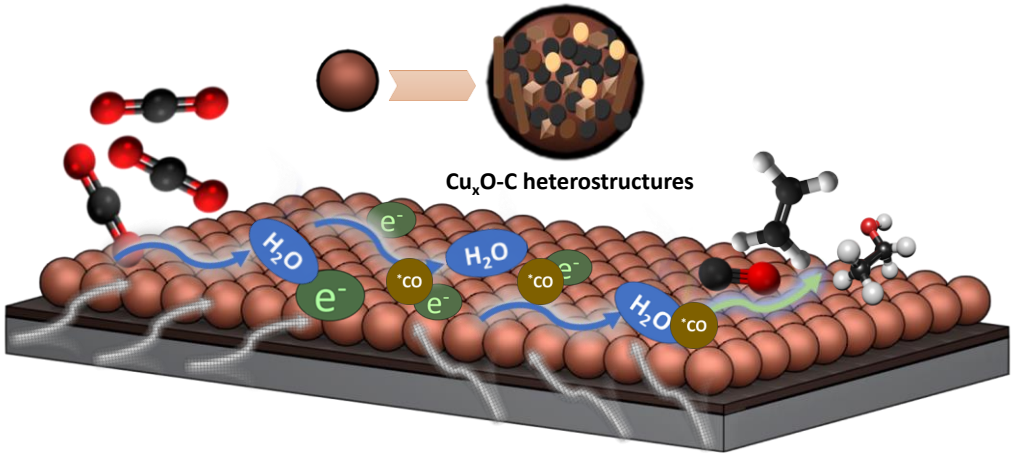


Figure 4.4 Schematic representation of fabricated GDE with Cu_xO-C for ECO_2R towards C_2H_4.

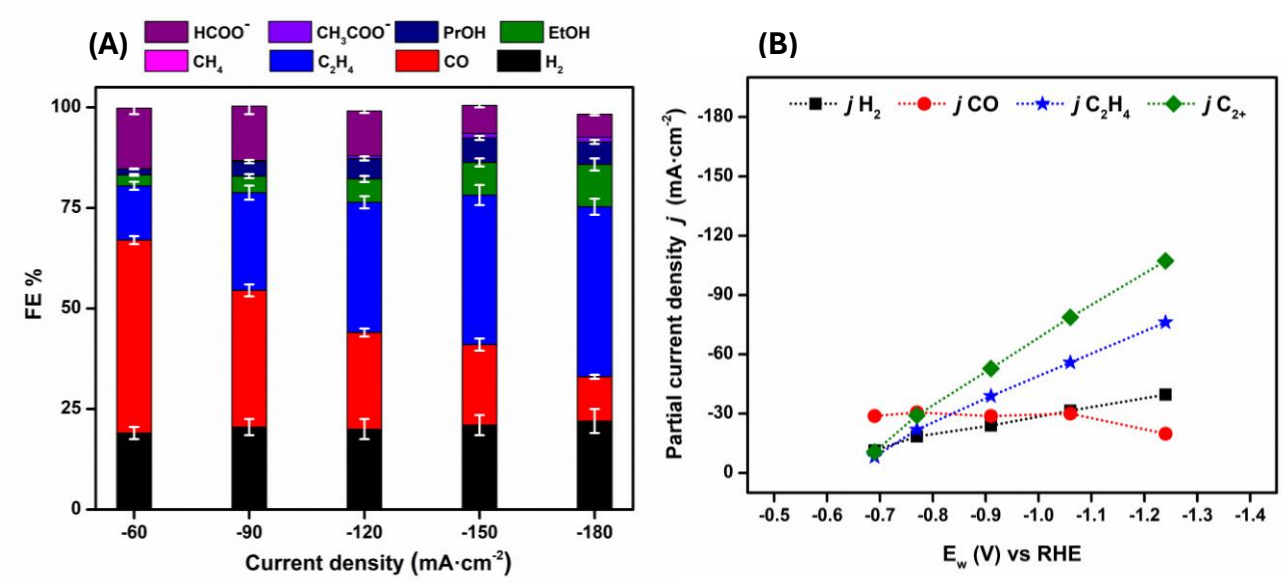


Figure 4.5 ECO_2R of Cu_xO-C **(A)** and respective cathodic potentials with observed partial current densities **(B)**.

4.6.2 Tandem Catalysts

After the initial evaluation of individual catalysts, the focus was levied on understanding the tandem effect by dispersing the desired ratios of Ni to Cu indicating a tandem approach. In the tandem catalyst, TC Ni:Cu for the ECO_2R, As mentioned above, four different combinations of Ni:Cu (TC Ni1:Cu1, TC Ni1:Cu3, TC Ni1:Cu5, TC Ni1:Cu10) were prepared, and the electrodes were examined under similar conditions to the individual electrode of Cu_xO-C. The gaseous products were determined and quantified using an online GC while the alcohols were estimated using the HS-GC. Both acetate and formate were calculated using an HPLC. Figure 4.6 compares the ECO_2R performance of all the samples analyzed under varying current densities. The FE of each majorly obtained product (> 0.5%) is shown with error bars. Initially, the screening of TCs began with TC Ni1:Cu1 (Figure 4.6 A) where Ni and Cu are present in equal ratios. At the initial applied current densities, CO selectivity was favoured substantially with an average FE of 81% while H_2 and C_2H_4 were minimal. With increasing applied current densities, although a noticeable CO was detected, a surge in the FE of H_2 was noticed. When compared with C_2H_4, which peaked at just 16% at a current density of -180 $mA{\cdot}cm^{-2}$, H_2 dominated over 30%. From the obtained product distribution, it was evident that Ni-SAC completely dominated the Cu-active sites thereby promoting CO while suppressing the C-C dimerization. TC Ni1:Cu3 (Figure 4.6 B) yielded a better performance when compared to the former showing a maximum FE of 37% of C_2H_4 at a current density of -180 $mA{\cdot}cm^{-2}$. Although CO was initially more favoured, C_2H_4 was generated by increasing the applied currents while managing to minimize the FE of H_2. The increase in the loadings of Cu_xO-C facilitated higher Cu-active sites which in turn took advantage of in-situ generated CO and promoted the C-C dimerization. Further analysis of TC Ni1:Cu5 (Figure 4.6 C) proved to enhance the C_2H_4 selectivity with an FE over 45% while lowering the FE of H_2 to less than 20%. Additionally, formate was also promoted more at the initial currents while ethanol rose to 10% at higher currents. The combination of tandem catalysts was concluded with the final evaluation of TC Ni1:Cu10 (Figure 4.6 D). It can be observed that the performance is very similar to that of 1:5 in terms of initial FE for CO and C_{2+} products. With the increased applied current densities, the electrode suffered from higher overpotentials which can again be attributed to the dominant Cu-active sites. Additionally, the minimal presence of Ni-active sites offered a lowered in-situ CO generation thereby failing to promote the required CO*-CO* coupling. With a glance at

the FE % from different combinations of TC-based GDEs, it is well understood that the optimized Cu-Ni active site ratio shall be the crucial factor in maximizing the stir in selectivity towards C_2H_4 which is majorly TC Ni1:Cu5. In addition to the FE, the observed cathodic potentials at each applied current were compared to the partial current densities of each product as demonstrated in Figure 4.7. Additionally, the designed electrodes and the subsequent mechanistic pathway for ECO_2R are demonstrated in Figure 4.8.

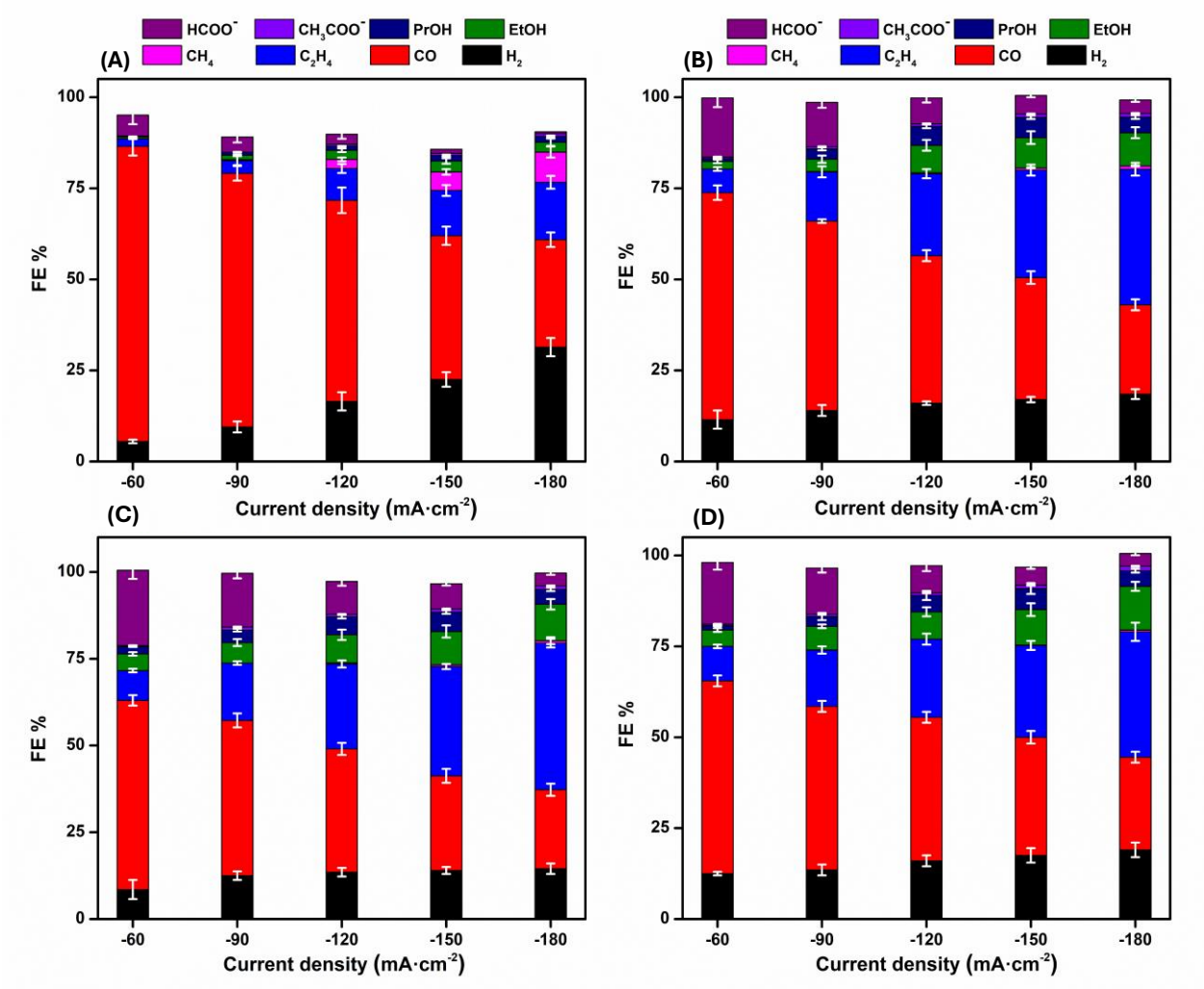


Figure 4.6 Product distribution (FE %) during the ECO_2R with **(A)** TC Ni1:Cu1, **(B)** TC Ni1:Cu3 **(C)** TC Ni1:Cu5, and **(D)** TC Ni1:Cu10.

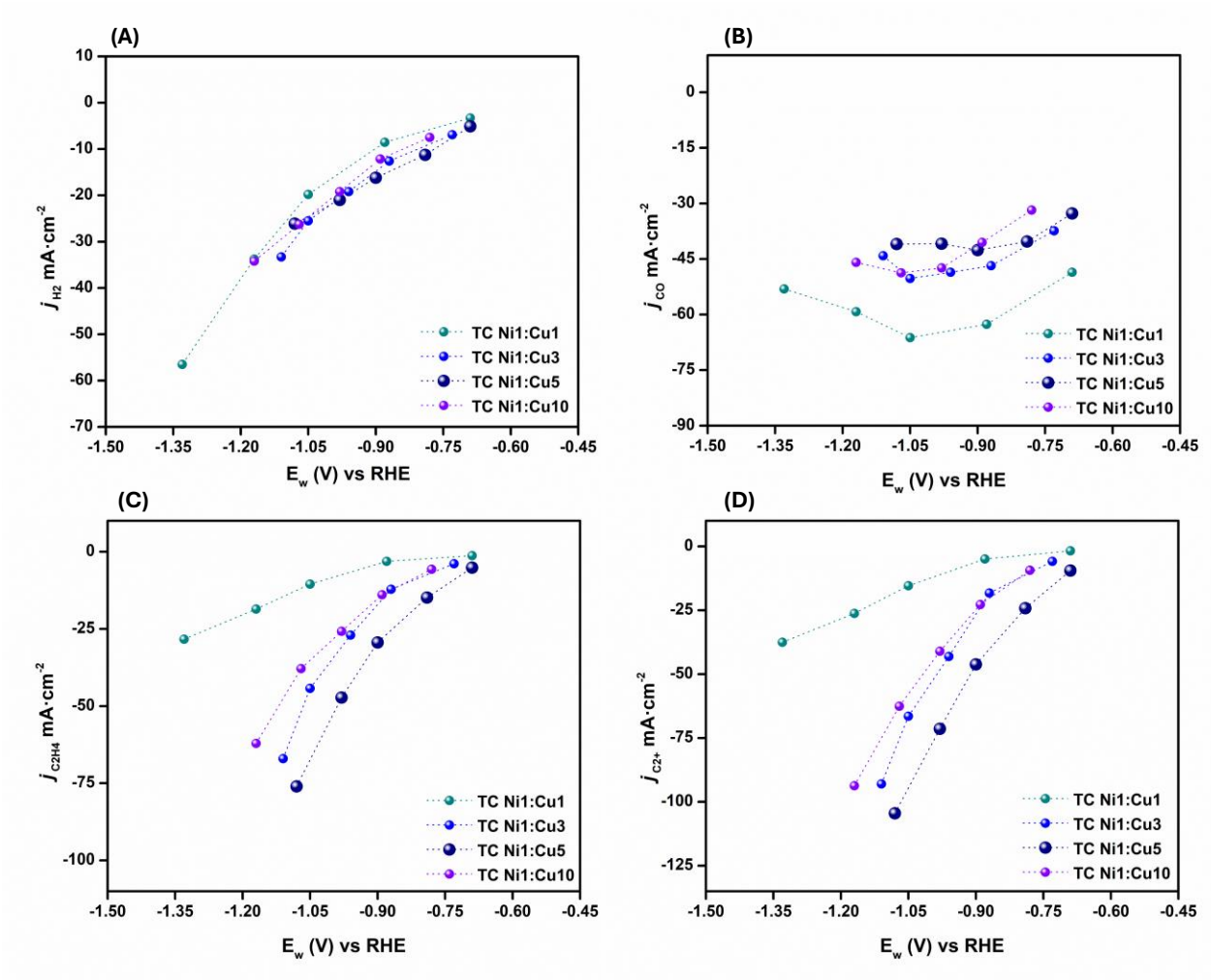


Figure 4.7 Product-wise comparison of partial current densities with the observed cathodic potentials during the ECO_2R with TCs **(A)** *j* H_2, **(B)** *j* CO **(C)** *j* C_2H_4, and **(D)** *j* C_{2+}.

It is evident that the TC Ni1:Cu1 yields higher partial currents for CO and is minimal towards the C_{2+} products compared to the counter combinations at higher overpotentials. A higher CO partial current (j_{CO}) was noticed with the TC Ni1:Cu1 than the Ni-N-AC due to the incorporation of Cu-active sites. Although a higher CO selectivity was favoured initially, it can be inferred that Ni-active sites outperform Cu in minimizing the selectivity towards C_2H_4. While the TC Ni1:Cu10 encountered higher overpotentials due to the dominating Cu-active sites, both 1:3 and 1:5 combinations are relatively similar in the trends of both partial currents and FE the optimized combination, TC Ni1:Cu10 seemed to perform at relatively lowered cathodic potentials thus making it the right combination of TC-based GDEs.

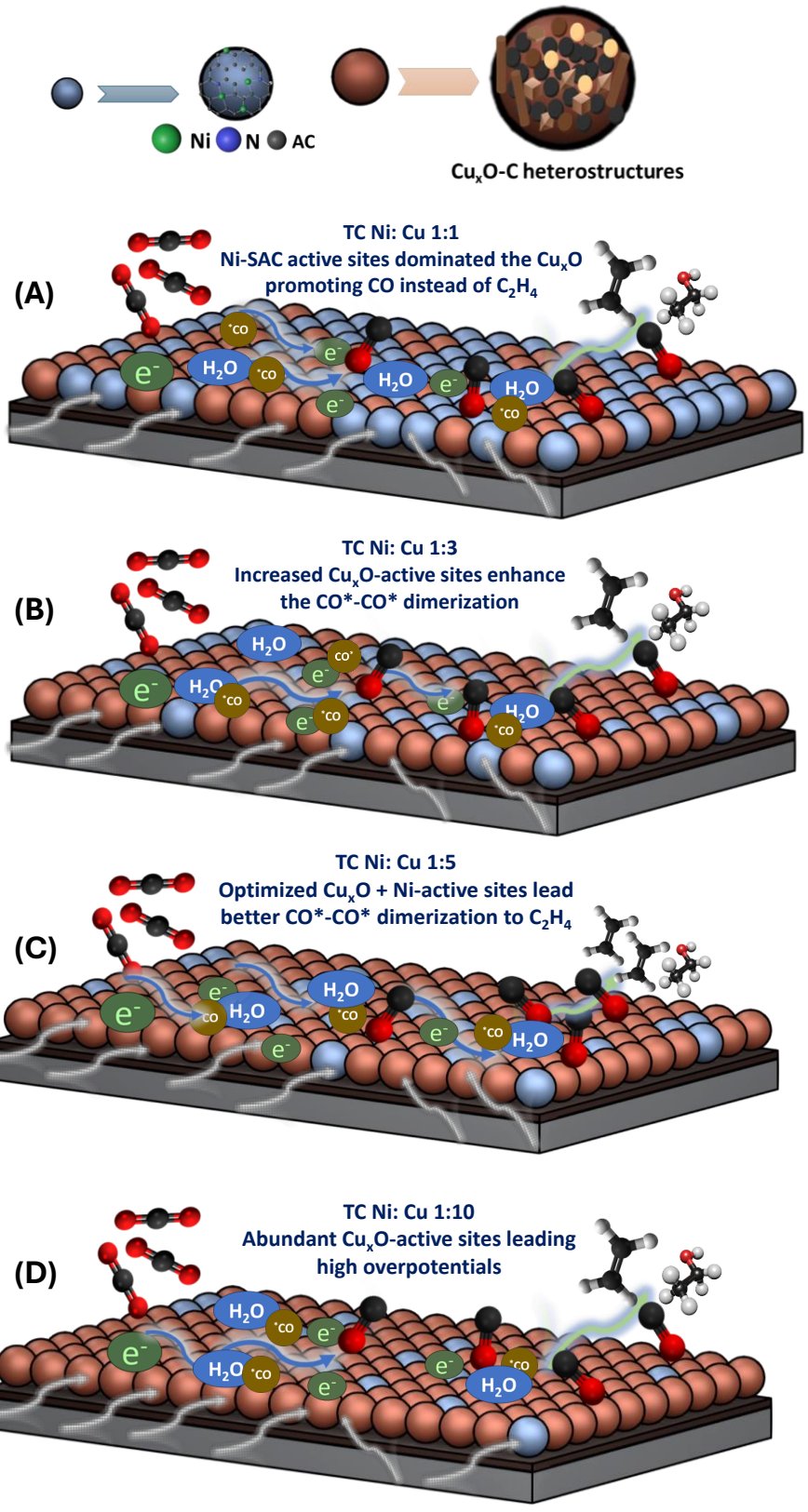


Figure 4.8 Schematic representation of fabricated TC-GDEs with Ni and Cu-active sites. **(A)** TC Ni1:Cu1, **(B)** TC Ni1:Cu3 **(C)** TC Ni1:Cu5 and **(D)** TC Ni1:Cu10.

4.6.3 Tandem Electrodes

With the initial assessment of the TC and choosing the best-performing combination, the focus was further levied on fabricating and evaluating the tandem electrodes with Ni:Cu in a 1:5 combination. The layer-by-layer deposition of the catalysts seemed to deliver superior performance over the previously analyzed TCs. The TEs are designed to exploit the in-situ generated CO flux generated from the Ni-layer and make it available over the Cu-layer resembling a tandem reaction pathway.

Initially, the layer-by-layer (LbL) method of depositing the Ni and Cu catalyst materials was chosen followed by evaluating the role of a segmented electrode. The designed electrodes and the subsequent mechanistic pathway for ECO_2R towards C_2H_4 are demonstrated in Figure 4.9. As seen in Figure 4.9 A, TE LbL Ni1/Cu5, the initial electrode was fabricated with a Ni layer on the GDE, delving into the idea of initial catalyst contact for the feed CO_2, where Ni acts as the in-situ CO generation site while the superficial deposited Cu-layer operates as the site for CO*-CO* coupling facilitating a higher production of C_{2+} products. It is well known that the tandem electrodes uphold the intrinsic benefits of not only lowering the initial onset potentials but also significantly elevating the partial current densities when compared to the Cu-electrode (see Figure 4.4 and 4.11). As seen in Figure 4.9 A, with Ni as the initial catalyst layer, CO is extensively generated at the initial currents followed by the stir in selectivity towards the FE of C_2H_4 reaching around 45% at a maximum current density of -180 $mA{\cdot}cm^{-2}$ (Figure 4.10 A). The Ni/Cu TE suffered from higher HER activity at the maximum currents making it not the desirable approach. In the Ni/Cu LbL TE, it was believed that the inlet CO_2 first gets in contact with the Ni-layer followed by the in-situ generated CO diffusing through the Cu-layer eventually generating C_{2+} products. In a continuum effort, the catalyst layers were interchanged by depositing the Cu layer initially on the GDE followed by the superficial Ni layer (TE LbL Cu5/Ni1) as shown in Figure 4.9 B. Similar to its counterpart, Cu5/Ni1 initially promoted higher CO followed by enhanced C_2H_4 at higher currents as demonstrated in Figure 4.10 B. In this present study it was observed that by interchanging the catalyst layers, the superficial Ni-layer of Cu/Ni moderates the necessary CO onto the Cu layer spiking the high local surface CO* coverage and boosting the selectivity towards C_2H_4 leaving a minor enhancement in the FE nearing 50% and at a lowered cathodic potential than the counterpart Ni/Cu.

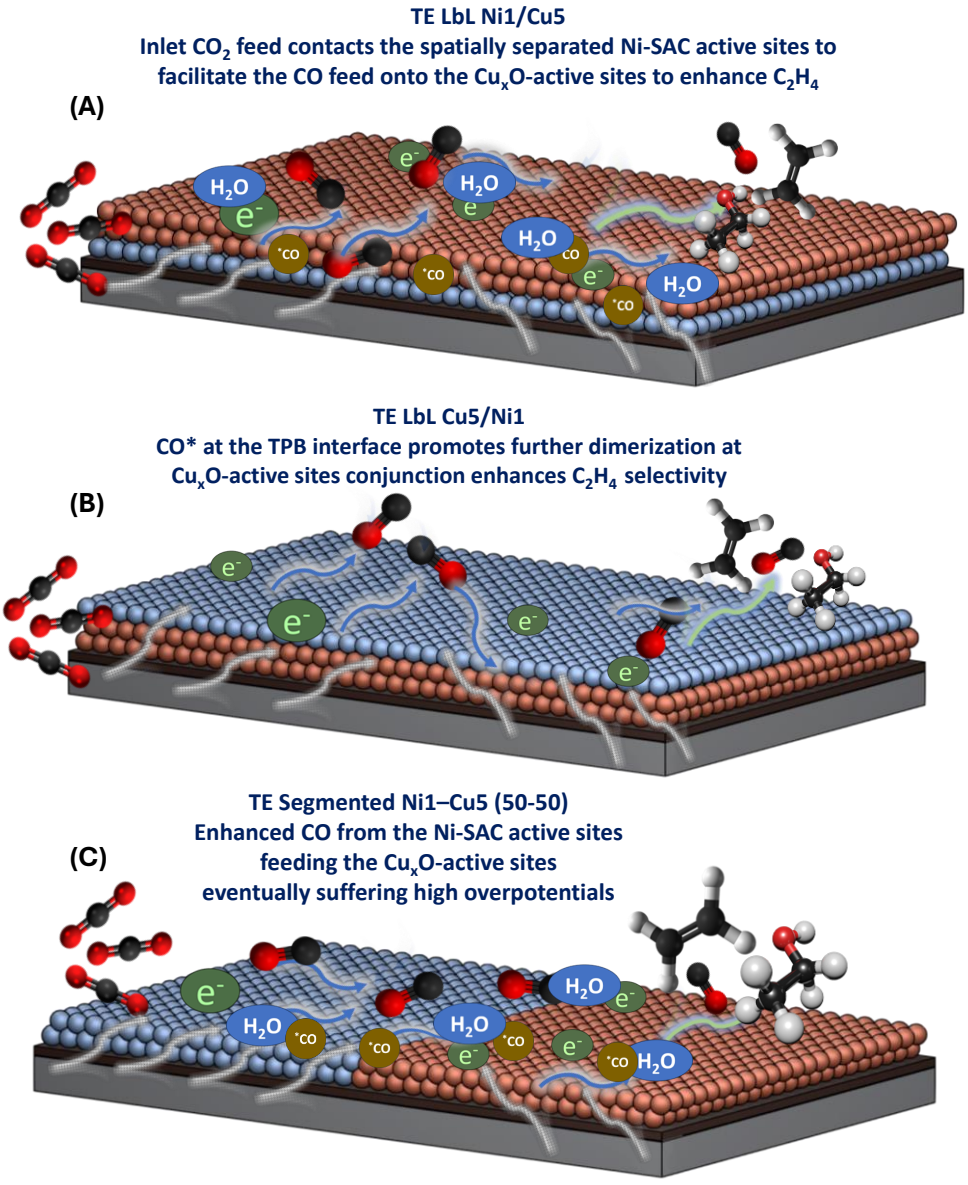


Figure 4.9 Schematic representation of fabricated TC-GDEs with Ni and Cu active sites. **(A)** TE LbL Ni1/Cu5, **(B)** TE LbL Cu5/Ni1 **(C)** TE Seg Ni1-Cu5.

Along with LbL TEs, a segmented (seg) electrode as seen in Figure 4.9 C was also evaluated. The seg TE was designed with the concept of the feed CO_2 initially reaching the first half of the seg electrode which is covered with Ni-segment and later to the Cu segments. The feed CO_2 upon interaction with the highly selective Ni-active sites promotes CO generation. The generated CO flux spills onto the adjacent segment of densely covered Cu-active sites further facilitating the C_2H_4 before exiting the electrolyzer.

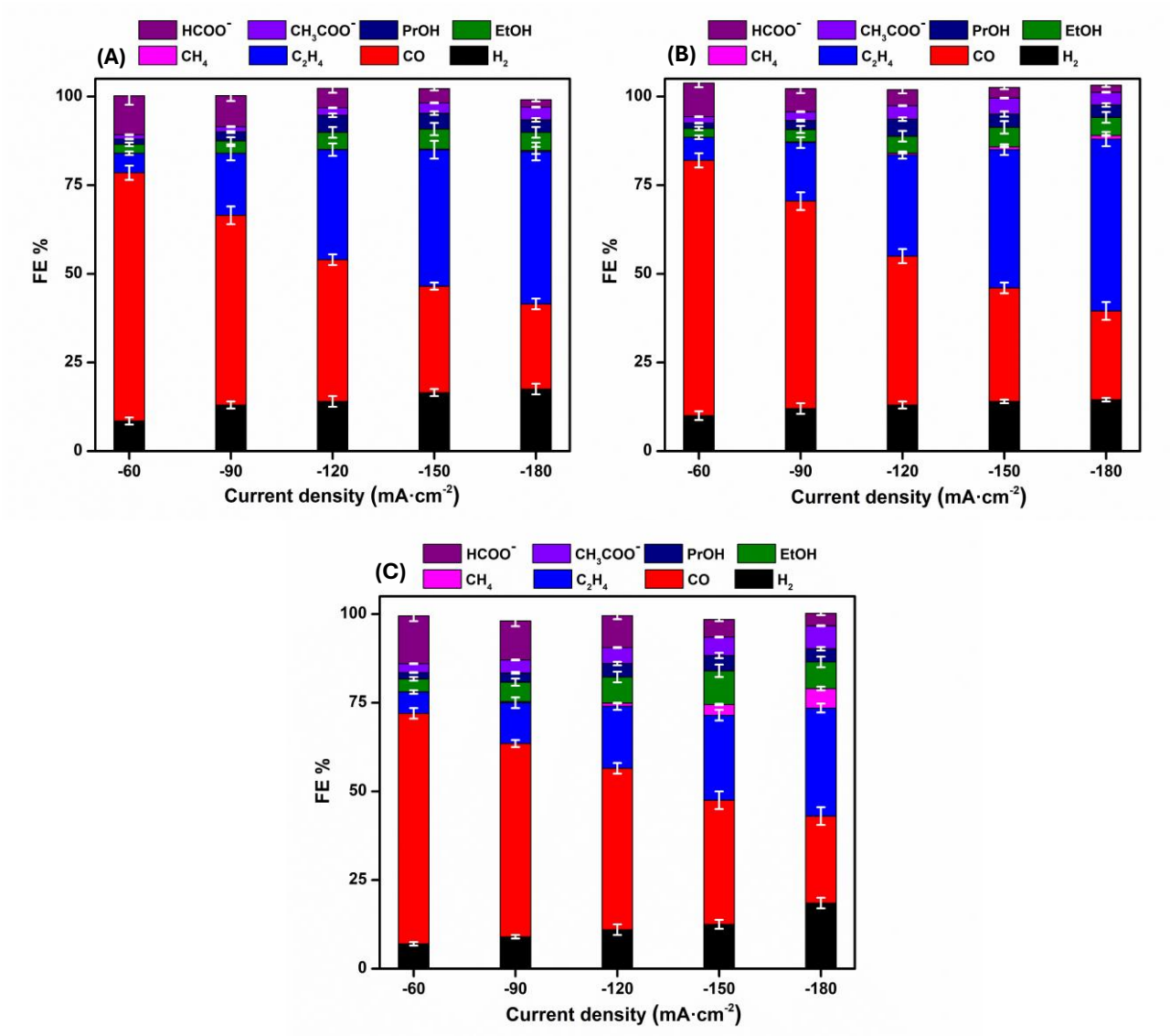


Figure 4.10 Product distribution (FE %) during the ECO_2R with **(A)** TE LbL Ni1/Cu5, **(B)** TE LbL Cu5/Ni1 **(C)** TE Seg Ni1-Cu5.

Unlike the LbL electrodes, the seg electrode performed drastically below par with the LbL electrode in C_2H_4 selectivity as depicted in Figure 4.10 C, making it less desirable in the present study. Interestingly, it was also noticed that the seg electrode favoured the hydrocarbons like methane, ethanol and acetate. Yet, several other combinations of segmented TEs can be fabricated as reported by Zhang, T., et al. [13] to boost the selectivity towards which C_2H_4 which eventually does not fall into the present focus of this study. Interestingly, upon comparing the partial currents concerning the observed cathodic potentials as demonstrated in Figure 4.11, LbL TEs are advantageous in achieving higher partial current densities than the seg electrode and lowered cathodic overpotentials at higher applied currents. Although only minor

differences were observed in terms of C_2H_4 selectivity between the LbL electrodes, Cu/Ni takes the upper hand in attaining a higher C_2H_4 FE of around 50%.

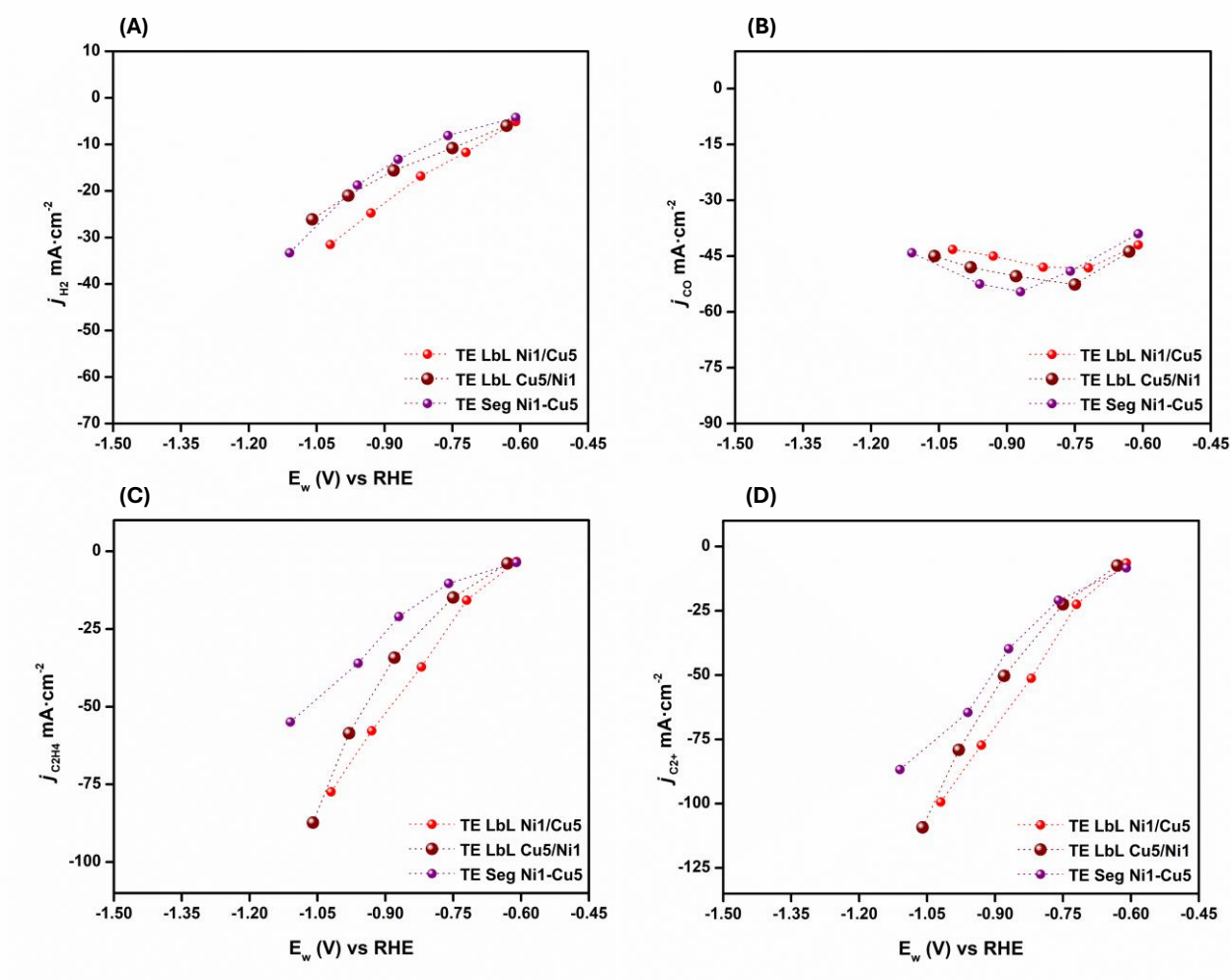


Figure 4.11 Product-wise comparison of partial current densities with the observed cathodic potentials during the ECO_2R with TEs **(A)** *j* H_2, **(B)** *j* CO **(C)** *j* C_2H_4, and **(D)** *j* C_{2+}.

It is also well established from the studies presented in the previous chapter that the Cu-layer which is mainly composed of carbon support (oxide-derived Cu heterostructures supported over carbon) acts as the additional MPL facilitating the diffusion of CO back onto the Cu-layer. The diffused CO, on the Cu, eventually promotes the CO*-CO* coupling which is again well presented by a previous study [22] elaborating the positive effect of the presence of an intermediate carbon layer. Upon comparison with the previously tested TCs and Cu_xO-C GDE, TEs perform significantly better in both lowering the cathodic potentials and attaining higher partial currents. Of the TEs, TE LbL Cu/Ni was identified as the optimized electrode in steering the selectivity towards C_2H_4. From the above findings of TEs, it was understood that the spatial

separation of catalyst layers delivered promising results, the tandem approach further deconvoluted to having the catalysts completely separated mounted in individual electrolyzers and further coupled in a cascade manner depicting tandem devices (TD). Thus, the final focus of this study advances to tandem devices where independent electrolyzers are set up and the products from cell-1 are fed as the reactants in the cell-2 resembling the tandem pathway. It is to be noted that the numbering, cell 1 and cell 2 indicate the order of deployment in the TD set-up.

4.6.4 Tandem Devices

Before advancing to the TDs, it is highly recommended to study the individual electrolyzer performances mounted with electrodes of Ni and Cu-based GDEs. The observed results are demonstrated in Figures 4.1 and 4.4. Along with these, the study was aimed at understanding the influence of pure CO feed (ECOR), and the combinations of CO with both CO_2 and H_2 ($CO+CO_2$ and CO_2+H_2) with the electrolyzer mounted with Cu_xO-C -GDE.

Initially, pure CO was directly fed to the electrolyzer under similar conditions used previously. The evaluated performance of ECOR is depicted in Figure 4.12 A. For comparison purposes, the results of ECO_2R with Cu GDE were also depicted in Figure 4.12 D. Under the CO presence, the FE for each detected product was quantified with the reduced number of electrons (for example towards C_2H_4, while 12 e^- are necessary for direct CO_2 feed, only 8 e^- are needed under CO feed). A surge in the FE of C_2H_4 is detected at the initial applied currents contrary to the ECO_2R outcome indicating the energetically favorable ECOR pathway. Undoubtedly, pure CO aids in enhancing the C_2H_4 selectivity even at higher applied current densities while suppressing the undesired HER activity and the results are in full agreement with the previous studies [33]. Interestingly, at the initial currents, a noticeable FE towards acetate over 25% was noticed which again deteriorated at the higher currents. While ethanol also seemed to have an increasing trend along with C_2H_4 over increased current densities, other C_{2+} products suffered to sustain over higher current densities. At a current density of -150 $mA \cdot cm^{-2}$, an overall FE of 85% is recorded for C_{2+} products with C_2H_4 dominating over 58 % of FE. It is worth noting from the previous chapter, that the deployed catalyst, Cu_xO-C heterostructures evolves in situ during the ECO_2R favouring the sole selectivity towards C_2H_4 over other C_{2+} products making it a highly robust electrocatalyst with major selectivity towards C_2H_4.

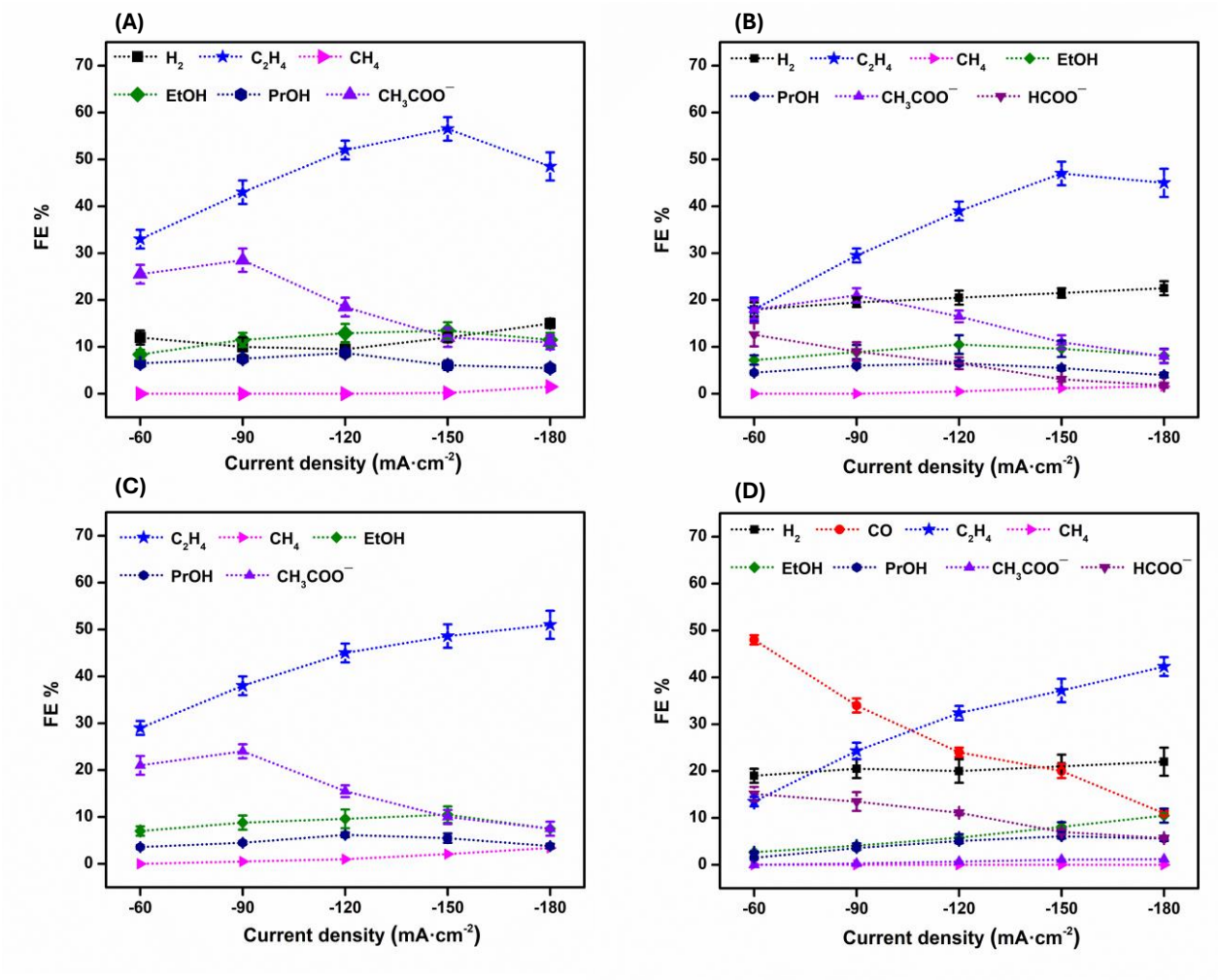


Figure 4.12 Product distribution (FE %) during the ECO_2R/ECOR with **(A)** Pure CO feed, **(B)** CO/CO_2 (0.5:0.5), **(C)** CO/H_2 (0.8:0.2), **(D)** Pure CO_2 feed.

After evaluating the performance of the electrolyzer for ECOR, further focus was invested in the mixtures of CO with CO_2 and H_2. Figures 4.12 B and C depict the FE obtained by varying current densities. With the stream of CO and CO_2 mixture, equal ratios of CO/CO_2 in the mixture were chosen accordingly and tested under similar conditions to that of CO with the Cu_xO-C deployed electrolyzer. With equal amounts of CO and CO_2 in a 50-50 combination, it was estimated that a total of 10 e^- [25] are required for the reduction to C_2H_4. As seen in Figure 4.12 B, C_2H_4 was the initially favoured product while maintaining the selectivity at elevated currents, HER activity was also predominant over 20 % of FE of H_2. The increase in the HER can be attributed to the presence of CO_2 requiring higher energy consumption for further reduction and the reduction of CO_2 to CO is also to be considered with the use of Cu_xO-C. However, it is to be noted that FE % of CO was not reported as it is a highly difficult task to

detect the generated amounts of CO when the reactant stream also had CO. In the end, a total of 75% of FE is recorded for C_{2+} products at an applied current of -150 mA·cm^{-2} while C_2H_4 kept increasing with currents.

In another attempt, a combination of CO and H_2 was chosen in a ratio of 0.8:0.2 (80:20) and evaluated under similar circumstances. A higher amount of acetate was noticed at the initial currents as shown in Figure 4.12 C which further foreseen a decay at higher currents. Almost 5 % of FE for CH_4 was also estimated at the maximum applied currents. A dip in total FE of C_{2+} products was noticed when compared with the streams of pure CO and CO/CO_2 mixture combinations. Similar to the CO, in the stream of CO and H_2, it is complicated to evaluate the HER activity resulting from the Cu_xO-C electrolyzer. A significant surge in the FE of C_{2+} products (particularly C_2H_4) was observed with all the streams of inlet reactant feed gas streams usually at higher current densities which again can be attributed to the presence of CO in the reactant stream thus enabling the CO*-CO* dimerization.

After the careful evaluation of pure and mixed gas stream reduction with Cu_xO-C, the present study finally transcends to the use of tandem devices. As depicted in Figure 4.13, two individual electrolyzers were mounted in a series combination where the product outlet of cell-1 was directly connected to the inlet of cell-2. Considering the experiments of individual catalyst performance of Ni-N-AC and the electrolyzer (see Figure 4.1), electrolysis took off by operating the cell-1 at -50 mA·cm^{-2} with a constant CO_2 supply of 20 mL·min^{-1}. Initially, the outlet was connected to the GC to quantify the amounts of CO and H_2 before connecting to cell-2. A total of 95.2 ± 0.5 % of CO FE was detected with H_2 being < 5% of the total FE. Additionally, to understand the distribution of product stream from cell-1, a long-term quantification was carried out depicting the gas composition. Figure 4.14 demonstrates the gas composition analysis from the outlet of cell-1. The product gas stream at the initial hours of operation constitutes 80% of CO_2 with 15-16% of CO and less than 5% of H_2. As time progressed, the amount of CO_2 was lowered reaching less than 70% while the high production of CO kept accumulating around 22-25% along with a surge in H_2 was also noticed. A mass-flow meter was placed to quantify the amount of gas exiting cell-1. While 20 mL·min^{-1} of inlet CO_2 is fed to the electrolyzer, an average flow of 17-18 mL·min^{-1} was recorded at the outlet during the electrolysis.

After the estimations of the gas composition, the electrolyzer was mounted as cell-1 with a fresh electrode of Ni-N-AC. Again, as described above, similar conditions were used to perform the CO_2 electrolysis. A second electrolyzer was mounted with the electrode of Cu_xO-C as the working electrode and Ni foam as the counter electrode. Unlike the cell-1, cell-2 was operated with 1M KOH as the electrolyte reflecting the similar conditions of TCs and TEs. Once cell-1 reached the steady-state condition, the outlet was directly connected to the inlet channel of cell-2 as seen in Figure 4.13.

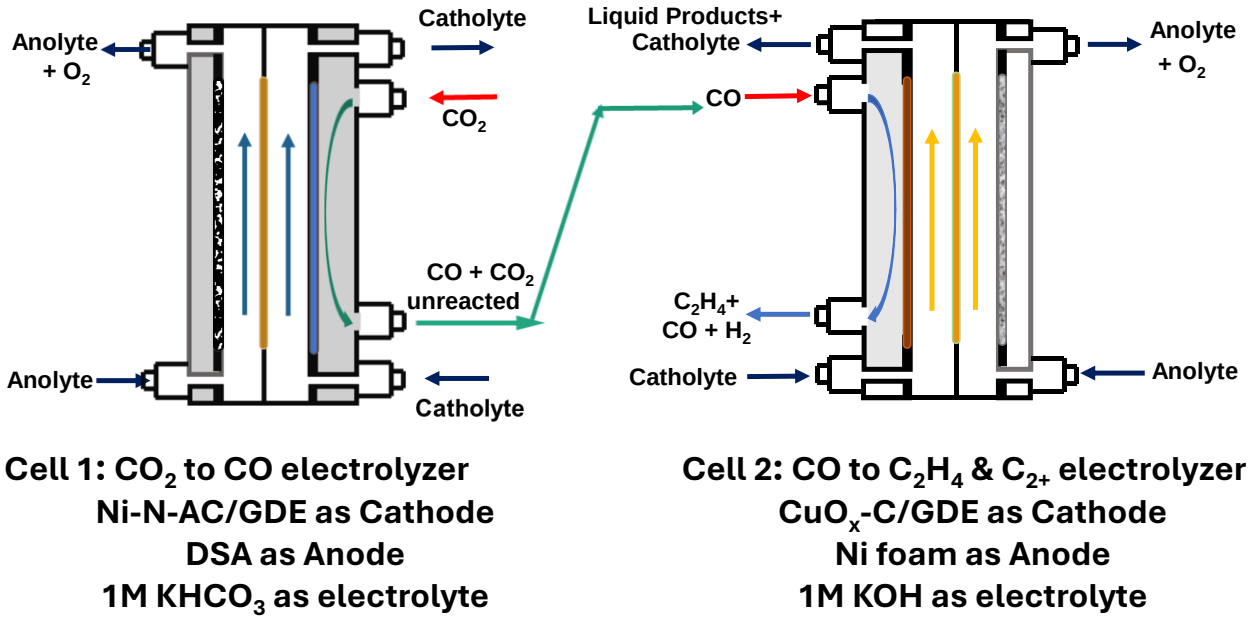


Figure 4.13 Schematic representation of the Tandem devices depicting a cascade mechanistic pathway along with mounted electrodes represented in the text below as cell-1 and cell 2.

By ensuring a stable outlet gas flow from cell-2 was noticed, electrolysis was carried out under similar conditions of TCs and TEs over a range of current densities from -60 to -180 $mA \cdot cm^{-2}$. It is to be noted that for H_2 and CO quantification, the total currents applied on both the cells were taken into account while for the products from cell-2 like C_2H_4 and ethanol, only the applied currents on cell-2 were considered along with the required electrons for reduction (8 e^- for CO as the reactant). It is important to know the differences in electron transfer numbers involved in the electrochemical reactions of both ECO_2R and ECOR. Based on the reactant moiety, i.e., either CO_2 or CO, a certain number of varying electrons are required towards the generation of C_2H_4 and ethanol and other C_{2+} products during the prescribed electrolysis.

Therefore, the major half-cell electrochemical reaction equations specifying the number of e^- and H^+ required for each reaction during ECO_2R and ECOR are listed for C_2H_4, ethanol and propanol. Based on the decreased number of e^- required, it is practically understood that ECOR shall generally be expected to generate a higher rate of C_{2+} products (C_2H_4 and ethanol) when compared to the traditional ECO_2R. Figure 4.15 demonstrates the overall product distribution obtained from the TD. The evaluated FE seemed to be largely similar to the previous pure gas stream mixture feed of CO/CO_2 and CO/H_2. Like the pure stream, C_2H_4 was the dominating product with a maximum FE of around 50% at a current density of -150 to -180 $mA{\cdot}cm^{-2}$ and a total C_{2+} FE of over 65%. From the depicted results, it was well understood that target of maximizing the C_2H_4 selectivity was only partially fulfilled and requires further advancements in TDs. It is critical that the presence of unreacted CO_2 in the gas stream reaching the cell-2 makes the whole TD setup perform poorly which needs to be avoided to enhance the selectivity of C_2H_4.

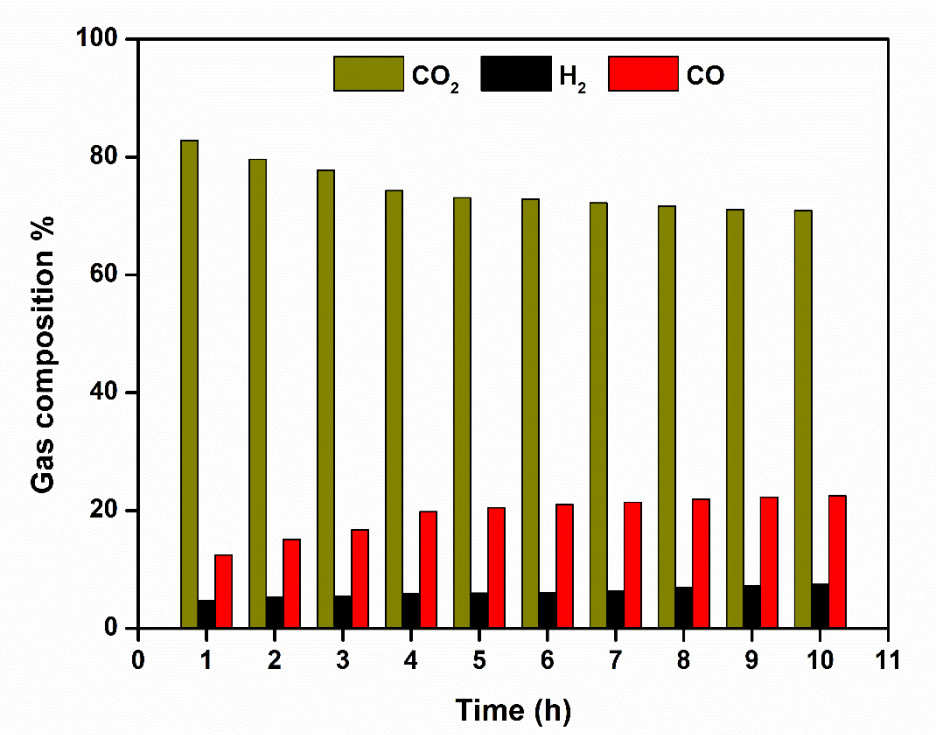


Figure 4.14 Gas composition (%) after the electrolysis in cell-1/before reaching the cell-2.

Electrochemical half-cell reactions at the cathode during ECO_2R:

$2\ H^+ + 2\ e^- \rightarrow H_2$ *(equivalent in both ECO_2R and ECOR)* *(1)*

$CO_2 + 2\ H^+ + 2\ e^- \rightarrow CO_{(g)} + H_2O$ *(2)*

$2\ CO_2 + 12\ H^+ + 12\ e^- \rightarrow C_2H_{4\ (g)} + 4\ H_2O$ *(3)*

$2\ CO_2 + 12\ H^+ + 12\ e^- \rightarrow C_2H_5OH_{\ (aq)} + 3\ H_2O$ *(4)*

Electrochemical half-cell reactions at the cathode during ECOR:

$2\ CO + 8\ H^+ + 8\ e^- \rightarrow C_2H_{4\ (g)} + 2\ H_2O$ *(5)*

$2\ CO + 8\ H^+ + 8\ e^- \rightarrow C_2H_5OH_{\ (aq)} + 2\ H_2O$ *(6)*

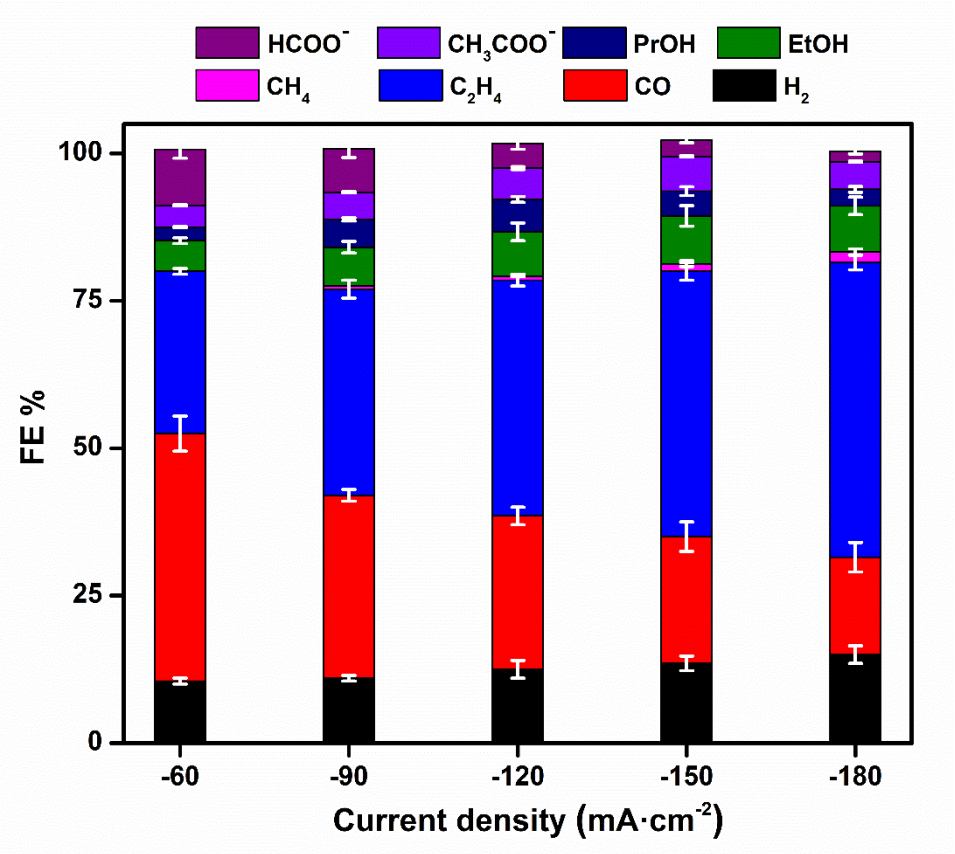


Figure 4.15 Product distribution (FE %) with the TD set-up with coupled cell-1 and cell-2 connected in a series combination.

After monitoring the results from the previous evaluations, to avoid the supply of unreacted CO_2 to the cell-2, an intermediate absorption chamber was incorporated after cell-1. To absorb

the unreacted CO_2, a 6M KOH solution was used and the chamber was referred to as trap. Once the trap was placed and prior to sending the CO_2-filtered stream to cell-2, analyzing the composition of the gas stream after the trap is highly essential. The gas stream after the trap was directly connected to the online GC and the gas composition was estimated over 10 h and depicted as shown in Figure 4.16. As mentioned previously, upon a constant feed of 20 $mL \cdot min^{-1}$ of inlet CO_2 to the electrolyzer, an average flow of 17-18 $mL \cdot min^{-1}$ was recorded at the outlet during the electrolysis. With the incorporation of the trap and CO_2 being absorbed, an average of 4-5 $mL \cdot min^{-1}$ mainly constituting CO with minimal amounts of H_2 of the gas stream was detected constantly which is further fed to the cell-2. A relatively lower flow of inlet gas was fed continuously to cell-2. Based on the volume of the trap chamber used and the time of electrolysis, a periodical replenishment of the KOH was suggested to ensure that CO_2 was not supplied to cell-2. Figure 4.17 depicts the mounted electrolyzers coupled with an intermediate CO_2 trap chamber representing a cascade pathway of TDs. Figure 4.18 shows the photographs of the experimental set-up of tandem device set-up in the laboratory highlighting the individual electrolyzers.

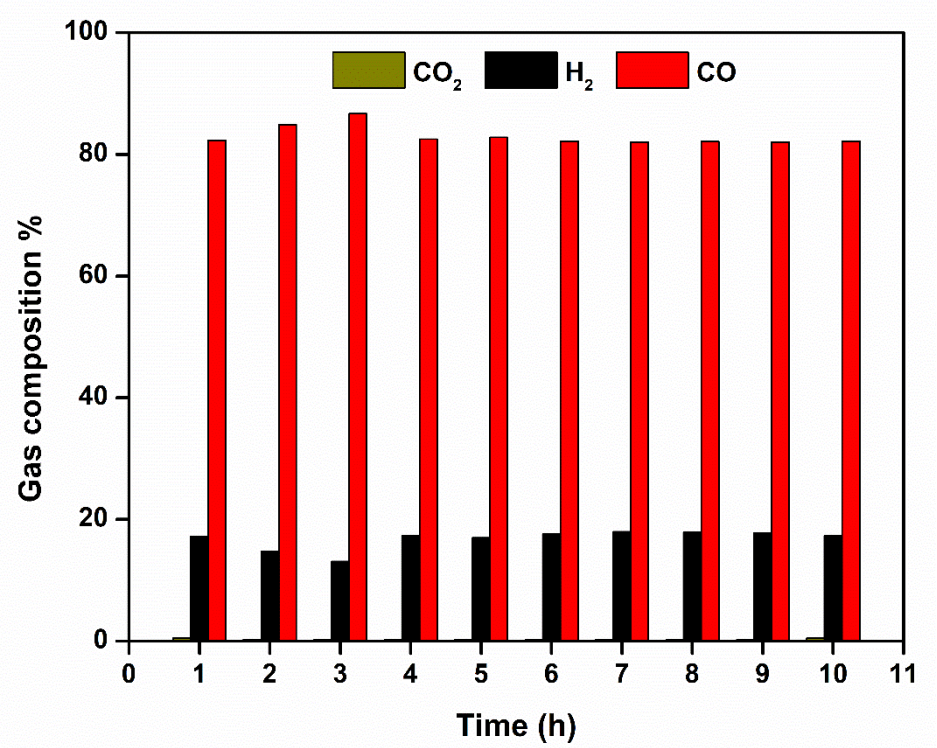


Figure 4.16 Gas composition (%) after the electrolysis in cell-1 and after the incorporated KOH trap before reaching the cell-2.

Eventually, the TD setup with the trap was subjected to electrolysis under similar conditions alike the previous TD set-up. Figure 4.19 demonstrates the electrolysis performance in two steps resembling a tandem approach and how the incorporation of a CO_2 trap chamber aided in enhancing the selectivity towards C_2H_4.

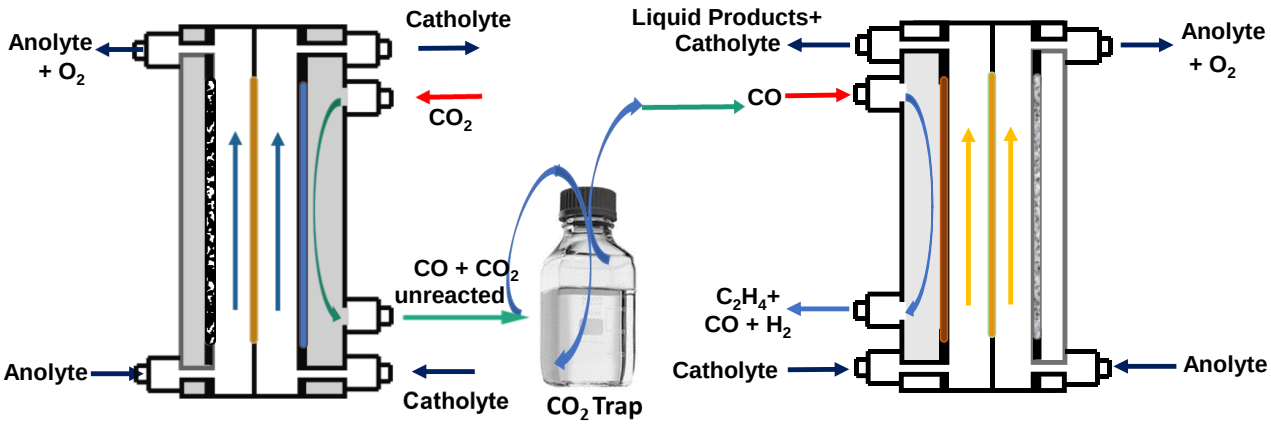


Figure 4.17 Schematic representation of the Tandem devices with an intermediate CO_2 trap chamber depicting a cascade mechanistic pathway.

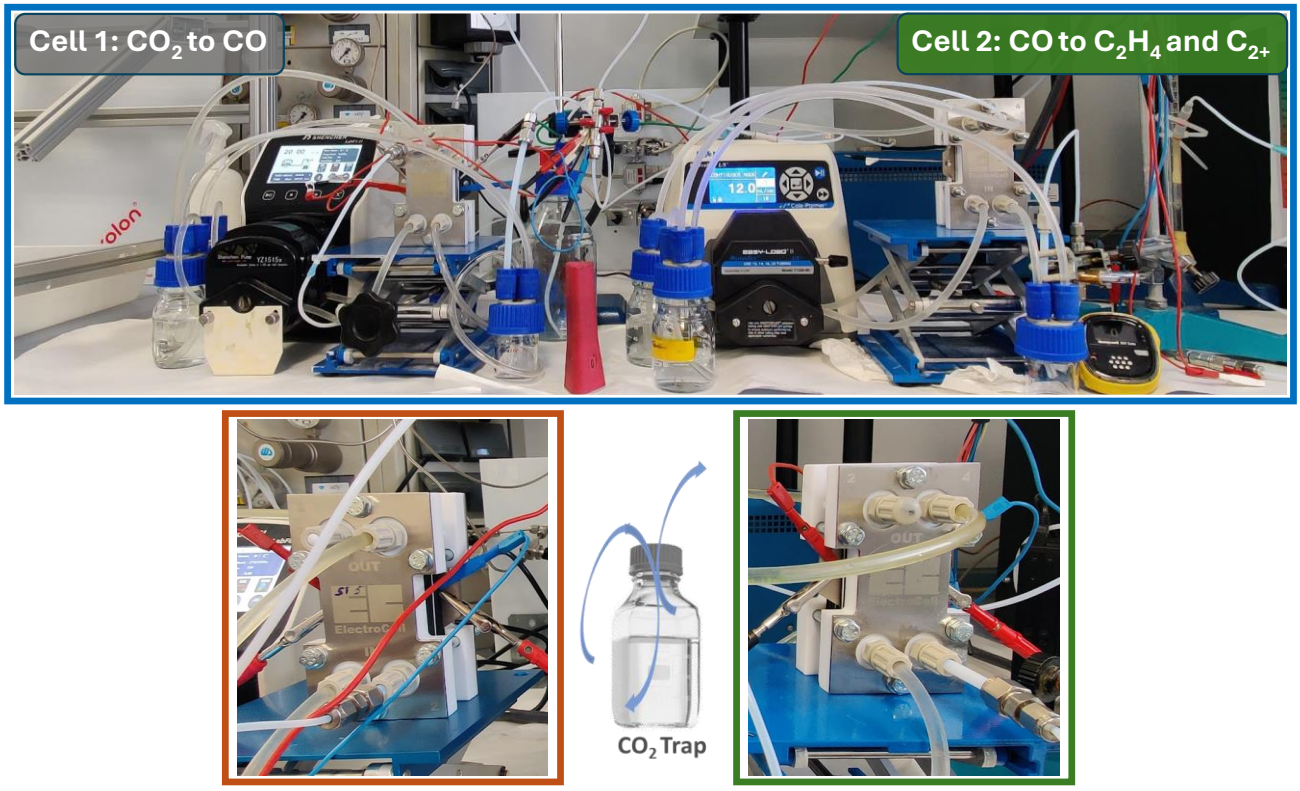


Figure 4.18 Photograph of the actual experimental set-up of a tandem device set-up with an intermediate CO_2 trap in the laboratory with insets showcasing individual electrolyzers.

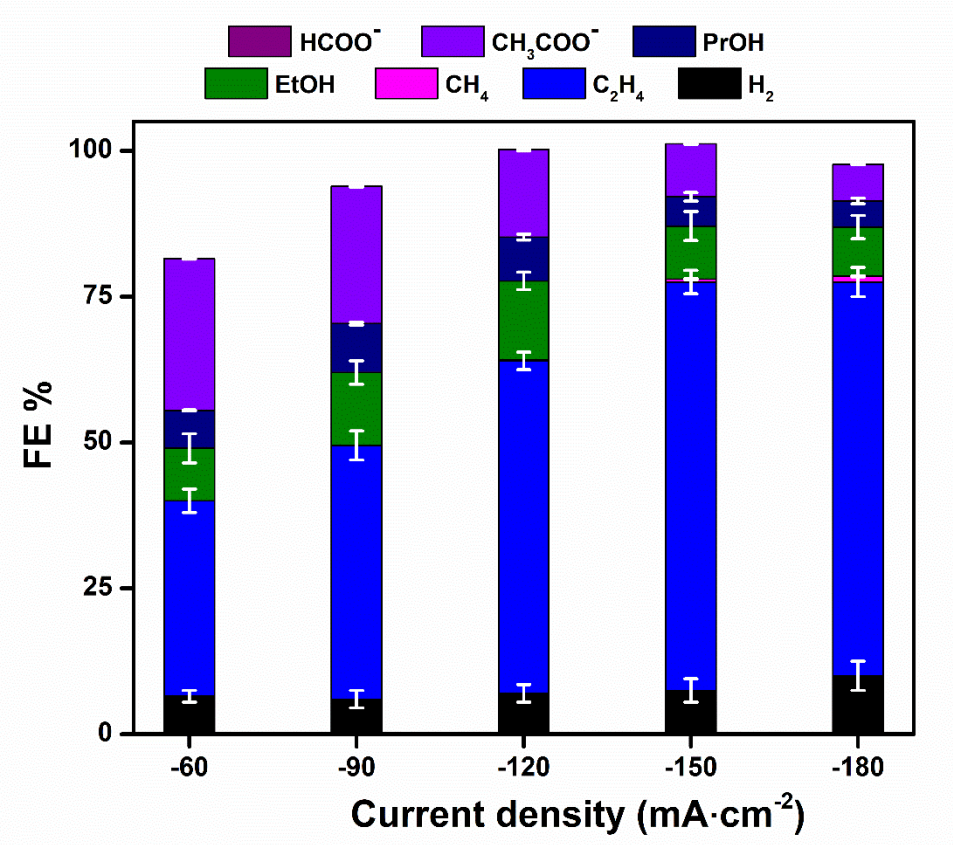


Figure 4.19 Product distribution (FE %) with the TD set-up with cell-1 and cell-2 connected in a series combination with an intermediate CO_2 trap chamber.

Initially at the lowest applied currents, along with C_2H_4 both acetate and formates were the most favoured products. Concerning the performance of the Cu_xO-C mounted in cell-2, only C_2H_4 had increments in FE while acetate's selectivity diminished with increasing applied currents. A maximum FE of 20-25 % of acetate was initially favoured which was later reduced at higher currents. Ethanol also saw a peak FE of 13-15 % at a current density of -120 mA·cm^{-2} which again diminished. The desired product, C_2H_4 seemed to dominate even at the initial currents reflecting the electrolysis with pure CO feed. It was noticed that at a current density of -150 mA·cm^{-2}, the peak FE of C_2H_4 was noticed to be more than 70 ± 3 % and with 87 ± 5 % of total C_{2+} products were obtained thus ensuring the significance of the TD setup coupled with an intermediate CO_2 trap chamber. The FE of C_2H_4 was further declined to 65- 67 % at the maximum applied current density of 180 mA·cm^{-2}. It was interesting to notice that the HER activity was very limited although the total applied current (of cell-1 and cell-2) was considered while estimating the FE of H_2. Throughout the electrolysis, less than 10% FE of H_2 was detected indicating the superior performance of the coupled electrolyzers. The depicted

results outperform the results of pure CO feed which further indicates the impact of CO/CO* residence time over the Cu-active sites. It was a known fact that the feed flow rate to cell-2 was lowered by 3 times (when compared to the CO_2 feed to cell-1) with the incorporation of the trap chamber facilitating the slower immobilization over the Cu-GDE thus enhancing the residence time of CO at the electrode-electrolyte interface.

Figure 4.20 demonstrates the product-wise partial current density comparison with the observed cathodic potentials of the TDs along with the direct gas stream in combination with CO. With pure CO as the reactant feed gas, the onset potentials were drastically lowered. At a working electrode potential of -0.84 V vs RHE, high partial currents of C_2H_4 were noticed with minimal HER activity. The performance of TD setup without the trap chamber with both partial current densities and cathodic potentials aligns in between the mixture gas streams of CO/CO_2 and pure CO feeds thus directing the importance of eliminating the unreacted CO_2. The superior performing TD setup (in terms of FE) with trap also demonstrates the superiority with cathodic potentials. At an applied current density of -150 $mA{\cdot}cm^{-2}$, the recorded cathodic potential was just -0.79 V vs RHE which again represents the energetically efficient TD setup. While the recorded partial currents and cathodic potentials are one step ahead when compared with pure CO feed, it is important to notice that with the incorporation of an intermediate trap chamber, the inlet flow to cell-2 was reduced by 3 times (4.5 $mL{\cdot}min^{-1}$) when compared to the actual flow of pure CO feed (12 $mL{\cdot}min^{-1}$) and pure CO_2 feed (12 $mL{\cdot}min^{-1}$) over TCs and TEs. It was hypothesized that the lowered flow of the CO_2-filtered gas stream aids in enhancing the local CO residence time on the surface of the Cu-GDE which further requires a low energy input (in terms of the number of e^- required) thus making it an industrially viable alternative when compared to the traditional individual electrolyzers and possibly with stack configurations. Furthermore, the best-performing combinations of all the tandem approaches examined in the present study were compared to the ECOR and ECO_2R over Cu_xO-C as depicted in Figure 4.21. Undoubtedly, TD set-up coupled with an intermediate CO_2 trap chamber was found to be superior not only in terms of enhancing the selectivity of C_2H_4 while minimizing HER along with lowering the cathodic working potentials. However, the need for separation of the unreacted CO_2 was a foreseen disadvantage from techno-economical aspects in the operation of the electrolyzers but the lowered energy inputs with respect to the operating cathodic potentials have a positive impact in terms of energy

efficiencies. Eventually, the carbonate or bicarbonate reservoir can be subjected to further direct electroreduction to C-products like CO [22] and CH_4 [34].

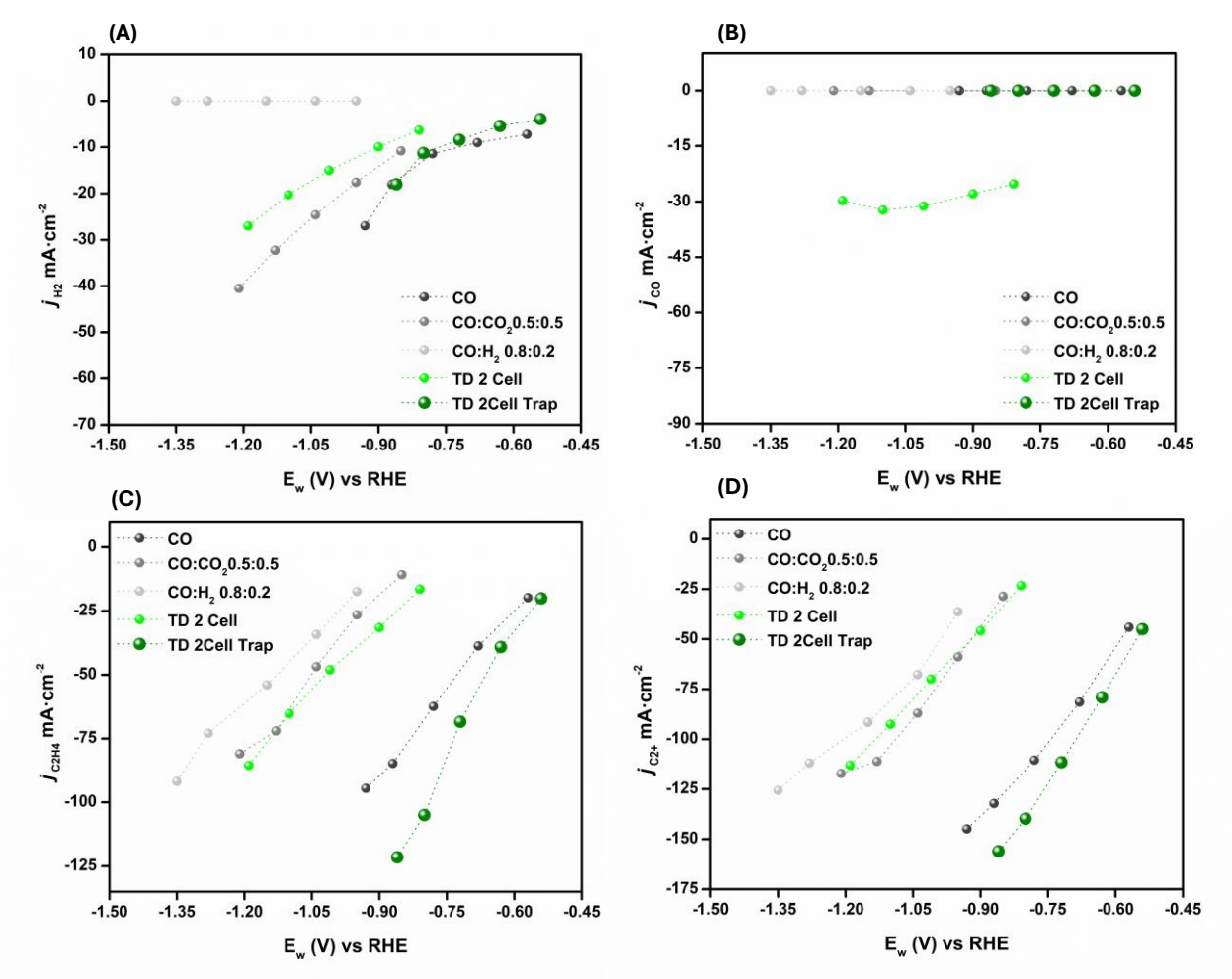


Figure 4.20 Product-wise comparison of partial current densities with the observed cathodic potentials during the ECOR/ECO_2R and TDs **(A)** *j* H_2, **(B)** *j* CO **(C)** *j* C_2H_4, and **(D)** *j* C_{2+}.

In this regard, upscaling to commercial-scale TD set-up is quite feasible to achieve a significant enhancement in the generation of C_2H_4 and other C_{2+} products by following similar or improved operational procedures.

The present study was finally concluded by evaluating the stability of the coupled electrolyzers as a tandem setup. The exceptional stability of the Ni-N-AC-based electrolyzer was already demonstrated in Figure 4.3. Furthermore, a long-term test was necessitated to demonstrate the stability of the TD set-up coupled with an intermediate CO_2 trap chamber. As depicted in Figure 4.19, the best-applied current density was deemed to be -150 $mA{\cdot}cm^{-2}$. Under similar conditions, the electrolysis was performed for several hours with periodical replenishment of

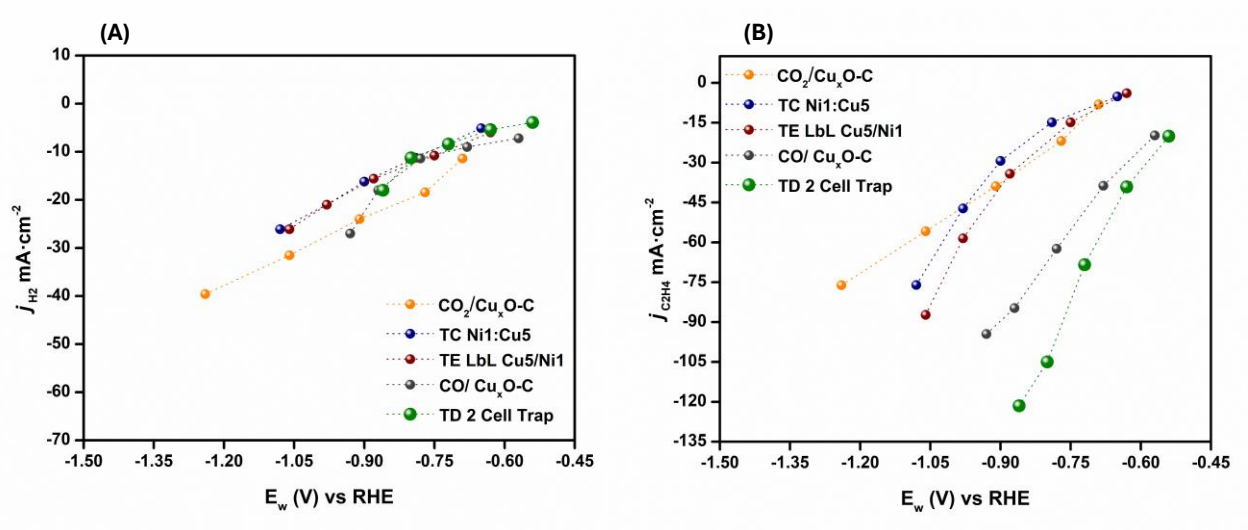


Figure 4.21 Comparison of best-performed tandem approach. Product-wise comparison of partial current densities with the observed cathodic potentials **(A)** *j* H_2, **(B)** *j* C_2H_4.

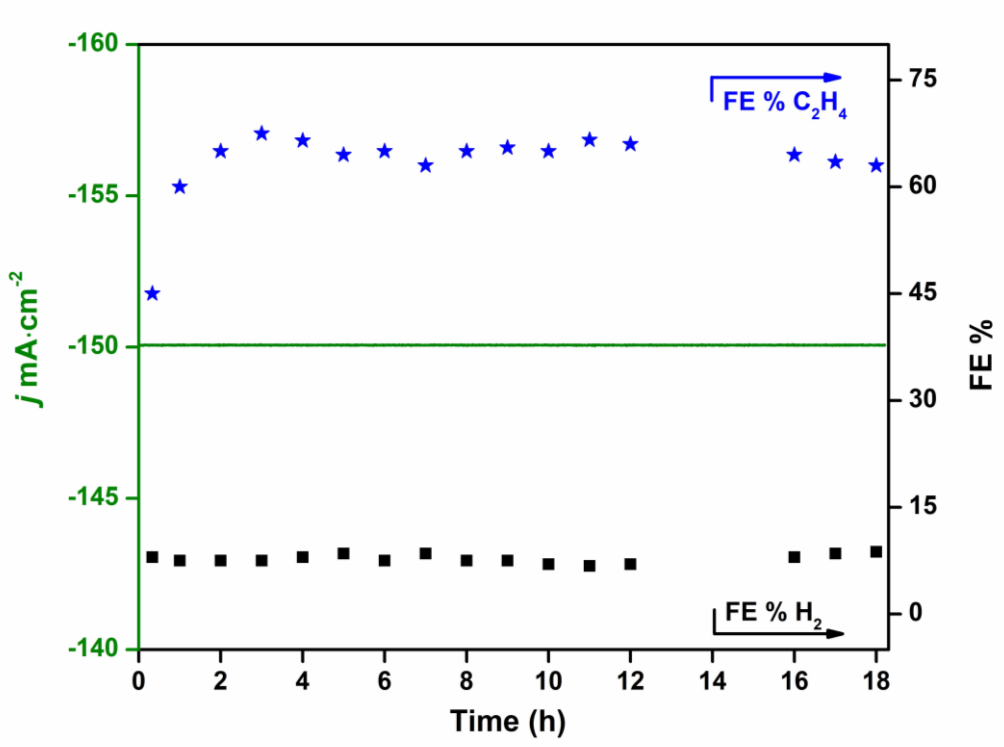


Figure 4.22 Long-term stability test of TD setup enabled by an intermediate CO_2 trap chamber.

both the catholyte and the KOH of the trap chamber. During the stability evaluation, a constant FE of C_2H_4, averaging 65-66% was achieved while the HER activity was kept low as depicted in Figure 4.22. The FE of C_2H_4 was well maintained over a period of 18 h at -150 mA·cm^{-2} averaging 65% indicating the exceptional stability of the overall tandem device set-up further implying the viability of industrial-scale operations.

The Energy Efficiency (EE%) for C_2H_4 production was calculated using an industry viewpoint based on the estimations of the total energy content of the products divided by the total energy input to the system. Table 4.1 depicts the parameters and the EE % obtained for a set of experiments. The obtained results demonstrate that the TD setup reached higher EE % values when compared to the traditional single-device electrolyzers. The increase in EE % can be attributed to the fact of breaking down to the multi-step reaction pathway thereby decreasing the cell potentials and to the high FE % towards both CO in cell-1 and C_2H_4 in cell-2 under the prescribed conditions. The one-step approach with ECOR shows the highest EE % indicating the importance of working under lowered cell potentials. While the direct one-step ECO_2R demonstrated an EE of 12.21% with Cu_xO-C, ECOR delivered a staggering EE of 27.5% for the generation of C_2H_4 with Cu_xO-C. Interestingly, the best-fit tandem approach, TD setup coupled with a CO_2 absorption/trap chamber delivered a promising EE of 24.3% indicating the on-par performance of the ECOR.

Table 4.1. Operating parameters of the electrolyzers and EE % comparison for the Tandem Device setup system and individual electrolyzers for ECO_2R and ECOR to C_2H_4.

	One cell – ECO_2R CO_2 to C_2H_4	**One cell – ECOR CO to C_2H_4**	**Two cells – Tandem**	
			Cell 1 – CO_2 to CO	**Cell 2 – CO to C_2H_4**
E_{cell} (V)	4.5	3.5	3.8	3.6
j (A/cm^2)	0.2	0.15	0.05	0.15
FE %	48	57	95	70
EE %	**12.21**	**27.5**	**24.3**	

4.7 Conclusions

The study presented in this chapter elucidates the importance of examining the best-fit tandem approach to enhance the selectivity of C_2H_4. The study began with assessing the performance of individual Ni and Cu-based GDEs mounted electrolyzers. Initially, different combinations of TCs with varying Cu content to constant Ni were fabricated and evaluated for C_2H_4 selectivity of ECO_2R. TC Ni1:Cu5 was found to be the best-performing combination at a lowered cathodic potential. The aforementioned combination was chosen to fabricate the TEs as layer-by-layer and segmented electrodes. TE LbL Cu5/Ni1 was found to have superior performance when compared to the TCs with improved C_2H_4 selectivity and further lowered cathodic potentials. Finally, TDs were set up by coupling the individual electrolyzers of Ni and Cu as cell-1 and cell-2. Along with the evaluation of the initial TD set-up and pure and mixed gas streams, it was well-confirmed that the presence of CO_2 was undesirable as it lowered the total FE of C_2H_4 and C_{2+} products. Furthermore, the undesired CO_2 was eliminated by introducing an intermediate trap chamber to absorb the unreacted CO_2 which resulted in directing the concentrated CO feed onto the Cu-GDE which further yielded higher C_2H_4 generation with improved partial currents and lowered cathodic potentials. An overall FE of 70 ± 3 % of C_2H_4 and a total of 87 ± 5 % C_{2+} products were obtained with an applied current density of -150 $mA{\cdot}cm^{-2}$ and at a cathodic potential of just -0.79 V vs RHE were reported. The reported FE and cathodic potentials are proof of the superior performance of TDs over TCs and TEs including the traditional single-step ECO_2R. The overall exceptional stability of more than 18 h of continuous operation of the coupled electrolyzers further demonstrates the feasibility of incorporating the TD set-up at an industrial scale to obtain higher selectivity towards the value-added carbon products with improved energy efficiencies.

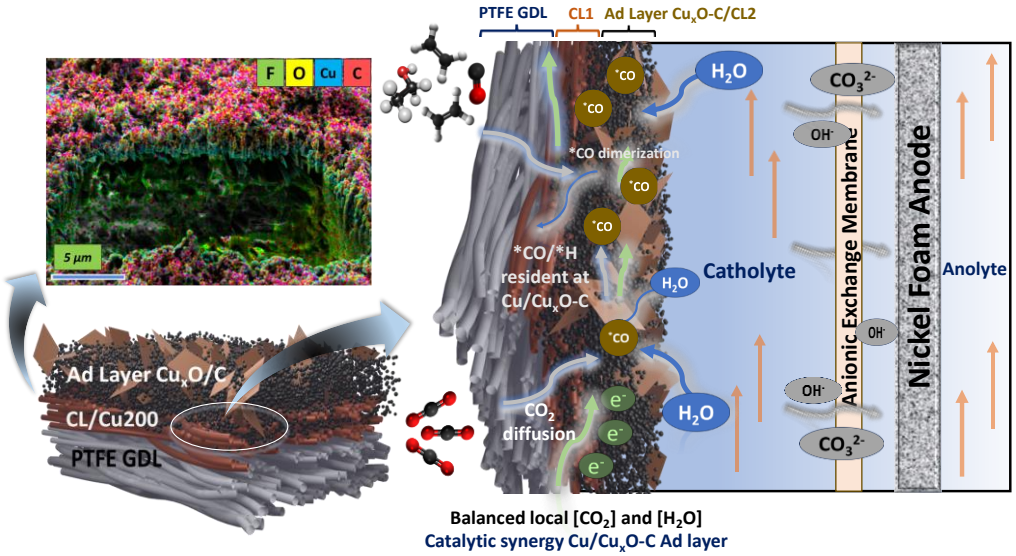
4.8 References

1. Zhang. H, Li. J, Cheng. M-J, Lu, Q. CO, *ACS Catal*. **2018** 9, 49–65.
2. Li. J, Wang. Z, McCallum. C, Xu. Y, Li. F. Wang, Gabardo. C, Dinh. C-T, Zhuang. T-T, Wang. L, Howe. J.Y, Ren. Y, Sargent. E. H, Sinton. D, *Nat Catal.* **2019,** 2, 1124–1131.
3. Jouny, M., Luc, W. & Jiao, F. **2018** *Nat Catal.* 1, 748–755.
4. Eriksson. B, Asset. T, Spanu. F, Lecoeur. F, Dupont. M, Garcés-Pineda. F A, Galán-Mascarós. J R, Cavaliere. S, Rozière. J, Jaouen. F., *J. Electrochem. Soc.* **2022**, 169, 034508.
5. Casadevall. A V, W. Li. C, Johansson. T. P, Scott. S. B, McKeown. J. T, Kumar. M, Stephens. I. E. L, Kanan. M. W, Chorkendorff. Ib, **2015**, *J. Am. Chem. Soc.* 137, 31, 9808–9811.
6. C. Wei, Y. Yang, H. Ma, G. Sun, X. Wang, Y. Cheng, C. Zhang, B. S. Yeo, C. He, A. B. Wong, *Adv. Funct. Mater.* **2023**, 33, 2214992.
7. F. Li, Y. C. Li, Z. Wang, J. Li, D. H. Nam, Y. Lum, M. Luo, X. Wang, A. Ozden, S. F. Hung, B. Chen, *Nat. Catal.* **2020**, 3, 75.
8. C. Choi, J. Cai, C. Lee, H. M. Lee, M. Xu, Y. Huang, *Nano Res.* **2021**, 14, 3497.
9. C. G. Morales-Guio, E. R. Cave, S. A. Nitopi, J. T. Feaster, L. Wang, K. P. Kuhl, A. Jackson, N. C. Johnson, D. N. Abram, T. Hatsukade, C. Hahn, *Nat. Catal.* **2018**, 1, 764.
10. X. Su, Y. Sun, L. Jin, L. Zhang, Y. Yang, P. Kerns, B. Liu, S. Li, J. He, *Appl. Catal. B Environ*. **2020**, 269, 118800.
11. M. Feng, X. Wu, H. Cheng, Z. Fan, X. Li, F. Cui, S. Fan, Y. Dai, G. Lei, G. He, *J. Mater. Chem. A* **2021**, 9, 23817.
12. B. Zhang, L. Wang, D. Li, Z. Li, R. Bu, Y. Lu, *Chem. Catal.* **2022**, 2, 3395.
13. Y. Lum, J. W. Ager, *Energy Environ. Sci.* **2018**, 11, 2935.
14. J. Gao, D. Ren, X. Guo, S. M. Zakeeruddin, M. Grätzel, *Faraday Discuss.* **2019**, 215, 282.
15. C. B. Chen, Y. F. Li, S. Yu, S. Louisia, J. B. Jin, M. F. Li, M. B. Ross, P. D. Yang, *Joule* **2020**, 4, 1688.
16. D. Ren, J. Gao, L. F. Pan, Z. W. Wang, J. S. Luo, S. M. Zakeeruddin, A. Hagfeldt, M. Gratzel, Angew. *Chem. Int. Ed.* **2019**, 58, 15036.
17. D. L. Meng, M. D. Zhang, D. H. Si, M. J. Mao, Y. Hou, Y. B. Huang, R. Cao, *Angew. Chem. Int. Ed.* **2021**, 60, 25485.
18. T. Zhang, J. C. Bui, Z. Li, A. T. Bell, A. Z. Weber, J. Wu, *Nat. Catal.* **2022**, 5, 202.

19. T. A. Al-Attas, N. N. Marei, X. Yong, N. G. Yasri, V. Thangadurai, G. Shimizu, S. Siahrostami, M. G. Kibria, *ACS Catal.* **2021**, 11, 7350.
20. S. Lin, C. S. Diercks, Y. B. Zhang, N. Kornienko, E. M. Nichols, Y. Zhao, A. R. Paris, D. Kim, P. Yang, O. M. Yaghi, C. J. Chang, *Science* **2015**, 349, 1208.
21. S. Louisia, D. Kim, Y. Li, M. Gao, S. Yu, I. Roh, P. Yang, *Proc. Natl. Acad. Sci.* **2022**, 119, e2201922119.
22. T. Zhang, Z. Li, J. Zhang, J. Wu, *J. Catal.* **2020**, 387, 163.
23. X. She, T. Zhang, Z. Li, H. Li, H. Xu, J. Wu, *Cell Rep. Phys. Sci.* **2020**, 1, 100051.
24. N. Theaker, J. M. Strain, B. Kumar, J. P. Brian, S. Kumari, J. M. Spurgeon, *Electrochim. Acta* **2018**, 274, 1.
25. N.S. Romero Cuellar, C. Scherer, B. Kaçkar, W. Eisenreich, C. Huber, K. Wiesner-Fleischer, M. Fleischer, O. Hinrichsen, *J. CO2 Util*. **2020**, 36, 263.
26. T. Li, E. W. Lees, M. Goldman, D. A. Salvatore, D. M. Weekes, C. P. Berlinguette, *Joule* **2019**, 3, 1487.
27. T. Zheng, K. Jiang, N. Ta, Y. Hu, J. Zeng, J. Liu, H. Wang, *Joule* **2019**, 3, 265.
28. V. S. R. K. Tandava, M. C. Spadaro, J. Arbiol, S. Murcia-López, J. R. Morante, *ChemSusChem* **2023**, 16, e202300344.
29. Ana Sofia Varela, Current Op in Green and Sustainable Chem, 2020, 26, 100371.
30. A.J. Garza, A.T. Bell, M. Head-Gordon, ACS Catal, **2018**, 8, 1490-1499.
31. Mistry. H, Varela. A, Bonifacio. C, I. Zegkinoglou, I. Sinev, Y-W. Choi, Kim. K, Eric A. S, J. C. Yang, P. Strasser, B. R. Cuenya, Nat Commun, 2016, 7, 12123.
32. C.W. Li, M.W. Kanan, J Am Chem Soc, **2012**, 134, 7231-7234.
33. N.S. Romero Cuellar, K. Wiesner-Fleischer, M. Fleischer, A. Rucki, O. Hinrichsen, Electrochim. Acta, **2019**, 307, 164.
34. Cornelius. A.O, Guorui. G, Jackson. C, Viktoria. G, F. P. García de Arquer, Dinh. C-T al. Nat Commun. **2023** 14, 3176.

Chapter 5

Modulating the Surface Interface of PTFE/Copper-based Gas Diffusion Electrodes



The contents of this chapter are submitted as a manuscript to a reputed journal and are currently under revision after peer review. The contents of the submitted manuscript were modified according to the Thesis structure by moving certain aspects of the general introduction and experimental section to the respective Chapters 1 and 2. Additional figures from the Supporting information were used in this text.

Modulating the Surface Interface of PTFE/Cu-based GDEs to Boost the Electrochemical Conversion of CO_2 to C_2H_4 at Ultra-low Overpotential

Venkata S.R.K. Tandava, Mayra S. Tovar-Oliva, Martí Biset-Peiró, Diouldé Sylla, Joan Ramón Morante, Ignacio Tudela, Sebastián Murcia-López**

5.1 Abstract

Electrochemical CO_2 reduction to valuable chemical commodities has received significant attention from the research community over the past decade with the successful implementation of gas diffusion electrodes in advanced flow electrolyzers, where achieving high faradaic efficiencies towards multi-carbon products at industrially relevant current densities has become the ultimate goal. In this present chapter, the convenience of systematically modulating the surface interface microenvironment of copper-based gas diffusion electrodes to boost the selectivity towards the efficient production of C_2H_4 and beyond was presented. Tailored gas diffusion electrodes fabricated by sputtering copper on polytetrafluoroethylene porous membranes and applying an additive layer proved to be very effective in boosting selectivity towards C_2H_4 and other C_{2+} products. The results presented here indicate that the thickness of the copper layer sputtered on the PTFE membrane directly influenced the cathodic potential at which the different reactions studied would occur; this was further influenced by modulating the surface microenvironment of the copper with an additive layer (i.e. carbon black-ionomer and/or catalyst-ionomer). A comparative study of sputtered copper aided by the additive layers led us to understand the role of the catalyst/catalyst-additive layer heterojunction interface in tuning the selectivity towards multicarbon products. It was noticed that the additive layer aids not only in tuning the selectivity towards C_2H_4 as the prime product but also significantly lowers the cathodic overpotential required to achieve industrially relevant high current densities. Moreover, PTFE/Copper-based catalyst layers with an appropriate additive layer loading (i.e. carbon-supported copper-oxide heterostructures) converted CO_2 to C_2H_4 with a faradaic efficiency over 70 ± 2% including a combined faradaic efficiency of 90 ± 3 % for C_{2+} products with an *iR*-corrected potential of -0.55 V *vs* RHE and at an industrially relevant current density of -250 $mA \cdot cm^{-2}$ in a flow electrolyzer. In such conditions, the PTFE/Cu/Cu_xO-C gas diffusion electrode exhibited excellent stability, delivering a consistently high yield of C_2H_4 over 25 hours while effectively suppressing the competitive hydrogen evolution reaction.

5.2 Introduction

To give the reader a thorough understanding and follow up with this chapter, a brief introduction is mentioned to delve straightaway into the focus of this chapter.

As discussed in the previous chapters, copper and copper-based materials when adapted in flow electrolyzers with GDEs can achieve the required current density threshold for commercial applications while delivering substantial FEs for a wide variety of products[1-3]. As mentioned in the introduction, in the commercial GDEs the catalyst layer is often supported on a porous GDL generally consisting of a macroporous carbon fibrous layer and a microporous layer usually having PTFE to provide the required hydrophobicity, thereby enabling the CO_2 to diffuse through and reach the surface of the catalyst applied over its surface, establishing a triple-phase (gas-solid-liquid) boundary (TPB) [4,5]. Most GDEs commercially available are prone to experience carbon corrosion, pore degradation and reduced hydrophobicity over time due to their brittle carbonaceous nature, leading to flooding and resulting in poor stability and selectivity [6-8]. Despite the partial hydrophobicity of its surface, swift degradation of the GDL supervene at high current densities where the electrolyte (i.e. carbonate salts in aqueous solution) may precipitate within the pores of the GDL. The hydrated GDE may then favour the undesired HER due to the similar standard potentials of both HER and ECO_2R [9]. Therefore, it is recommended to engineer a highly stable triple-phase boundary for the long-term operation of CO_2 electrolyzers operating at industrially relevant current densities.

To minimise flooding issues and increase their lifespan, the research community has proposed diverse solutions aimed at enhancing the hydrophobicity of GDEs, such as the use of highly hydrophobic polymeric PTFE membranes as GDLs [10-12] or modifying the catalytic layer composition by adding PTFE in various forms [13]. PTFE membrane-based GDEs are usually developed by sputtering a thin metal layer (e.g. copper) that acts as a conductive layer and/or catalyst layer; their PTFE nature and structure provide them with superior hydrophobicity, whereas the sputtered layer reduces the electrical resistance. PTFE-based GDEs have exhibited excellent stability in terms of hydrophobicity with enhanced diffusion of CO_2 during ECO_2R. In addition, PTFE-based GDEs are often modified by ionomers/catalysts to enhance their stability further and improve their selectivity towards the chemical commodities [14,15.] Overall, the enhanced selectivity and stability are attributed to both improved hydrophobicity

and optimum gas-electrolyte balance at the catalyst surface by properly maintaining the triple-phase boundary. To further exploit the PTFE-based GDEs and enhance the ECO_2R to valuable chemical commodities, it is critical to evaluate and analyze how the modulation of the surface interface and microenvironments generated within catalyst layers with varying thicknesses and compositions (e.g. with and without additional additive layers) can affect the stability of the GDE and its selectivity to multi-carbon products with C_2H_4 as the main target at high current densities.

In this chapter, a thorough study on systematic evaluation of commercial PTFE membranes acting as GDLs over which tailor-made conductive polycrystalline copper catalyst layers with varying thicknesses (100-300 nm) is reported. The as-prepared Cu-deposited PTFE (henceforth referred to as PTFE/Cu) based GDEs were initially evaluated to understand the electrochemical behaviour. The surface of the PTFE/Cu was initially modulated by using a cationic ionomer, Nafion and further by depositing an additive layer over the surface of the sputtered copper layer consisting of carbon black (C) and Nafion, acting as a binder [16] and later followed by carbon-supported copper-oxide heterostructures and Nafion (Cu_xO/C) [17], the robust electrocatalyst which was previously discussed in Chapter 3. The study was further extended with efforts to elucidate the role of PTFE with a commercially available GDL, Sigracet39BB by depositing Cu followed by the additive layer Cu_xO/C. Our results indicate that the thickness and structure of the sputtered copper catalyst layer and the catalyst/additive layer heterojunction influenced the surface microenvironment and the resulting ECO_2R product distribution, facilitating the understanding of its role in tuning the selectivity towards C_2H_4 and other by-products. Moreover, when optimized, hierarchically constructed PTFE/Cu-based GDEs with the Cu_xO-C additive layer exhibited a significant enhancement in the selectivity towards C_2H_4 with a faradaic efficiency of 70 ± 2% and a combined faradaic efficiency of 90 ± 3 % for C_{2+} products while minimizing the undesired HER at an industrially relevant current density of 250 $mA \cdot cm^{-2}$ and a remarkable ultra-low cathodic overpotential (*iR*-corrected potential of -0.55V *vs* RHE) was observed. Systematic modulation of PTFE/Cu-based GDEs with an optimum thickness and an appropriate additive layer loading of Cu_xO-C originated a favourable surface microenvironment for steering the selectivity of ECO_2R towards C_2H_4. Furthermore, the optimized PTFE/Cu/Cu_xO-C GDE exhibited excellent stability over 25 hours of operation in a flow electrolyzer with a geometrical electrode area of 5 cm^2 operating in such

conditions, consistently delivering a FE of around 70% for C_2H_4 while effectively suppressing HER. The approach here presented therefore has the potential to strongly contribute to further the development and scale-up of ECO_2R processes to convert CO_2 into valuable chemical feedstocks and renewable fuels.

5.3 Objectives

The main objectives of the present study are

- To fabricate improved GDEs based on non-conventional gas diffusion layers like PTFE with strong hydrophobic properties and modified by depositing copper catalyst layers.
- To evaluate the influence of the thickness of sputtered Cu catalyst layers.
- To modulate the surface interface microenvironment with an additive layer deposited over the copper catalyst layer and its role in tuning the selectivity and lowering the overpotentials.
- To understand how the optimized additive layer with the appropriate loading can steer the selectivity of the ECO_2R to C_2H_4 as the prime product.
- To estimate the parameters like exchange current densities using the Butler-Volmer-based electrochemical kinetic modelling.

5.4 Highlights

As emphasized in the objectives of the chapter, to engineer a highly stable triple-phase boundary for the long-term performance of CO_2 electrolyzers operating at industrially relevant current densities, thorough investigations were performed and eventually the observations are highlighted hereunder.

- Super hydrophobic PTFE-based GDEs were fabricated by depositing Cu catalyst layers with different thicknesses. Initial electrochemical behaviour was assessed and the product selectivity of the ECO_2R was evaluated at different current densities.
- By modulating the surface interface with a non-catalytic additive layer of carbon, the product distribution was tuned and the selectivity towards C_2H_4 was enhanced at higher current densities compared to the pristine PTFE/Cu GDEs.

- Further modulating the surface with a catalytic additive layer of Cu_xO-C resulted in enhanced selectivity towards C_2H_4.
- Peak FE of C_2H_4 over 70% is reported with a cumulative FE over 90% for C_{2+} products was reported with the optimized PTFE/Cu200/Cu_xO-C electrode while minimizing the undesired HER at an industrially relevant current density of 250 mA·cm^{-2}.
- An ultra-low cathodic overpotential, *iR*-corrected potential of -0.55V vs RHE was observed.
- Optimized PTFE/Cu/Cu_xO-C GDE exhibited excellent stability over 25 hours of operation in a flow electrolyzer with a geometrical electrode area of 5 cm^2.

5.5 Experimental Methods

A note to the reader

The general experimental methods and materials from this chapter have been discussed in detail in Chapter 2, *Experimental Materials, Methods, and Systems involved in Electrochemical CO_2 Reduction.* A detailed explanation concerning the electrode fabrication techniques, characterization techniques and experimental setup involving the flow electrolyzer was also included in Chapter 2. However, to enable the reader to delve into this chapter straightaway, a brief description of electrode fabrication and techniques involved in this chapter are mentioned hereunder.

Fabrication of PTFE/Cu-based GDEs

Pristine PTFE/Cu GDEs

PTFE/Cu GDEs were prepared by depositing thin copper catalyst layers on the hydrophobic PTFE membranes. The thin Cu films were deposited with a direct-current AC450 magnetron sputtering system. Here, pristine PTFE/Cu gas diffusion layers of 5 cm^2 (2*2.5 cm^2) with varying thicknesses notably 100, 200 and 300 nm (namely Cu100, Cu200 and Cu300) were chosen. These samples were initially used as cathode materials directly exposed to the electrolyte and CO_2 interaction without any further modification. Similarly, on the Sigracet 39BB, a 200nm thick Cu layer was sputtered and further evaluated, labelled as SGL/Cu200.

Fabrication of PTFE/Cu: Nafion additive layer

Initial modulation of the PTFE/Cu GDEs was achieved by applying a thin film of Nafion, a cationic ionomer, on the surface of the sputtered Cu catalyst layers. This was achieved by adding 100 µL of Nafion 5% perfluorinated resin solution to 2 mL of isopropanol, which was thoroughly dispersed under ultrasonication for 1 h and then uniformly spray-coated onto PTFE/Cu200 GDE uniformly covering the copper films and dried in a vacuum oven at 60 °C for at least 12 h before use. Nafion-coated Cu200 (Cu200/Nafion) was directly tested without any further modification and compared with the pristine Cu200.

Fabrication of PTFE/Cu: Carbon additive layer

The prepared GDEs were modified by spray-coating a carbon black-ionomer ink solution over their active surface. For this purpose, 20 mg of commercial carbon black (Vulcan XC-72) and 100 µL of Nafion 5% perfluorinated resin solution were thoroughly dispersed in 2 mL of isopropanol under ultrasonication for 1 h and spray-coated on the PTFE/Cu200. The effective final mass loadings ≈ 0.5 and ≈ 1mg·cm^{-2} on Cu200 respectively were obtained and labelled as Cu200/C0.5 and Cu200/C1. The as-prepared electrodes were dried in a vacuum oven at 60 °C for at least 12 h before use.

Fabrication of PTFE/Cu: Cu_xO-C additive layer

Note to the reader: A detailed protocol for synthesizing the Cu_xO-C electrocatalyst and characterization was extensively discussed in Chapters 2 and 3.

Further modulation of prepared PTFE/Cu GDEs was achieved with a different additive layer consisting of a Cu_xO-C electrocatalyst reported in the previous chapter. 20 mg of Cu_xO-C was thoroughly dispersed in 2 mL of isopropanol containing 100 µL of Nafion 5% perfluorinated resin solution by ultrasonication for 1 h and then spray-coated onto the pristine PTFE/Cu200 layers using an airbrush with an effective final mass loading of ≈ 0.5 and ≈ 1 mg·cm^{-2} and labelled as Cu200/Cu_xO-C0.5 and Cu200/Cu_xO-C1. Similarly, ≈1 mg·cm^{-2} loading of Cu_xO-C was deposited on SGL/Cu200 and labelled as SGL/Cu200/Cu_xO-C1. The as-prepared electrodes were then dried in a vacuum oven at 60 °C for at least 12 hours before use. A summary of all the electrode structures is included in Table 5.1.

Table 5.1 Description of PTE/SGL-Cu GDE with additive layer thickness

Sample ID	Gas Diffusion Layer	Sputtered Cu (Thickness)	Additive Layer*
Cu100	PTFE	100nm	-
Cu200	PTFE	200nm	-
Cu300	PTFE	300nm	-
SGL/Cu200	Sigracet 39BB	200nm	-
Cu200/C0.5mg	PTFE	200nm	C 0.5 $mg.cm^{-2}$
Cu200/C1	PTFE	200nm	C 1 $mg.cm^{-2}$
Cu200/Cu_xO-C0.5	PTFE	200nm	Cu_xO-C 0.5 $mg.cm^{-2}$
Cu200/Cu_xO-C1	PTFE	200nm	Cu_xO-C 1 $mg.cm^{-2}$
SGL/Cu200/Cu_xO-C1	Sigracet 39BB	200nm	Cu_xO-C 1 $mg.cm^{-2}$

*All additive layers are mixed with 0.25wt% of ionomer (Nafion)

5.6 Results and Discussion

Three main GDE architectures were developed and evaluated to study the effect of modulating the surface interface of PTFE/Cu-based GDEs for ECO_2R.

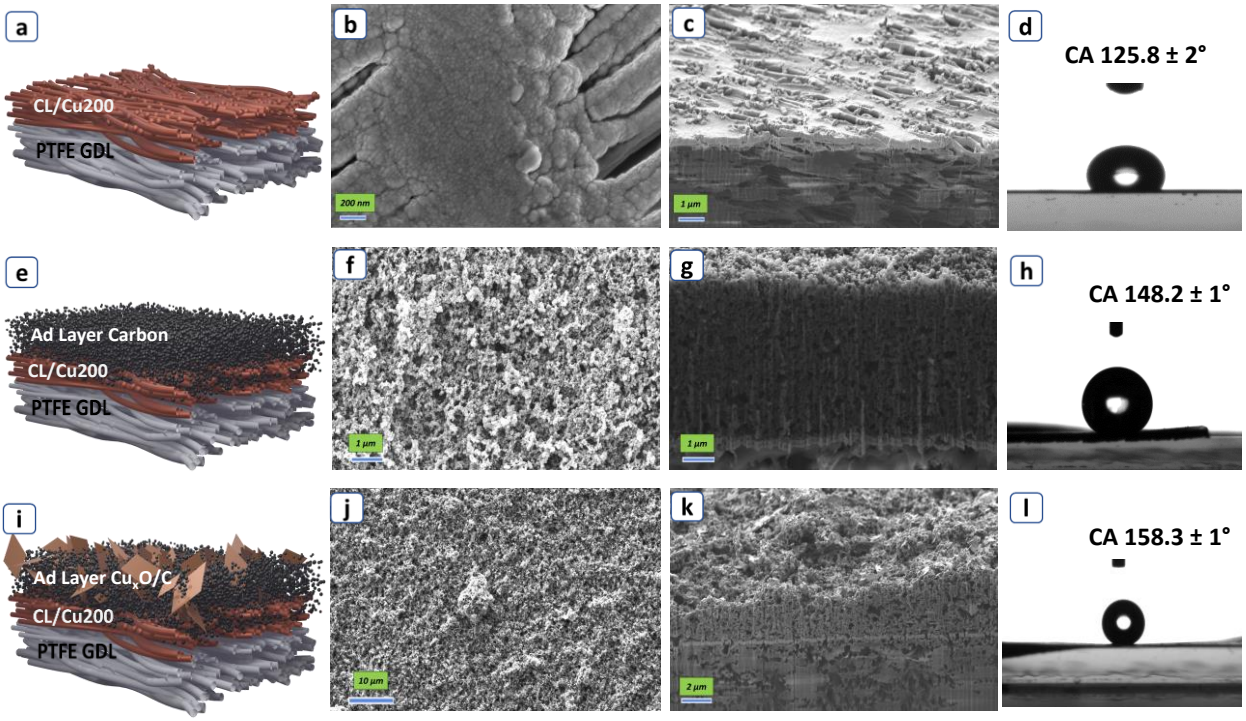


Figure 5.1. Scheme of the developed electrode configurations **(a, e, i)**; characterization summary with FIB-SEM top-view and cross-sections, and contact angle measurements for pristine Cu200 **(b, c, d)**, Cu200/C1 **(f, g, h)** and Cu200/Cu_xO-C1 **(j, k, l)**.

i) GDEs consisting of hydrophobic PTFE membranes with thin Cu catalyst layers sputtered over their surface.

ii) PTFE/Cu-based GDEs with an additive layer over their surface consisting of carbon black (C) with Nafion.

iii) PTFE/Cu-based GDEs with an additive layer consisting of carbon-supported copper-oxide heterostructures and Nafion (Cu_xO-C)

A representation showcasing the scheme of developed electrode configurations with a brief characterization summary is depicted in Figure 5.1 to give a glimpse of this chapter to the reader.

5.6.1 Surface interface modulation of PTFE/Cu GDEs by thickness variation of Cu catalyst layer

In the first instance, thin Cu catalyst layers with varying thicknesses were sputtered on glass substrates to evaluate their properties. After calibration and confirming the thicknesses (from 100 to 500 nm) by XRF, four-point probe measurements indicated that the resistivity of the Cu catalyst layer was inversely proportional to the thickness of the thin Cu film as depicted in Figure 5.2. XRD analysis was then conducted to shed more light on the reason for this relation between resistivity and thickness of the sputtered Cu catalyst layers.

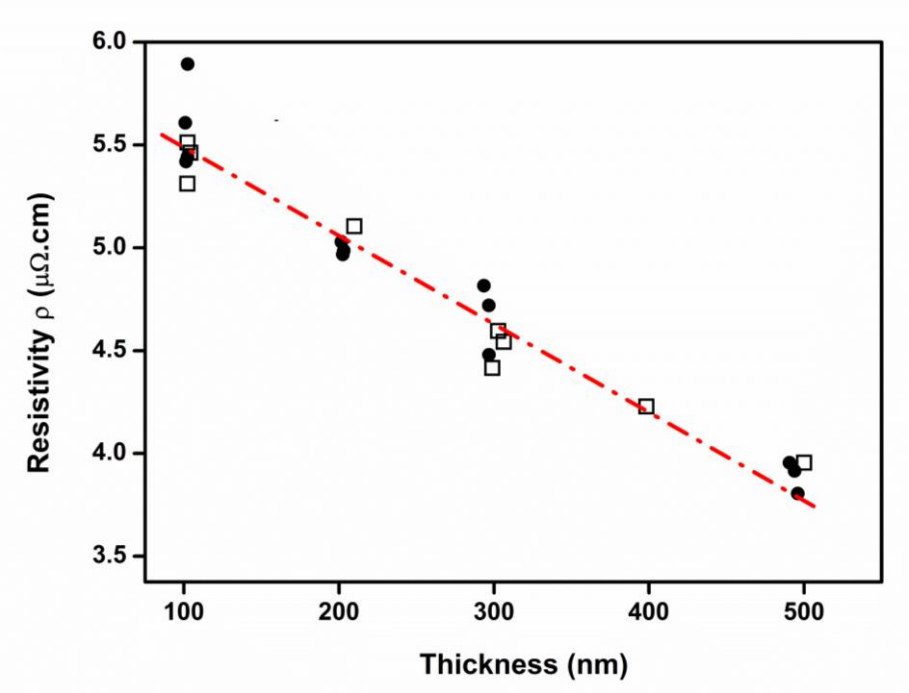


Figure 5.2 Resistivity vs. thickness of Cu layers sputtered on soda lime glass.

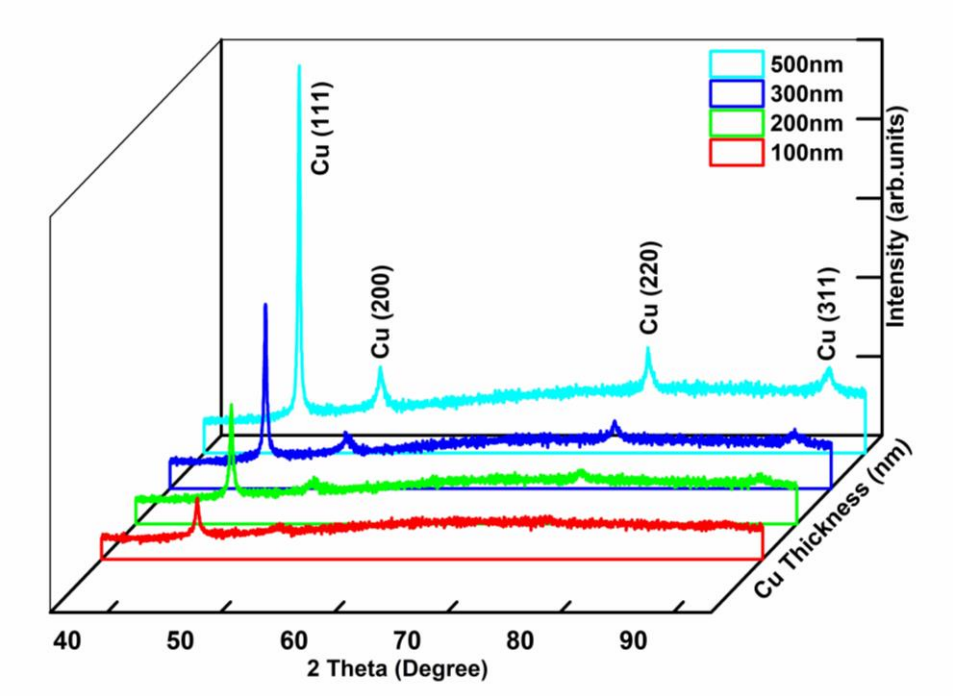


Figure 5.3 XRD measurements of sputtered Cu layers of different thicknesses on soda lime glass.

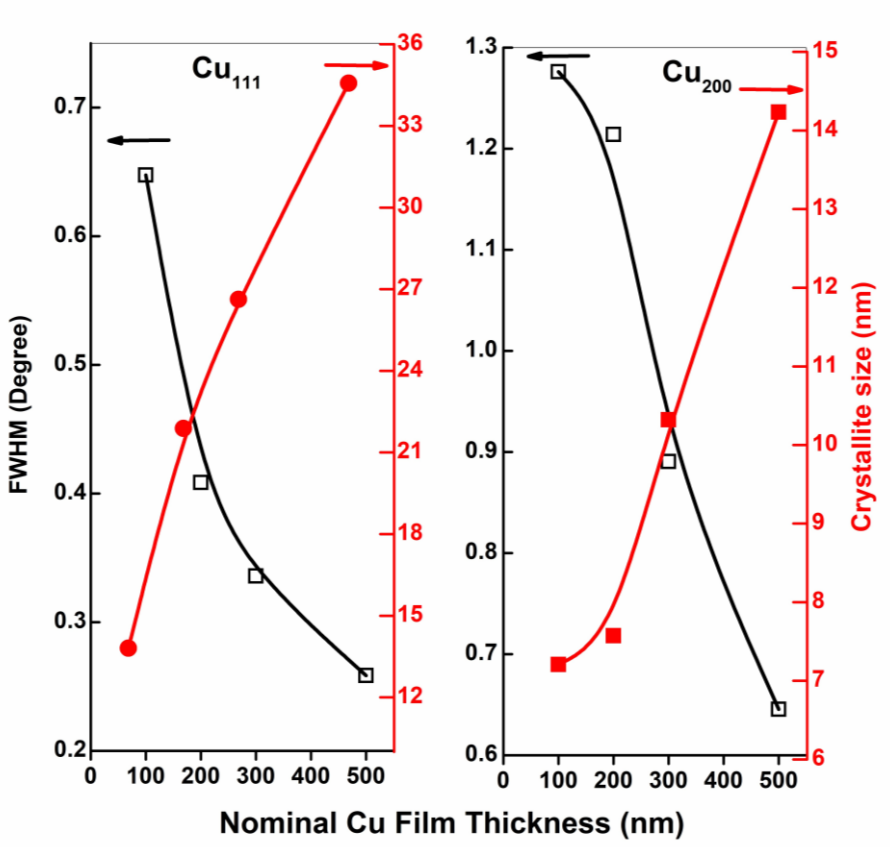


Figure 5.4 XRD measurements depicting crystallinity of deposited Cu. The relation between FWHM of Cu_{111} and Cu_{200} vs Thickness (in nm).

XRD data as depicted in Figure 5.3, indicated the existence of Cu (111), (200), (220) and (311) crystal planes in all thin Cu films, where (111) was the dominant facet orientation. Further evaluation and analysis of the full width at half maximum (FWHM) of both (111) and (200) indicated that the FWHM decreased as the thickness of the sputtered Cu layer increased, leading to crystallites with larger sizes as depicted in Figure 5.4. This larger crystallite size of the thicker Cu films indicates a higher degree of crystallinity, explaining why the thicker and more crystalline Cu catalyst layers exhibited lower resistivity.

FIB-SEM coupled with EDX mapping analysis of PTFE/Cu GDEs with varying Cu catalyst layer thicknesses showed (Figure 5.5- 5.7) that the PTFE fibres were homogeneously covered by the conformal thin Cu films.

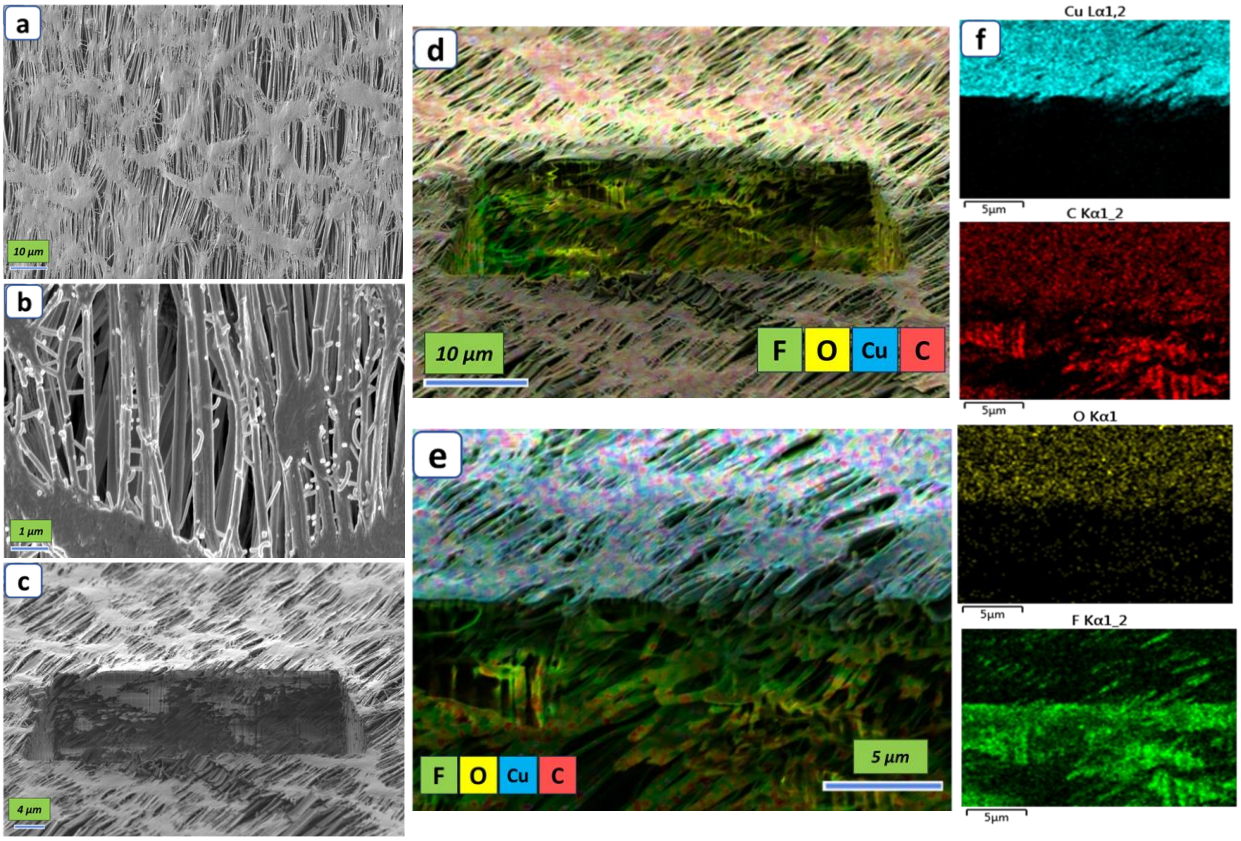


Figure 5.5 FIB-SEM of the surface, cross-sectional and EDX Mapping of the as-deposited Cu on PTFE membranes for Cu100. Top view of the surface **(a, b, c)**; cross-sectional view by FIB **(d, e)**; EDX elemental mapping **(f)**

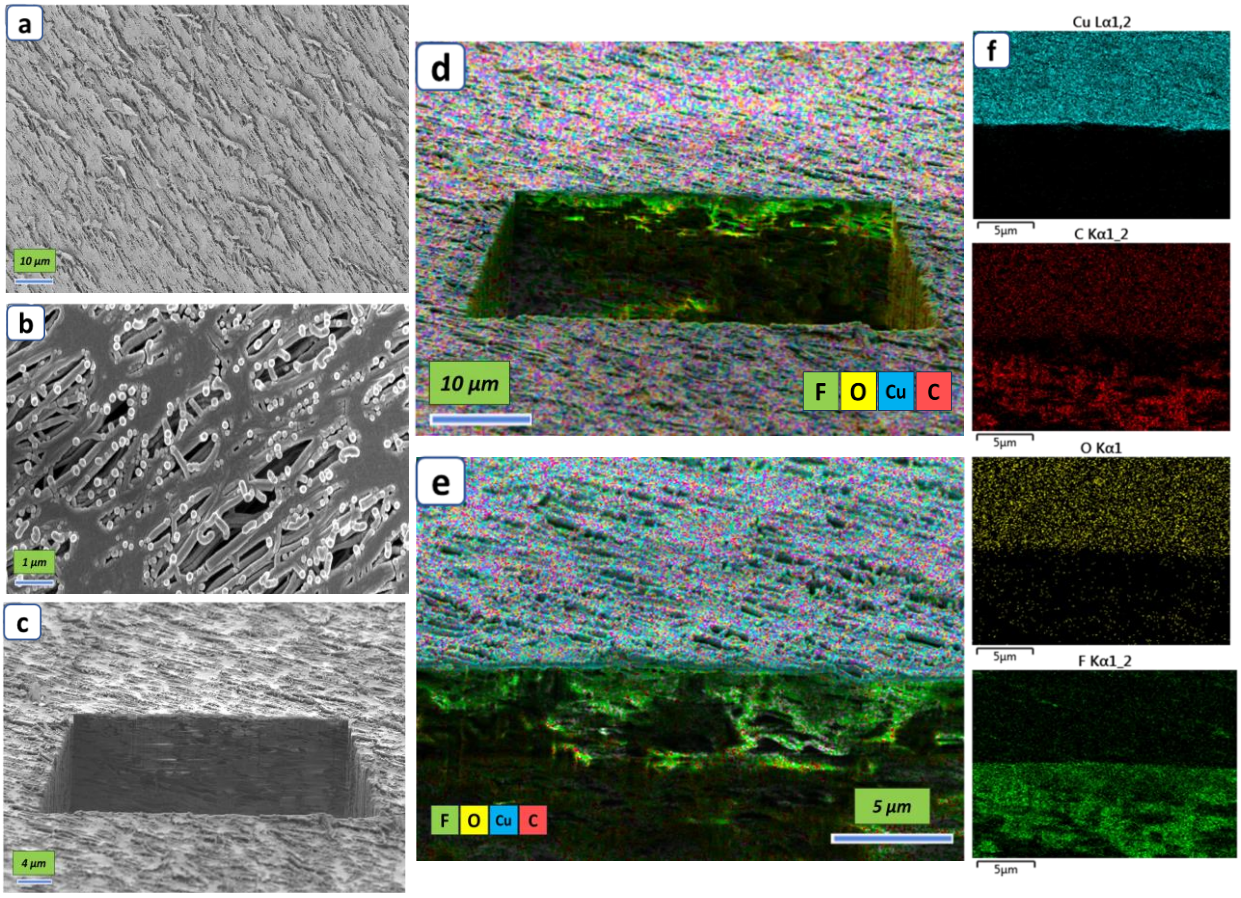


Figure 5.6 FIB-SEM of the surface, cross-sectional and EDX Mapping of the as-deposited Cu on PTFE membranes for Cu200. Top view of the surface **(a, b, c)**; cross-sectional view by FIB **(d, e)**; EDX elemental mapping **(f)**

The intrinsic porosity of the PTFE support is also observed, which could potentially influence the mass-transport phenomena at the triple-phase boundary. Cross-sectional images of the studied GDEs showed a close physical interaction between the sputtered Cu catalyst layer and the hydrophobic PTFE membranes acting as GDLs, where a distinct Cu catalyst layer covering PTFE fibres at the surface of the membrane was observed. In addition, the milled zone enabled the observation of the PTFE fibres of the bulk membrane identified by the strong signal of fluorine and carbon in the EDX mappings.

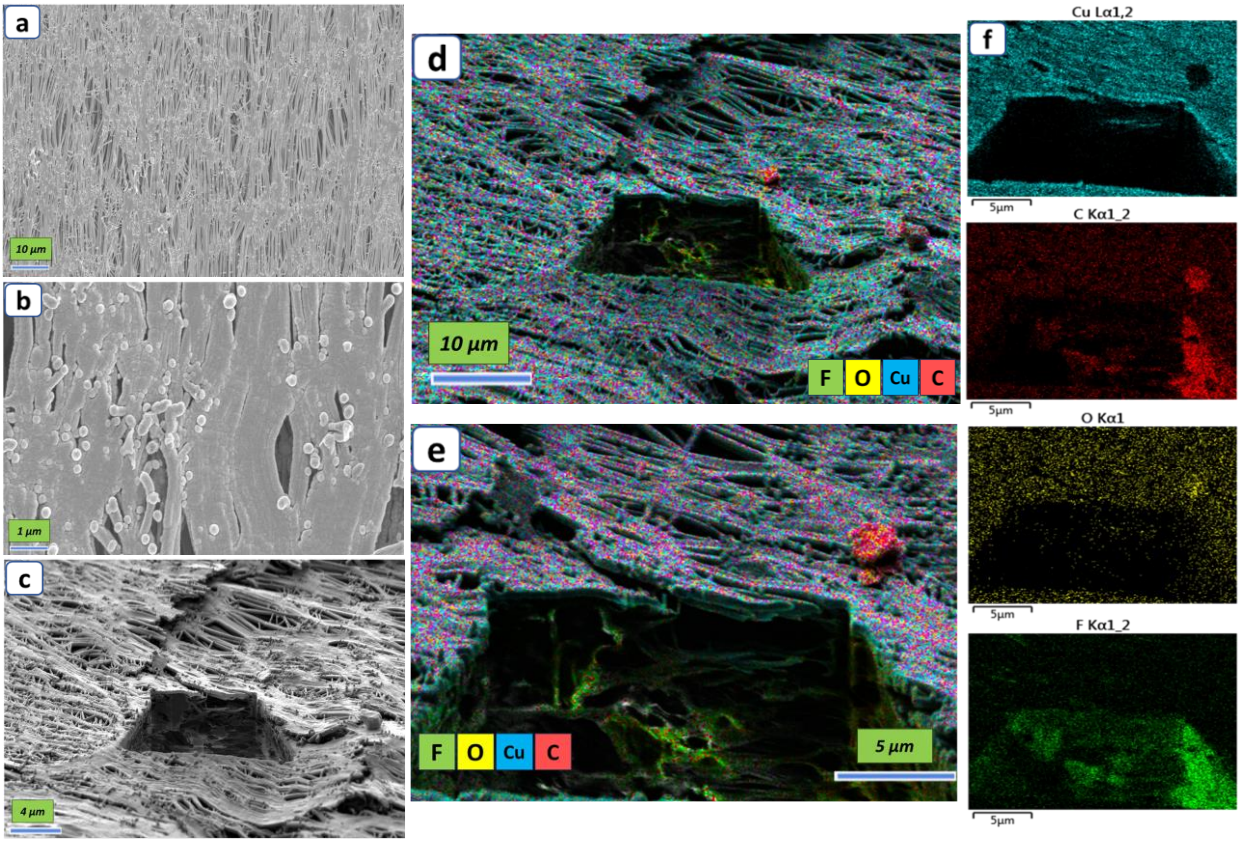


Figure 5.7 FIB-SEM of the surface, cross-sectional and EDX Mapping of the as-deposited Cu on PTFE membranes for Cu200. Top view of the surface **(a, b, c)**; cross-sectional view by FIB **(d, e)**; EDX elemental mapping **(f)**

C_{DL} values obtained by CVs conducted on PTFE/Cu GDEs with Cu catalyst layers with a thickness of 100, 200 and 300 nm (i.e. Cu100, Cu200 and Cu300, respectively) suggested a nearly proportional relationship between C_{DL} and the thickness of the thin Cu film for the range of samples studied (Figure 5.8). Comparatively, the GDEs consisting of the commercial Sigracet 39 BB GDL with a sputtered 200 nm Cu catalyst layer (i.e. SGL/Cu200) presented C_{DL} values that were twofold the value of C_{DL} for the same-thickness Cu catalyst layer deposited over the surface of PTFE (Cu200).

Special emphasis was put into identifying the hydrophobicity of the PTFE/Cu-based GDEs, as it would be expected to improve as a result of employing a hydrophobic PTFE membrane as GDL. Figure 5.9A shows the results of CA measurements of PTFE/Cu GDEs with varying thin

Cu film thickness and no additive layer on top (i.e. Cu100, Cu200 and Cu300) before and after electrolysis experiments (raw data is included in Figure 5.10).

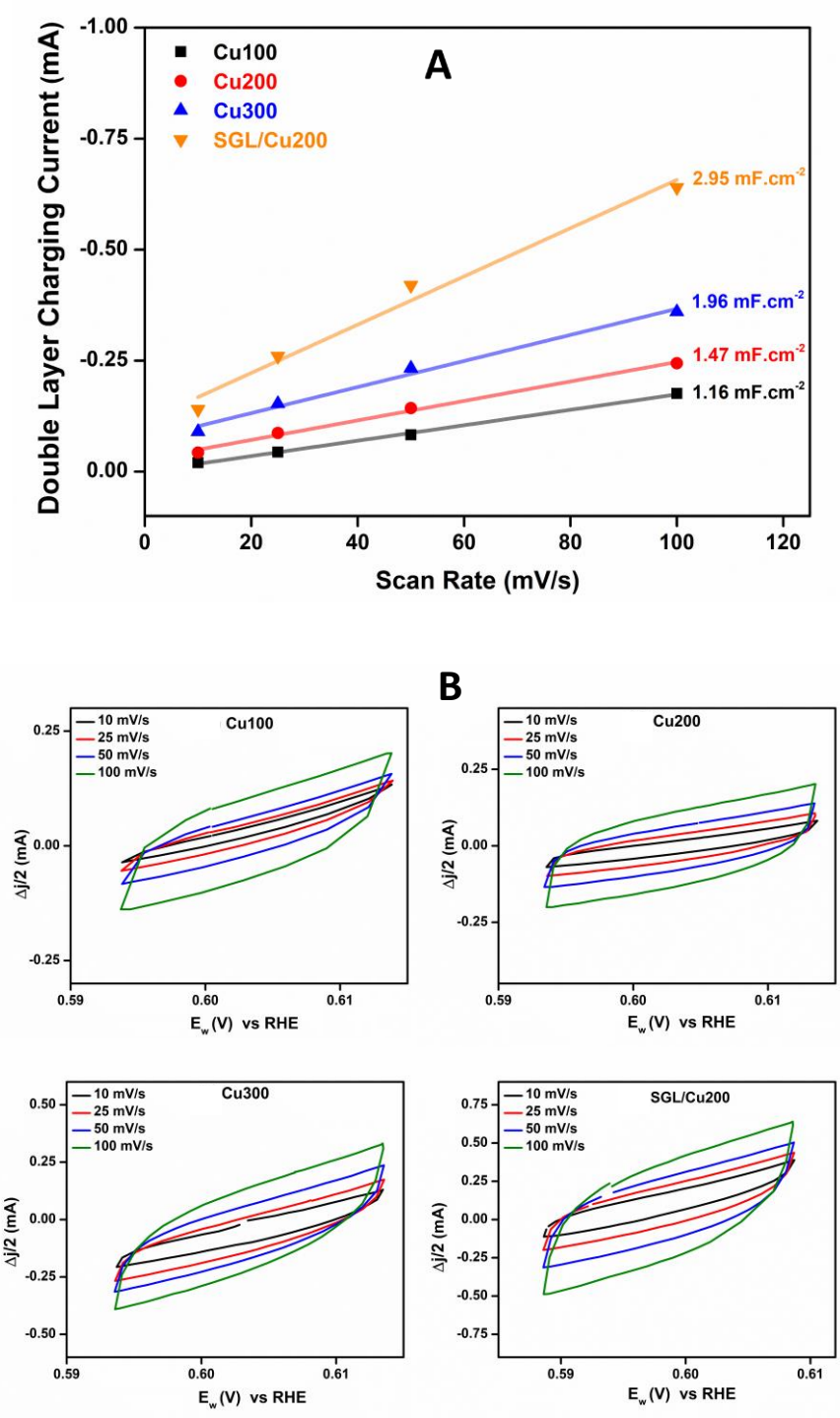


Figure 5.8 The plot **(A)** of double-layer charging currents (mA) vs Scan rate (mV/s) for the pristine Cu electrodes deposited on PTFE and commercial SGL. The slope of the above plots indicates the double-layer capacitance (C_{DL}) **(B)** cyclic voltammograms at different scan rates of each pristine sample.

Freshly prepared GDEs exhibited CAs higher than 110°, indicating a strongly hydrophobic interaction between the surface interface of the electrodes and the aqueous electrolyte. However, when handling the PTFE/Cu GDEs, it was noticed that the thin Cu films were partially detached from the PTFE membrane, especially after operating at high current densities. Post-electrolysis CA measurements also indicated a transition from the hydrophobic to hydrophilic nature of the PTFE/Cu GDEs, aligned with a certain degree of hydroxylation.

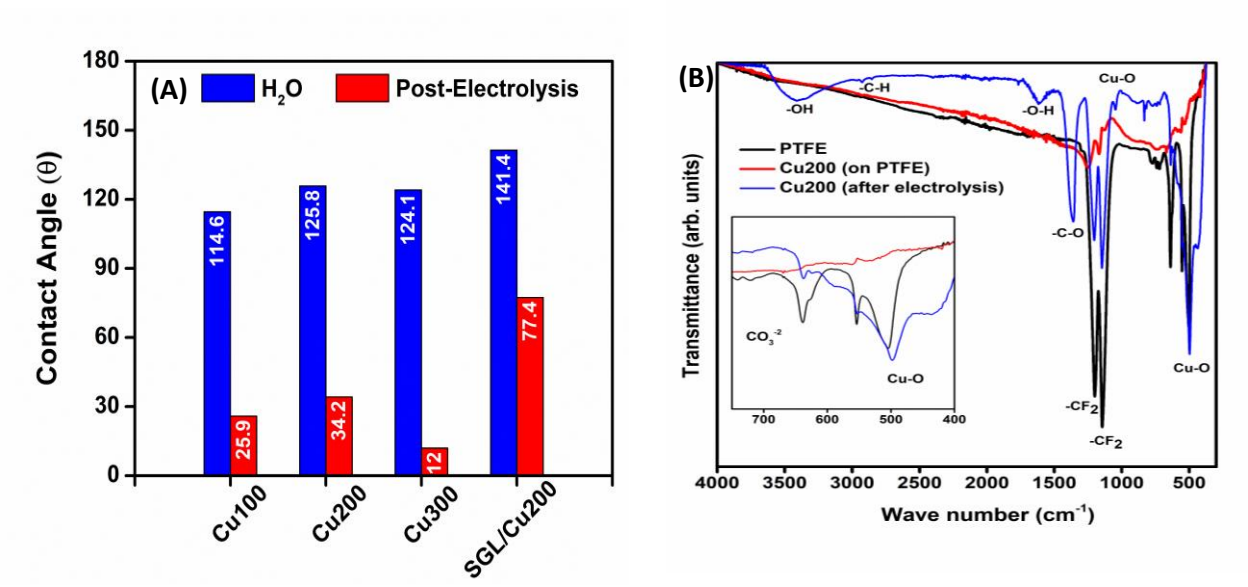


Figure 5.9 Contact angle measurements **(A)** to characterize the hydrophobicity of PTE/SGL/Cu- with H_2O and post-electrolysis. **(B)** ATR-FTIR comparative evaluation of the pristine PTFE, PTFE/Cu200 and PTFE/Cu200-after electrolysis samples.

This was suggested by ATR-FTIR analysis of a used Cu200 GDE compared to a freshly prepared Cu200 GDE and a pristine PTFE membrane (Figure 5.9B), which showed the appearance of broad bands related to hydroxyl-stretching and adsorbed water (3000-400 cm^{-1}), as well as -CO bands that could be associated to the presence of CO_3^{2-}groups (1500-750 cm^{-1}) and several vibration peaks corresponding to the vibrations between Cu^{2+} and $[CO_3]^{2-}$ and $[OH]^-$ units [18-19]. Moreover, the higher prevalence of -CF_2 peaks in the used Cu200 GDE compared to the unused Cu200 one indicates a certain loss of material. Nevertheless, as depicted in Figure 5.9A, out of the PTFE/Cu GDEs with varying thicknesses evaluated, Cu200 were the ones that kept a higher hydrophobicity after being used, whereas the thicker Cu catalyst layers (e.g. Cu300) would not necessarily imply a higher degree of protection of the hydrophobicity of the PTFE membrane. Interestingly, SGL/Cu200 exhibited a fairly constant high hydrophobicity

before and after electrolysis experiments compared to the PTFE/Cu GDE with an equivalent Cu catalyst layer (i.e. Cu200), possibly due to the presence of the hydrophobic microporous layer in the substrate.

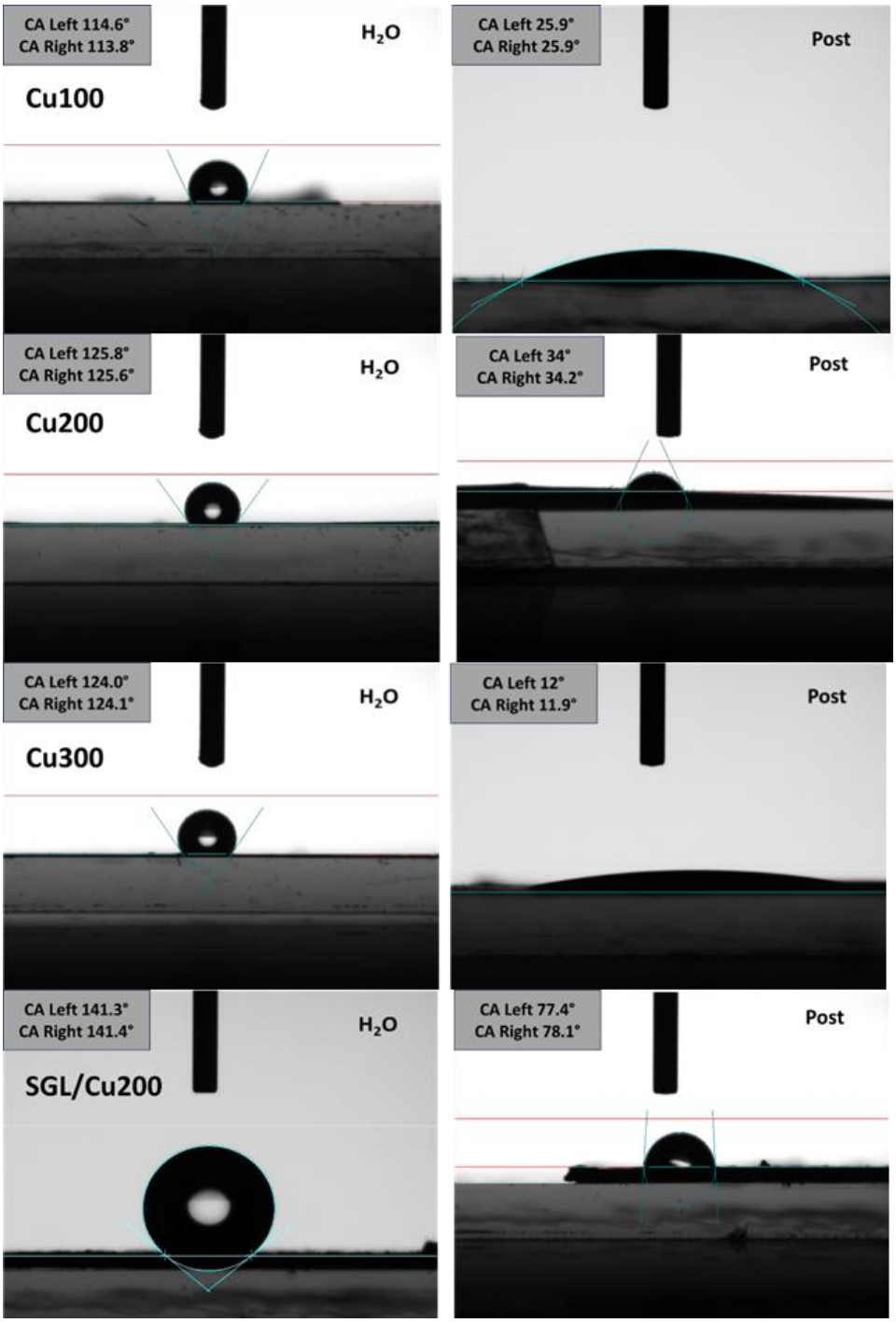


Figure 5.10 Contact angle measurement to characterize the hydrophobicity of pristine PTFE-Cu and SGL-Cu before and after the electrolysis.

After the initial characterization, the performance of PTFE/Cu GDEs with varying thicknesses of the sputtered catalyst layer for ECO_2R was evaluated at different current densities Figure 5.11. In general, all the GDEs exhibited electrocatalytic activity for ECO_2R, although their performance varied with both operation conditions and the nature of the GDE. Cu100 GDE seemed to favour the selectivity of C_2H_4 at lower current densities (of -50 $mA{\cdot}cm^{-2}$) with an average FE of 35- 40 % which further had a continuous drop of C_2H_4 selectivity at increasing current densities, whereas Cu200 and Cu300 were able to maintain a C_2H_4 selectivity at intermediate current densities, reaching a maximum value of FE around 40- 45% at -150 $mA{\cdot}cm^{-2}$. The H_2 selectivity followed an opposite trend, as the FE of H_2 rose over 40- 55% at -250 $mA{\cdot}cm^{-2}$ for all the three evaluated PTFE/Cu GDEs. Upon comparing the cathode potentials required to achieve the current densities defined (Figure 5.11E), it was evident that Cu100 GDE required more negative potentials to reach the defined current densities, especially at -250 $mA{\cdot}cm^{-2}$. On the other hand, both Cu200 and Cu300 exhibit very similar trends, not only in terms of FE towards H_2 but also regarding the cathode potential required.

Cu100 GDE exhibited the highest CH_4/C_2H_4 ratios at intermediate and high current densities, in accordance with a prevalence of Cu(111) orientation ascribed to CH_4 promotion, as it favours the protonation of *CO to form key *CHO intermediate instead of the dimerization to form *OCCO [20]. Figures 5.3 and 5.4 previously discussed revealed the presence of Cu(200) planes with increasing crystallite size in thicker Cu layers, such as Cu200 and Cu300. This growth is accompanied by a progressive decrease in the CH_4 formation and the consequential higher selectivity towards C_2H_4. Interestingly, once the cathode potential was *iR*-corrected and the current density was normalized based on ECSA estimation, it was possible to see that the performance of all PTFE/Cu GDEs studied (i.e. Cu100, Cu200 and Cu300) was fairly similar for C_2H_4 and H_2, all of the GDEs were negatively affected at higher current densities leading to significant H_2 formation and limited efficiencies towards C-products, reaching limiting partial currents for CO, C_2H_4 and CH_4 within the evaluated current values as depicted in Figure 5.12. This can be explained by limited local adsorbed CO_2 availability and promoted HER, particularly exacerbated at high overpotential values. Besides this, a certain wettability variation and partial Cu loss were observed on all PTFE/Cu GDEs after electrolysis.

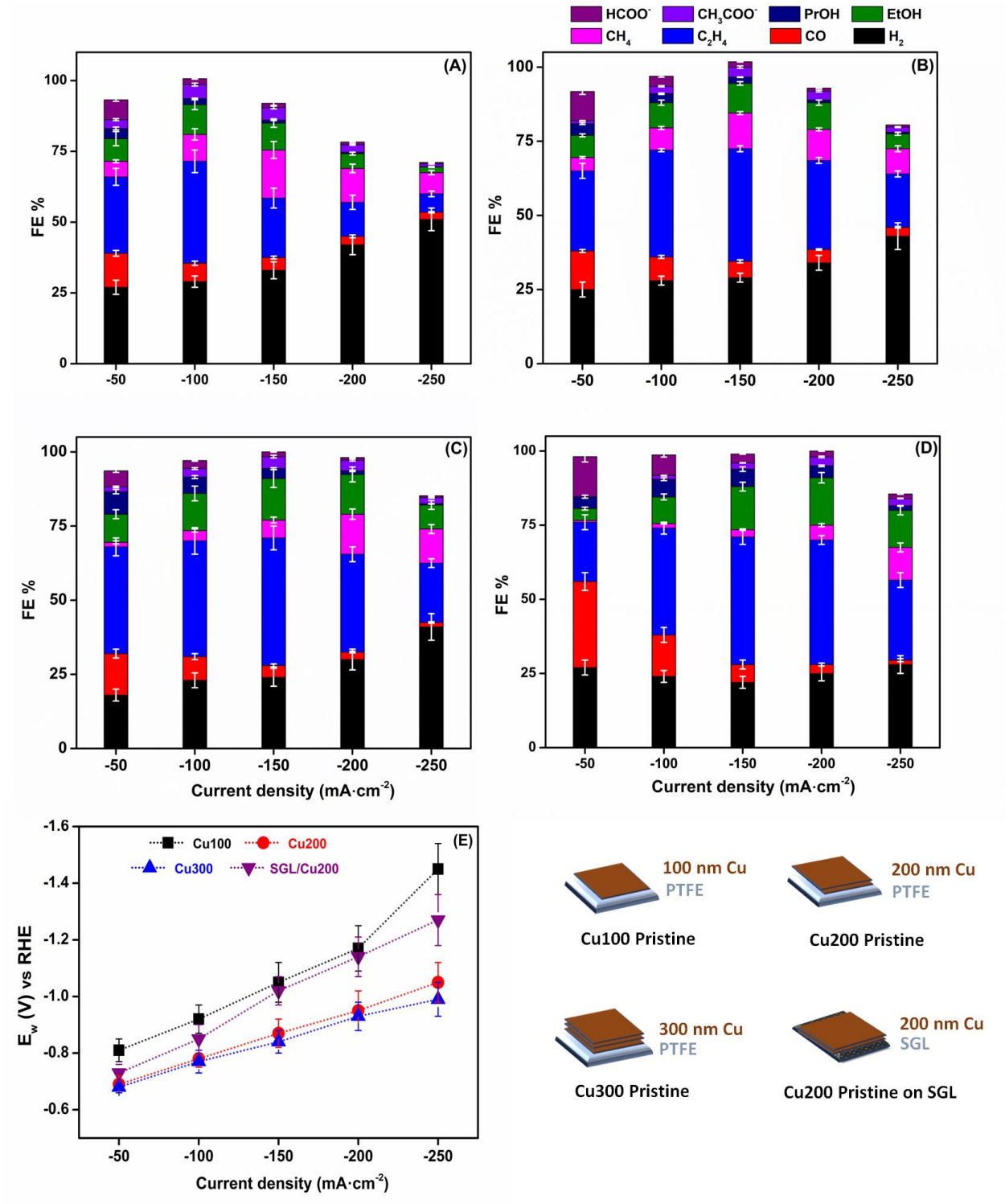


Figure 5.11 Electrocatalytic CO_2 Reduction with **(A)** Cu100, **(B)** Cu200, **(C)** Cu300 pristine electrodes on PTFE; **(D)** Cu200 pristine electrode on SGL; **(E)** cathodic potentials at different current densities on the evaluated electrodes.

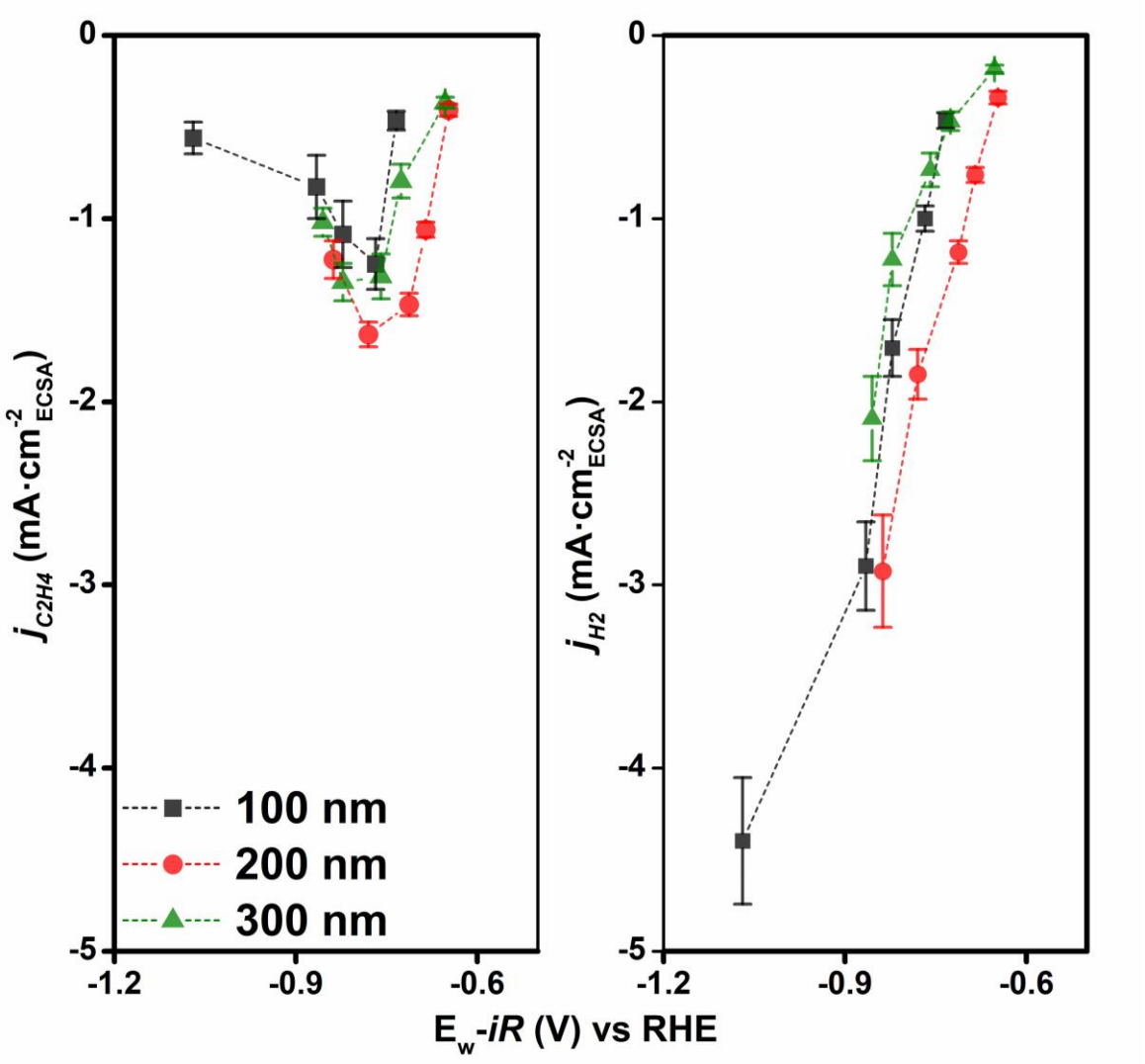


Figure 5.12. Partial current densities normalized per ECSA, considering the variation of C_{DL}, with respect to *iR* corrected cathode potentials, with an 85% correction factor from *Rs* estimation.

Comparative electrolysis experiments were also conducted with the commercial Sigracet 39BB GDL with a 200 nm thick sputtered Cu layer as depicted in Figure 5.11D. SGL/Cu200 GDE seemed to generate higher CO FE values at lower current densities, suggesting higher selectivity towards CO in those conditions, following a similar trend to those exhibited by Cu200 and Cu300 as the current density was increased. Regarding C_2H_4 selectivity, SGL/Cu200 apparently outperformed both Cu200 and Cu300 GDEs at higher current densities (> -200 mA·cm^{-2}) following a similarly decaying trend as the current density was further increased. Nevertheless, there has been a significant increase in the cathode potentials with the SGL/Cu200 GDE.

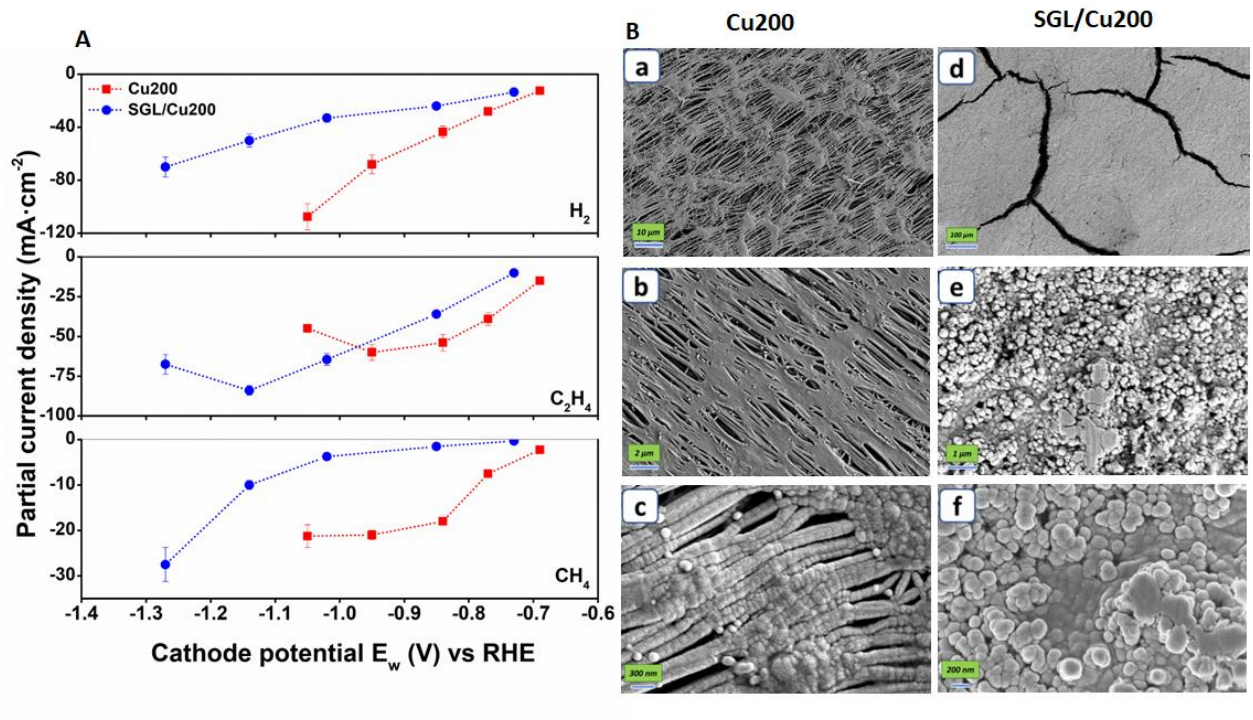


Figure 5.13 (A) Comparative of partial current density vs cathode potential for pristine Cu200 and SGL/Cu200 electrodes; **(B)**SEM images (top-view) of Cu200 **(a-c)**, and SGL/Cu200 **(d-f).**

Considering that both electrodes have sputtered Cu catalyst layers of similar thickness, these preliminary results evidence the relevance of the existing microenvironment, particularly the role of the GDL, besides the intrinsic nature of the catalytic active sites (e.g. apart from its carbonaceous nature, the commercial GDL has a highly hydrophobic microporous layer). The characteristics of the Cu catalyst layer sputtered over the surface of the Sigracet 39 BB GDL were also studied by XRD analysis. XRD and FWHM analysis (calculations depicted in Chapter 2/ not included in this chapter) indicated similar structural characteristics with dominant Cu(111) orientation and only a marginally larger crystallite size for Cu(200) in the case of the SGL/Cu200 compared to Cu200 (7.6 and 10.2 nm, respectively) while the SEM images as depicted in Figure 5.13 B show slightly different morphologies following a conformal deposition on the corresponding underlayer, where the thin Cu film seems to completely cover the porous matrix of the Sigracet 39 BB, with the risk of completely blocking the pores of the GDL part of the SGL/Cu200 GDE. This could be part of the reason for the significantly more negative cathode potentials required to reach the defined current densities. Also, from Figure 5.13A, it was noticed that the overpotentials for H_2 and CH_4 are higher with the SGL/Cu200 electrode and the bare Cu200 reaches a lower limit partial current for C_2H_4. This

further can be hypothesized that the presence of the MPL as mentioned above, aids in facilitating the diffusion of the CO_2 to the TPB, and also leads to higher overpotentials when compared to the pristine Cu200 as a result of the strong hydrophobicity.

Based on the preliminary results previously discussed, 200 nm was chosen as the benchmark thickness of Cu catalyst layers in PTFE/Cu-based GDEs (i.e. Cu200) as it represented the best balance between resistivity (Figure 5.2), hydrophobicity before/after (Figure 5.9), ECO_2R performance (Figure 5.11) having minimum Cu deposited on the GDL.

5.6.2 Surface interface modulation of PTFE/Cu GDEs by additive layer

In the first instance, the addition of a cationic ionomer layer on Cu200 was evaluated by directly depositing a 0.25wt% Nafion ink on the sputtered Cu layer. As depicted in Figure 5.14 the presence of the cationic ionomer on the surface of the thin catalyst layer led to significant variations at both low and high current densities i.e., at -50 and -100 $mA{\cdot}cm^{-2}$, the product distribution significantly changes, with important inhibition of more hydrogenated products (i.e. H_2 and CH_4) resulting in an enhancement in the FE of C_2H_4 at intermediate and higher current densities, the cathode potential became significantly more negative, probably due to the higher electrical resistance generated by the Nafion layer, whereas no significant changes were observed in the FE values for the gas products.

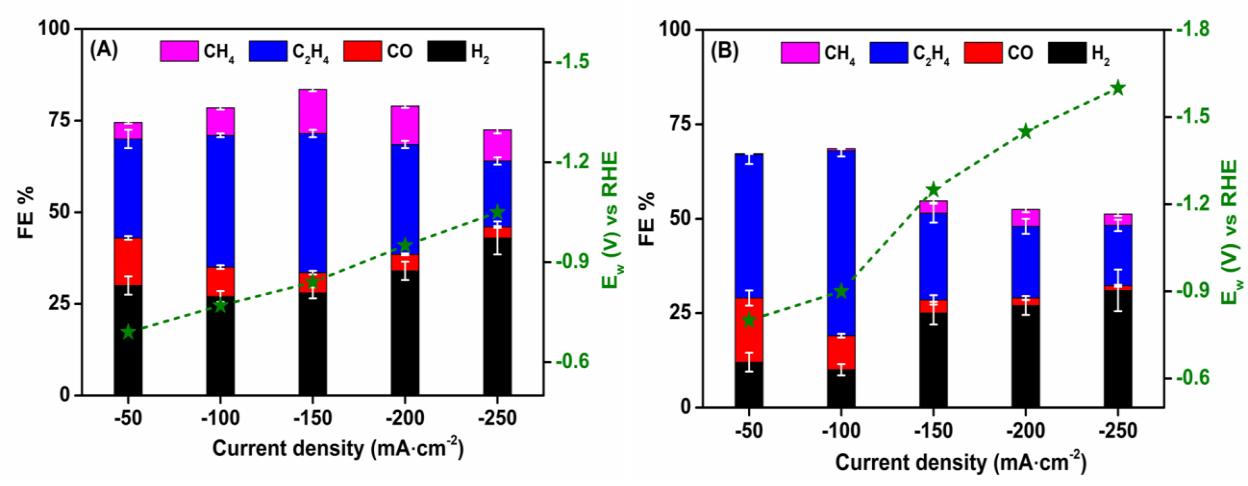


Figure 5.14. Electrocatalytic CO_2 reduction with **(A)** Cu200, and **(B)** Cu200/Nafion electrodes. The Cu200/Nafion electrode was prepared by airbrush method from a 0.25wt% Nafion ink.

The conductivity of Nafion thin films has already been studied and compared with bulk Nafion, showing a significant dependence on the thickness and relative humidity [21,22]. Moreover, surface wettability has also been correlated with film thickness, with thinner films (< 55 nm) being associated with a more hydrophobic character [23]. In prior studies, Kim et al [14] showed the influence of cationic and anionic ionomers on Cu-based electrodes, estimating higher CO_2/H_2O molar ratios on Nafion-coated Cu, with respect to pristine electrodes, while also finding decreased FE towards H_2 and CH_4. These aspects highlight the intrinsic importance of balancing the fluxes of CO_2 and protons at the triple-phase boundary and the applied current density to promote the generation of C-products.

Further modulation of the surface interface of PTFE/Cu GDEs was achieved by depositing an additive layer consisting of carbon black with Nafion, where different mass loadings (approximately 0.5 and 1 mg·cm^{-2}) by spray-coating using the airbrush method.

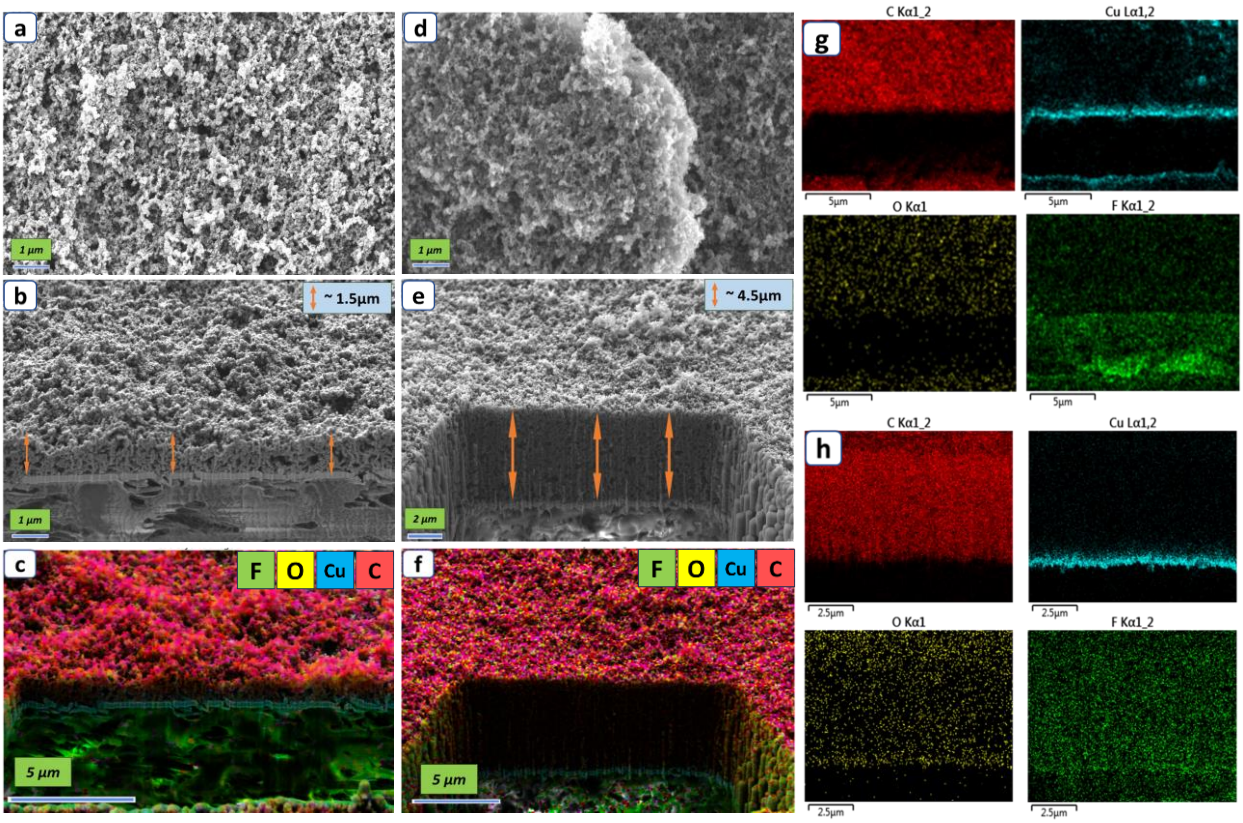


Figure 5.15 FIB-SEM of the surface, cross-sectional and EDX Mapping of the Cu200 with the additive layer Carbon. **(a)** surface of Cu200/C0.5; **(b, c)** cross-section by FIB of the Cu200/C 0.5 and EDX mapping; **(d)** surface of Cu200/C1; **(e, f)** cross-section by FIB of the Cu200/C1 and EDX mapping; **(g, h)** Elemental mapping of Cu200/C0.5 and Cu200/C1.

Varying the mass loading of the carbon black additive layer over the thin Cu catalyst film resulted in significantly different thicknesses ranging from 1.5 to 4.5 µm as depicted in Figure 5.15 (b, e) suggesting that a higher degree of porosity within the additive layer corresponding to a loading of 1 mg·cm^{-2}. Besides showing the thickness of the carbon black additive layer containing the cationic ionomer, cross-sectional images also showed how uniform and conformal the 200-µm-thick Cu film is when properly sandwiched between the carbon black additive layer and the hydrophobic PTFE membrane acting as GDL.

The carbon black additive layer was further replaced by the electrocatalyst reported and discussed in Chapter 3, carbon-supported copper-oxide heterostructures (Cu_xO-C)and Nafion. The resulting Cu_xO-C additive layer was deposited over the surface of PTFE/Cu GDEs in a similar manner to that used for the carbon black additive layer.

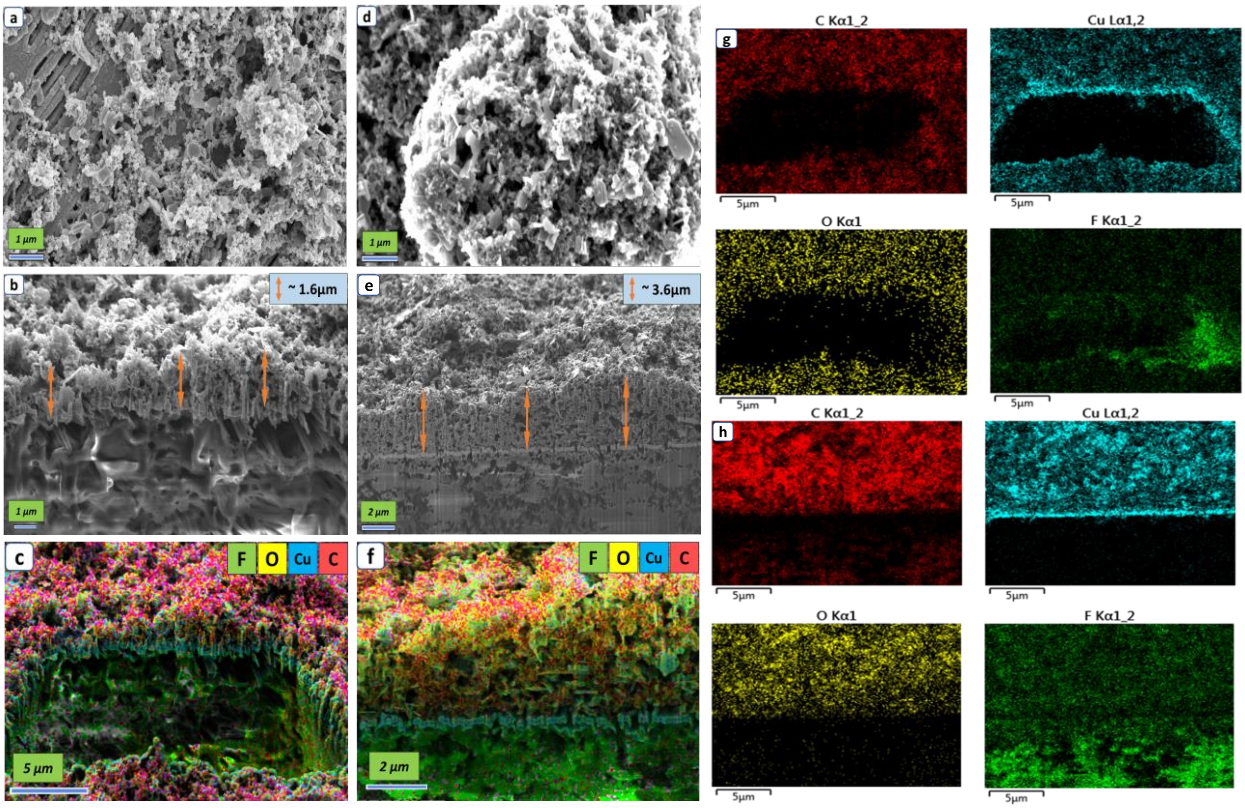


Figure 5.16 FIB-SEM of the surface, cross-sectional and EDX Mapping of the Cu200 with the additive layer Cu_xO-C. **(a)** surface of Cu200/Cu_xO-C0.5; **(b, c)** cross-section by FIB of the Cu200/Cu_xO-C0.5 and EDX mapping; **(d)** surface of Cu200/Cu_xO-C1; **(e, f)** cross-section by FIB of the Cu200/Cu_xO-C1 and EDX mapping, **(g, h)** Elemental mapping of Cu200/Cu_xO-C0.5 and Cu200/Cu_xO-C1.

Again, two Cu_xO-C additive layer loadings were evaluated (approximately 0.5 and 1 mg· cm^{-2}). Due to the presence of carbon and its role as the support matrix of the copper-oxide heterostructures in the additive layer, the porosity was well maintained and depending on the mass loading, the thickness of the Cu_xO-C additive layer ranged from 1.6 to 3.6 µm Figure 5.15 (b, e). EDX analysis further confirmed the well-distributed presence of Cu, O and C on the surface of the PTFE/Cu-based GDEs, as well as the uniform distribution of Cu_xO within the C matrix of the additive layer.

PTFE/Cu-based GDEs with the modulated surface interface by an additive layer resulted in higher C_{DL} values than the pristine PTFE/Cu GDEs as depicted in Figure 5.17. The PTFE/Cu-based GDE with 1 mg·cm^{-2} of the additive layer consisting of C-Black and Nafion (i.e. Cu200/C1) exhibited the highest double layer capacitance (4.73 mF·cm^{-2}) due to the presence of a thick and highly porous carbon with the precedented high surface area. Nonetheless, the PTFE/Cu-based GDEs with the same mass loading (1 mg·cm^{-2}) of the additive layer containing the oxide-derived copper heterostructures (i.e. Cu200/Cu_xO-C1) exhibited a fairly high capacitance (3.42 mF·cm^{-2}) despite its slightly thinner nature and the presence of copper-carbon heterojunctions. It is important to highlight the distinct role of the C and Cu_xO-C additive layers: in the former, no additional catalyst was incorporated; therefore, its higher ECSA does not account for the presence of catalytic active sites. Moreover, the Cu200/Cu_xO-C1 GDE exhibited the greater hydrophobicity of all the GDEs evaluated in this study, with CA values > 150° as depicted in Figures 5.1 and 5.18 along with the raw data Figure 5.19.

Previous studies by Tan et al. [24] revealed that a high degree of porosity within the surface of the electrode could be achieved by using the airbrush method to deposit the catalyst/additive layers on GDEs, which in turn would enhance CO_2 mass transport, thus serving as a strategy to modulate the local concentration of CO_2. Based on the electrolysis experiments, it is evident that product selectivity was tuned and enhanced towards the production of C_2H_4 as the surface of Cu200 GDEs was further modulated with the addition of different additive layers. Unlike the pristine Cu200 electrodes, GDEs with the carbon black additive layer with mass loadings of 0.5 and 1 mg·cm^{-2} (i.e. Cu200/C0.5 and Cu200/C1, respectively) achieved low FE values towards C_2H_4 values at lower current densities as depicted in Figure 5.20. In those conditions, the production of CO was favoured (FE of CO > 50%), which could be associated with the effective abundance of surface-adsorbed *CO intermediate at the interface

boundary. In this regard, the optimum amount of *CO absorbed is the crucial step for effective C-C dimerization, which eventually leads to C_2H_4 generation at high current densities [25].

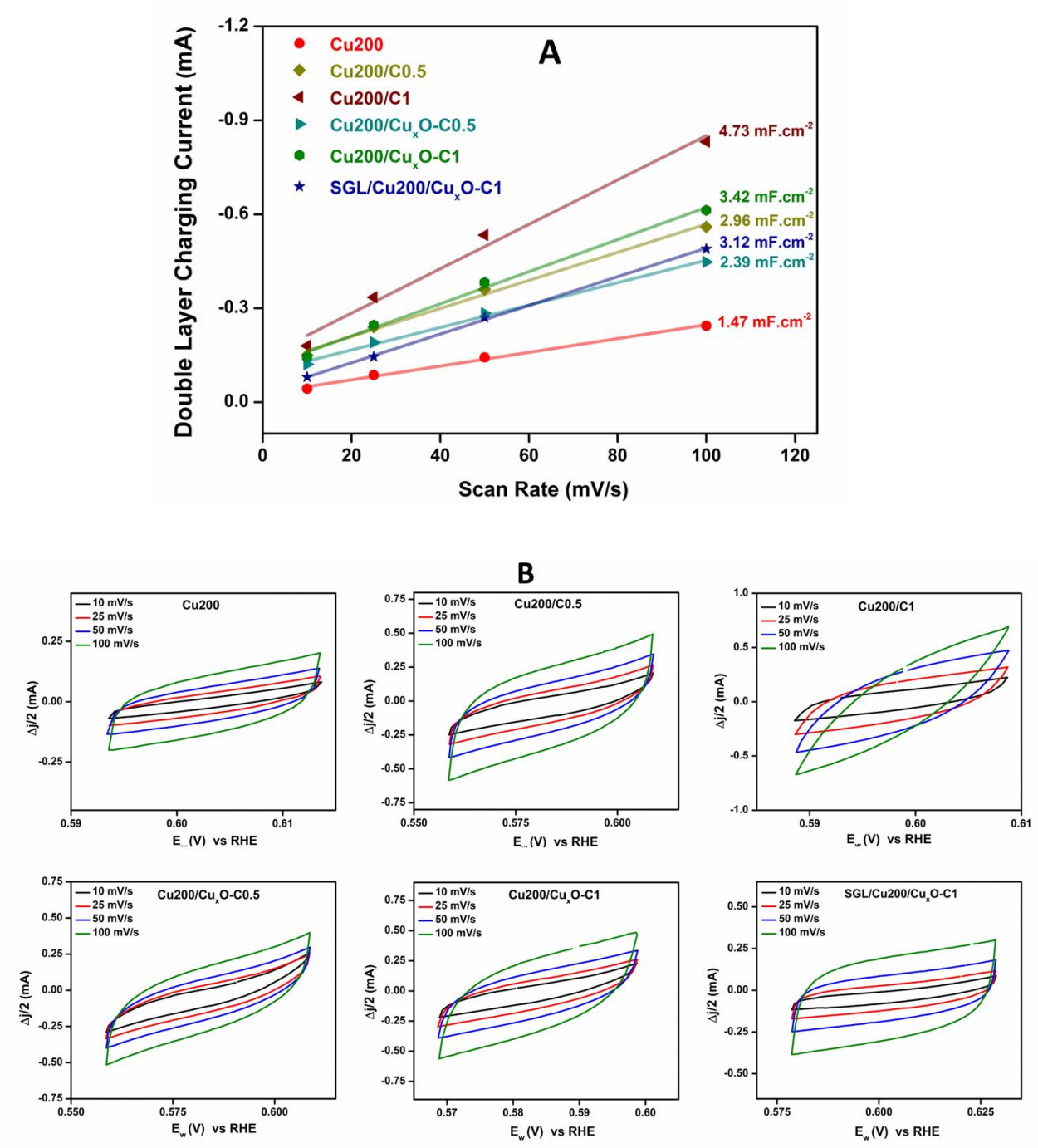


Figure 5.17. The plot **(A)** of double-layer charging currents (mA) vs Scan rate (mV/s) for the Cu electrodes deposited on PTFE and commercial SGL plus additive layer. The slope of the above plots indicates the double-layer Capacitance (C_{DL}). **(B)** cyclic voltammograms and the respective samples with the additive layers.

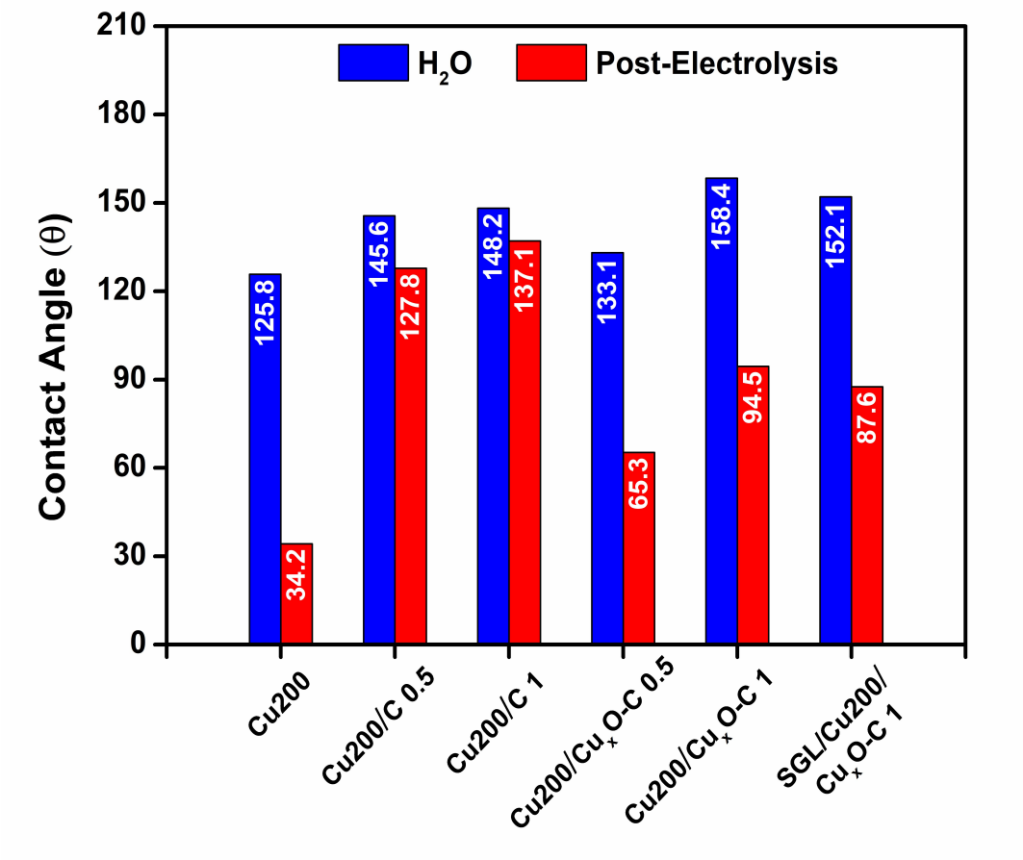


Figure 5.18. Contact angle measurements to characterize the hydrophobicity of PTE/SGL/ Cu-Additive Layer with H_2O and post-electrolysis.

Thus, C_2H_4 generation seemed to peak at a current density of -200 mA·cm^{-2}, while negligible amounts of CO were observed at -250 mA·cm^{-2}. FE values also dropped significantly for the undesired HER activity as the current density was increased. (FE of H_2 accounted for less than 25% at -250 mA·cm^{-2}). The drop in FE of H_2 and CH_4 was more remarkable with the greater mass loading of carbon black (Cu200/C1), demonstrating the role of the additive layer in improving the selectivity towards C_{2+} product. On another hand, more negative cathode potentials were required to reach the defined current densities with the 0.5 mg·cm^{-2} carbon black additive layer (Cu200/C0.5) as depicted in Figure 5.20 D. This would be caused by the more electrically resistive nature of the carbon black additive layer when compared to the Cu catalyst layer. Moreover, its porous and non-catalytic nature would create a longer path for the protons to reach the electrocatalytic Cu active sites and react with CO_2 and *CO intermediate species. Surprisingly, a greater mass loading of this additive layer (Cu200/C1) would counteract this issue due to the higher porosity of the carbon black additive layer and the resulting increase in its surface area.

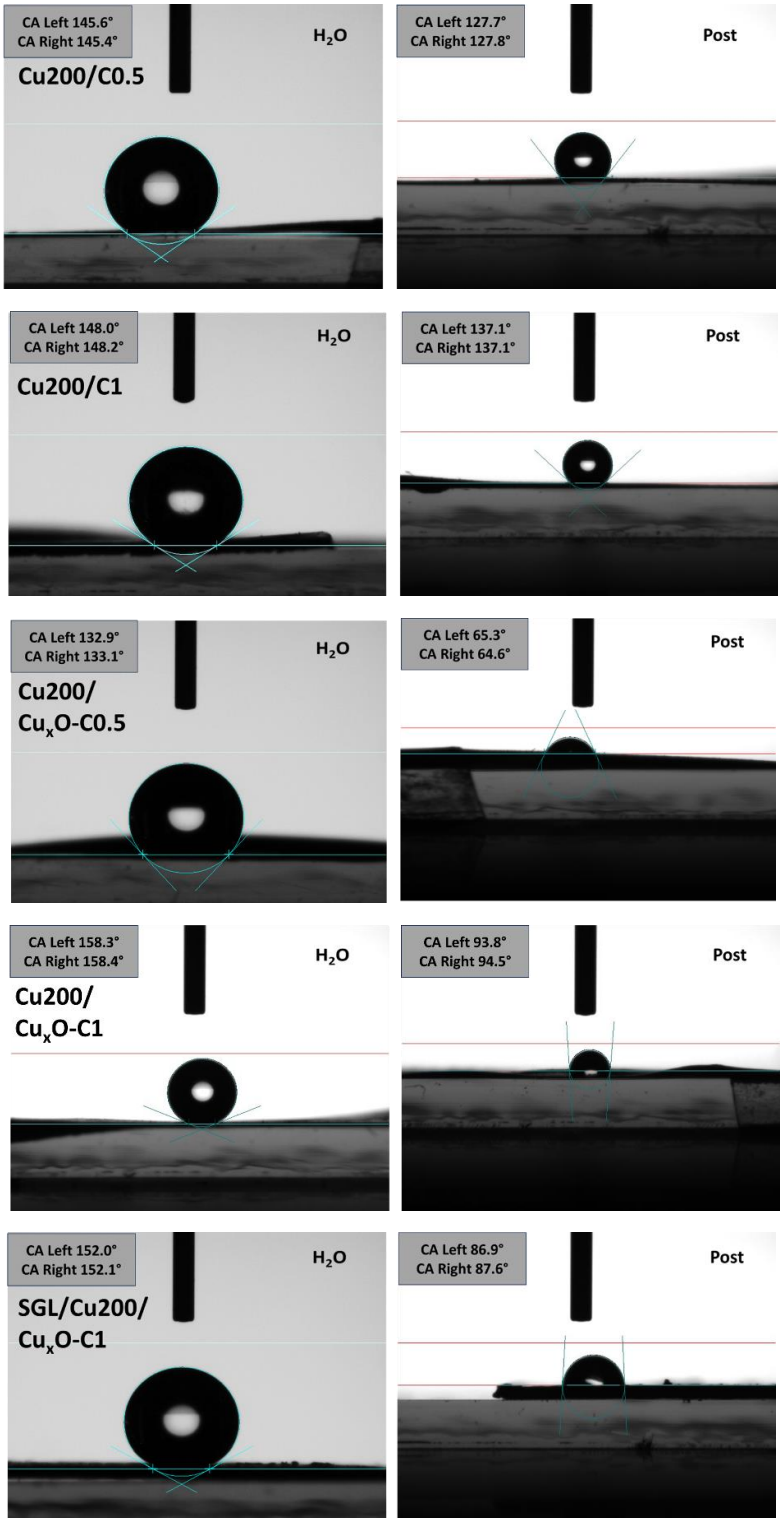


Figure 5.19. Contact angle measurement to characterize the hydrophobicity of various electrodes: Cu200/C0.5, Cu200/C1, Cu200/Cu_xO-C0.5, Cu200/Cu_xO-C1, SGL/Cu200/C1.

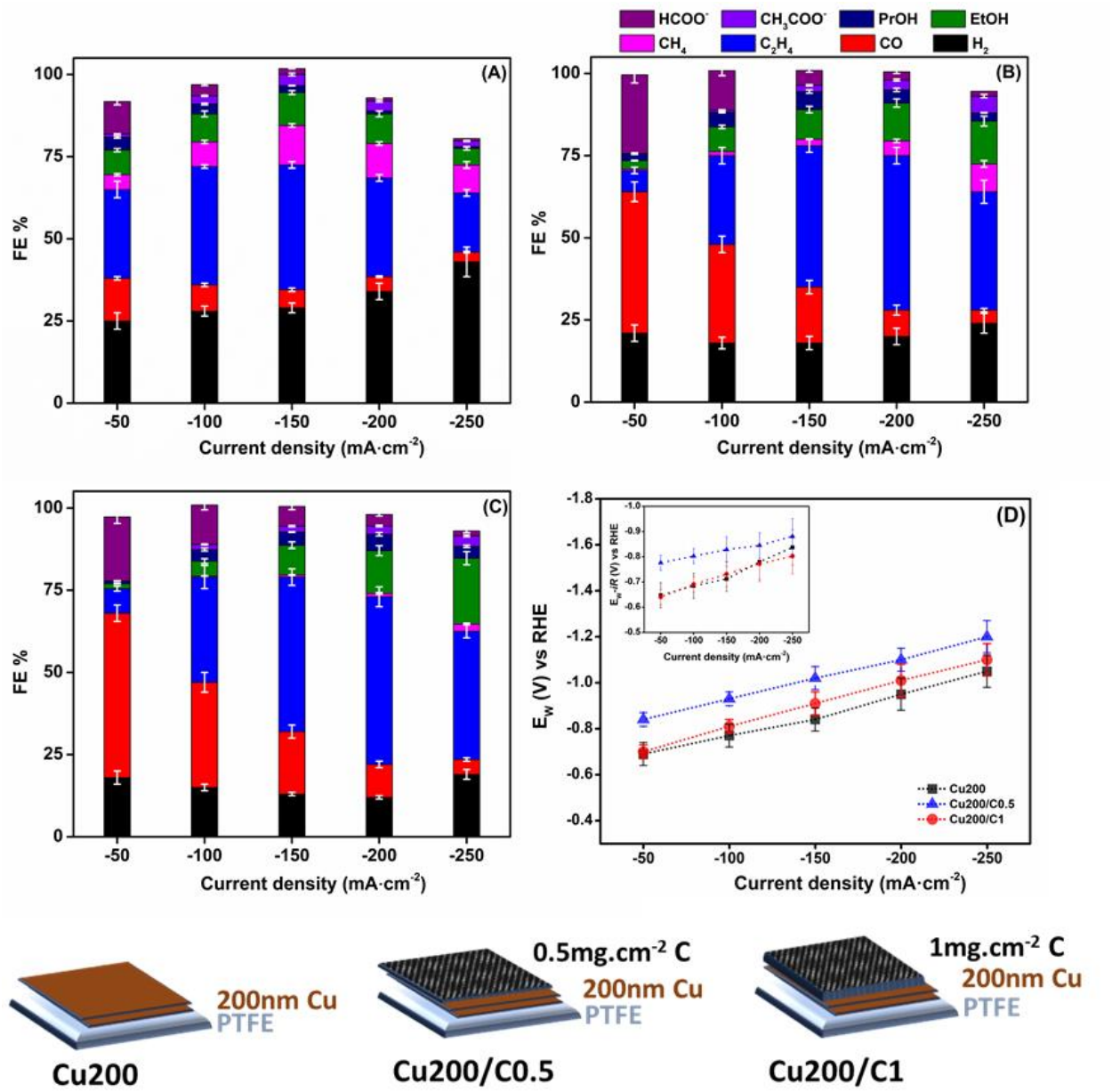


Figure 5.20. Product distribution (FE %) during the ECO_2R with **(A)** Cu200, **(B)** Cu200/C0.5 **(C)** Cu200/C1, and **(D)** cathode potentials at different current densities (in the inset, *iR* corrected values) along with the schematic representation of developed electrode configurations.

Although the addition of a carbon black additive layer containing a cationic ionomer on PTFE/Cu-based GDEs delivered a noticeable increase in the selectivity and efficiency of ECO_2R towards C_2H_4, there is still room for improvement to try to achieve a performance beyond the state of the art for PTFE/Cu GDEs [14]. That being said, further modulation of the surface interface of PTFE/Cu-based GDES with an additive layer consisting of carbon-supported copper-oxide heterostructures (Cu_xO-C) with Nafion.

In the previous chapters, the development of the Cu_xO-C, a robust electrocatalyst to enhance the ECO_2R to C_2H_4 was already discussed with a detailed characterization to understand the morphological and structural properties [17]. In Chapter 3, it was demonstrated that the electrocatalyst, Cu_xO-C was drop-casted on Toray Carbon paper and the performed ECO_2R resulted in a FE over 45% towards C_2H_4 at a current density of -200 $mA{\cdot}cm^{-2}$ under neutral pH conditions in an aqueous solution containing 1 M $KHCO_3$. In Chapter 4, Cu_xO-C was deposited by spray coating onto the Sigracet 39BB and further evaluated under alkaline conditions. Although the cathodic potentials were lowered under alkaline conditions, evaluation at higher current densities was further required.

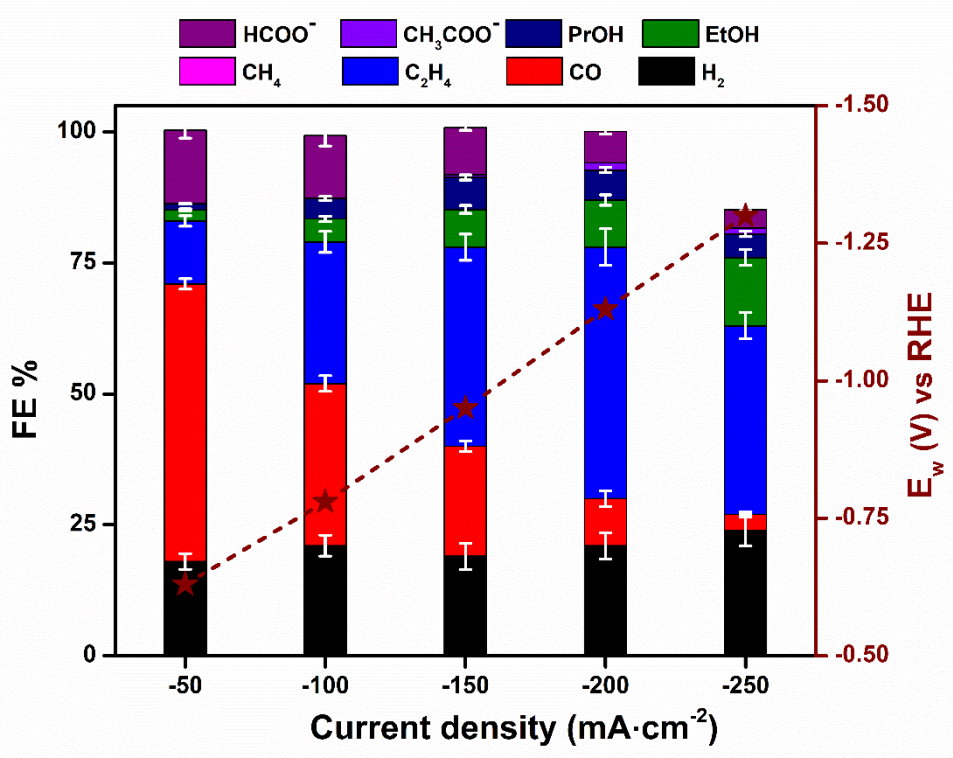


Figure 5.21 ECO_2R of SGL/Cu_xO-C1 and respective cathodic potentials at different current densities along with the schematic representation of developed electrode configuration.

In this present study, 1 $mg{\cdot}cm^{-2}$ of Cu_xO-C the electrocatalyst, Cu_xO-C was deposited by spray-coating using the airbrush method on the commercial Sigracet 39 BB GDL (i.e. SGL/Cu_xO-C). Further evaluation of SGL/Cu_xO-C, the performance under alkaline conditions alike the other PTFE/Cu electrodes, delivered a FE over 48% towards C_2H_4 at -200 $mA{\cdot}cm^{-2}$. The evaluated performance of SGL/Cu_xO-C was depicted in Figure 5.21 while also reducing the FE of H_2 to half the values previously reported [17]. The decrease in the cathodic potentials when compared to the results from the previous chapter was possibly due to lowered internal resistance from

the membrane used in the present study, the FAA-PE-50 having a lower thickness when compared to the previously used both the FAB-PK-130 and FAA-PK-150 respectively.

PTFE/Cu-based GDEs were prepared by depositing the Cu_xO-C additive layer onto Cu200 electrodes with two mass loadings of 0.5 and 1 $mg \cdot cm^{-2}$ (i.e. Cu200/Cu_xO-C0.5 and Cu200/Cu_xO-C1, respectively). The formation of C1 products was favoured with both mass loadings, delivering combined FE values over 70% for CO and formate at low current densities as depicted in Figure 5.22. Again, the low availability of surface-adsorbed *CO intermediates at the interface could explain the low selectivity towards C_2H_4 at the initial current density which is -50 $mA \cdot cm^{-2}$. However, the FE of C_2H_4 surged as the current density was increased, indicating a more effective utilization of *CO intermediates, promoting dimerization. The undesired HER was kept under control in all cases, with the FE of H_2 routinely under 20% with both mass loadings at current densities between -50 and -250 $mA \cdot cm^{-2}$. The best results were achieved with a mass loading of 1 $mg \cdot cm^{-2}$ (i.e. Cu200/Cu_xO-C1), where outstanding FE towards C_2H_4 over 70 ± 2 % was achieved at commercially relevant current densities of -250 $mA \cdot cm^{-2}$ while the FE of H_2 was completely minimized to 6.5%, setting a new performance record for PTFE/Cu-based GDEs in ECO_2R to C_2H_4 under realistic electrolyte conditions (1 M KOH) and industrially relevant current densities. In addition, ethanol, propanol and acetate were also produced at noticeable ratios (FE of C_2H_5OH, FE of C_3H_7OH and FE of CH_3COO^- values of approximately 13.5%, 5% and 1.5 respectively), resulting in remarkable combined FE 90 ± 3 % for C_{2+} products.

To illustrate the importance of the hydrophobic PTFE membrane acting as GDL in the results achieved with the Cu200/Cu_xO-C1 GDE, a Cu_xO-C additive layer with the same mass loading was applied over the surface of a GDE consisting of a commercial Sigracet 39 BB GDL and a 200nm-thick Cu catalyst layer sputtered over its surface (i.e. SGL/Cu200/Cu_xO-C1). Fairly similar results in terms of FE values for all products were observed on GDEs having either a Sigracet 39 BB GDL or a hydrophobic PTFE membrane at low current densities as depicted in Figure 5.22 C and D. However, at intermediate and high current densities, HER seemed to be more favoured by the SGL/Cu200/Cu_xO-C1 GDE at expense of C_2H_4, leading to significantly lower selectivity towards C_2H_4 as the current density increased. Moreover, significantly more negative cathode potentials were required to achieve the current densities defined in this study with the SGL/Cu200/Cu_xO-C1 electrode (Figure 5.22E), whereas significantly less

negative cathodic potentials were necessary to achieve the same current densities with the Cu200/Cu_xO-C1 electrodes.

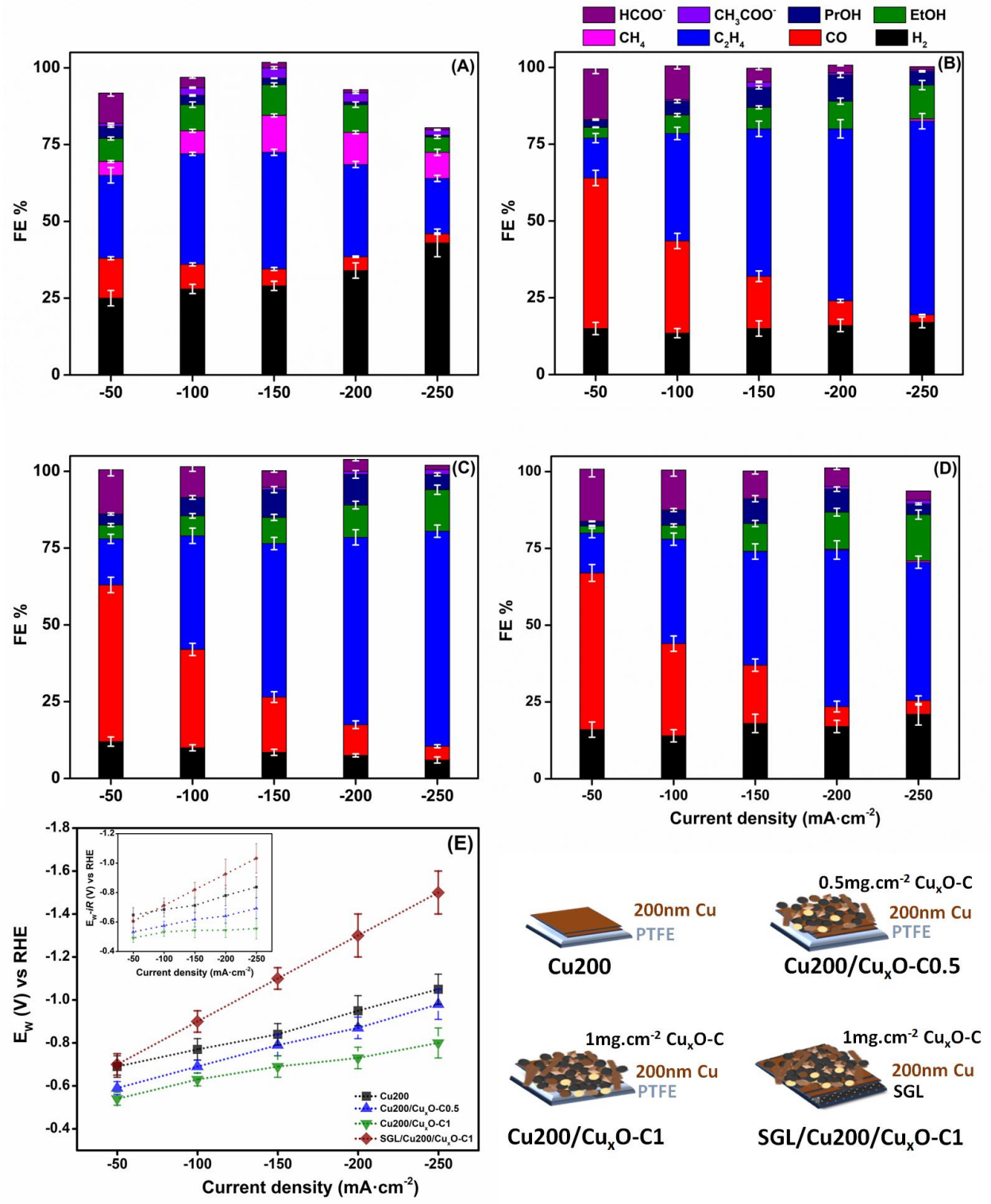


Figure 5.22 Product distribution (FE %) during the ECO_2R with **(A)** Cu200, **(B)** Cu200/Cu_xO-C0.5 **(C)** Cu200/Cu_xO-C1 and **(D)** SGL/Cu200/Cu200/Cu_xO-C **(E)** cathode potentials at different current densities (in the inset, *iR* corrected values).

In fact, a closer look at the inset included in Figure 5.22E reveals that, once the cathode potentials have been *iR*-corrected, the Cu200/Cu_xO-C1 only required ultra-low overpotentials to achieve the commercially relevant current density of 250 mA·cm^{-2} with an outstanding FE of C_2H_4 over 70 %. From these obtained results, an EE value of 39.7% for C_2H_4 can be estimated at a current density of -250 mA·cm^{-2}, while further addition of ethanol would result in an EE of 47.2%, demonstrating the strong performance delivered by the Cu200/Cu_xO-C1 electrodes developed in this study when compared with the previously reported GDEs by other researchers [26].

As illustrated by the results depicted and discussions made to this point, the outstanding performance of the Cu200/Cu_xO-C1 here presented is a consequence of the use of hydrophobic PTFE membranes as GDLs, the deposition and optimization of a 200nm-thick Cu catalyst layer sputtered over the surface of the PTFE membrane, and then the optimized deposition of 1 mg.cm^{-2} of the additive layer consisting of carbon-supported copper-oxide heterostructures (Cu_xO-C) with Nafion. This was achieved by taking a holistic approach towards the optimization of the GDE as a whole rather than a specific focus on each component separately. To illustrate the benefits of this approach, it is worth now taking a closer look at the partial current densities estimated for all products obtained with a wide range of electrodes as depicted in Figure 5.23. These partial currents are presented, in most cases, along with predicted theoretical curves according to the simple kinetic modelling proposed in the methodology, which is based on the Butler-Volmer equation.

The predicted curves generally showed a very good fitting with experimental data, especially in the case of the four main products obtained (i.e. C_2H_4, C_2H_5OH, C_3H_7OH and H_2), which would suggest that classical transport limitations would not be as critical as one might think when considering the nature of ECO_2R, at least in the operating conditions and setup used in this study at current densities up to -250 mA·cm^{-2}. On the other hand, CO and $HCOO^-$ did not follow the Butler-Volmer equation, to the point that no theoretical curves were determined. This was expected in the case of CO, as *CO acts as a reaction intermediate, promoting dimerization when adsorbed at the surface of the electrode which eventually results in the generation of C_{2+} products like C_2H_4. However, comparing the $HCOO^-$ is more controversial as it is commonly considered an end-product [27], and in some cases, it has even been treated as a potential contributor to electrode passivation, particularly in acidic conditions [28,29].

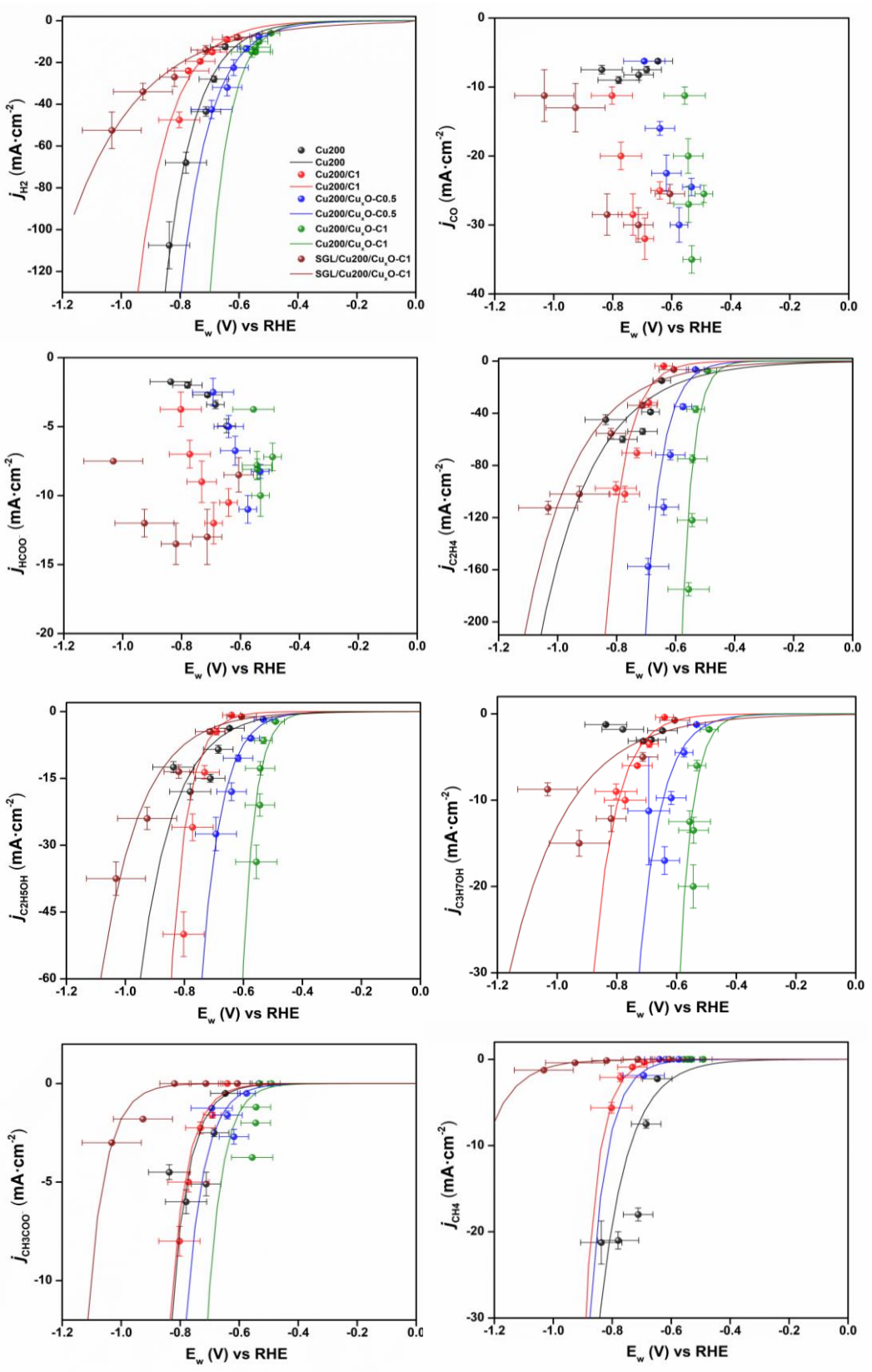


Figure 5.23. Comparative evolution of the partial current densities with respect to the observed cathode potentials based on the Butler-Volmer model. The lines correspond to the fitting and the data points with the experimental values.

Nevertheless, these same studies also presented experimental evidence and discussions suggesting formate as another potential intermediate in ECO_2R to other products demonstrating very similar trends observed for both CO and $HCOO^-$ in nearly all of the electrodes used in this study strongly suggest that this may indeed be the case.

The analysis of the partial current densities for the different products provides very useful information for further research and upscaling of the technology. In the case of C_2H_4, it could be seen that PTFE/Cu GDEs with no additive layers (Cu200) performed analogously to the GDEs equipped with a commercial Sigracet 39 BB GDL, even if these had the optimized Cu catalyst and additive layers (SGL/Cu200/Cu_xO-C1). On the other hand, the PTFE/Cu-based GDEs modulated with an additive layer performed much better towards the production of C_2H_4, whereas the Cu200/Cu_xO-C1 GDE was clearly the best-modulated surface interface. Similar observations can be made for ethanol, propanol, and acetate demonstrating the need to holistically develop and optimize the GDL, catalyst layer and additive layer to enhance the ECO_2R processes. In this regard, the performance of the Cu200 GDE was so poor towards propanol that no fitting with the Butler-Volmer equation was possible due to the extremely low partial current densities achieved with the said electrode; however, by just adding a Cu_xO-C additive layer to that very same structure, a significant improvement could be achieved in the production of propanol (i.e. Cu200/Cu_xO-C0.5 and Cu200/Cu_xO-C1).

Interestingly enough, the PTFE/Cu-based GDEs seemed to perform better for HER than what one would have expected based on the FE of H_2 reported above. The reason for those values was quite obvious: PTFE/Cu-based GDEs with an additive layer had such an excellent performance for ECO_2R to C_{2+} products requiring significantly lowered cathodic potentials in order to reach the applied current densities. The case of the Cu200/Cu_xO-C1 GDE is paradigmatic in this regard: the experimental data perfectly fits the Butler-Volmer equation, and the theoretical curves indicate that it would be the best GDE for HER of all the electrodes evaluated. However, its performance for ECO_2R to C_2H_4 primarily, but also ethanol is so outstanding, that very low overpotentials are required to achieve the current densities set to the point that very low HER activity was observed for this GDE. Something analogous occurs with methane, while no methane was observed in any of the experiments conducted with Cu200/Cu_xO-C1 GDEs, Cu200/Cu_xO-C0.5 did yield some methane at -250 $mA \cdot cm^{-2}$. This might again seem surprising, as the only difference between both electrodes is the mass loading of

the Cu_xO-C additive layer; moreover, one would expect to see at least the same amount of methane being produced when doubling the mass loading of the additive layer. However, it precisely illustrates that the optimized modulated surface interface of the GDE boosts the electrocatalytic performance to the point that significantly lowers the overpotentials required to achieve the set current density, along with the ability to completely inhibit a side reaction (in this case ECO_2R to CH_4) that requires an overpotential greater than the one being applied.

For further comparison purposes, Table 5.2 displays the values of α_{C_i} and $j^e{}_i$ estimated for the ECO_2R to C_2H_4, CH_4, C_2H_5OH, C_3H_7OH and CH_3COO^-, as well as HER where H_2 is the product. As expected, Cu200/Cu_xO-C1 GDEs presented the highest values of $\alpha_{C_{C_2H_4}}$, $\alpha_{C_{C_2H_5OH}}$ $\alpha_{C_{C_3H_7OH}}$, generally followed by either Cu200/Cu_xO-C0.5 or Cu200/ C1 electrodes. Regarding $j^e{}_i$, it was more difficult to establish a trend due to the lack of experimental data at very low current densities and potentials close to equilibrium for all of the reactions. Again, it must be noted that the values of both α_{C_i} and $j^e{}_i$ must be taken cautiously as they do not provide any mechanistic information based on the simplifications adopted for the kinetic modelling.

However, based on the generally good agreement between the experimental results and predicted j_i curves, these kinetic parameters could be used for further electrolyzer design and optimization as well as design and engineering calculations to further scale up the ECO_2R to C_2H_4 and other C_{2+} products.

Table 5.2. Values of α_c and j^e estimated from the kinetic modelling proposed based on the Butler-Volmer equation to fit the experimental results depicted in Figure 5.23.

Electrode	H_2		C_2H_4		CH_4		C_2H_5OH		C_3H_7OH		CH_3CO^-	
	α_c	j^e ($mA \cdot cm^{-2}$)	α_c	j^e ($mA \cdot cm^{-2}$)	α_c	j^e ($mA \cdot cm^{-2}$)	α_c	j^e ($mA \cdot cm^{-2}$)	α_c	j^e ($mA \cdot cm^{-2}$)	α_c	j^e ($mA \cdot cm^{-2}$)
Cu200	0.133	$1.9 \cdot 10^{-2}$	0.012	$4.5 \cdot 10^{-1}$	0.034	$1.3 \cdot 10^{-3}$	0.018	$7.6 \cdot 10^{-3}$	n/a	n/a	0.072	$1.8 \cdot 10^{-6}$
Cu200/C1	0.115	$2.8 \cdot 10^{-2}$	0.033	$1.3 \cdot 10^{-4}$	0.065	$5.1 \cdot 10^{-8}$	0.038	$3.6 \cdot 10^{-6}$	0.019	$6.6 \cdot 10^{-5}$	0.076	$5.7 \cdot 10^{-7}$
Cu200/Cu_xO-C0.5	0.130	$4.0 \cdot 10^{-2}$	0.038	$1.8 \cdot 10^{-4}$	0.055	$1.5 \cdot 10^{-6}$	0.032	$2.8 \cdot 10^{-4}$	0.020	$3.6 \cdot 10^{-4}$	0.072	$4.1 \cdot 10^{-6}$
Cu200/Cu_xO-C1	0.190	$4.1 \cdot 10^{-3}$	0.058	$3.7 \cdot 10^{-6}$	n/a	n/a	0.052	$3.2 \cdot 10^{-6}$	0.033	$4.0 \cdot 10^{-6}$	0.086	$1.9 \cdot 10^{-6}$
SGL/Cu200/Cu_xO-C1	0.054	$7.1 \cdot 10^{-1}$	0.012	$2.3 \cdot 10^{-1}$	0.036	$3.5 \cdot 10^{-6}$	0.016	$1.0 \cdot 10^{-2}$	0.007	$4.5 \cdot 10^{-2}$	0.071	$1.7 \cdot 10^{-8}$

5.6.3 Performance of PTFE/Cu-based GDEs at high current densities

The commercial feasibility of ECO_2R to C_2H_4 with PTFE/Cu-based GDEs was further evaluated by conducting electrolysis experiments at increasing current densities ranging from -100 to -500 $mA{\cdot}cm^{-2}$ using the electrode that exhibited the best performance, namely $Cu200/Cu_xO$-C1. The maximum FE of C_2H_4, as depicted in Figure 5.24 was observed at current densities around -200 and -300 $mA{\cdot}cm^{-2}$, followed by a subsequent decrease at increased currents. However, a maximum FE of 20% for C_2H_5OH was achieved at -400 $mA{\cdot}cm^{-2}$. Thus, operating at even higher current densities showed that the selectivity towards C_2H_4 was negatively affected, which would be an issue if C_2H_4 was mainly targeted as the major product.

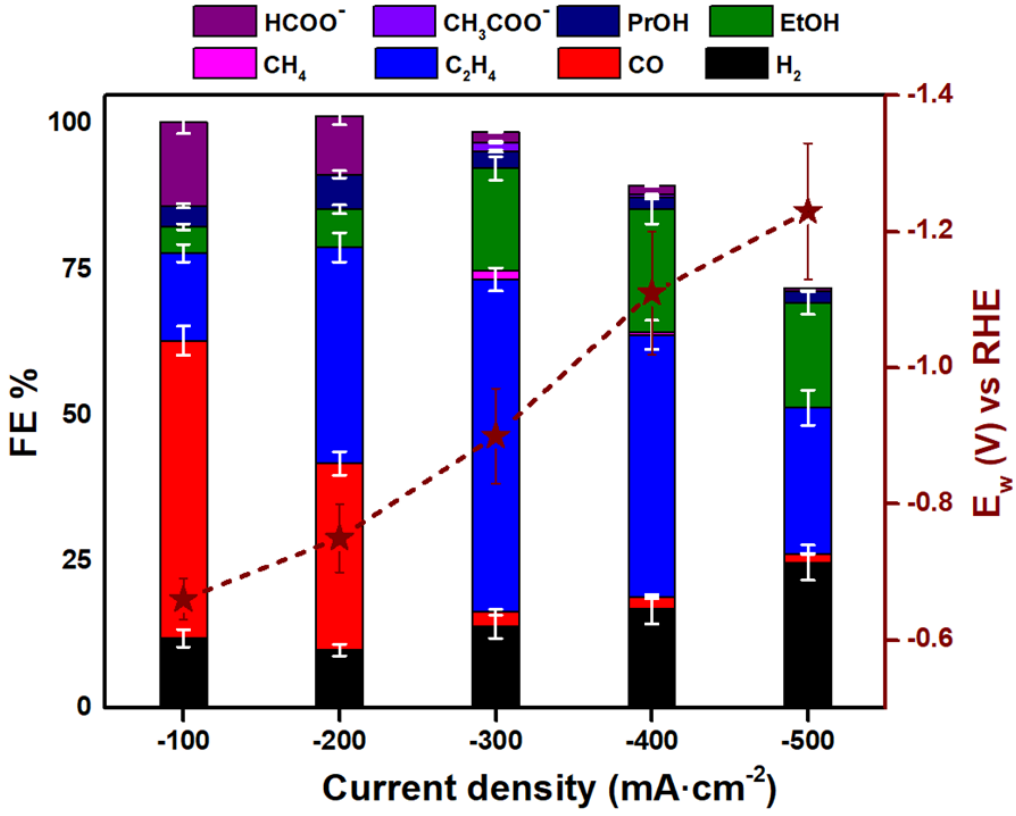


Figure 5.24 Electrocatalytic CO_2 Reduction of $Cu200/Cu_xO$-C1 at high current densities indicating the respective cathode potentials.

Further analysis of partial current densities to several products is depicted in Figure 5.25, indicating that the limiting current densities were reached for ECO_2R to CO and C_2H_4 at ≥ -300 $mA{\cdot}cm^{-2}$, implying that the kinetic modelling proposed could not be used at very high current densities. That was not the case for HER, as one would expect, as well as for ECO_2R to C_2H_5OH,

suggesting different reaction mechanisms for varying the product selectivity obtained from the ECO_2R.

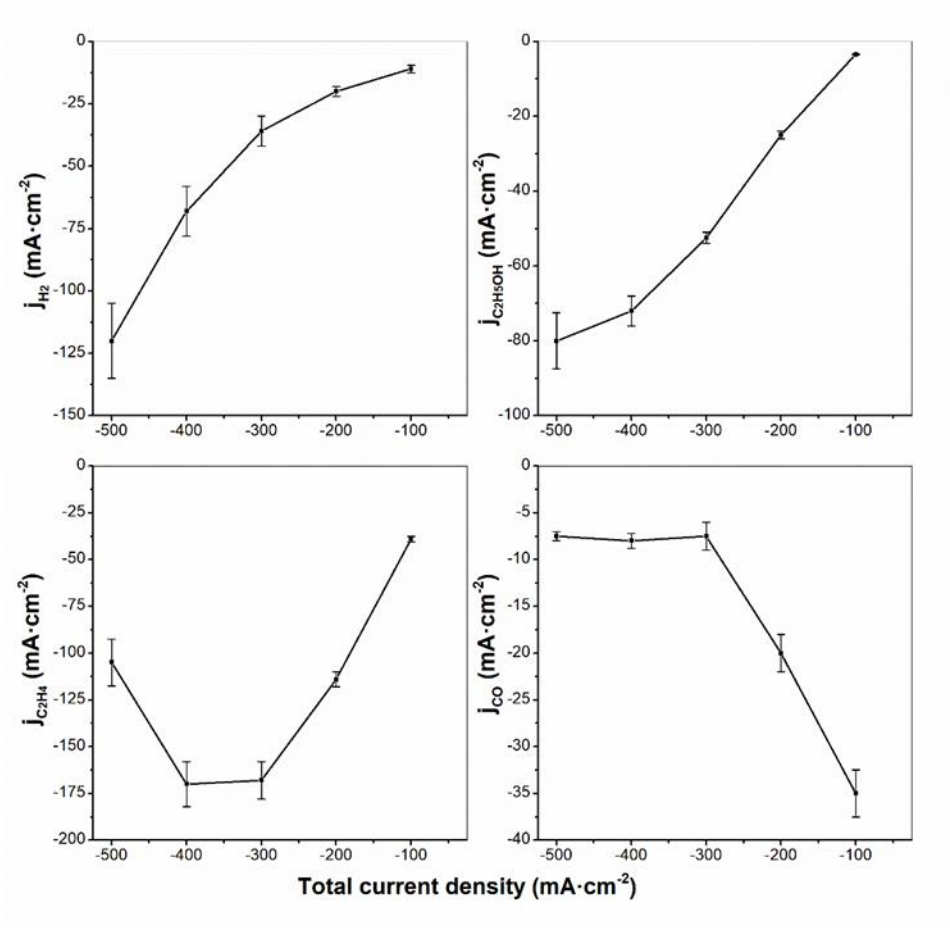


Figure 5.25. Partial current densities with respect to total current density in the test with Cu200/Cu_xO-C1. The points correspond to the values obtained in the test with standard current conditions.

5.6.4 Stability of PTFE/Cu-based GDEs during continuous operation

The stability of the Cu200/Cu_xO-C1 GDEs was further evaluated by conducting the electrolysis experiments for several hours in the flow electrolyzer operating at the maximum current density of -250 mA·cm^{-2}. During the operation, a fairly constant FE of C_2H_4 around 60- 70 % was achieved, whereas the FE of H_2 remained low throughout the experiments as depicted in Figure. 5.26. A negligible amount of CO was also measured throughout the tests. After 5 hours of testing, the cell potential started to rise due to the variation of pH towards more acidic conditions, especially in the anolyte, which was exacerbated by the anionic transfer of carbonate species through the membrane. This seemed to have a slightly detrimental effect

on the ECO_2R to C_2H_4 production, as the FE of C_2H_4 dropped to less than 60%. After 7-8 hours of continuous electrolysis, the electrolyte was replaced with fresh 1 M KOH solution and resumed the stability trials with the same GDEs and operating conditions. Bringing the pH back to the specified alkaline conditions clearly contributed to improved performance of the electrode with the FE of C_2H_4 rising to 70% again while keeping the undesired HER activity under control. Overall, the Cu200/Cu_xO-C1 GDE performed very well with no signs of decrease in performance for over 25 hours at -250 mA·cm^{-2}, where the need to replace the electrolyte due to the change in pH was the only minor inconvenience. Besides proving the need to optimize the anode side of the electrolyzer and incorporate a dosing system that would enable a constant control of the pH of both catholyte and anolyte, the stability tests indicate a high stability of the Cu200/Cu_xO-C1 GDE under continuous operation.

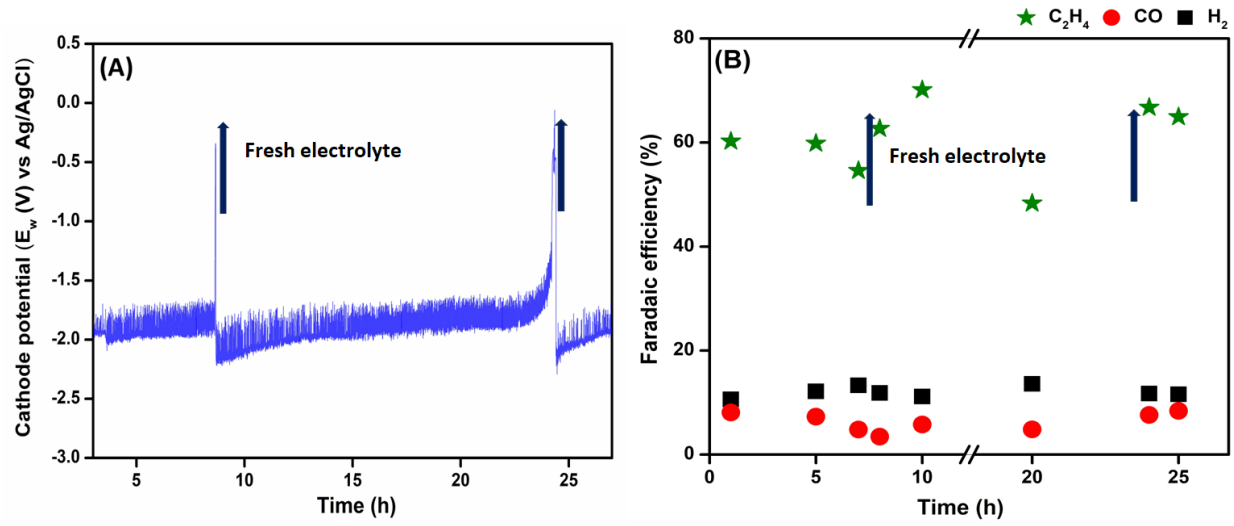


Figure 5.26. ECO_2R stability test with Cu200/Cu_xO-C1 at a current density of -250 mA·cm^{-2}, with Ni foam as anode and 1M KOH electrolyte. **(A)** electrochemical data and **(B)** FE data of C_2H_4, CO and H_2 with respect to time.

As hypothesized at the beginning of this study, by holistically optimizing all the components of GDEs for ECO_2R (e.g. selection of hydrophobic PTFE membrane; deposition of the Cu catalyst layer further by modulating the surface interface microenvironment with an optimized additive layer loading and thickness i.e., carbon-supported copper-oxide heterostructures with Nafion as a binder (Cu200/Cu_xO-C1) promoted a moderated residence time and optimal concentration of reaction intermediates (CO*) at the interface boundary as demonstrated in Figure 5.27. The presence of underlying supportive C-Black in the additive

layer of the catalyst would ideally act as the additional microporous layer blocking excessive H^+ (arising from water) from reaching the thin Cu catalyst layer. Consequently, the Cu_xO-C additive layer modulates the proton source, which is another crucial factor in the production of C_2H_4 and other C_{2+} products from ECO_2R [14,15]. This can be attributed to the control of the surface-adsorbed *H and the residence time of the $*CO_2$ /*CO concentration at the TPB to further promote CO dimerization [30,31] under energetically favourable conditions thereby steering the maximum selectivity of the ECO_2R to C_2H_4.

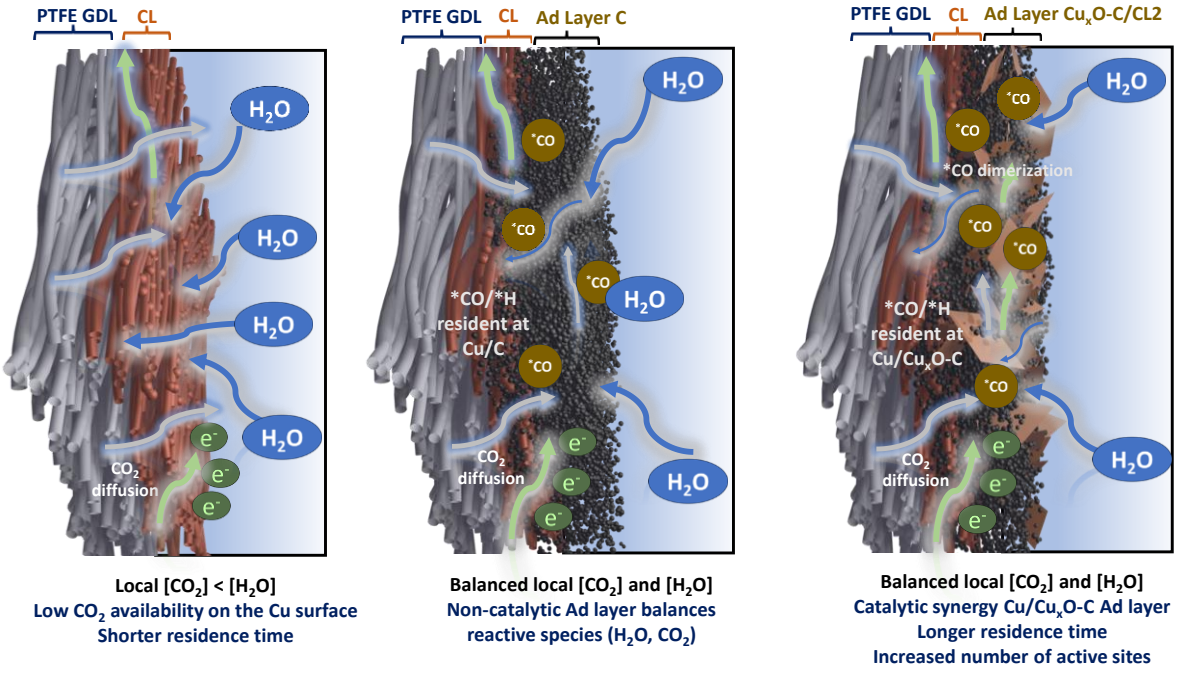


Figure 5.27. Illustrating the ECO_2R at the surface interface of pristine Cu200, the modulated surface interfaces of Cu200/C1 and Cu200/Cu_xO-C1.

5.6.5 Scaling up of the PTFE/Cu-based GDEs deployed electrolyzers

Even though it was quite interesting to notice the benchmarking FE values with the Cu200/Cu_xO-C1 GDE at industrially relevant current densities, the full-scale deployment of the GDEs in commercial electrolyzers to increase the productivity of the desired ECO_2R product is a requirement for actual technological deployment. In this regard, as demonstrated in Figure 5.28, three different areas of GDEs were fabricated and deployed in the flow electrolyzers. Although the study presented in this chapter majorly comprises the 5 cm^2 GDEs, initially a 2 cm^2 GDE was studied and further scaled up to a 10 cm^2 GDE-mounted flow electrolyzer. As

depicted in Figure 5.28 A, upon comparing the cathodic potentials, the 10 cm^2 GDE showed a lowered cathodic potential when compared to both 5 and 2 cm^2 GDEs demonstrating the superior performance with the scaled-up electrolyzers at the applied current density of -250 $mA{\cdot}cm^{-2}$. Furthermore, the productivity comparison of all three GDEs as depicted in Figure 5.28 B revealed the benchmarking productivity towards C_2H_4 of the 10 cm^2 GDE. Upon comparing the productivities, it is interesting to notice that the 5 cm^2 GDE has the productivity multiplied by 3.5 times when compared with the initially evaluated 2 cm^2 GDEs and almost multiplied to 7.5 times with the 10 cm^2 GDEs at a current density over -200 to -225 $mA{\cdot}cm^{-2}$ with partial depreciation at -250 $mA{\cdot}cm^{-2}$. The productivity comparison reveals the superior performance in both productivity and efficiency indicating the scope for successful upscaling of the Cu200/Cu_xO-C1 GDEs at optimal conditions.

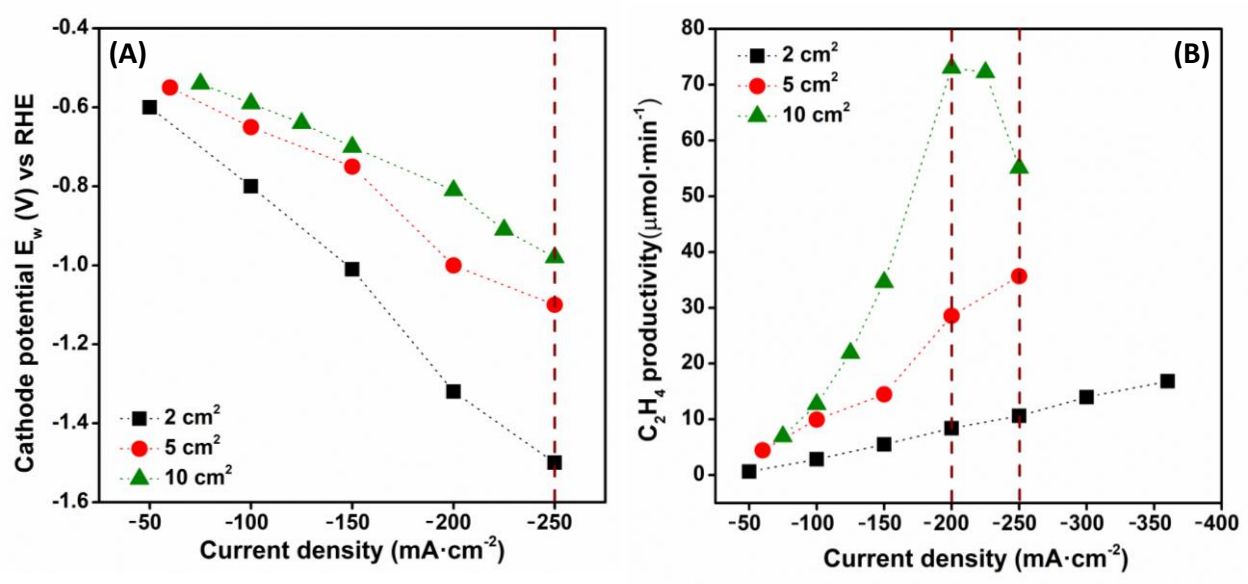


Figure 5.28. Scaled-up performance of the various areas of GDE mounted electrolyzer for ECO_2R with Cu200/Cu_xO-C1. **(A)** cathodic potential comparison **(B)** Productivity comparison of C_2H_4 with all three GDEs at increasing applied current densities.

5.7 Conclusions

The study presented in this chapter was aimed at designing tailor-made PTFE/Cu GDEs that are highly stable and maximizing the selectivity towards the generation of C_2H_4. As bare PTFE/Cu GDEs suffered from selectivity and stability due to a not-so-well-maintained surface interface at the TPB, a systematic modulation of the surface interface of the thin Cu catalyst layers was conducted by depositing an optimized additive layer. The results here demonstrated that, by effectively modulating the surface interface of the PTFE/Cu with an additive layer to optimize its thickness and porosity, the selectivity of ECO_2R to C_2H_4 and other C_{2+} products can be finely tuned and enhanced. The presence of an additive layer, carbon-supported copper-oxide heterostructures and Nafion (Cu_xO-C) resulted in an effective modulation of the surface interface at the TPB, thereby optimizing the mass transport of CO_2 to active sites and the presence and interaction of reaction intermediates. This Cu_xO-C additive layer therefore contributes to the local availability of adsorbed reaction intermediates like *CO, which are crucial for dimerization and generation of C_2H_4 and other C_{2+} products. With a minimum feed supply of CO_2 and a flow electrolyzer operating at industrially relevant current densities i.e. -250 $mA \cdot cm^{-2}$, outstanding faradaic efficiencies for C_2H_4 over 70 ± 2 % and a combined FE of 90 ± 3 % for C_{2+} products like C_2H_4, C_2H_5OH, C_3H_7OH and CH_3COO^- was achieved. Moreover, the optimized Cu200/Cu_xO-C1 GDEs were able to deliver consistently high performance over 25 hours, which can be further extended by implementing a pH control dosing system to manage the pH of both catholyte and anolyte. These excellent figures of merit achieved under realistic alkaline conditions open the room to deploy these electrodes in GDE-based large-scale ECO_2R flow electrolyzers operating at pilot plant scale and even at full-fledged industrial level.

5.8 References

1. D. Higgins, C. Hahn, C. Xiang, T. F. Jaramillo, A. Z. Weber, ACS Energy Lett. 2019, 4, 317.
2. D. A. Salvatore, D. M. Weekes, J. He, K. E. Dettelbach, Y. C. Li, T. E. Mallouk, C. P. Berlinguette, *ACS Energy Lett.* **2018**, 3, 149.
3. T. T. H. Hoang, S. Verma, S. Ma, T. T. Fister, J. Timoshenko, A. I. Frenkel, P. J. A. Kenis, A. A. Gewirth, J. Am. Chem. Soc. 2018, 140, 5791.
4. L. Weng, A. T. Bell, A. Z. Weber, *Phys. Chem. Chem. Phys.* **2018**, 20, 16973.
5. S. Hernandez-Aldave, E. Andreoli, *Catalysts* **2020**, 10, 713.
6. B. De Mot, J. Hereijgers, M. Duarte, T. Breugelmans, *Chem. Eng. J.* **2019**, 378, 122224.
7. M. E. Leonard, L. E. Clarke, A. Forner-Cuenca, S. M. Brown, F. R. Brushett, *ChemSusChem* **2020**, 13, 400.
8. T. Zhang, Z. Li, X. Lyu, J. Raj, G. Zhang, H. Kim, X. Wang, S. Chae, L. Lemen, V. N. Shanov, J. Wu, *J. Electrochem. Soc.* **2022**, 169, 104506.
9. K. Yang, R. Kas, W. A. Smith, T. Burdyny, *ACS Energy Lett.* **2021**, 6, 33.
10. J. W. Blake, J. T. Padding, J. W. Haverkort, *Electrochim. Acta* **2021**, 393, 138987.
11. C. T. Dinh, T. Burdyny, M. G. Kibria, A. Seifitokaldani, C. M. Gabardo, F. P. García de Arquer, A. Kiani, J. P. Edwards, P. De Luna, O. S. Bushuyev, C. Zou, *Science* **2018**, 360, 783.
12. F. Huq, I. Sanjuán, S. Baha, M. Braun, A. Kostka, V. Chanda, J. R. C. Junqueira, N. Sikdar, A. Ludwig, C. Andronescu, *ChemElectroChem* **2022**, 9, e202101279.
13. Z. Xing, L. Hu, D. S. Ripatti, X. Hu, X. Feng, *Nat. Commun.* **2021**, 12, 136.
14. C. Kim, J. C. Bui, X. Luo, J. K. Cooper, A. Kusoglu, A. Z. Weber, A. T. Bell, *Nat. Energy* **2021**, 6, 1026.
15. F. P. García de Arquer, C. T. Dinh, A. Ozden, J. Wicks, C. McCallum, A. R. Kirmani, D. H. Nam, C. Gabardo, A. Seifitokaldani, X. Wang, Y. C. Li, *Science* **2020**, 367, 661
16. A. Kusoglu, A. Z. Weber, *Chem. Rev.* **2017**, 117, 987.
17. V. S. R. K. Tandava, M. C. Spadaro, J. Arbiol, S. Murcia-López, J. R. Morante, *ChemSusChem* **2023**, 16, e202300344.
18. N. B. Tanvir, O. Yurchenko, C. Wilbertz, G. Urban, *J. Mater. Chem. A* **2016**, 14, 5294.
19. J. Gao, X. Yuan, *Minerals* **2020**, 10, 277.
20. B. Zhang, J. Zhang, P. An, Z. Su, Q. Wan, X. Tan, L. Zheng, *Nano Energy* **2021**, 88, 106239.

21. P. Adesina, J. A. Elliott, A. A. Lapkin, *Chem. Eng. J.* **2023**, 478, 147461.
22. X. Li, F. Tang, Q. Wang, B. Li, H. Dai, G. Chang, C. Zhang, W. Zheng, P. Ming, *Int. J. Hydrogen Energy* **2024**, 50, 1228.
23. D. K. Paul, R. McCreery, K. Karan, *J. Electrochem. Soc.* **2014**, 161, F1395.
24. Y. C. Tan, K. B. Lee, H. Song, J. Oh, *Joule* **2020**, 4, 1104.
25. A. Ozden, J. Li, S. Kandambeth, X. Y. Li, S. Liu, O. Shekhah, P. Ou, Y. Zou Finfrock, Y. K. Wang, T. Alkayyali, F. Pelayo García de Arquer, *Nat. Energy* **2023**, 8, 179.
26. J. Zhang, C. Guo, S. Fang, X. Zhao, L. Li, H. Jiang, Z. Liu, Z. Fan, W. Xu, J. Xiao, M. Zhong, *Nat. Commun*. **2023**, 14, 1298.
27. S. Nitopi, E. Bertheussen, S. B. Scott, X. Liu, A. K. Engstfeld, S. Horch, B. Seger, I. E. Stephens, K. Chan, C. Hahn, J. K. Norskov, *Chem. Rev.* **2019**, 119, 7610.
28. D. W. DeWulf, T. Jin, A. J. Bard, *J. Electrochem. Soc.* **1989**, 136, 1686.
29. R. L. Cook, R. C. MacDuff, A. F. Sammells, *J. Electrochem. Soc.* **1989**, 136, 1982.
30. M. Schreier, Y. Yoon, M. N. Jackson, Y. Surendranath, *Angew. Chem. Int. Ed.* **2018**, 57, 10221.
31. Y. Lum, B. Yue, P. Lobaccaro, A. T. Bell, J. W. Ager, *J. Phys. Chem. C* **2017**, 121, 14191.

Chapter 6

Conclusions and

Future Perspectives



The present thesis concludes by summarizing the highlights and obtained scientific outcomes from Chapter 3 to Chapter 5. Additionally, an outlook on the future perspectives concerning the Electrochemical CO_2 reduction to C_2H_4 and other value-added products, the challenges on further scaling up and recent progress associated with ECO_2R processes are highlighted.

6.1 Conclusions

The presented thesis was focused on addressing the development of advanced catalyst materials and systems for the electroconversion of CO_2 to C_2H_4. Initially, the research was dedicated to the design and synthesis of a robust electrocatalyst having high catalytic activity, selectivity and overall stability. In this regard, the study aimed to synthesize a highly robust electrocatalyst, carbon-supported oxide-derived copper (Cu_xO/C) heterostructures. Upon thorough physicochemical and electrochemical characterization of Cu_xO/C, the ECO_2R was performed to understand the selectivity and efficiency towards C_2H_4. In continuation, Ni-based SAC catalysts were developed and incorporated with Cu_xO/C depicting a tandem system. The developed Cu and Ni-based tandem electrocatalysts were further systematically evaluated in different approaches to understand the product selectivity and demonstrate the best-fit tandem approach to enhance the selectivity of C_2H_4. Furthermore, it was intended to modify the gas diffusion layer (GDL) by fabricating the PTFE/Cu-based gas diffusion electrodes (GDE) with strong hydrophobicity. The tailor-made PTFE/Cu-based electrodes were improvised by modulating the surface interface at the triple-phase boundary with an additive layer and further evaluated to elucidate the stir in selectivity towards C_2H_4 with increasing current densities. In relevance to the major findings and conclusions of the thesis are listed hereunder according to the list of chapters included.

Chapter 3: Cu_xO-C for ECO_2R

- An easy, facile and scalable hydrothermal route to synthesize a robust electrocatalyst having C-Black supported oxide-derived copper heterostructures was designed highlighting the initial reduction of the copper precursor followed by the in-situ growth of CuO and Cu_2O heterostructures over C-Black and depicted as Cu_xO/C.
- The as-synthesized blends of Cu_xO/C were quantified by using XRD studies to evaluate the Cu, Cu_2O and CuO phase variations and the optimum blend of $Cu_xO/C2$ depicted the initial dominating CuO phases involving platelet-like morphologies which are homogenously surrounded by cloud-like carbon structures later confirmed by HR-TEM studies. Cu_xO/C heterostructures were deposited on GDEs and evaluated in a flow electrolyzer with the direction towards enhancing the selectivity towards C_2H_4 and the results were compared to evaluate the best blend and morphology.

- In addition, the evaluated approaches of the gas-electrolyte configurations namely flow-through and flow-by, flow-by mode was found beneficial in reaching the industrial scale of operation.
- At the interface of CuO−Cu_2O/C-Black deposited over the GDE, an overall faradaic efficiency of 46 % at a current density of 200 mA · cm^{-2} in an aqueous flow electrolyzer under neutral conditions and room temperature electrolysis conditions holding stability over 12 hours was reported.
- From the post-electrolysis characterization, it was understood that the in-situ evolution of the active site from CuO to Cu_2O at lower polarization conditions is found to be the active catalytic site for the highly selective conversion of CO_2 to C_2H_4.
- The effective reduction of CuO to Cu_2O indicates the initial self-evolution of the catalysts at low polarization conditions. Additionally, the presence of C-Black had a cumulative effect in not only enabling the high local CO_2 diffusion but also high current densities while having an impact on the formation of more oxidized Cu phases with more homogeneous morphologies during the synthetic procedure.
- This work from the thesis helped in understanding the concept of carbon-supported metal (Cu) oxide heterostructures synthesized by a facile hydrothermal route as robust and highly efficient electrocatalysts in achieving higher selectivity towards ethylene operating at elevated current densities thus paving the way for developing industrially viable alternatives to produce high value-added products.

Chapter 4: Best-fit Tandem Approach

- Inspired by nature, mimicking the cascade catalytic process was incorporated to articulate the sequential reduction of CO_2 to CO and further CO to C_2H_4 resembling the tandem approach.
- Two different catalytic systems comprising Ni and Cu active sites were chosen to fabricate the tandem electrocatalysts. Initially, Tandem catalysts (TC) with varying compositions of Ni to Cu were formulated to evaluate the selectivity towards C_2H_4.
- Under alkaline conditions, TC Ni1:Cu5 was found to be the right combination delivering superior performance by lowering the HER activity and overpotential when compared to the formerly evaluated pure Cu_xO/C.

- In continuation, Tandem electrodes (TE) with layer-by-layer (LbL) and segmented (seg) electrodes were fabricated with the best-performing TC Ni1:Cu5 combination. At the initial currents, TE LbL Cu5/Ni1 was found to dominate the TCs by maximizing the CO selectivity followed by promoting C_2H_4 at the higher currents at further lowered cathodic potentials.
- Furthermore, with the motivation of device integration, Tandem devices (TD) were set up by coupling the individual electrolyzers where the products of cell-1 acted as the reactants in cell-2. TD was found to generate C_2H_4 at a relatively lower onset potential when compared to TC and TE.
- Simultaneously, ECOR was also performed with pure CO and further combined with CO_2 and H_2 gas streams to evaluate the ECOR selectivity. The proposed TD set up along with the CO/ CO_2 mixture stream confirmed that the presence of unreacted CO_2 was undesirable as it lowered the total FE of C_2H_4 and C_{2+} products.
- In this regard, the undesired CO_2 was eliminated by introducing an intermediate trap chamber to absorb the unreacted CO_2 which resulted in directing the concentrated CO feed onto the Cu-GDE which further yielded higher C_2H_4 generation with improved partial currents and lowered cathodic potentials.
- With TD set up coupled with an intermediate trap chamber, at an applied current density of -150 $mA{\cdot}cm^{-2}$, an overall FE of 70 ± 3 % of C_2H_4 and a total of 87 ± 5 % C_{2+} products were obtained with a cathodic potential of just -0.79 V vs RHE was recorded.
- The reported FE and cathodic potentials indicated the superior performance of TDs by coupling with a trap chamber resembling the ECOR. TEs performed better than TCs by enhancing the CO concentration over the Cu active sites reflecting a plug-flow reactor.
- While the direct one-step ECO_2R demonstrated an EE of 12.21% with Cu_xO-C, ECOR delivered a staggering EE of 27.5% for the generation of C_2H_4 with Cu_xO-C. Interestingly, the best-fit tandem approach, TD setup coupled with an intermediate CO_2 trap chamber delivered a promising EE of 24.3% indicating the on-par performance of the ECOR.
- Additionally, the exceptional overall stability of more than 18 h of continuous operation of the coupled electrolyzers further demonstrated the feasibility of incorporating the TD set-up at an industrial scale to obtain higher selectivity towards the value-added carbon products with improved energy efficiencies.

Chapter 5: Interface Modulated PTFE/Copper-based GDEs

- To minimize flooding issues and improve the lifespan, the conventional carbon-based GDEs were replaced by incorporating the superhydrophobic polymeric PTFE membranes supported by a thin Cu layer.
- A thorough investigation of commercial PTFE membranes acting as GDLs by depositing tailor-made conductive polycrystalline copper catalyst layers with varying thicknesses (100-300 nm) was demonstrated.
- The as-prepared PTFE/Cu-based GDEs were initially evaluated to understand the electrochemical behaviour and product selectivity. The pristine PTFE/Cu GDEs suffered from selectivity and stability due to a not-so-well-maintained surface interface at the triple-phase boundary.
- To circumvent this, the surface of the PTFE/Cu was initially modulated by using a cationic ionomer, Nafion, and later by depositing an additive layer consisting of carbon black (C) and Nafion over the surface of the sputtered copper layer.
- With the additive layer of carbon, the product distribution was tuned majorly as the selectivity towards C_2H_4 was enhanced at higher current densities compared to the pristine PTFE/Cu GDEs.
- In continuation, the surface interface modified with Cu_xO/C demonstrated that the selectivity of ECO_2R to C_2H_4 and other C_{2+} products are finely tuned and enhanced by effective surface interface modulation of the PTFE/Cu with an optimized additive layer.
- The fabricated PTFE/Cu/Cu_xO-C optimized the transport of CO_2 to active sites and the presence and interaction of reaction intermediate at the triple-phase boundary. The deposited Cu_xO-C additive layer therefore contributes to the local availability of adsorbed reaction intermediates like *CO, which are crucial for the dimerization and generation of C_2H_4 and other C_{2+} products.
- Additionally, the electrocatalytic performance was boosted to the point that significantly lower overpotentials were required to achieve the set current density, along with the ability to completely inhibit an undesired reaction ECO_2R to CH_4.
- The hierarchically constructed PTFE/Cu/Cu_xO-C exhibited a significant enhancement in the selectivity towards C_2H_4 in particular of FE over 70 % and C_{2+} products in general (combined FE over 90 % for C_2H_4, C_2H_5OH and C_3H_7OH) while minimizing the undesired

HER at an industrially relevant current density of 250 mA·cm^{-2} and a remarkable ultra-low cathodic overpotential (*iR*-corrected potential of -0.55V *vs* RHE) was observed.

- ❖ Moreover, the optimized Cu200/Cu_xO-C1 GDEs were able to deliver a consistently high performance over 25 hours, which can be further extended by implementing a pH control dosing system to manage the pH of both catholyte and anolyte.
- ❖ The figures of merit achieved under realistic alkaline conditions open the room to deploy these electrodes in GDE-based large-scale ECO_2R flow electrolyzers operating at pilot plant scale and even at full-fledged industrial level.

To summarize, this work began with the motivation to fabricate robust electrocatalyst materials to tune the major selectivity of ECO_2R to C_2H_4. While the developed electrocatalyst, Cu_xO/C, demonstrated the major selectivity towards C_2H_4, additional factors like optimizing the surface of the GDE along with monitoring the local pH conditions significantly boosted the selectivity towards C_2H_4. It was also demonstrated that incorporating optimized individual electrolyzers and integrating them at the device level depicting a cascade mechanistic pathway further demonstrated significant improvement of ECO_2R to C_2H_4 at industrially relevant conditions. Therefore, it can be concluded that it is not only the advanced catalyst materials but also the optimization of the electrode and electrolyzer systems that play a substantial role in the overall enhancement of the electroconversion of CO_2 to C_2H_4.

6.2 Future Perspectives

The field of electrocatalysis for energy-related applications has seen substantial growth during the past decade by coupling with renewable energy. Precisely with ECO_2R, there has been a quest from the scientific community in order to attain benchmark selectivity towards C_2H_4 at industrial-relevant current densities and improved energy efficiency. However, it is evident that ECO_2R involves a multi-step reaction pathway often with complex and unstable reaction intermediates thus making it a challenging task for scalability. Currently, ECO_2R to CO holds the industrial-level operations due to the minimal complexity and thermodynamic potentials. Nevertheless, significant progress has been attained towards an efficient ECO_2R to C_2H_4, potentially laying a pathway to drift away from the traditional methods of C_2H_4 synthesis based on fossil fuels. In this regard, there is still a lot of work to be done to attain an economical and

scalable deployment of ECO_2R to C_2H_4 technology. In order to meet this, I will further discuss the key areas intended for future research.

- Till date, Cu is the only material capable of selectively converting CO_2 to C_2H_4 and there has been a surplus of novel strategies to fabricate the ideal and stable surface state of Cu. However, a rational design and fabrication of Cu and Cu-based catalysts is extremely important to curb the undesirable side reactions.
- Although there has been an increasing trend in the development and implementation of in-situ and operando techniques to characterize the evolution of electrocatalysts, there is further scope to adopt more advanced and even hyphenated techniques to better understand the surface of the electrocatalyst, compositional and morphological changes along with the evolution of critical reaction intermediate. For instance, the presented thesis mentions the importance of *CO residence time which can be evaluated using appropriate in-situ/operando techniques.
- Theoretical and computational modelling like DFT has seen a vast development pertaining to analyzing the thermodynamics and reaction energetics of the electrocatalytic process, but the investigations should further extend to elucidate the kinetic modelling to better understand the key metrics like the potential dependent activation energies and pH effects.
- Further investigations to be carried out in fabricating advanced GDEs with optimized thickness and porosity to modulate the local CO_2 concentration at the electrode-electrolyte interface.
- Enhancing the conversion efficiency has been a major concern in ECO_2R. In recent times, many scientific outcomes depicted the use of alkaline electrolytes to suppress HER activity and enhance the selectivity towards C_{2+} products. As a result, carbonate concentration becomes dominant at the cathode leading to a significant loss of incoming CO_2 in addition to the other key factors of the catalyst microenvironment, stability of the GDE along with the fluid dynamics associated thereby leaving the single-pass conversion efficiency (SPCE) of just 25 % when targeting the selectivity towards value-added products like C_2H_4.
- In this regard, acid or ionic liquid-based electrolytes can hold the upper hand in the effective utilization of CO_2. However, appropriate electrocatalysts capable of

withstanding the abnormal pH conditions and high H^+ accumulation at the electrode are to be developed along with the pathways to suppress the HER activity.

- Dedicated efforts shall be invested to enhance the overall stability of the CO_2 electrolyzers ensuring product efficient operations of at least 100+ hours.
- The actual commercial integration of the CO_2 electrolyzer demands equivalent efforts at the anode level to study the H_2O-based oxidation reactions. By incorporating stable and efficient OER electrocatalysts, a sharp increase in energy efficiency shall be noticed by lowering the overall cell potential.
- In addition to the above tasks for the future, it is also important for the direct use of actual CO_2 from the point sources comprising the mixture of other gases needs to be implemented under realistic environments along with monitoring of variable supplies of intermittent renewable energy sources, separation of ECO_2R products and life cycle assessment are extremely critical.

In terms of commercialization, the direct ECO_2R has seen several promising startup groups worldwide with a focus on developing the technology to generate products like CO, C_2H_4 etc. Companies like Twelve (USA), Dioxycle (Paris), Avantium (The Netherlands) and eChemicals (Hungary) have demonstrated the technology and attracted significant funding. To conclude, it shall be an interesting path to see the progress of ECO_2R technology at the industrial scale as this electrochemical approach can potentially aid in mitigating global warming.



Tandava, Venkata Siva Rama Krishna

Early-Stage Researcher, Catalonia Institute for Energy Research (IREC)
Autonomous University of Barcelona, Spain.

vtandava.siva79@gmail.com; vsrktandava@irec.cat +34-612284483
https://www.linkedin.com/in/siva-tandava +91-9676794479
https://scholar.google.co.in/citations?user=XY_Le0AAAAAJ&hl=e @Tandava_SayS

I am a final year doctoral candidate at the Catalonia Institute for Energy Research (IREC), affiliated with the Autonomous University of Barcelona, Spain under the supervision of Prof. Dr. Joan Ramon Morante and Dr. Sebastian Murcia López in the Advanced Materials for Energy group. My ongoing research work explores electrocatalytic CO_2 conversion to alternative fuels. I have extensive expertise in the design and synthesis of new catalyst materials, testing of flow electrolyzers for electrochemical CO_2 reduction and the assessment of pre- and post-electrocatalytic processes.

Education

Autonomous University of Barcelona, (UAB) Spain. **October 2019 – Present**
Ph.D. Material Sciences | Tutor. Prof. Dr. Jordi Arbiol.
Doctoral Dissertation: *Advanced Catalyst Materials and Systems for Electro Conversion of CO_2.* ***(Thesis submitted)***

National Institute of Technology Warangal (NIT W), Telangana, India. **July 2014 – May 2016**
Master of Science, Chemistry. (Analytical Chemistry) (First Division)
Master's Thesis: *Synthesis and Characterization of Graphene-based Nanostructured Materials for Photocatalytic Applications under Sun-light Irradiation.*

Osmania University, Hyderabad, India **June 2011- April 2014**
Bachelor of Science, Life Sciences (First Division)
Triple Major Program in Chemistry, Genetics and Microbiology.

Research Experience and Academic Training

Catalonia Institute for Energy Research (IREC) **October 2019 – Present**
Ph.D. Material Sciences under the supervision of Prof. Dr. Joan Ramon Morante and Dr. Sebastian Murcia Lopez.

- **Marie Skłodowska-Curie Actions (MSCA) DOC-FAM COFUND** sponsored Early-Stage Researcher working on a doctoral thesis project titled *Advanced Catalyst Materials and Systems for Electro Conversion of CO_2.*
- Early-Stage Researcher R1.4 in the Horizon Europe project *Full Spectrum Solar Direct Air Capture & Conversion – SolDAC.*

Catalan Institute of Nanoscience and Nanotechnology (ICN2) **September 2022**
Visiting Ph.D. researcher as a part of secondment in the group of Prof. Dr. Jordi Arbiol.

- Advanced Electron Microscopy (TEM and HR-TEM)

CSIR-Indian Institute of Chemical Technology (IICT), Hyderabad, India. **January 2017 – March 2018**
Research Assistant under the supervision of Dr. BLA Prabhavathi Devi, Chief Scientist.

- *Generation of Data on Pesticide Residues and Metal Contaminants in Edible Vegetable Oils of Different Regions sponsored by the **F**ood **S**afety and **S**tandards **A**uthority of **I**ndia **(FSSAI).***

National Institute of Technology Warangal (NIT W), Telangana, India. **Sept 2015 – July 2016**
Master's Thesis student under the supervision of Prof. Vishnu Shanker.

- *Synthesis and Characterization of Graphene-based Nanostructured Materials for Photocatalytic applications under sunlight irradiation.*

Jawaharlal Nehru Institute for Advanced Studies (JNIAS), Telangana, India. **May 2015 – July 2015**

Project student under the supervision of Dr. Kaiser Jamil, Dean, JNIAS.

- *Green Synthesis of Silver Nano Particles, Characterization, and their Anti-Microbial Properties.*

Indigenèse Biotechnologies, Hyderabad, India. **May 2013 - June 2013**

- Project Trainee; *In-silico design of primers for 16S r-RNA gene and in-vitro analysis and confirmation*

Hyderabad Science Society (HSS). **May 2012 - June 2012**

- Student Trainee at Vasavi Hospital & Research Centre Kamineni Hospitals, Hyderabad, India.

Research Interests

❖ Tailoring the advanced gas diffusion electrodes and catalytic materials (focusing on biohybrid/ molecular structures as the electrocatalyst and electrolyte interface) for (photo)electrochemical conversion of CO_2 and N_2 with a strong intersest to learn and understand the electrode-electrolyte interactions using operando / in-situ techniques. I also find a greater affinity towards Electrochemical Reactor Design and Implementation exploring the potential industrial applications.

Awards and Fellowships

- **Best Poster Award – MATSUS24** (Materials for Sustainable Development Conference)**,** Barcelona 2024.
- **Young Researcher Award – E MRS** (European Materials Research Society), Spring Meeting 2022.
- **Graduate Student Award – E MRS** (European Materials Research Society), Fall Meeting 2021.
- **Marie Skłodowska-Curie Actions (MSCA) DOC-FAM COFUND Fellowship, October 2019 – September 2022.** Awarded the prestigious MSCA DOC-FAM COFUND fellowship and started the PhD program as an Early-Stage Researcher at IREC and UAB.

Publications in International peer-reviewed journals

- Hydrothermal Fabrication of Carbon-Supported Oxide-Derived Copper Heterostructures: A Robust Catalyst System for Enhanced Electro-Reduction of CO_2 to C_2H_4.
  V. S. R. K. Tandava, Dr. Maria Chiara Spadaro, Prof. Dr. Jordi Arbiol, Dr. Sebastián Murcia-López*, Prof. Dr. Joan Ramón Morante. ChemSusChem2023, e202300344 *DOI: https://doi.org/10.1002/cssc.202300344*.

- Novel and Highly Efficient Strategy for the Green Synthesis of Soluble Graphene by Aqueous Polyphenol Extracts of Eucalyptus Bark and Its Applications in High-Performance Supercapacitors.
  Saikumar Manchala, **V. S. R. K. Tandava**, Deshetti Jampaiah, Suresh K Bhargava*, Vishnu Shanker*.
  ACS Sustainable Chem. Eng. 2019, 7, 13, 11612–11620 *DOI: https://doi.org/10.1021/acssuschemeng.9b01506*.

- Fabrication of a novel $ZnIn_2S_4$/g-C_3N_4/graphene ternary nanocomposite with enhanced charge separation for efficient photocatalytic H_2 evolution under solar light illumination.
  Saikumar Manchala, **V. S. R. K. Tandava**, Lakshmana Reddy Nagappagari, Shankar Muthukonda Venkatakrishnan, Deshetti Jampaiah, Ylias M. Sabri, Suresh K. Bhargava & Vishnu Shanker*.
  Photochemical & Photobiological Sciences volume 18, 2952–2964 (2019). *DOI: https://doi.org/10.1039/c9pp00234k*.

- A Novel Strategy for Sustainable Synthesis of Soluble-Graphene by a Herb *Delphinium denudatum* Root Extract for Use as Light-Weight Supercapacitors.
  Saikumar Manchala, **V. S. R. K. Tandava**, Dr. Deshetti Jampaiah, Prof. Suresh K. Bhargava*, Dr. Vishnu Shanker*.
  ChemistrySelect2020, 5, 2701–2709. *DOI: https://doi.org/10.1002/slct.202000101*.

Articles under Communication.

- Modulating the Surface Interface of PTFE/Copper Gas Diffusion Electrodes for Steering the Selectivity of Electroconversion of CO_2 to $C2H_4$ at an Ultra-low Potential. **(Under revision after peer-review)**
  V. S. R. K. Tandava, MST Oliva, MB-Peiró, D Sylla, Joan Ramón Morante, Ignacio T-Montes*, Sebastián Murcia-López*.

- Elucidating the Best-Fit Tandem Approach for the Upscaled Electroconversion of CO_2 to Ethylene. (under communication) **V. S. R. K. Tandava**, Andrés A García, MB-Peiró, Joan Ramón Morante, Sebastián Murcia-López*.
- Effect of the electrodeposition parameters on the performance of Cu catalysts for the electrochemical conversion of CO_2. (In Preparation) MST Oliva, **V. S. R. K. Tandava,** Sebastián Murcia-López, Ignacio T-Montes*.
- Optimised Electrodeposition technique for in-situ fabrication of CuAg-based catalysts on Gas Diffusion Layers for electrochemical CO_2 reduction. (In Preparation) MST Oliva, **V. S. R. K. Tandava,** SM López, Ig T-Montes*

Book Chapter/s.

- CHAPTER 5: Two-dimensional Metal Oxide Nanomaterials for Electrochemical Conversion of CO_2 Into Energy-rich Chemicals. Anirban Das; Laxmi Devi; **V. S. R. K. Tandava**; Saikumar Manchala.
  2D Nanomaterials for CO2 Conversion into Chemicals and Fuels. DOI: https://doi.org/10.1039/9781839165542-00171.

Conference Proceedings (Selected)

- Oral presentation at the Workshop Mexico-Europe: Advanced Sustainable Materials for Energy Applications (virtual), August 2024, titled *"Enhanced Electroreduction of CO_2 to C_2H_4 by Systematic Screening of the Best-Fit Tandem Approach".*
- Poster presentation at the symposium #MatInter - Materials and Interfaces for emerging electrocatalytic reactions, Materials for Sustainable Development Conference (MATSUS24) from the 4-8, March 2024, in Barcelona, Spain titled *"Elucidating the Best-Fit Tandem Approach for the Upscaled Electroconversion of CO_2 to C_2H_4"* ***Best Poster Award**
- Oral presentation at the symposium #e-FuelSyn - Electrocatalysis for the Production of Fuels and Chemicals, MATSUS23 & Sustainable Technology Forum Valencia (STECH23) from Mar 06, 2023, to Mar 10, 2023, in Fundació Scito, València, Spain titled *"Enhanced Electrocatalytic CO_2 reduction: A Cascade Mechanistic approach enabled by a tandem setup."* Conference Proceedings DOI: 10.29363/nanoge.matsus.2023.359.
- Oral presentation entitled *"Exploring the Advanced Tailor-made Catalyst Materials and Systems for the Up-scaled Electro conversion of CO_2"* presented in the frame of Symposium I- Sustainable approaches for renewable energy conversion to fuels and chemicals of E MRS (European Materials Research Society), Spring Meeting 2022. ***Young Researcher Award**
- Oral presentation entitled *"Enhancing the Selectivity Towards C_2 and C_{2+} Products on Tunable Carbon Supported $Cu_2O/CuO/Cu$ Gas Diffusion Electrodes: A Systematic CO_2 Electroreduction Study"* at the E-MRS 2021 Fall Meeting, Symposium C-Advanced catalytic materials for (photo)electrochemical energy conversion II. *** Graduate Student Award**
- Oral presentation entitled *"Optimizing Cu/CuOx/Carbon Black Supported Gas Diffusion Electrodes. A Systematic Electrocatalytic CO_2 Reduction Study enhancing Selectivity towards C_2 and C_{2+} Value-added Products"* in the 72nd Annual Meeting of the International Society of Electrochemistry, Korea/Online (Hybrid) from 29th Aug to 3rd Sept 2021.
- Oral Presentation at 2021 MRS Virtual Spring Meeting on April 22, 2021, titled *"Electrocatalytic CO_2 Reduction on Green Synthesized Copper Nanoarchitectures to C_2 and C_{2+} Value-Added Products Supported Over Gas Diffusion Layers."*
- Generation of Data on Pesticide Residues and Metal Contaminants in Edible Vegetable Oils of Different Regions of India. Poster presented at 26th Indian Convention of Food Scientists and Technologists (ICFoST- 2017), held on December 7-9, 2017, at Centre for Lipid Research, CSIR-IICT, Hyderabad, India.

Technical Expertise and Skills

- Experienced in fundamental electrochemical characterization techniques including electrosynthesis.
- Expertise in the synthesis of nanomaterials using wet-chemistry synthesis and high-temperature Furnaces.
- Expertise in handling Electrochemical Reactor Design and Implementation, Gas Diffusion Electrodes, Electrode fabrications and handling the ion exchange membranes involved in electrochemical CO_2 reduction.
- Experienced in material characterization techniques like FE-SEM, XRD, AFM, and data interpretation from XPS.
- Experienced in handling analytical instruments like Inductively Coupled Plasma Optical Emission Spectrometry (ICP-OES), Gas Chromatography (GC) (different detectors), High-Pressure Liquid Chromatography (HPLC), Ion Chromatography (IC), UV-Visible-NIR and UV- Visible-DRS Spectrophotometers, ATR-FTIR Spectrometer.
- Experienced in data visualization and interpretation using Origin, MS Excel and currently learning Python.

Academic Affiliations and Achievements.

- Annual Student Member - International Society of Electrochemistry **(ISE).**
- Member of the National Graphene Association (**NGA**), United States.
- Member, Volunteer and Donator at **Greenpeace India**.
- Annual Student Member of the **Indian Science Congress Association**.
- Worked as an Executive Member of "**CHEMISTRY ASSOCIATION**" of the Department of Chemistry, NIT Warangal during the academic year 2014-15.
- Recognized and Rated as a **Very Good** Contribution towards Class Representation and Member of "Student Activity and Governing Cell" during the academic year 2013-14.

Personal Details

Father	Late. Mr. Yogaiah Tandava
Mother	Mrs. Lakshmi Devi Tandava
Date and Place of Birth	3rd August 1993, Hyderabad, India.
Gender & Marital Status	Male, Single
Blood Group	AB+
Nationality	Indian
Languages known	English-Competent User/Proficient| Hindi-Proficient| Spanish- Basic Level | French- Basic Level | Telugu-Mother Tongue.
Hobbies	Photography, Travelling, Reading books, Cricket and Movies.

References

1. **Prof. Dr. Joan Ramon Morante (Doctoral Thesis supervisor)**

Contact: jrmorante@irec.cat; Office: +34 933 562 615

2. **Dr. Sebastian Murcia Lopez (Doctoral Thesis co-supervisor)**

Contact: smurcia@irec.cat; Office: +34 933 562 615

3. **Dr. Ignacio Tudela-Montes, PhD SFHEA MRSC**

Contact: ignacio.tudela@ed.ac.uk; Office: +44 131 650 5545

4. **Dr. Kaki Shiva Shanker (Personal Mentor)**

Contact: sskaki@iict.res.in, shivaiict@gmail.com; Mobile: +91-8125510097.

Thank you for your time in reading this PhD thesis.

--- **VSRK Tandava**